BEHAVIOR AND DESIGN OF CONCENTRICALLY LOADED DUPLEX STAINLESS STEEL SINGLE EQUAL-LEG ANGLE STRUTS

A Dissertation
Presented to
The Academic Faculty

By

Nicholas A. Reynolds

In Partial Fulfillment
Of the Requirements for the Degree
Doctor of Philosophy in Civil Engineering in the
School of Civil and Environmental Engineering

Georgia Institute of Technology

August 2013

BEHAVIOR AND DESIGN OF CONCENTRICALLY LOADED DUPLEX STAINLESS STEEL SINGLE EQUAL-LEG ANGLE STRUTS

Approved By:

Dr. Abdul-Hamid Zureick, Advisor
School of Civil and Environmental Engineering
Georgia Institute of Technology

Dr. David Bergstrom
Stainless and Alloy Product Development
ATI Allegheny Ludlum

Dr. Bruce Ellingwood
School of Civil and Environmental Engineering
Georgia Institute of Technology

Dr. George Kardomateas
School of Aerospace Engineering
Georgia Institute of Technology

Dr. Leroy Emkin
School of Civil and Environmental Engineering
Georgia Institute of Technology

Date Approved: May 6, 2013

ACKNOWLEDGEMENTS

I would like to thank my advisor, Dr. Abdul-Hamid Zureick, for mentoring me as his student. His wisdom guided my intellectual development, and without his input this work would not have been possible. I would also like to thank Dr. Bruce Ellingwood for his many helpful insights throughout the progress of this work. Thanks are also due to my defense committee members, Dr. Leroy Emkin, and Dr. George Kardomateas, and Dr. David Bergstrom for their time and input.

I would like to thank my wife, Eleanor, for her loving support throughout my graduate studies and research. Her presence and kindness have kept me balanced throughout the highs and lows of this journey. I also express sincere appreciation for my family for their constant encouragement and the role they have had on my course in life: my parents Tim and Lisa Reynolds, my sister Amy Cannon, my in-laws Jessie Durham and James Durham, and my grandparents Arnold and Jean Davis and R. B. Reynolds.

I would like to acknowledge the following Georgia Tech staff who aided my research: Jeremy Mitchell, Cliff Tribble, Mike Sorenson, and Andy Udell. I would also like to thank my fellow graduate students who assisted me in conducting research: Falak Shah, Sung-Hu Kim, Dr. Robert Moser, Dr. Cliff Bishop, Amal Jayapalan, Dr. Andrew Bechtel, Josh Gresham, Daniel Schuetz, Mitchell McKay, and Tim Wright.

The research described in this thesis was made possible through the donation of ATI 2003® stainless steel, which was generously arranged by Dr. David Bergstrom and Dr. Ronald Bailey of ATI Allegheny Ludlum, and laser-welded by Stainless Structurals,

LLC (USA) and Montanstahl (CHE). Financial assistance was also provided by the U.S. Department of Defense through its SMART Scholarship Program.

TABLE OF CONTENTS

LIST OF TABLES

LIST OF FIGURES

LIST OF SYMBOLS

A	Cross-sectional area
A_e	Effective cross-sectional area
A_g	Gross cross-sectional area
A_n	Design cross-sectional area
A^o	Solution point in load-displacement space (Wempner-Riks method)
A^1	Potential solution point in load-displacement space (Wempner-Riks method)
A^{i-1}	Previous solution point
b	Leg width (measured from toe to shear center)
$\bar{b}$	Leg width (measured from heel to toe)
$\bar{b}_{eff}$	Effective leg width
b_1	Width of left leg (measured from heel to toe)
b_2	Width of right leg (measured from heel to toe)
C_p	Sample size adjustment factor
C_w	Warping constant
c_i^N	Displacement vector associated with stress residuals (Wempner-Riks method)
D_n	Nominal dead load
E	Modulus of elasticity (Young's Modulus)
E_o	Initial modulus of elasticity
E_s	Secant modulus
E_t	Tangent modulus

E_y	Tangent modulus at F_y
E_1	Elastic modulus in the 1-direction
E_2	Elastic modulus in the 2-direction
e	Load eccentricity
e	Non-dimensional yield stress, F_y/E_o (*AS/NZS 4673*)
F	Hill's anisotropic yield parameter
$F_{cr,ft}$	Flexural-torsional buckling stress (*AISC 2012*)
$F_{cr,fx}$	Flexural buckling stress (*AISC 2012*)
F_e	Elastic buckling stress (*AISC 2012*)
F_{ft}	Flexural-torsional buckling stress
F_{fx}	Flexural buckling stress for rotation about the x-axis
F_{fy}	Flexural buckling stress for rotation about the y-axis
$F_{fy,e}$	Elastic flexural buckling stress for rotation about the y-axis
F_m	Mean fabrication bias
F_t	Torsional buckling stress
$F_{t,e}$	Elastic torsional buckling stress
F_p	Proportional limit (0.01% proof stress)
F_y	Yield stress (0.2% proof stress)
$F_{y,c}$	Yield stress in compression
$F_{0.5}$	0.5% proof stress
$F_{1.0}$	1.0% proof stress
f	Design stress (*SEI/ASCE 8-02* and *AS/NZS 4673*)
f	Hill's normalized anisotropic yield criterion
G	Hill's anisotropic yield parameter

G	Shear modulus
$G_{o,back}$	Shear modulus calculated for shear coupon's back face
$G_{o,front}$	Shear modulus calculated for shear coupon's front face
G_{12}	In-plane shear modulus
G_{23}	Shear modulus in the 2-3 plane
G_{31}	Shear modulus in the 3-1 plane
H	Hill's anisotropic yield parameter
I	Moment of inertia
I_{ps}	Polar moment of inertia about the shear center
I_x	Modulus of elasticity about the minor x-axis
I_y	Modulus of elasticity about the major y-axis
I_i^N	Internal state of stress
J	St. Venant torsion constant
K_t	Effective length factor for torsion
K_x	Effective length factor for flexural about the x-axis
K_y	Effective length factor for flexural about the y-axis
K_o^{NM}	Tangent stiffness at current solution point
$K_{i\text{-}1}^{NM}$	Tangent stiffness to previous solution point
k_σ	Plate buckling coefficient
L	Length
L	Hill's anisotropic yield parameter
L_{actual}	Distance between the tips of the knife edges
L_e	Effective length
L_f	Final length

L_i	Initial length
L_n	Nominal live load
L_t	Member length for torsional buckling
L_x	Column length for flexural buckling about the x-axis
L_y	Column length for flexural buckling about the y-axis
M	Hill's anisotropic yield parameter
M_m	Mean material properties bias
N	Hill's anisotropic yield parameter
n	Ramberg-Osgood hardening parameter
n	Sample size
$n'_{0.2,1.0}$	Post-yield hardening parameter
P	Load
$P_{cr,e}$	Critical elastic buckling force
P_{exp}	Experimental buckling strength
P_{ft}	Flexural-torsional buckling strength
P_{fx}	Minor-axis flexural buckling strength
$P_{fx,e}$	Elastic minor-axis flexural buckling strength
P_{fy}	Major axis flexural buckling strength
$P_{fy,e}$	Elastic major axis flexural buckling strength
P_l	Local buckling strength
P_m	Mean strength ratio
P_n	Nominal design strength
$P_{Southwell}$	Inverse of the slope determined from Southwell plotting
P_t	Tangent modulus buckling strength

P_t	Torsional buckling strength
$P_{t,e}$	Elastic torsional buckling strength
P_u	Factored load
P^N	Loading pattern vector (Wempner-Riks method)
Q	Cross-sectional reduction factor for slender compression elements
Q_s	Reduction factor for slender unstiffened compression elements
R_{11}	Yield stress ratio in the 11-direction (transverse to loading)
R_{22}	Yield stress ratio in the 22-direction (longitudinal/loading direction)
R_{33}	Yield stress ratio in the 33-direction (through-thickness)
R_{12}	In-plane yield stress ratio (in shear)
R_{23}	Yield stress ratio in the 23 plane (in shear)
R_{31}	Yield stress ratio in the 31 plane (in shear)
R_i^N	Stress residual
r	Radius of gyration
r_o	Polar radius of gyration about the shear center
r_x	Radius of gyration about the x-axis
r_y	Radius of gyration about the y-axis
T_w	Twist factor
t	Plate thickness
t_1	Thickness of the left leg
t_2	Thickness of the right leg
u^N	Displacement pattern (Wempner-Riks method)
V_D	Coefficient of variation for dead loads

V_F	Coefficient of variation of fabrication
V_L	Coefficient of variation for live loads
V_M	Coefficient of variation of material properties
V_P	Strength coefficient of variation
v_i^N	Previous increment's displacement vector
y_o	Distance between the centroid and the shear center
α	*AS/NZS 4673* flexural buckling parameter
α	Imperfection factor (EC3, 1-4)
β	*AS/NZS 4673* flexural buckling parameter
β	$1 - \frac{y_o^2}{r_o^2}$
β_o	Reliability index
δ	Deflection
δ_o	Out-of-straightness
δ_p	Plate out-of-straightness
δ_y	Deflection in the global Y-direction
ε	Engineering strain
$\dot{\varepsilon}$	Strain increment
$\dot{\varepsilon}_{1.el}$	Elastic strain increment in the 1 (transverse) direction
$\dot{\varepsilon}_{1.pl}$	Plastic strain increment in the 1 (transverse) direction
$\dot{\varepsilon}_{2.el}$	Elastic strain increment in the 2 (longitudinal) direction
$\dot{\varepsilon}_{2.pl}$	Plastic strain increment in the 2 (longitudinal) direction
ε_t^{pl}	Cauchy (true) plastic strain
ε_y	Strain at F_y
$\varepsilon_{+45°}$	Strain measured 45° above horizontal

$\varepsilon_{-45°}$	Strain measured 45° below horizontal
η	Imperfection parameter (*AS/NZS 4673*)
η	Nonlinear reduction factor
η_s	Nonlinear reduction factor for shear
θ	Slope at the ends of a deflected, pinned-end column
κ	Plastic strain increment ratio
λ	Non-dimensional slenderness ratio, $\frac{K_x L}{r_x}\sqrt{\frac{F_y}{\pi^2 E_o}}$
λ_p	Slenderness factor, $\frac{1.052}{\sqrt{k}}\frac{b}{t}\sqrt{\frac{f}{E_o}}$
λ_o	Limiting slenderness parameter (EC3, 1-4)
λ_o	Load proportionality factor at solution point (Wempner-Riks method)
λ_0	*AS/NZS 4673* flexural buckling parameter
λ_1	Limiting slenderness parameter (*AS/NZS 4673*)
λ^N	Load-proportionality factor (Wempner-Riks method)
μ	Wempner-Riks correction scale factor
ρ	Effective width reduction factor
σ	Engineering stress
σ_{11}	Normal stress in the 11-direction
σ_{22}	Normal stress in the 22-direction
σ_{33}	Normal stress in the 33-direction
σ_{12}	In-plane shear stress (in the 12-plane)
σ_{23}	Shear stress in the 23-plane
σ_{31}	Shear stress in the 31-plane
$\bar{\sigma}_{11}$	Yield stress in the 11-direction

$\bar{\sigma}_{22}$	Yield stress in the 22-direction
$\bar{\sigma}_{33}$	Yield stress in the 33-direction
$\bar{\sigma}_{12}$	In-plane shear stress (in the 12-plane)
$\bar{\sigma}_{23}$	Shear stress in the 23-plane
$\bar{\sigma}_{31}$	Shear stress in the 31-plane
σ^{o}	User-specified yield stress
σ_b	Balanced residual stress magnitude
σ_{exp}	Average stress at P_{exp}
σ_{mj}	Residual stress correction for major axis bending
σ_{mn}	Residual stress correction for minor axis bending
σ_n	Design stress
σ_n	Residual stress correction for axial loading
σ_r	Residual stress
$\sigma_{r,c}$	Compressive residual stress
$\sigma_{r,HAZ}$	Residual stress in the heat-affected zone
$\sigma_{r,t}$	Tensile residual stress
σ_t	Torsional buckling stress
σ_t	Cauchy (true) stress
σ_u	Ultimate material strength
υ	Poisson’s ratio
φ	Perry-Robertson parameter
φ_{fx}	Resistance factor for flexural buckling
φ_{ft}	Resistance factor for flexural-torsional buckling
χ	Perry curve reduction factor (EC3, 1-4 and AS/NZS 4673)

Ø	Diameter

SUMMARY

Stainless steel has garnered attention as an alternative structural material to conventional carbon steel due to its corrosion resistance properties and aesthetic appearance. Of interest are single angles, which are frequently used in trusses, transmission towers, and as bracing diaphragms. When subjected to compression, knowledge concerning the behavior, analysis, and design of stainless steel single angles is very limited.

This thesis addresses the behavior of duplex stainless steel single equal-leg angles subject to concentric compressive loading. Two complementary approaches are used in this study, the first of which was experimental and consisted of conducting 33 full-scale buckling tests on S32003 duplex stainless steel single equal-leg angle components. Angles specimens had slenderness ratios ranging from 35 to 350 and leg width-to-thickness ratios of 7.5 to 12.3. In the second approach, computational models that accounted for material nonlinearity, material anisotropy, and geometric out-of-straightness were developed and validated using the experimentally obtained test results. These models were subsequently used to perform numerical buckling experiments to shed light on the behavior of axially loaded compression duplex stainless steel single angles for a wide range of practical leg width-to-thickness ratios.

Results from the full-scale tests and from the numerical models are shown to correlate well with the classical mechanics-based formulae, which considers nonlinear stress-strain relationships, for predicting flexural and flexural-torsional buckling strengths of singly-symmetric stainless steel members. Finally, design criteria in the form of load

and resistance factor design (LRFD) with a reliability index of 3 for buckling limit states are proposed for possible adoption in future U.S. national standards.

CHAPTER 1

INTRODUCTION

1.1 MOTIVATION

Stainless steel has attracted attention as a structural material in recent years due to its corrosion resistance and aesthetic appearance. A class of high strength grades of austenitic-ferritic stainless steel, called duplex, offers excellent strength and corrosion properties and gives indication of being a cost-effective material alternative to carbon steel for industrial and nuclear applications. Of particular interest are single angles which are frequently used in built-up sections, bracing systems, and lattice structures. While nearly all angle struts used in construction are eccentrically loaded, the eccentric strength of any compressive member requires understanding of its concentric strength. When subjected to compression, knowledge concerning the behavior, analysis, and design of stainless steel single angles is very limited.

1.2 OBJECTIVES AND SCOPE

The objectives of this research were to study the behavior of concentrically loaded duplex stainless steel single equal-leg angles experimentally and analytically across all practical slenderness and leg width-to-thickness ratios. The results of this study were used to determine an appropriate method for predicting the strength of single equal-leg angles for design.

1.3 THESIS OUTLINE

This thesis is organized according to the objectives identified above. The first focus of this investigation is the experimental behavior of duplex stainless steel single equal-leg angle struts, which was achieved through full-scale buckling tests. This data was then used to evaluate the design formulations given in current standards, using the material properties determined experimentally for the duplex grade used in the buckling tests. Numerical buckling analyses were used to further examine the design rules and standards.

Chapter 2 presents the results of a literature review which introduces the theoretical buckling formulations for singly-symmetric sections as well as experimental tests that have been conducted on equal-leg angles. Inelastic buckling theory for various buckling modes is also reviewed. The focus transitions to stainless steel compression members, which are considered in reviewing the experimental studies of concentrically-loaded struts and the existing stainless steel design standards. Lastly, the numerical methods that have been used to model the behavior of stainless steel struts are covered.

Chapter 3 presents the results from material tests, including compression, shear, and flexure, which were used to determine the material properties of grade S32003 duplex stainless steel necessary to analyze the structural response of single equal-leg angles. The distribution of residual stresses for built-up S32003 stainless steel equal-leg angle sections was also investigated.

Chapter 4 describes the experimental test program on duplex stainless steel single equal-leg angle struts. The experimental data was compared to the strengths predicted by

existing design formulations, using the material properties determined in Chapter 3. A first-order reliability analysis was performed to calculate resistance factors for design.

Chapter 5 discusses a finite element study that was performed to further evaluate the concentric strengths of single equal-leg angle sections for all practical slenderness ratios and leg slenderness. This modeling procedure was used to examine the effect of boundary conditions, out-of-straightness, and material anisotropy on column strength.

Chapter 6 presents the findings and conclusions of this thesis. The future work section gives recommendations for related topics to investigate.

CHAPTER 2

BACKGROUND

This investigation relates to both the stability of singly-symmetric sections and the inelastic buckling of columns. This chapter reviews the literature relevant to both topics. Particular attention is paid to stainless steel columns and current stainless steel design standards.

2.1 EQUAL-LEG SINGLE ANGLE STRUT

Linear Elastic Behavior

For an equal-leg single angle member, shown in Figure 2.1 wherein the shear center and centroid do not coincide, loaded concentrically in compression, the strength can be determined from consideration of four limit states including the material strength, local buckling, and overall buckling limit states, whose formulations are given by Timoshenko and Gere (1961).

1. When material strength governs the limit state, the nominal axial compression strength can be estimated from:

$$P_n = A\sigma_u \tag{2-1}$$

2. The nominal flexural buckling strength about the minor x-axis, P_{fx}, can be estimated from:

$$P_{fx} = \frac{\pi^2 E I_x}{(K_x L_x)^2} \tag{2-2}$$

3. The nominal flexural-torsional buckling strength, P_{ft}, can be estimated from:

$$P_{ft} = \frac{1}{2\beta}\left[\left(P_{fy} + P_t\right) - \sqrt{\left(P_{fy} + P_t\right)^2 - 4\beta P_t P_{fy}}\right] \tag{2-3}$$

Where

$$P_{fy} = \frac{\pi^2 E I_y}{\left(K_y L_y\right)^2} \tag{2-4}$$

$$P_t = \frac{A}{I_{ps}}\left[GJ + \frac{\pi^2 E C_w}{(K_t L_t)^2}\right] \tag{2-5}$$

$$\beta = 1 - \left(\frac{y_o}{r_o}\right)^2 \tag{2-6}$$

4. The load associated with plate buckling, P_l, can be estimated from:

$$P_l = \frac{\pi^2 E k}{12(1-\nu^2)\left(\frac{b}{t}\right)^2} A \tag{2-7}$$

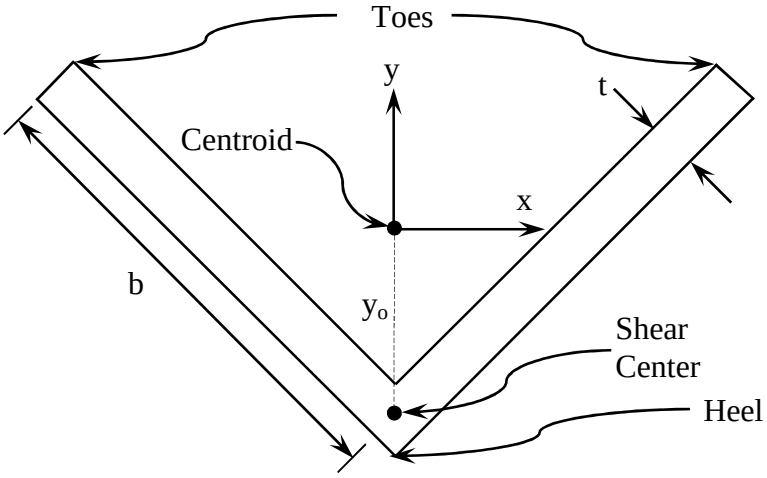

Figure 2.1- Cross-section of an equal-leg angle

The local buckling stress for equal-leg angles can be determined by treating a leg as a plate simply supported along three of the sides and free along the fourth side. It has been noted by Zureick and Steffen (2000) that the formulation for the torsional buckling stress of an equal-leg angle is identical to the plate buckling stress formulation for orthotropic materials. For linearly-elastic, isotropic, and initially straight plate members, Bleich (1952) suggested that plate buckling and flexural-torsional buckling modes are indistinguishable for equal-leg angles because they buckle simultaneously.

Since equal-leg angle sections are open thin-walled members, the warping term in Eq. (2-5) is small in comparison to the St. Venant torsion term, *GJ*, and the torsional buckling strength is often ignored (Galambos 1991; Kitipornchai and Lee 1986a; Zureick and Steffen 2000). Additionally, when considered, the difference in calculated capacities between warping restrained, K_t=0.5, and warping unrestrained, K_t=1.0, was shown to be less than 2% for carbon steel angles (Adluri and Madugula 1996b).

Review of Experimental Research Performed on Angle Struts

Hot-Rolled Mild-Steel Sections

The earliest research concerning hot-rolled carbon steel equal-leg single angles as compression members was performed on sections loaded through common construction connections by Stang and Strickenberg (1922). Later studies that investigated the behavior of concentrically loaded equal-leg carbon steel angles in compression include (Adluri and Madugula 1996b; Adluri and Murty 1996; Al-Sayed and Bjorhovde 1989a; Kennedy and Murty 1972; Kitipornchai and Lee 1986b; Thurlimann and Haaijer 1953; Wakabayashi and Nonaka 1965).

Aluminum Angles Sections

Much of the early research involving angle compression members was devoted to aeronautical applications, which focused heavily on aluminum sections based on weight considerations. The earliest experimental work of this nature was performed on concentrically loaded single duralumin angles by Jenkin (1920). A study was later conducted that focused primarily on the torsional buckling modes of plain and lipped aluminum sections (Lundquist 1930). The database was later augmented by experimental testing of approximately 250 aluminum equal-leg angles (Kollbrunner 1935). The buckling mode transition point for the local and torsional buckling modes was investigated in a parametric study on *b/t* ratios in extruded aluminum angles by Thomas (1941). The strength of aluminum angles was later tested as part of a larger survey on aluminum cross-sections by Leary and Holt (1946). Experimental work was later performed on angles loaded through one leg (Marshall et al. 1963).

Light Gage Steel Angles Sections

Light gage steel angles were tested along with the aluminum angles in the investigations by Kollbrunner (1935) and Thomas (1941). Lipped and plane brake-pressed steel angles sections were included in a study, which examined inelastic flexural-torsional buckling (Fang and Winter 1965). Slender columns with outstanding leg width/thickness (*b/t*) ratios of 15 were investigated and compared against local buckling parameters outlined in existing design specifications byMadugula et al. (1983). A later study by the same authors examined the effects of eccentric loading of cold-formed steel angles (Madugula and Ray 1984). Testing of cold-formed steel specimens, representing three *b/t* ratios and loaded with an L/1000 eccentricity, revealed that coupled flexural and

flexural-torsional buckling occurs for columns in the intermediate slenderness range and pure flexural-torsional buckling occurs for the shortest specimens (Popovic et al. 1999). Additionally, a decrease in member capacity was observed when the load eccentricity was applied toward the unrestrained edges (toes). The effective width provisions of the *b/t* ratio on member capacity was investigated using both experimental and finite element analyses and compared to the effective width provision outlined in *AS/NZS 4673* by Ellobody and Young (2005). Lipped angle sections were also tested and compared to the effective area provisions of the 2001 North American Standard and the 1996 Australian/New Zealand Standard for light gage sections (Young 2005).

Inelastic Formulations of Overall Member Buckling

Inelastic buckling was first considered by Engesser in 1889, who replaced the longitudinal modulus, E_o, with the tangent modulus, E_t, in the Euler buckling equation. This can be represented by multiplying the elastic equation by a nonlinear reduction factor, η, as shown in Eq. (2-8). This strength was later shown by Shanley (1947) to correspond to the maximum load at which an initially straight column would remain straight. Although this is considered the bifurcation solution of inelastic column buckling, load may continue to increase with bending and the tangent modulus load can be considered a lower bound of column strength. Due to imperfections in actual columns, the tangent modulus method for strength prediction corresponds well with experimental data and has frequently been adopted for design purposes.

$$P_{fx} = \frac{\pi^2 E_o I_x}{(K_x L)^2}\eta;\ \eta = \frac{E_t}{E_o} \tag{2-8}$$

The actual strengths for imperfect columns in the inelastic range cannot be as easily determined as for linear-elastic materials, since the deformed shape is not sinusoidal and changes as a function of the applied load as illustrated by Figure 2.2. Von Karman used nonlinear moment-curvature relationships to predict the flexural behavior of inelastic beam-columns (1910). Chwalla's (1934; 1935) generalized procedure, which extended on von Karman's work to concentrically loaded columns, relies on a graphical interpretation for determining column strength. Unlike similar studies concerning elastic-perfectly plastic material models for which closed form solutions could be obtained (Horne 1956; Ježek 1934), Chwalla's method may be applied to materials with rounded nonlinear stress-strain relationships. It has been suggested by Bažant and Cedolin (1991) that the strengths of imperfect columns in the inelastic range are today best determined according to the finite element method.

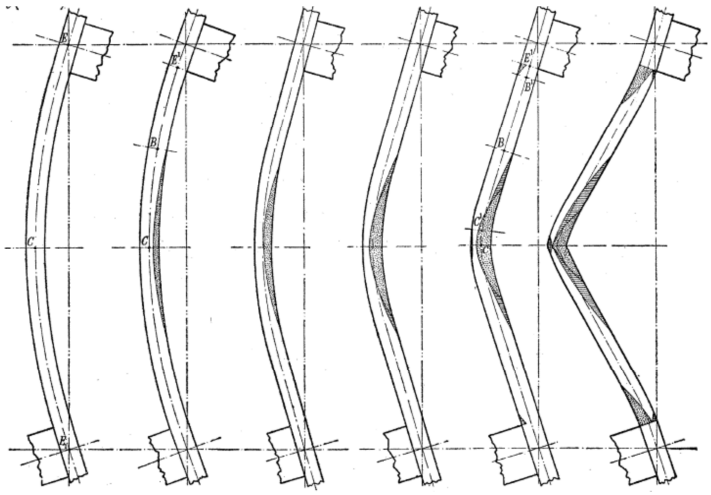

Figure 2.2- Buckled shape for increased nonlinear material behavior (Baker et al. 1949)

Experimental Buckling Tests

Experimental results for equal-leg single angle members which buckled inelastically in the flexural mode generally showed agreement with loads predicted using the tangent modulus formula, given by Eq. (2-8), which sometimes gave unconservative strength predictions based on the initially-straight assumption of tangent modulus theory (Bredenkamp and van den Berg 1995; Kennedy and Murty 1972; Wakabayashi and Nonaka 1965). Later studies considered the patterning of residual stresses in predicting inelastic column strength (Al-Sayed and Bjorhovde 1989b; Kitipornchai and Lee 1986a).

The majority of experimental equal-leg single angle test specimens have buckled flexurally; however, in the few tests which considered the flexural-torsional buckling of equal-leg angles, buckling was characterized by sudden deformation in comparison to both the flexural-torsional buckling of unequal-leg angles or the flexural buckling of equal-leg angles (Adluri and Madugula 1996b; Al-Sayed and Bjorhovde 1989a; Kennedy and Murty 1972; Wakabayashi and Nonaka 1965). The increasing susceptibility of single equal-leg angles to flexural-torsional buckling with increasing *b/t* ratios for equal-leg angles was noted by Al-Sayed and Bjorhovde (1989a). Formulations used to estimate the inelastic flexural-torsional buckling strength have generally involved applying nonlinear reduction factors to the elastic and shear moduli to account for nonlinear behavior. The tangent modulus is used in place of the longitudinal modulus for the flexural buckling about the major axis Eq. (2-9), as in Eq. (2-8), but different approaches have been taken concerning the shear modulus plasticity reduction factor, η_s. The most common approach involves keeping the shear modulus proportional to the longitudinal tangent modulus ($\eta_s=\eta$) for the torsional buckling strength, Eq. (2-10) (Adluri and Madugula 1996b; Al-

Sayed and Bjorhovde 1989b; Fang and Winter 1965; van den Berg and van der Merwe 1988). This approach was found to be very conservative based on the experimental data of aluminum angles (Leary and Holt 1946) and has prompted other researchers to use the initial shear modulus (η_s=1) (Kitipornchai and Lee 1986a). It was later shown that the flexural-torsional buckling load governs the capacities of stocky carbon steel equal-leg single angle columns if the shear modulus remained proportional to the tangent modulus, but would never govern if it remained unreduced, as shown in Figure 2.3 (Galambos 1991).

$$P_{fy} = \frac{\pi^2 E_o I_y}{(K_y L)^2}\eta;\ \eta = \frac{E_t}{E_o} \tag{2-9}$$

$$P_t = \frac{A}{I_{ps}}\left[G_o J\eta_s + \frac{\pi^2 E_o C_w}{(K_t L)^2}\eta\right];\ \eta = \frac{E_t}{E_o} \tag{2-10}$$

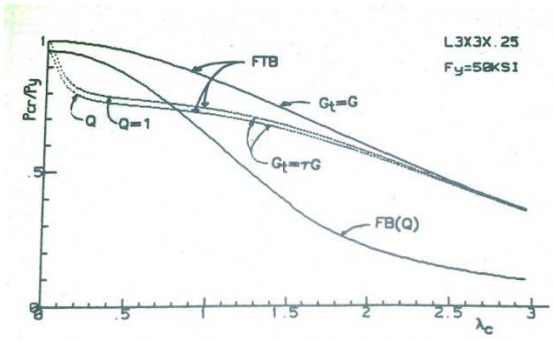

Figure 2.3- Flexural-torsional buckling sensitivity to shear (Galambos 1991)

Inelastic Formulations for Local Plate Buckling

Unlike treatment of the minor axis flexural buckling strength, inelastic plate buckling involves biaxial bending. The material stiffness in the transverse direction may not remain proportional to the longitudinal modulus for increased nonlinear behavior.

This implies increased orthotropic behavior beyond the elastic range. Solutions for the buckling strength of uniformly loaded orthotropic plates simply supported on three sides have been derived by Haaijer (1957) and Holston (1970). Inelastic buckling of plates, however, has been treated differently by various researchers. Several empirical nonlinear reduction factors have been proposed for Eq. (2-7) to account for the differing stiffness in the longitudinal and transverse directions: $\frac{3\left(E_t/E_o\right)+\sqrt{E_t/E_o}}{\left(1+\sqrt{E_t/E_o}\right)^2}$ (Kollbrunner 1935), E_s/E_o (Gerard 1946), $\sqrt[3]{E_t/E_o}$ (Leary and Holt 1946), and $\sqrt{E_t/E_o}$ (Bleich 1952).

Plasticity theories were later employed to develop expressions for the plate buckling stresses. Ilyushin (1947) developed a plastic plate buckling theory based on deformation plasticity theory, which was modified by Stowell (1948) to account for lateral deflection prior to buckling. A formulation for inelastic plate buckling was developed based on the J_2 incremental flow theory by Handelman and Prager (1948), which did not follow the behavior observed by Pride and Heimerl (1949) on tests of aluminum SHS sections. A formulation based on incremental plasticity theory later showed agreement with experimental results of outstanding elements when orthotropic material behavior was considered (Haaijer 1957). More recently, flow theory was used shown to predict the inelastic buckling stress of anisotropic plates when inelastic shear stiffness was considered (Becque 2010). This study gave theoretical justification to the empirical nonlinear reduction factors proposed by Bleich for a long simply supported plate on four sides and Gerard for a long simply supported plate on three sides.

2.2 COMPRESSIVE BEHAVIOR OF STAINLESS STEELS

Material Characterization of Stainless Steels

Unlike carbon steels, stainless steels exhibit nonlinear stress-strain behavior for all stress values. This can be seen based on their low proportional limits, indistinct yield points, and strain-hardening as shown in Figure 2.4. The stress-strain relationship is commonly characterized using a three-parameter modified Ramberg-Osgood relationship, given by Eq. (2-11), which was developed by Ramberg and Osgood (1943) and subsequently modified by Hill (1944). The Ramberg-Osgood hardening parameter, *n,* varies depending on the grade of stainless steel as well as whether loading is tensile or compressive. The tensile stress-strain behavior of stainless steels is typically characterized by larger values of *n,* which corresponds to sharper changes in curvature around the yield stress and less pronounced strain-hardening. Stainless steels in compression exhibit more gradual yielding than in tension and are described using a smaller strain hardening parameter. As *n* approaches infinity, the Ramberg-Osgood stress-strain curve becomes identical to that of an elastic-perfectly plastic material.

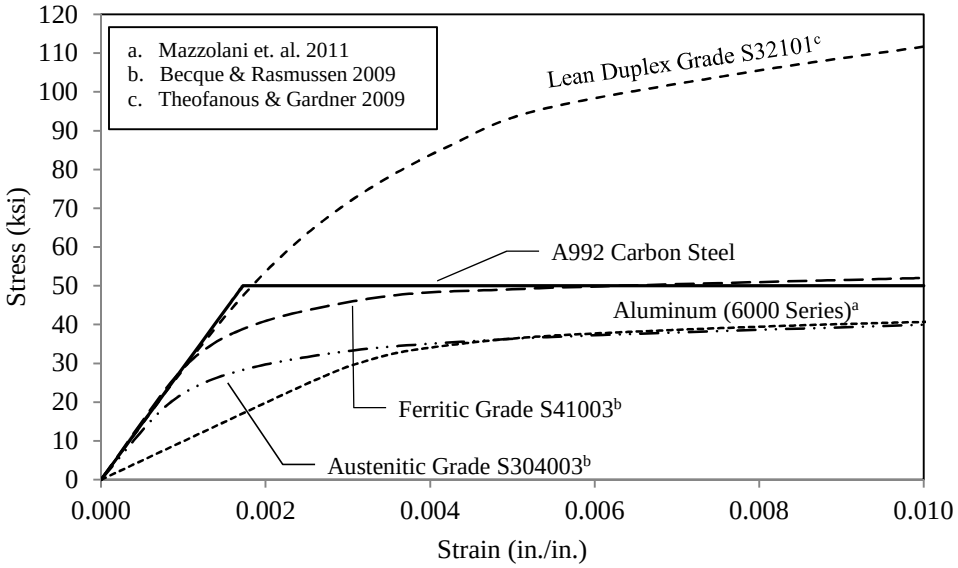

Figure 2.4- Idealized stress-strain behavior for various engineering metals

$$\varepsilon = \frac{\sigma}{E_o} + 0.002\left(\frac{\sigma}{F_y}\right)^n ; \sigma \leq F_y \tag{2-11}$$

Where

E_o = Initial Modulus of Elasticity

F_y = Yield Stress, (0.2% Proof Stress)

F_p = Proportional Limit, (0.01% Proof Stress)

$$n = \frac{\ln(0.05)}{\ln\left(\frac{F_p}{F_y}\right)} \tag{2-12}$$

σ = Engineering Stress

ε = Engineering Strain

Beyond F_y, Eq. (2-11) mischaracterizes the stress-strain relationship of stainless steel. To describe full-range stress-strain behavior of stainless steel in compression, a

post-yield Ramberg-Osgood relationship was developed by Gardner and Nethercot (2004a) based on a similar relationship developed for stainless steel in tension by Rasmussen (2003). This relationship uses Eq. (2-11) to describe the stress-strain relationship up to F_y, and Eq. (2-13) for F_y to the 1.0% proof stress, $F_{1.0.}$

$$\varepsilon = \frac{\sigma - F_y}{E_y} + \left(0.008 - \frac{F_{1.0} - F_y}{E_y}\right)\left(\frac{\sigma - F_y}{F_{1.0} - F_y}\right)^{n'_{0.2,1.0}} + \varepsilon_y;\ \sigma > F_y \tag{2-13}$$

Where

$F_{1.0}$ = 1.0% Proof Stress

$$\varepsilon_y = 0.002 + \frac{F_y}{E_o} \tag{2-14}$$

$$E_y = \frac{F_y E_o}{F_y + 0.002 n E_o} \tag{2-15}$$

Cold-formed Stainless Steel Columns

The majority of experimental research on stainless steel columns has been devoted to concentrically loaded cold-formed sections, which buckle in the flexural mode. Studies have mostly been limited to doubly-symmetric hollow sections including square hollow sections (SHS), rectangular hollow sections (RHS), and circular hollow sections (CHS), (Gardner and Nethercot 2004b; Liu and Young 2003; Rasmussen and Hancock 1990; Talja and Salmi 1995; Young and Hartono 2002; Young and Liu 2003; Young and Lui 2006). Additionally, closed hollow sections have been tested which were fabricated by bonding two open sections together (Hammer and Petersen 1955; Johnson and Winter 1966). Early stainless steel buckling tests involving open sections also examined flexural buckling (Coetsee et al. 1990; Johnson and Winter 1966), but recent

studies have focused on the interaction between global buckling modes and local buckling or distortional buckling (Becque and Rasmussen 2009a; Becque and Rasmussen 2009b; Lecce and Rasmussen 2006; Rossi et al. 2010). Test specimens have predominantly represented austenitic grades of stainless steel, S30100 and S30400. More recent tests involved sections made from high strength duplex stainless steel, (Ellobody 2007; Ellobody and Young 2005; Theofanous and Gardner 2009; Young and Lui 2006).

Interaction between flexural and local buckling modes was observed in many of these investigations due to the plate slenderness of cold-formed sections. Pure flexural buckling generally only occurs for slender columns or specimens which have nonslender cross-sections. Of the specimens which exhibited pure flexural buckling, close agreement was seen between experimental data and capacities predicted using the tangent modulus approach (Hammer and Petersen 1955; Johnson and Winter 1966; Rasmussen and Hancock 1990). The column strengths have been shown to be dependent on the cross-sectional shape. When corners, which undergo work-hardening in the fabrication process, are located near the extreme fibers of a cross-section, the cross-section exhibits a strength greater than the tangent modulus prediction, which does not take into account the location of the strained hardened regions in the cross-section (Hammer and Petersen 1955; Johnson and Winter 1966; Rasmussen and Hancock 1990).

The flexural-torsional buckling mode has not been explored as thoroughly for stainless steels as the flexural buckling mode. For singly-symmetric sections, it occurs at high stresses, which can also cause local or distortional buckling thereby making it difficult to investigate. Only one study has directly investigated the flexural-torsional buckling mode of failure for stainless steel members (van den Berg and van der Merwe

1988). The lengths of the hat specimens were selected to ensure flexural-torsional buckling mode of failure. It was not reported whether or not cross-sectional distortion occurred during testing, but several of the slender specimens failed due to flexural buckling. Experimental data were compared to the tangent modulus formulation given by Eq. (2-8), taking $\eta_s=\eta$, and are shown in Figure 2.5. The flexural-torsional buckling mode was also peripherally considered in a later study which investigated the interaction between distortional and flexural-torsional buckling (Rossi et al. 2010). All the lipped-channel sections were designed to undergo distortional buckling prior to global buckling, and uncoupled flexural-torsional buckling was only observed for the longest columns.

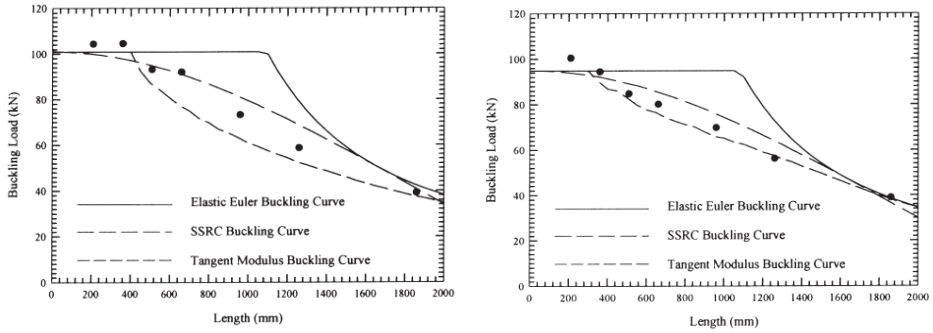

Figure 2.5- Results of flexural-torsional buckling tests. Left: S30400, Right S41003 (van den Berg 2000)

Hot-rolled and Built-up Stainless Steel Columns

Limited data exists on hot-rolled or built-up sections. The available data was performed on sections made of S41003 (3Cr12) grade stainless steel at Rand Afrikaans University. Built-up I-sections were fabricated by welding hot-rolled plates together and tested in compression to determine the flexural buckling strength (Bredenkamp and van den Berg 1995). Experimental results generally exceeded the stub column tangent

modulus predictions by approximately 20%, suggesting that the end fixtures exerted greater fixity than assumed. Similar tests were conducted on hot-rolled specimens of the same shape and material; however, experimental results showed better agreement with the tangent modulus predictions, as shown in Figure 2.6 (Bredenkamp et al. 1994).

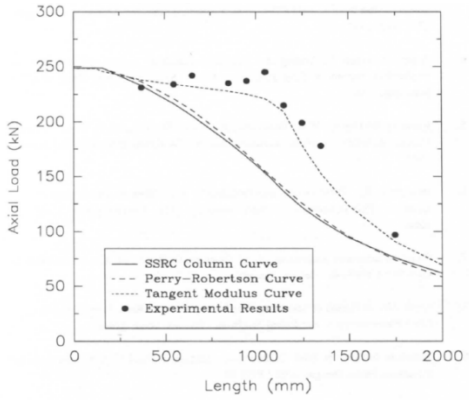

Figure 2.6- Hot-rolled S41003 I-column results (ABAQUS 2011; Bredenkamp et al. 1994)

An experimental investigation was conducted to determine the strengths of 17 hot-rolled compact equal-leg angles having the same cross-section, b/t=8 (van den Berg et al. 1995); however, all of the specimens buckled in the flexural mode. Like the hot-rolled wide-flange columns, data correlated well with the tangent modulus buckling load predictions; however, it should be noted that in these studies, columns were aligned by adjusting the loading eccentricity to achieve uniform strain at midheight.

Current Design Practice

Experimental research has been used in the development of structural stainless steel design rules and standards: *Design Manual for Structural Stainless Steel (Euro-Inox)* (SCI and Euro-Inox 2006), *Eurocode3 Part 1-4: General Rules – Supplementary*

rules for Stainless Stee s (EC3, 1-4) (Eurocode 3 2006), the *SEI/ASCE 8-02: Specification for the Design of Cold-formed Stainless Steel Structural members(SEI/ASCE 8-02), AS/NZS 4673:2001 Cold-formed Stainless Steel Structures(AS/NZS 4673),* and *AISC Design Guide: Structural Stainless Steel (AISC 2012)*. The treatment of concentrically loaded sections by each of these design rules is briefly described below, and further discussion is presented in Chapter 4. It should first be noted that four of the five design rules are suitable for the design of cold-formed members, while the (draft) *AISC Design Guide* for stainless steel limits its scope to hot-rolled and welded sections. The European standards can be used to design built-up thick plate members in addition to cold-formed sections.

Slender elements

It is important to note that each standard and design rule accounts for slender elements differently. Most design rules use some form of the effective width concept, which was first used by von Karman et al. (1932) and later formulated by Winter (1947). Additionally two other approaches exist, including the Continuous Strength Method (Gardner and Nethercot 2004c) and the Direct Strength Method (Schafer 2008), which are not considered in this review.

The draft *AISC Design Guide* for stainless steel utilizes the Q-reduction method incorporated in its carbon steel design manual (AISC 2005). Both *AS/NZS 4673* and *SEI/ASCE 8-02* calculate the effective widths based on both cross-sectional dimensions and the limit state stress, which is multiplied by the effective cross-sectional area to calculate the design strength. *EC3, 1-4* and *Euro-Inox* only consider cross-sectional

dimensions in computing effective widths, which are used in computing effective column slenderness.

SEI/ASCE 8-02: Specification for the Design of Cold-formed Stainless Steel Structural Members

The *SEI/ASCE 8-02* utilizes the tangent modulus approach defined in Eq. (2-8) for minor-axis flexural buckling. The tangent modulus approach is also employed in calculating the flexural-torsional buckling load, Eq. (2-3), of singly-symmetric sections, using E_t/E_o for both η Eq. (2-10) and η_s Eq. (2-9). Both equations require iterative calculations to determine the buckling load. For singly-symmetric sections, the design stress is taken as the stress associated with the lower of the flexural or flexural-torsional buckling loads (SEI/ASCE 8-02).

Eurocode 3 EN 1993 1-4: Design of Steel Structures, Supplementary Rules for Stainless Steels; Design Manual for Structural Stainless Steel

These design rules utilize an explicit approach to calculate the flexural buckling strength of a stainless steel member. The design stress is computed using the Perry-Robertson Curve given by Eq. (2-16), which is also used in *Eurocode 3, 1993 1-1* for carbon steel; however, different values are used for the parameters, λ_o and α, which are based on calibrations against the stainless steel test data. These values vary depending on the method by which the section was fabricated. Additionally, alternate values exist for λ_o and α if the flexural-torsional buckling mode is considered. An equivalent column slenderness ratio, λ, must be used in computing the flexural-torsional buckling strength. It is noted that these design rules generalize the behavior of all grades of duplex and austenitic stainless steel, making no adjustment to consider the stress-strain relationship

of the stainless steel being used (specifically the Ramberg-Osgood hardening parameter *n*) (Eurocode 3 2006; SCI and Euro-Inox 2006).

$$\sigma_n = \frac{F_y}{\varphi(\alpha, \lambda_o, \lambda) + \sqrt{\varphi^2(\alpha, \lambda_o, \lambda) - \lambda^2}} \leq F_y \qquad (2\text{-}16)$$

Australian/New Zealand 4673: Cold-Formed Stainless Steel Structures

The *AS/NZS 4673* standard allows for the strength of concentrically loaded columns to be computed using the same iterative methods as *SEI/ASCE 8-02*. Alternatively, an explicit Perry-Robertson formulation, given by Eq. (2-17), may be used to compute the flexural buckling strength (AS/NZS 4673 2001). Unlike the European standard, the imperfection parameter, φ, varies depending on the stress-strain relationship of the selected grade of stainless steel. It is computed using the parameters, α, β, λ_o, and λ_1, which can be calculated using the Ramberg-Osgood parameters of the selected grade. It has been observed that the iterative (tangent modulus) approach used in *SEI/ASCE 8-02* predicts higher column strengths than the Australian/New Zealand explicit formulation along with more scatter. As a result, the explicit formulation is associated with a higher resistance factor (Rasmussen and Rondal 1997a).

$$\sigma_n = \frac{\sigma_y}{\varphi(\alpha, \beta, \lambda_o, \lambda_1, \lambda) + \sqrt{\varphi^2(\alpha, \beta, \lambda_o, \lambda_1, \lambda) - \lambda^2}} \leq \sigma_y \qquad (2\text{-}17)$$

AISC Design Guide: Structural Stainless Steel

The *AISC Design Guide* for structural stainless steel, which is in draft form at the time that this thesis was written, adjusts the formulations found in (AISC 2005) based on experimental test data for stainless steel members. In compression, the buckling stresses are computed for stainless steel columns assuming linear elastic material behavior, which are substituted into stainless steel column curve formulations. Like the European standard, the *AISC Design Guide* does not consider the degree of nonlinearity of a stress-strain curve.

2.3 NUMERICAL BUCKLING ANALYSES

Numerical analyses have been effectively used by researchers to generate column curves for different sections. The earliest analyses were conducted on members that failed due to overall flexural buckling. Probabilistic column curves were generated based on variations in the values of residual stresses and magnitudes of column out-of-straightness (Bjorhovde 1972). The effect of residual-stresses on initially-straight angle sections was investigated numerically by Kitipornchai and Lee (1986a) and Al-Sayed and Bjorhovde (1989b). This method was later applied to the flexural buckling of hot-rolled angle sections using documented residual stress patterns and an out-of-straightness of L/1500 (Adluri and Madugula 1996a).

For columns made of materials with nonlinear stress-strain-relationships, it is necessary to model columns with local and global imperfections in order to cause non-axial/longitudinal deformations. An algorithm frequently used to investigate the load-displacement relationships of such cases is the Wempner-Riks loading procedure. One of the earliest applications of this algorithm in investigating stainless steel was in

determining the buckling strength of S310803 grade stainless steel plates, which closely matched experimental test results when a multi-linear isotropic hardening material model was used (Rasmussen et al. 2003) Additionally, it was also noted in this study that using anisotropic material models resulted almost no difference compared to an isotropic material model. This modeling procedure was later used to determine effective-width parameters in terms of Ramberg-Osgood properties (Bezkorovainy et al. 2003).

The Wempner-Riks procedure was extended to stainless steel columns to investigate the interaction of buckling modes. This was first used to perform a parametric study on plate slenderness values of cold-formed SHS and RHS S31803 columns for various slenderness ratios (Ellobody and Young 2005). A similar parametric study was undertaken to determine the strength increase associated with adding midplate stiffeners to the SHS and RHS sections (Ellobody 2007). The Wempner-Riks procedure has also been used to model S32101 lean-duplex stainless steel RHS and SHS sections (Huang and Young 2012; Theofanous and Gardner 2009). This procedure was also extended to open stainless steel sections to investigate the interaction between flexural and local buckling (Becque and Rasmussen 2009a; Becque and Rasmussen 2009b).

2.4 CRITICAL REVIEW

The behavior of stainless steel sections in compression is not a new topic, but the majority of this research has either focused on cold-formed sections or on ferritic stainless steels. For cold-formed sections, data often reflects work-hardening and interaction between local and global buckling modes. For ferritic stainless steel sections, data related to overall buckling modes often does not show deviation from linear material behavior since ferritic grades of stainless steel have a high proportional limit. Flexural

buckling data generally showed agreement with the strength predictions computed using the tangent modulus; however much of the data eliminated the effects of column out-of-straightness based on the alignment of their specimens. Less work has focused on the overall flexural-torsional buckling of stainless steel members, which is currently limited to hat sections (van den Berg and van der Merwe 1988).

Limited attention has been paid to equal-leg stainless steel angles. Ferritic stainless steel equal-leg single angles have been tested, which showed agreement with the tangent modulus column curve (van den Berg et al. 1995); however, data in this study were based on the results of one compact cross-section. As a result, specimens only buckled in the flexural mode, which prevented analysis of the effect of plate width/thickness ratios on flexural-torsional buckling in stainless steel.

This review of existing literature revealed that insufficient data exists for design recommendations to be made for stainless steel equal-leg single angle sections. Current limit-state design practice requires that concentrically loaded singly-symmetric columns be designed for flexural and flexural-torsional buckling modes; however, this requires that both the transition between two global buckling modes and their associated strengths be understood. Existing design standards will be evaluated through experimental and numerical testing, which is described in subsequent chapters.

CHAPTER 3

MATERIAL CHARACTERIZATION

The chapter presents the results of tests conducted to determine the material properties of UNS S32003 (ATI 2003®) grade duplex stainless steel which are relevant for the structural analysis of sections composed of S32003 in compression. Also presented are the residual stress patterns of welded S32003 stainless steel angles.

3.1 UNS S32003 MATERIAL DESCRIPTION

The microstructure of S32003, shown in Figure 3.1, contains both body-centered cubic (BCC) ferritic and face-centered cubic (FCC) austenitic phases. The elemental composition of S32003 is given in Table 3.1.

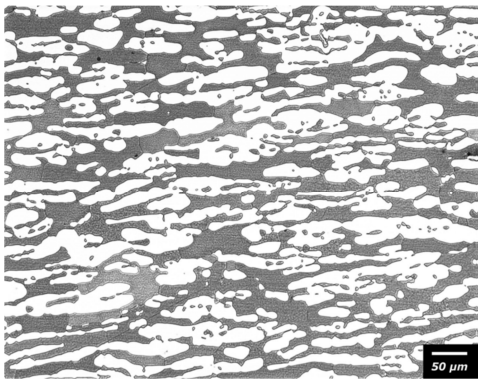

Figure 3.1- S32003 duplex microstructure (ATI Allegheny Ludlum)

® Registered trademark of ATI Properties, Inc.

Table 3.1- Elemental composition of S32003(ASTM A240-11)

Element	Composition, (% Weight)
C	0.030max.
Mn	2.00 max.
P	0.030max.
S	0.020max.
Si	1.00max.
Mo	1.50-2.00
N	0.14-0.20
Cr	19.5 - 22.5
Ni	3.0 – 4.0
Iron	Balance

Compressive Stress-strain Relationship

To construct the full-range compressive stress-strain curve for S32003, five stub column tests were conducted, guided by "Technical Memorandum No. 3" of the *Guide to Stability Design Criteria for Metal Structures* (Ziemian 2006). In order to avoid local buckling of angle sections tested in compression, doubly-symmetric tubular sections were tested. Due to the unavailability of laser-welded tubular sections, tubular sections were fabricated by TIG welding together two L2 x 2 x ¼ in. S32003 equal-leg angles positioned toe-to-toe. Each column was instrumented with four strain rosettes, with one rosette mounted at midheight on each face as shown in Figure 3.2. The test set-up also included a 200-kip load cell to measure load, which was applied using a SATEC testing machine. Data were recorded continuously using data acquisition software.

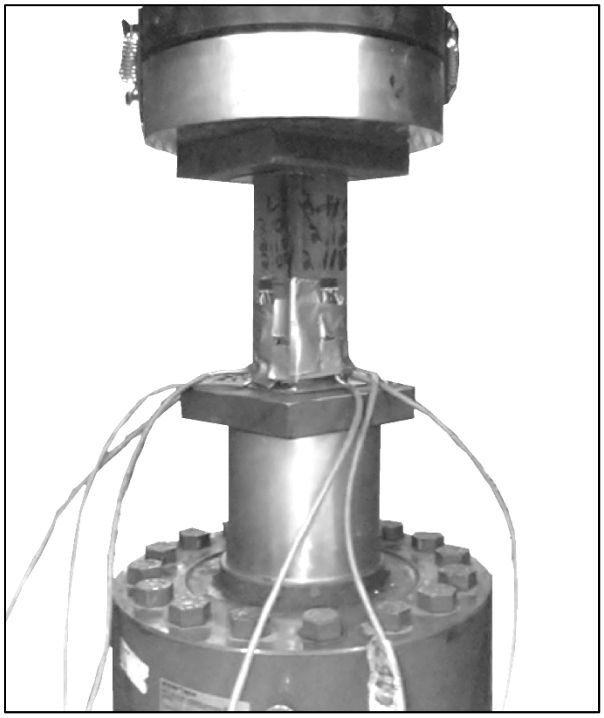

Figure 3.2- Stub column test set-up

Results

The experimental stress-strain curve of each stub column is plotted in Figure 3.3. During testing of Column 3, the soldering tabs disconnected from one of the strain rosettes prior to yield. As a result, only three strain rosettes were used to analyze the data for this specimen. Principal strains were calculated from the strain rosettes data. For each rosette, the compressive principal strain was found to be within 1% of the strain measured by the strain gage oriented parallel to the direction of loading. Poisson's ratio was computed using the data from each of the 19 functioning strain rosettes by dividing the principal strain in the direction transverse to loading by the principal strain parallel to the loading direction. The resulting values are plotted in Figure 3.4.

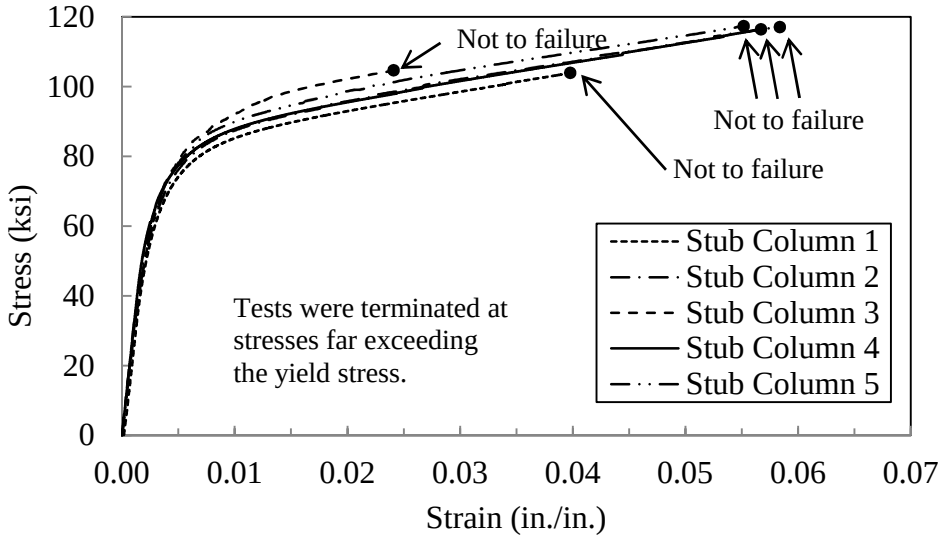

Figure 3.3- Stub column stress-strain behavior

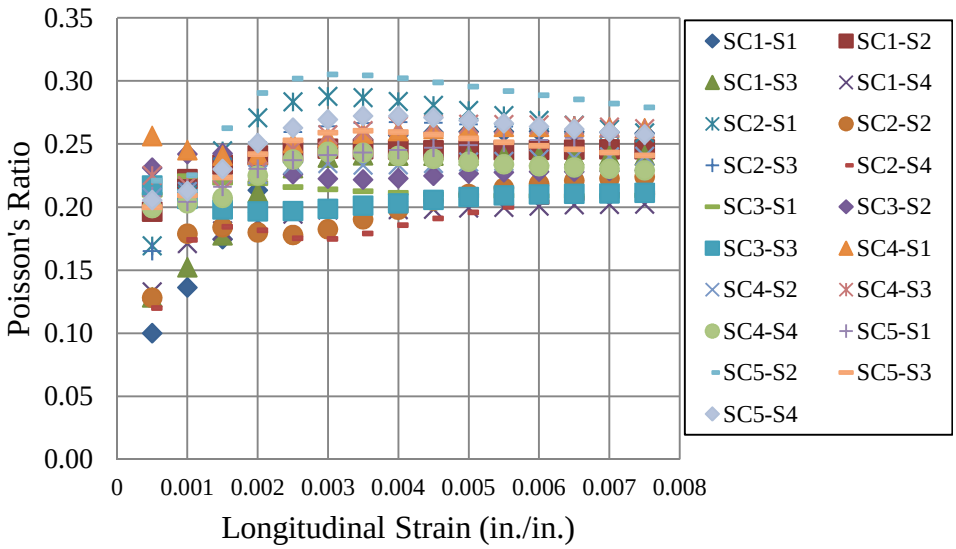

Figure 3.4- Poisson's ratio corresponding to various longitudinal strains

Discussions

Initial Modulus of Elasticity

The initial compression modulus of elasticity, E_o, was determined from stress-strain curves at strains less than 0.25% using the method proscribed by Section 9.4 of (ASTM E111-04). The resulting values for E_o are listed in Table 3.2.

Table 3.2- Modulus of elasticity based on ASTM E111-04

Specimen	E_o (ksi)
Stub column 1	28318
Stub column 2	27925
Stub column 3	28631
Stub column 4	29356
Stub column 5	28987
Average	28643

Poisson's Ratio

The mean and coefficient of variation of Poisson's ratio data were calculated at each 0.0005 in./in. increment; these values are given in Table 3.3. Large variability in the calculated Poisson's ratios existed for strains near 0.0005 (in./in.), but variability decreased for strains of 0.001 (in./in.) and higher. This can be seen in Figure 3.5. Poisson's ratio approaches 0.24 at strains of 0.003 (in./in.) and higher. This is less than the Poisson's ratio value of 0.3 reported in *AS/NZS 4673*, indicating that further examination of Poisson's ratio is necessary in the future.

Table 3.3- Poisson's ratio for longitudinal compression

Longitudinal Strain (in./in.)	Mean Poisson's Ratio	Coefficient of Variation
0.0005	0.185	0.238
0.0010	0.204	0.141
0.0015	0.215	0.121
0.0020	0.228	0.126
0.0025	0.235	0.140
0.0030	0.239	0.143
0.0035	0.241	0.139
0.0040	0.242	0.132
0.0045	0.242	0.124
0.0050	0.242	0.116
0.0055	0.242	0.110
0.0060	0.242	0.104
0.0065	0.242	0.099
0.0070	0.241	0.094
0.0075	0.241	0.091

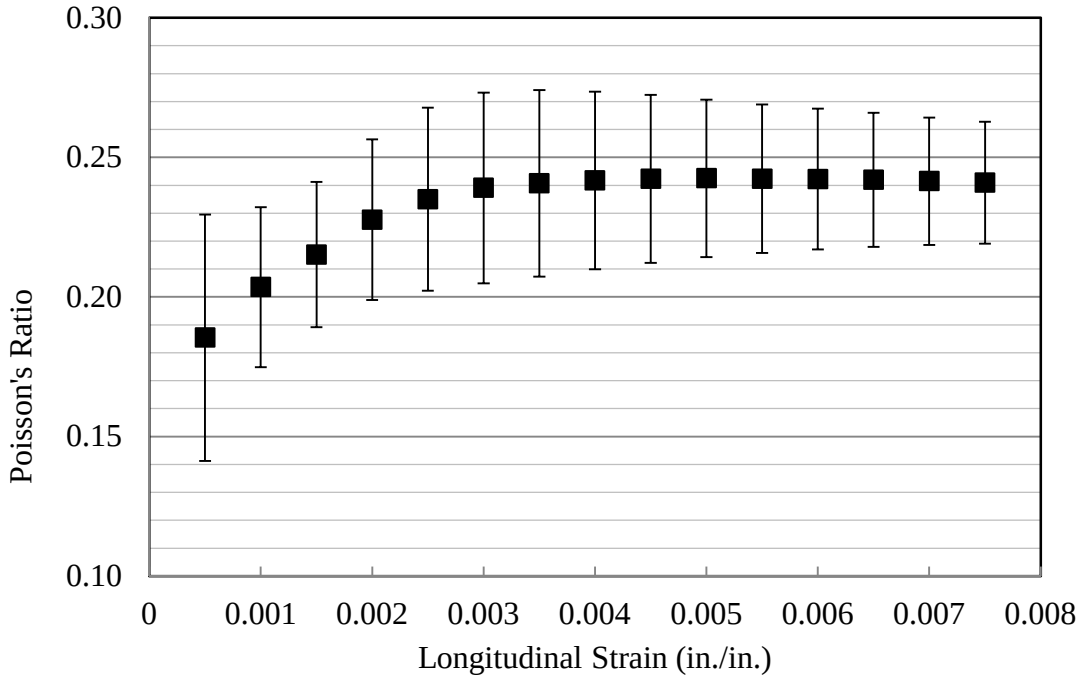

Figure 3.5- Poisson's ratio variability

Initial Shear Modulus

The initial shear modulus of S32003, G_o, was determined from eight tests conducted on notched coupons subject to a four-point asymmetric loading configuration. This test procedure is commonly used for determining the in-plane shear modulus of polymer composites and outlined in ASTM D-5379. The eight shear coupon specimens, of which four were oriented in the longitudinal direction and four were oriented in the transverse direction (as shown in Figure 3.6), were cut from S32003 L4 x 4 x $^{5}/_{16}$ angle sections using a water jet cutter.

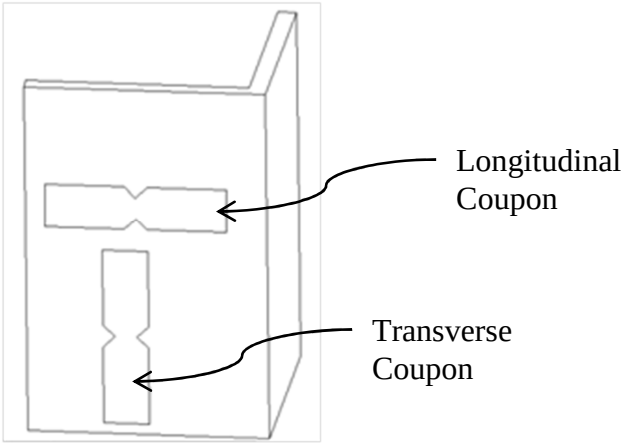

Figure 3.6- V-notched shear coupon orientations

The experimental test setup is shown in Figure 3.7. Each specimen was instrumented with two orthogonal strain gages on the front and back faces of the specimens, oriented at ±45° from horizontal. Tests were conducted in a SATEC testing machine where the load was applied to the loading fixture using a 0.5 in. diameter hardened steel ball. Load was measured using a 10-kip load cell. Data were recorded

continuously using data acquisition software. Due to limitations of the testing fixture, tests were terminated at 3 kips.

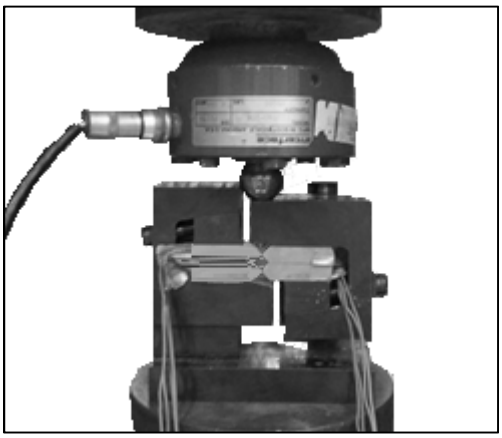

Figure 3.7- Shear testing setup

Results

Shear stress was calculated as the measured load divided by the cross-sectional area of the narrow section of the notch, and the shear strain was computed for each face as $|\varepsilon_{+45^\circ}| + |\varepsilon_{-45^\circ}|$. The in-plane shear moduli were determined through regression analyses of data.

Data were examined to determine how much bending and twisting was present during testing. Cho (1998) recommends that data meet the tolerances $\frac{|\varepsilon_{+45^\circ}|-|\varepsilon_{-45^\circ}|}{|\varepsilon_{+45^\circ}|+|\varepsilon_{-45^\circ}|} \leq 5\%$ and $0.9 \leq \frac{|\varepsilon_{+45^\circ}|}{|\varepsilon_{-45^\circ}|} \leq 1.1$ to satisfy pure shear loading conditions. ASTM D-5379 also requires that the twist factor, T_w, given by Eq. (3-1) does not exceed 3.0% at 0.4% absolute strain. Although strains never reached that level, values for the twist fell below 3%. The coupon bending/twisting indicators, reported in Table 3.4, generally fall within

these tolerances, demonstrating the validity of the testing procedure. The results from the shear testing are summarized below in Table 3.5.

$$T_w = \frac{\left|G_{o\_front} - G_{o\_back}\right|}{G_{o\_front} + G_{o\_back}} \tag{3-1}$$

Table 3.4- Shear tolerances

Specimen		T_w	Front Face		Back Face	
			$\frac{\left\|\varepsilon_{+45^\circ}\right\| - \left\|\varepsilon_{-45^\circ}\right\|}{\left\|\varepsilon_{+45^\circ}\right\| + \left\|\varepsilon_{-45^\circ}\right\|}$	$\frac{\left\|\varepsilon_{+45^\circ}\right\|}{\left\|\varepsilon_{-45^\circ}\right\|}$	$\frac{\left\|\varepsilon_{+45^\circ}\right\| - \left\|\varepsilon_{-45^\circ}\right\|}{\left\|\varepsilon_{+45^\circ}\right\| + \left\|\varepsilon_{-45^\circ}\right\|}$	$\frac{\left\|\varepsilon_{+45^\circ}\right\|}{\left\|\varepsilon_{-45^\circ}\right\|}$
Transverse	1	0.003	0.03	1.04	0.09	1.19
	2	0.025	0.07	0.87	0.07	0.88
	3	0.003	0.03	0.93	0.04	0.92
	4	0.009	0.07	1.15	0.04	1.08
Longitudinal	1	0.010	0.07	0.86	0.06	0.88
	2	0.027	0.01	0.97	0.06	0.89
	3	0.000	0.04	0.92	0.10	0.81
	4	0.008	0.01	1.02	0.03	1.07

Table 3.5- In-plane shear modulus results

	Specimen	Cross-Sectional Area (in.^{2})	G_{o_front} (ksi)	G_{o_back} (ksi)	$G_{o\_avg.}$ (ksi)
Transverse	1	0.127	9340	9279	9309
	2	0.127	9663	10161	9912
	3	0.128	9552	9498	9525
	4	0.127	9793	9625	9709
				Average	9610
Long.	1	0.127	9877	9976	9927
	2	0.126	9607	10131	9869
	3	0.127	9879	9870	9875
	4	0.127	10411	10571	10491
				Average	10,040

Discussion

Anisotropy of S32003 Angles

Although the average shear modulus from the longitudinally cut specimens was slightly higher than the average for transverse specimens (10040 ksi vs. 9610 ksi), the two values are close enough from a practical point of view to not consider anisotropy in shear. Thus, the in-plane shear modulus was calculated as 9830 ksi by averaging the moduli from the 8 coupons.

Alternative Approach for Determining the Initial Modulus of Elasticity

The purpose of this section is to develop an alternative approach for determining the initial modulus of elasticity, E_o, in order to eliminate the difficulty associated with fabricating and testing stub columns. Since the stress-strain behavior of S32003 is approximately linear at low strain values, the modulus of elasticity can be determined from experimental load-deflection data for long span beams, where flexural behavior dominates deflection response, tested at low strain values. A total of six specimens measuring 1.7 in. x 0.25 in. were cut from L2 x 2 x ¼ angle sections using a vertical bandsaw. Specimens were designed to have span-to-depth ratios greater or equal to 48, causing shear deformation to be negligible. The span lengths were 12 in., 18 in., and 24 in; two specimens were tested for each span length. Dimensions for these specimens are listed in Table 3.6.

Table 3.6- Three-point bending specimen dimensions

Specimen	Span/Depth Ratio	Span, L (in.)	Width, *b* (in.)	Thickness, *t* (in.)	Area, *A* (in^2)	Moment of Inertia, *I* (in^4)
12a	48.2	12	1.704	0.249	0.424	0.00219
12b	49.6	12	1.713	0.242	0.414	0.00202
18a	72.6	18	1.684	0.248	0.417	0.00213
18b	72.6	18	1.671	0.248	0.415	0.00213
24a	99.6	24	1.681	0.241	0.406	0.00197
24b	99.6	24	1.697	0.249	0.423	0.00219

The specimens were tested in a Tinius Olsen flexure fixture simulating simply supported conditions as shown in Figure 3.8. This fixture consisted of two movable 60° wedge supports. Loading was applied at midspan using a hydraulic jack and transferred to the specimens through a ¾ in. diameter cylindrical steel rod. Loading was applied such that the crosshead displacement rate did not exceed 0.009 in/sec. Loading continued until the displacement reached at least 0.4 inches. The applied load was measured using a 10-kip Interface® load cell, and the deflection was determined by averaging the displacements recorded from two linear variable differential transducers (LVDTs) attached to the ends of the cylindrical load applicator. Data were continuously recorded using data acquisition software. The load-deflection curves of the six test specimens are shown below in Figure 3.9.

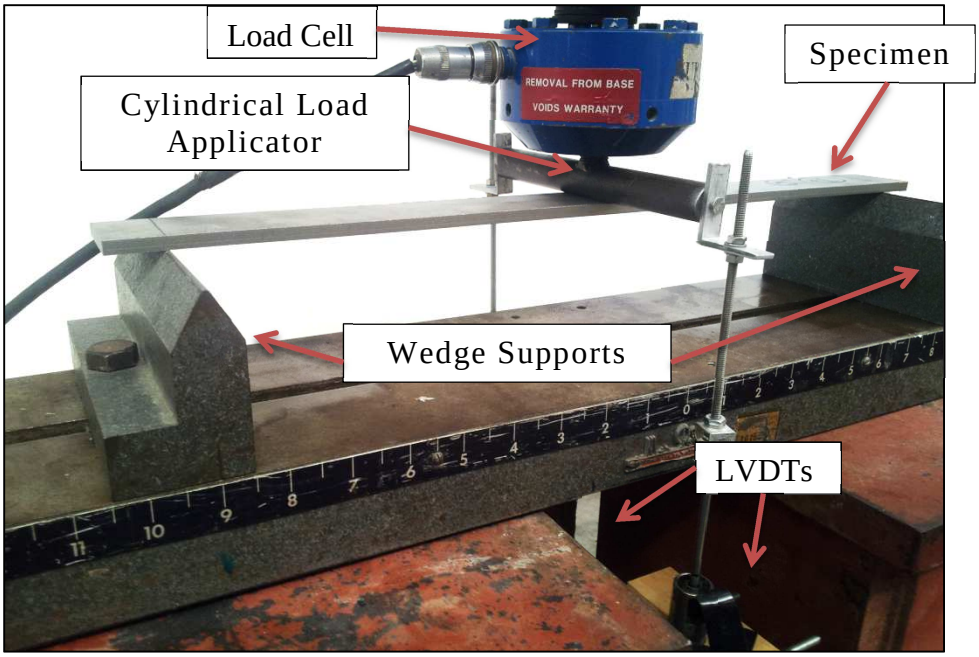

Figure 3.8- Three-point bending test set-up

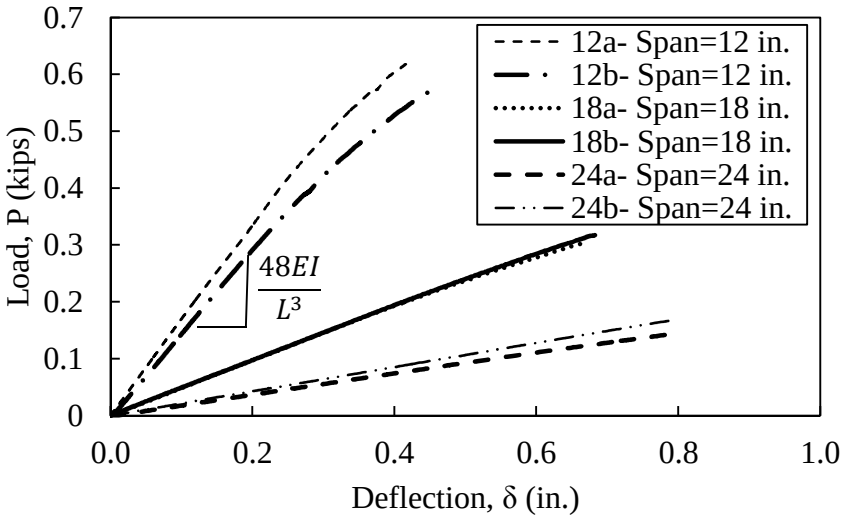

Figure 3.9- Load-deflection plot for three-point flexure tests

Discussion

The load and deflection data were normalized with the linear elastic equations, Eq. (3-2) and Eq. (3-3), to obtain stress and strain, respectively, which are plotted in Figure 3.10. The modulus of elasticity, *E*, was calculated at each data point by performing a linear regression of the data up to that point. Only data between 5 ksi and 30 ksi were considered. Plots of *E* versus its corresponding load, *P*, for the six specimens are shown in Figure 3.11. Average values of *E* for data in this range are listed in Table 3.7. The average value, 27,600 ksi, is within 3.5% of the the E_o determined from the stub column tests— 28,600 ksi; thus, the validity of this method in determining the modulus of elasticity has been verified against a validated procedure.

$$\sigma = \frac{\mathrm{PLt}}{8I} \tag{3-2}$$

$$\varepsilon = 6\frac{\delta \mathrm{t}}{L^2} \tag{3-3}$$

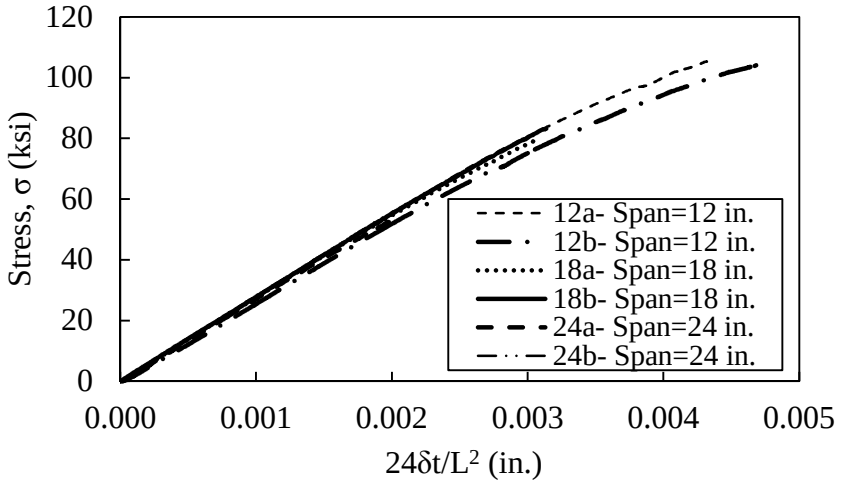

Figure 3.10- Transformed load-deflection data

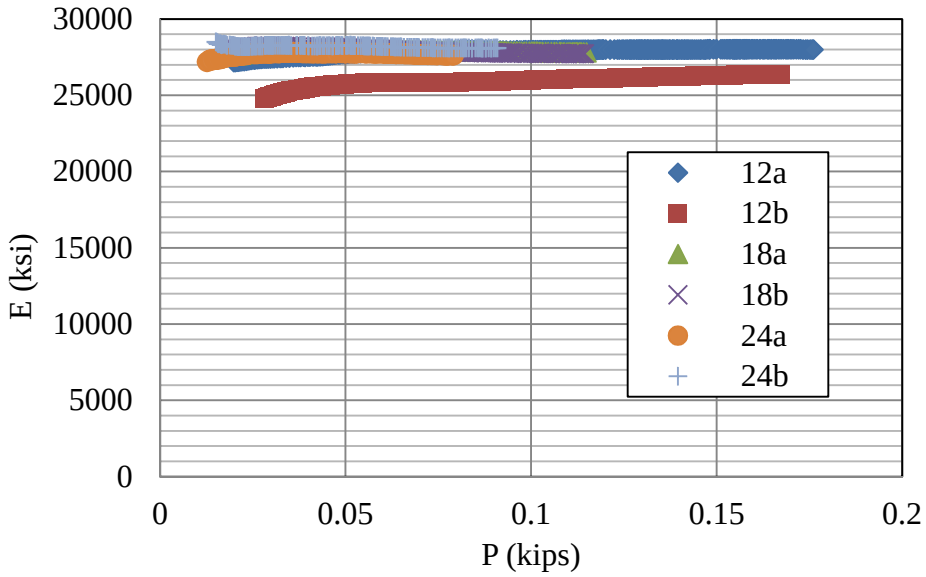

Figure 3.11- Three-point bending modulus determination plot

Table 3.7- Modulus of elasticity

Specimen	E_o (ksi)
12a	27900
12b	25900
18a	27900
18b	27800
24a	28200
24b	28900
Average	27600

Stress-strain Modeling

The stub column compressive stress-strain behavior was modeled in two parts. The preyield stress-strain data was modeled using the modified Ramberg-Osgood relationship, given by Eq. (2-11). The stress-strain behavior for stresses exceeding F_y was modeled using Eq. (2-13); however, it is to be noted that the post-yield hardening

parameter, $n'_{0.2,1.0}$ was computed in the present study using Eq. (3-4), which requires determination of the 0.5% proof stress, $F_{0.5}$.

$$n'_{0.2,1.0} = \frac{\ln\left[\dfrac{0.003 - 0.002n\left(\dfrac{F_{0.5} - F_y}{F_y}\right)}{0.008 - \dfrac{F_{1.0} - F_y}{E_y}}\right]}{\ln\left(\dfrac{F_{0.5} - F_y}{F_{1.0} - F_y}\right)} \tag{3-4}$$

A value of 28,200 ksi was adapted in subsequent sections for E_o based on results of the stub column and flexural tests and was used in determining all other parameters. These parameters are listed in Table 3.8. Comparisons between the experimental and modeled behavior are shown in Appendix A.

Table 3.8- Stub column modeling parameters

Parameter	**1**	**2**	**3**	**4**	**5**
Initial Modulus, E_o (ksi)	28200	28200	28200	28200	28200
0.2% Proof Stress, F_y (ksi)	72.76	74.57	77.38	76.29	76.87
0.01% Proof Stress, F_p (ksi)	40.48	42.56	41.20	54.96	49.07
Hardening Parameter, n	5.11	5.34	4.75	9.14	6.67
1% Proof Stress, $F_{1.0}$ (ksi)	88.38	90.64	96.46	90.96	93.29
Tangent Modulus at F_y, E_y (ksi)	5685	5595	6317	3637	4782
Strain at F_y, ε_y	0.00458	0.00464	0.00474	0.00471	0.00473
Post-yield Hardening Parameter, $n_{0.2,1.0}$	2.40	2.47	2.25	2.95	2.90
0.5% Proof Stress, $F_{0.5}$ (ksi)	82.39	84.53	88.87	85.12	87.23

Development of a typical stress-strain curve

A typical stress-strain curve was developed from the stub column stress-strain data of S32003, which enables values such as tangent and secant moduli and curvature of the stress-strain relationship to be calculated. From the S32003 stub column data, a typical stress-strain relationship was constructed based on the procedure described by "Technical Memorandum B.2.1" of the *Guide to Stability Design Criteria for Metal Structures* (Ziemian 2006). The resulting parameters are summarized in Table 3.9. The typical stress-strain curve is plotted alongside with the stub column data in Figure 3.12.

Table 3.9- S32003 Material properties

Parameter	Value
Initial Modulus, E_o (ksi)	28200
0.2% Proof Stress, F_y (ksi)	75.6
0.01% Proof Stress, F_p (ksi)	44.7
Hardening Parameter, n	5.71
1% Proof Stress, $F_{1.0}$ (ksi)	92.0
Tangent Modulus at F_y, E_y (ksi)	5363
Strain at F_y, ε_y	0.00468
Post-yield Hardening Parameter, $n_{0.2,1.0}$	2.63
0.5% Proof Stress, $F_{0.5}$ (ksi)	85.8
Poisson's Ratio	0.24
Initial Shear Modulus, G_o (ksi)	9830

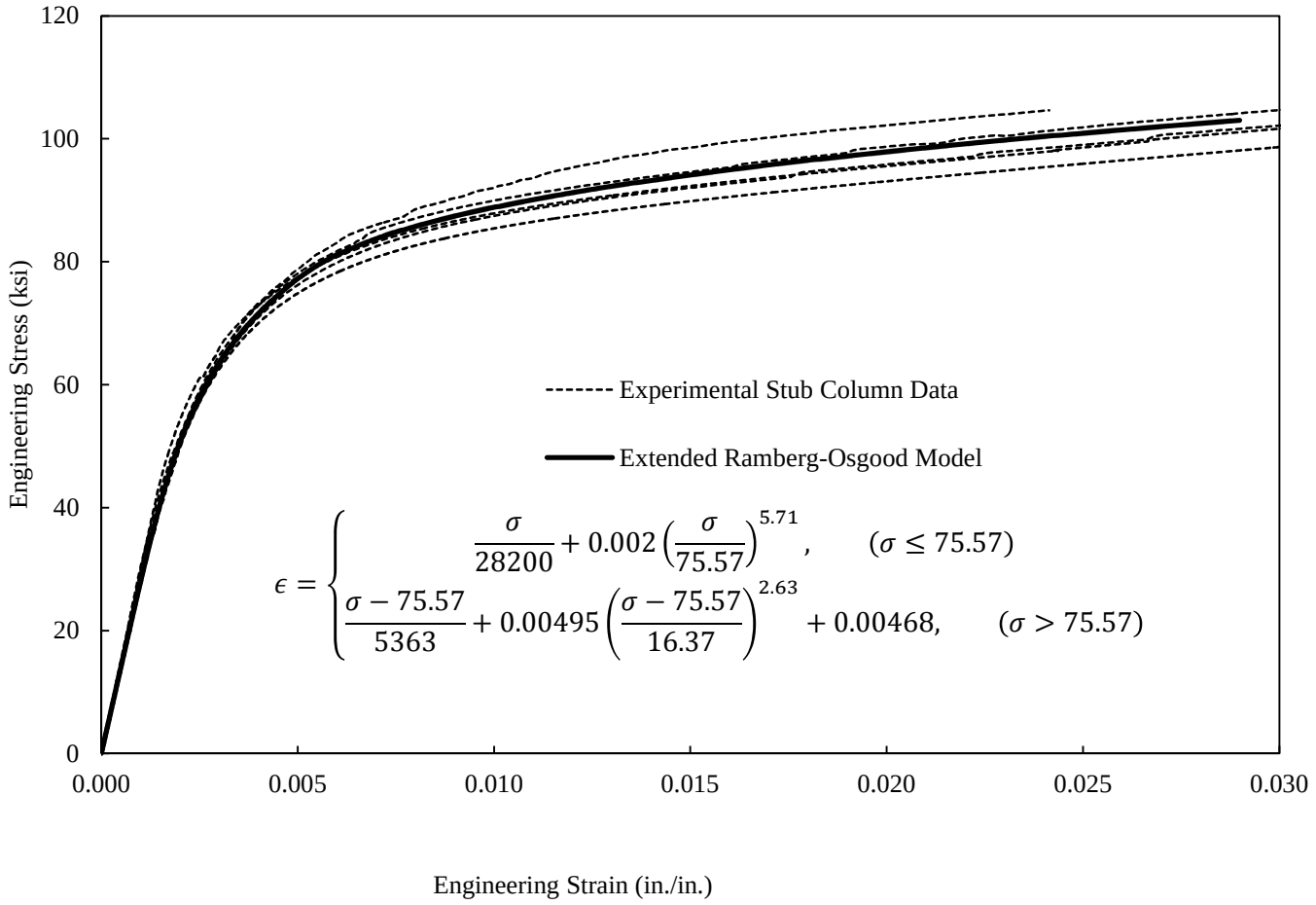

Figure 3.12- Full-range typical stress-strain curve comparison

3.2 RESIDUAL STRESSES

The distribution of residual stresses for S32003 built-up equal-leg angles was experimentally determined by the method of sectioning (Huber and Beedle 1954; Tebedge et al. 1972). Residual stress patterns for laser-welded duplex stainless steel structural shapes have not been investigated in the past, and an attempt is made here to present the pattern for the angle structural component.

Laser Welding

Laser welding is a high energy keyhole fusion welding technique, illustrated in Figure 3.13, where a laser with a power density on the order of magnitude of 10^4 W/mm^2 is focused along the union of two metals plates. Initial contact with the metal surface vaporizes the metals and forms a keyhole. The vapor pressure keeps the keyhole open and scatters the light of the laser. The energy of the scattered laser converts the metal adjacent to the keyhole into a molten state. As the laser is moved along the joint line, the molten walls rejoin where the laser had been and solidify. Because of the dependency on the laser's high energy density rather than heat conduction, this welding method results in heat affected zones (HAZ) that are smaller than those associated with arc welding (Dawes 1992).

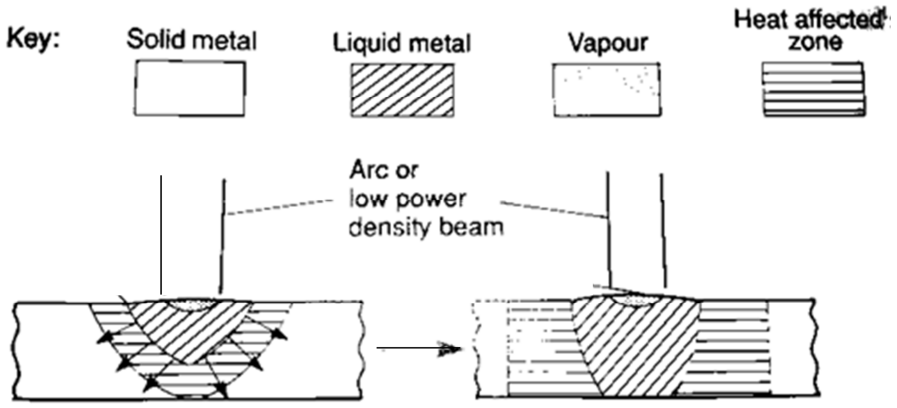

Figure 3.13- Mechanisms of laser welding (Dawes 1992)

Experimental Method

A total of four angles were investigated using the method of sectioning—two L2 x 2 x ¼ sections and two L4 x 4 x $^{5}/_{16}$ sections. The sectioning procedure is illustrated in Figure 3.14. The angles were cut 10 in. in length from longer sections, and 0.25 in. wide segments were marked along the cross-section. For each cross-sectional strip, two $^{1}/_{16}$ in. Ø gage holes were drilled 8 in. apart in the longitudinal direction on each exposed face, as shown in Figure 3.15. After specimens were placed in an environmental chamber for 6 hours, initial gage length measurements were made using digital calipers precise to 0.001 in. The calipers measured the shortest distance between the gage holes, as shown in Figure 3.16. Specimens were cut at the heel to separate their legs and then then cut into the 10 x 0.25 in strips. All cuts were made using a horizontal bandsaw with cutting coolant flowing continuously across the cut. The strips, as shown in Figure 3.17, were again placed in the environmental chamber for 6 hours before new length measurements were made.

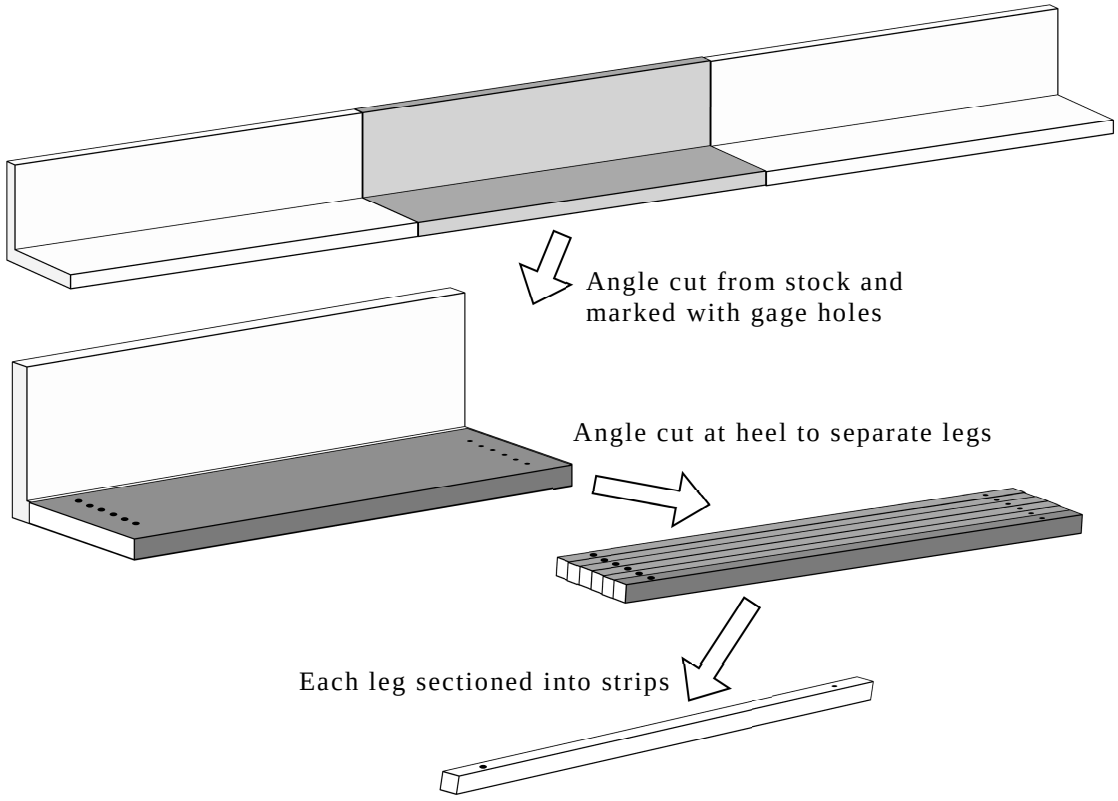

Figure 3.14- Sectioning procedure

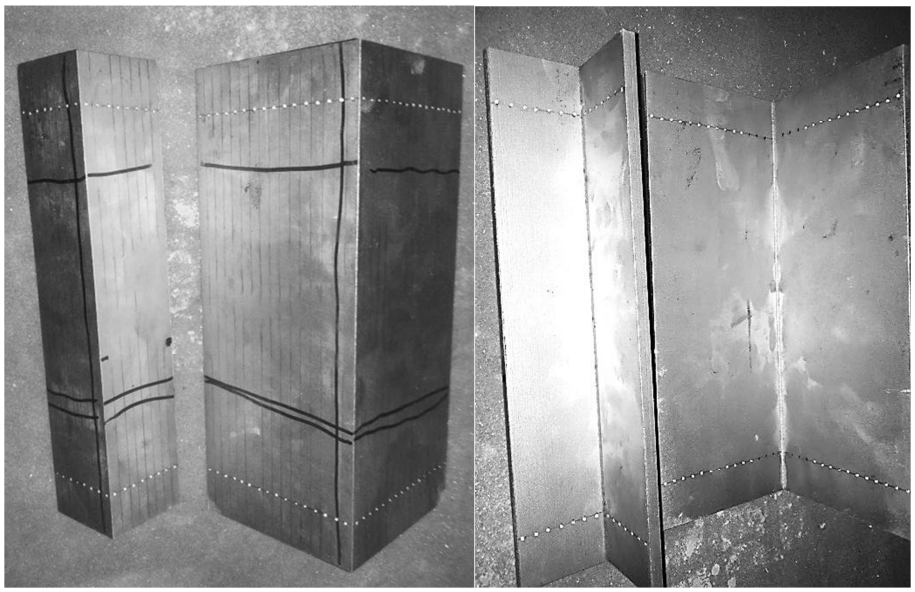

Figure 3.15- Gage marker patterns for residual stress specimens

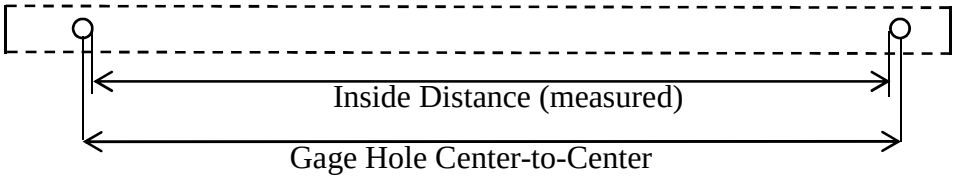

Figure 3.16- Method of sectioning measurement scheme

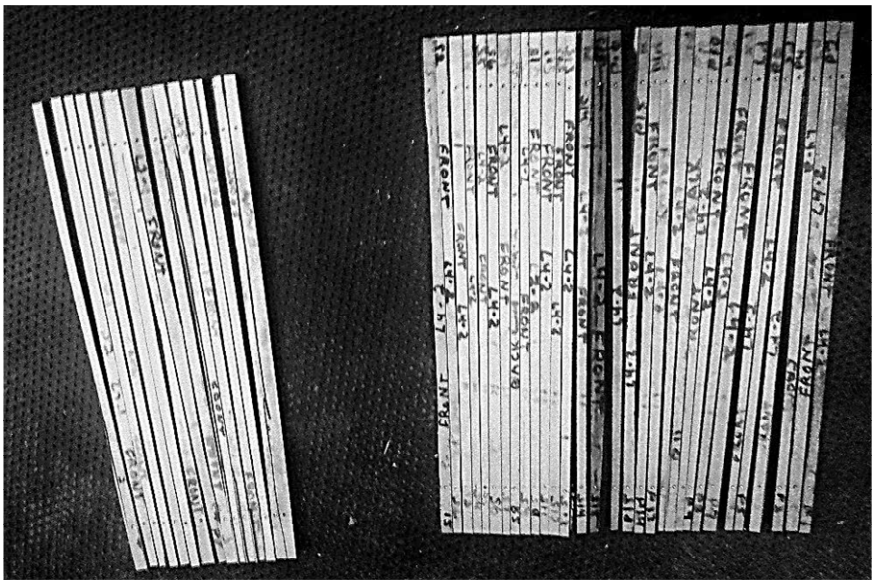

Figure 3.17- Sectioned residual stress specimens

Residual Stress Calculations

Prior to calculating the residual stresses, length measurements were corrected to account for errors caused by curvature of the strips and changes in temperature. The residual stresses were calculated using Eq. (3-5).

$$\sigma_r = -E_o \frac{(L_f - L_i)}{L_i} \tag{3-5}$$

Where

E_o = Initial Modulus of Elasticity

L_f = Final length

L_i = Initial length

σ_r = Residual Stress

Due to the discretization of the cross-section, the method of sectioning often indicates an internal force/moment imbalance. In several investigations of carbon steel angles, residual stress measurements were corrected to achieve equilibrium (Adluri and Murty 1996; Al-Sayed and Bjorhovde 1989a). The internal force/moment imbalance was checked and corrected numerically using a method summarized in Figure 3.18. Comparisons between the corrected and uncorrected residual stress profiles are shown in Figure 3.19(a)-(d). The equilibrium correction procedure caused the residual strains at the site of the weld to vary by approximately 11-16% for the L2 x 2 x ¼ sections and 8% for the L4 x 4 x $^{5}/_{16}$ sections, which are of the same order of magnitude as the equilibrium corrections seen in (Al-Sayed and Bjorhovde 1989a). The corrected residual stress patterns are shown in Figure 3.20 and Figure 3.21.

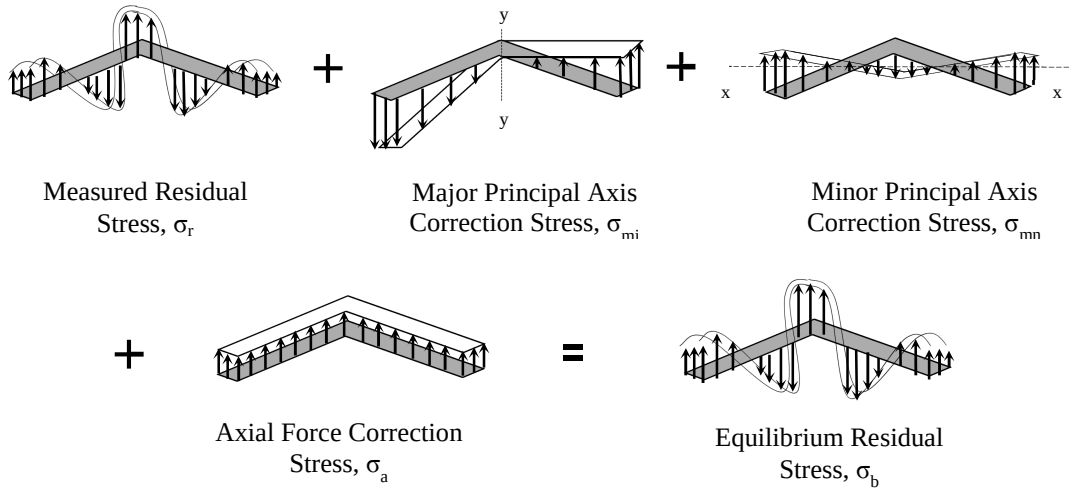

Figure 3.18- Equilibrium correction methodology

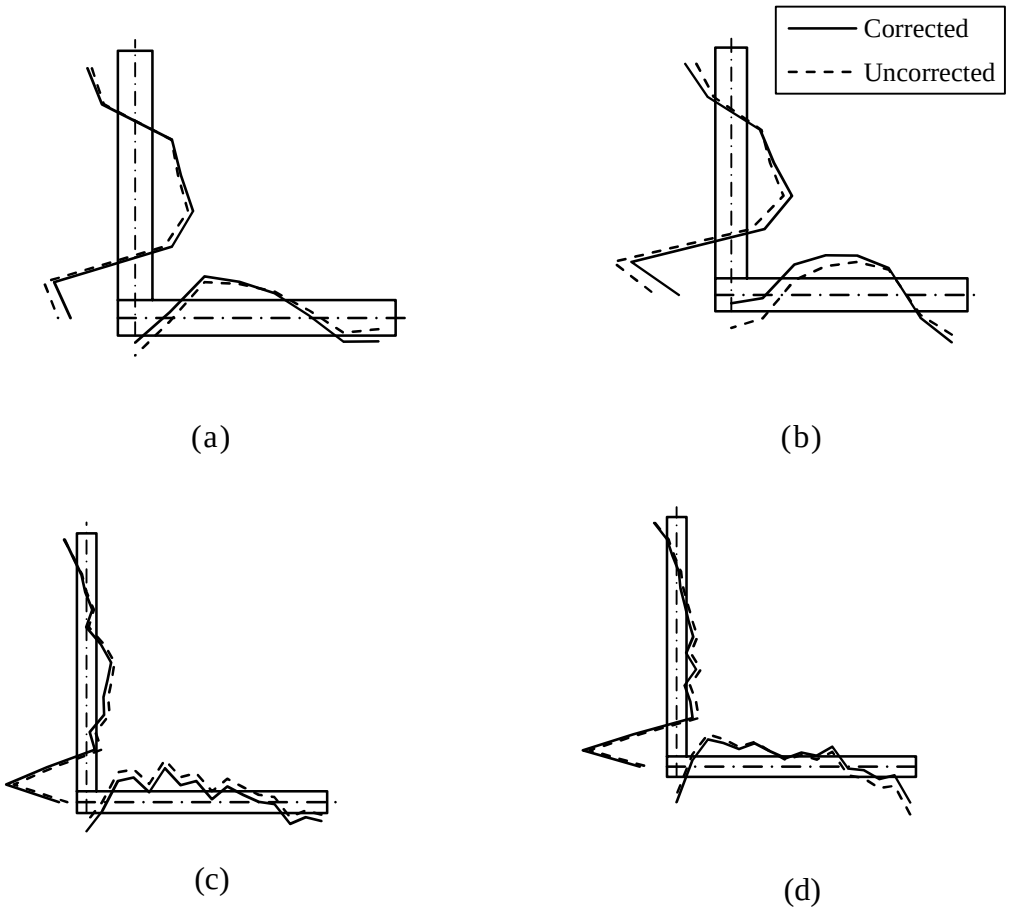

Figure 3.19- Equilibrium corrected/uncorrected residual stress profiles for (a) L2 x 2 x ¼ - A; (b) L2 x 2 x ¼ - B; (c) L4 x 4 x 5/16 - A; and (d) L4 x 4 x 5/16 - B

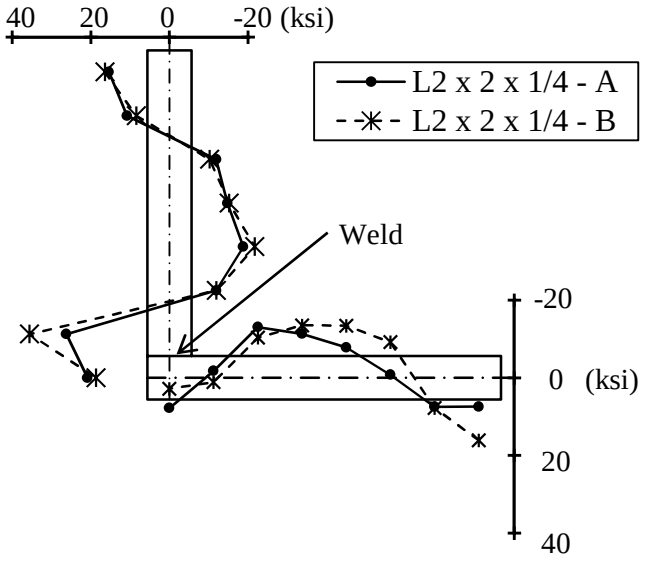

Figure 3.20- Residual stress pattern for S32003 L2 x 2 x 1/4 angle specimens

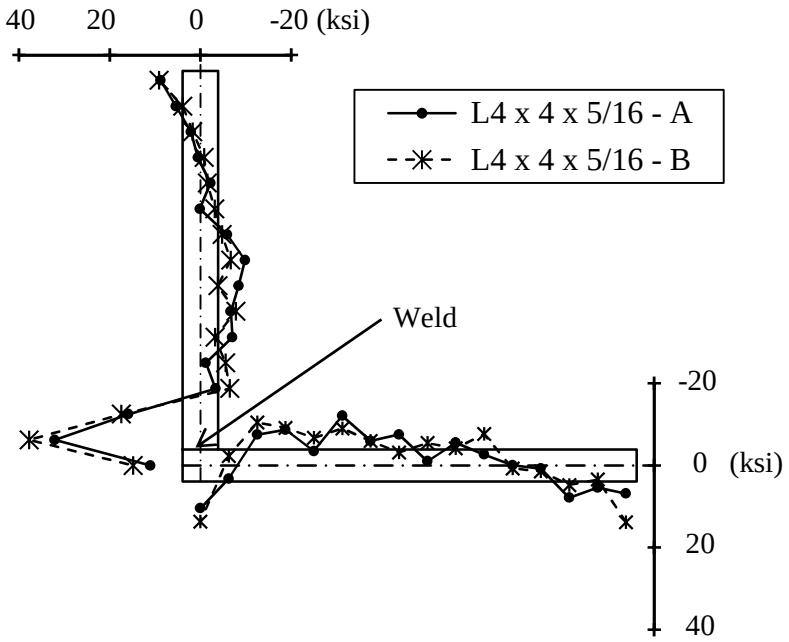

Figure 3.21- Residual stress pattern for S32003 L4 x 4 x $^{5}/_{16}$ angle specimens

Discussion of Residual Stress Pattern Results

The peak residual stresses at the HAZ, toes, and midplate are given in Table 3.10 The laser welding procedure created a concentration of tensile residual stresses at the weld zone whose value was as high as 50% of the yield stress in compression, $F_{y,c}$. This is similar to the residual stresses of a built-up I-section made with S32205 grade duplex stainless steel, wherein the residual stresses were approximately 50% of F_y at the HAZ in the flanges and 95% of F_y at the HAZ in the web (Lagerquist and Olsson 2001).

The middle of each leg was determined to be in residual compression, whereas the toes are in residual tension. This is similar to the residual stress pattern of the built-up L10 x 10 x ½ equal-leg angle made from mild steel plates at Lehigh University, as shown in Figure 3.22 (Rao et al. 1963). From Table 3.10, it can be seen based on two tests only, that the magnitudes of the residual stresses away from the HAZ are higher in the L2 x 2 x ¼ sections than in the L4 x 4 x $^5/_{16}$ sections. Since L2 x 2 x ¼ has a smaller cross-section than L4 x 4 x $^5/_{16}$, its greater residual stresses magnitudes are necessary to balance the residual stresses associated with the HAZ in order to achieve internal force and moment equilibrium.

Table 3.10- Peak residual stress values

Angle	HAZ		Midplate		Toe	
	$\sigma_{r,HAZ}$ (ksi)	$\frac{\sigma_{r,HAZ}}{F_{y,c}}$	$\sigma_{r,c}$ (ksi)	$\left\|\frac{\sigma_{r,c}}{F_{y,c}}\right\|$	$\sigma_{r,t}$ (ksi)	$\frac{\sigma_{r,t}}{F_{y,c}}$
L2 x 2 x ¼ -A	26.2	0.35	-18.8	0.25	15.4	0.20
L2 x 2 x ¼ - B	35.6	0.47	-21.8	0.29	16.4	0.22
L4 x 4 x $^5/_{16}$ - A	32.1	0.43	-12.1	0.16	8.8	0.12
L4 x 4 x $^5/_{16}$ - B	37.7	0.50	-10.5	0.14	13.8	0.18

Positive values indicate residual tensile stresses

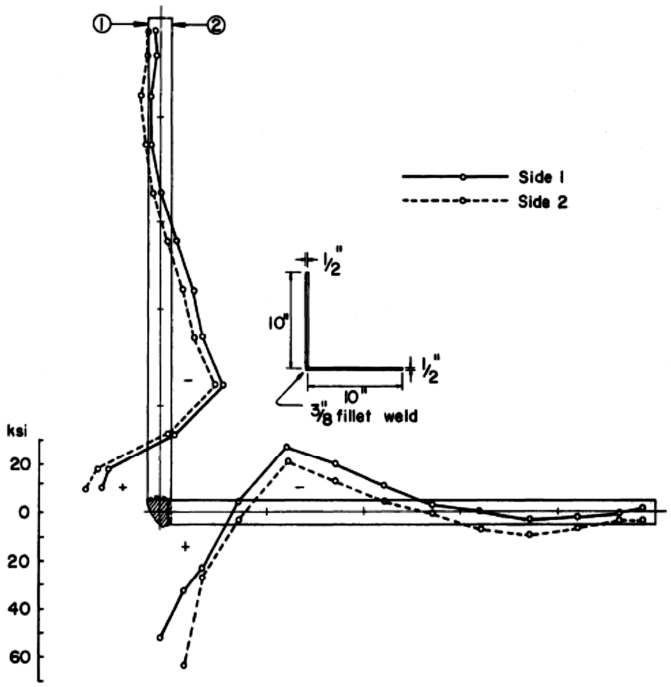

Figure 3.22- Residual stress pattern for a welded built-up mild steel angle (Rao et al. 1963)

Because laser welding is a less heat intensive process than arc welding and the thermal conductivity of mild steel, 49 W/(m·K) (Bentz and Prasad 2007), is nearly three times the thermal conductivity of S32003 at room temperature, 17 W/(m·K) (ATI Allegheny Ludlum), the size of the HAZ for built-up stainless steel angles was expected to be smaller than that of built-up carbon steel sections. No attempt was made to quantify the size of the HAZ; however, the size of the region surrounding the HAZ in residual tension was compared to corresponding regions in built-up carbon steel sections. The distance from the weld to a point of zero residual stress was approximately 17.5% of the outstanding leg dimension for the L2 x 2 x ¼ angles and 14% of the outstanding leg dimension for the L4 x 4 x $^{5}/_{16}$ angles. This is comparable to the same distances reported by Rao et al. (1963) for the stems of welded carbon-steel T-sections, which vary between

14% and 27% of the height of the stem. Additionally it should be noted that while the residual stresses in the HAZ are on the order of $0.50F_{y,c}$, the magnitude (38 ksi) of the residual stress at the HAZ is similar to that of welded carbon steel box (38 ksi) (Rao et al. 1963).

3.3 SECTION CHARACTERIZATION

Compressive stress-strain relationships that include the effect of residual stresses found in the laser-welded equal-leg angles could not be obtained by directly testing angle stub columns since their legs were susceptible to local buckling. Instead, tubular stub columns were fabricated and tested as described in Section 3.1; however, they had residual stresses which differed from those found in L2 x 2 x ¼ angles as a result of welding. Thus, the stress-strain curves from the stub column tests were approximations, rather than true representations, of the effect of the residual stresses found in the laser-welded equal-leg angles. These stress-strain relationships, however, are valid for analysis of single equal-leg angle columns for several reasons. Firstly, fabricating the stub columns did not reverse the residual stresses. Since the doubly-symmetric stub columns were fabricated by welding L2 x 2 x ¼ angles at their toes, which were already in residual tension, the toes would be subject to increased residual tensile stresses; thus, the residual stress patterns were not altered. Secondly, the stub columns were fabricated using TIG-welding rather than laser-welding. It was noted by Klopper et al. (2011) in fabricating ferritic steel T-sections, that the residual stresses associated with full-penetration laser-welding were up to 25% higher at the HAZ than full-penetration arc-welding. As a result, the change in the residual stresses would be less than if a laser-welded tubular section had been tested.

3.4 CONCLUSION

The material properties of S32003 angles, including their longitudinal modulus, compressive stress-strain relationship, Poisson's ratio, and shear modulus, were determined from experimental tests. The results from the residual stress investigation indicate a consistent pattern of residual tensile stresses in the toes and heels and residual compressive stresses at midplate of each leg. A summary of the material parameters determined from these tests is given in Table 3.9, which can be used in analysis of the S32003 angles in compression.

CHAPTER 4

EXPERIMENTAL BUCKLING TESTS

This chapter presents the results from a series of experimental buckling tests conducted on S32003 equal-leg angles loaded concentrically in compression. A total of 33 test specimens having three different cross-sections were tested. The results from these tests were then compared to the predicted strengths using existing stainless steel standards and design rules.

4.1 TEST SPECIMENS

Thirty-three equal-leg angles, representing three different cross-sections, were tested. These cross-sections consisted of ten L4 x 4 x $^{5}/_{16}$, eleven L3 x 3 x ¼, and twelve L2 x 2 x ¼ angles, designated hereafter as L4, L3, and L2, respectively. In all test components the overall slenderness ratio L_e/r_x ranged from 35 to 350 while the angle leg slenderness (b/t) ratio ranged from 7.5 to 12.3. Angle specimens were fabricated by butt-welding two hot-rolled plates using a laser-welding technique. The measured dimensions of each angle specimen, as defined by Figure 4.1 are listed alongside its Column ID in Table 4.1. The first number of the Column ID refers to the nominal leg width in inches, and the second number refers to the length of the angle specimen without end fixtures. From these measurements, cross-sectional properties were computed. These include the cross-sectional area (A), maximum and minimum moments of inertia (I_y and I_x, respectively), section torsion constant (J), and warping constant (C_w). All computed values are also reported in Table 4.1.

Table 4.1- Cross-sectional properties of angle specimens

	$\bar{b}_1$* (in.)	t_1* (in.)	$\bar{b}_2$* (in.)	t_2* (in.)	A† (in^2)	I_x† (in^4)	I_y† (in^4)	J† (in^4)	C_w† (in^6)	δ_o* (in.)	$\frac{L}{\delta_o}$
L2-18a	2.008	0.248	2.023	0.248	0.939	0.146	0.562	0.019	0.006	0.005	3801
L2-18b	2.021	0.248	2.010	0.248	0.938	0.146	0.562	0.019	0.006	0.005	3804
L2-24	1.999	0.248	2.023	0.248	0.935	0.145	0.558	0.019	0.006	0.004	6000
L2-36a	2.019	0.244	1.997	0.248	0.929	0.143	0.552	0.019	0.006	0.013	2763
L2-36b	1.995	0.248	2.024	0.243	0.927	0.143	0.552	0.019	0.006	0.005	6909
L2-48	2.027	0.247	2.012	0.250	0.942	0.147	0.566	0.019	0.006	0.036	1330
L2-60a	2.020	0.251	2.024	0.250	0.950	0.149	0.572	0.020	0.006	0.039	1535
L2-60b	2.012	0.250	2.024	0.249	0.945	0.147	0.567	0.020	0.006	0.029	2048
L2-72	2.025	0.247	2.005	0.250	0.939	0.146	0.562	0.019	0.006	0.067	1073
L2-84	2.019	0.250	2.024	0.249	0.946	0.148	0.570	0.020	0.006	0.065	1302
L2-96	2.027	0.250	2.023	0.250	0.950	0.149	0.574	0.020	0.006	0.068	1414
L2-132	2.006	0.252	2.024	0.251	0.951	0.148	0.568	0.020	0.006	0.044	3007
L3-18	3.023	0.249	2.994	0.249	1.436	0.507	1.994	0.030	0.021	0.012	1519
L3-24a	2.999	0.250	3.024	0.250	1.442	0.510	2.007	0.030	0.021	0.047	509
L3-24b	3.023	0.250	3.001	0.248	1.438	0.509	2.002	0.030	0.021	0.005	5082
L3-36	3.028	0.248	2.996	0.249	1.436	0.508	1.999	0.030	0.021	0.013	2754
L3-48a	3.021	0.250	2.998	0.250	1.444	0.510	2.006	0.030	0.021	0.009	5455
L3-48b	3.027	0.250	3.002	0.250	1.444	0.512	2.013	0.030	0.021	0.052	920
L3-60a	3.000	0.251	3.024	0.250	1.444	0.511	2.009	0.030	0.021	0.033	1807
L3-60b	3.024	0.250	3.004	0.251	1.446	0.512	2.015	0.030	0.021	0.014	4225
L3-72	3.030	0.249	3.001	0.250	1.443	0.512	2.014	0.030	0.021	0.044	1651
L3-84	3.023	0.249	2.999	0.250	1.442	0.510	2.006	0.030	0.021	0.030	2772
L3-132	3.024	0.249	2.999	0.251	1.444	0.511	2.009	0.030	0.021	0.030	4415
L4-24	3.986	0.313	3.996	0.312	2.395	1.492	5.879	0.078	0.095	0.024	1017
L4-36a	4.007	0.308	3.997	0.311	2.382	1.493	5.886	0.076	0.094	0.018	1989
L4-36b	4.004	0.312	4.000	0.309	2.390	1.497	5.902	0.077	0.095	0.016	2308
L4-48	4.009	0.305	4.000	0.311	2.370	1.487	5.866	0.075	0.092	0.010	4660
L4-60a	4.017	0.308	4.003	0.312	2.390	1.504	5.930	0.077	0.095	0.015	4054
L4-60b	3.992	0.308	4.015	0.312	2.388	1.498	5.900	0.076	0.094	0.014	4225
L4-72	4.001	0.312	4.006	0.311	2.398	1.504	5.925	0.078	0.096	0.011	6429
L4-84	3.999	0.312	4.007	0.313	2.402	1.505	5.933	0.078	0.096	0.018	4565
L4-96	4.025	0.317	4.019	0.315	2.442	1.544	6.085	0.081	0.101	0.033	2936
L4-132	3.997	0.314	3.988	0.313	2.405	1.499	5.908	0.079	0.097	0.055	2422

* Measured, refer to Figure 4.1
† Computed, Madugula and Kennedy (1984)

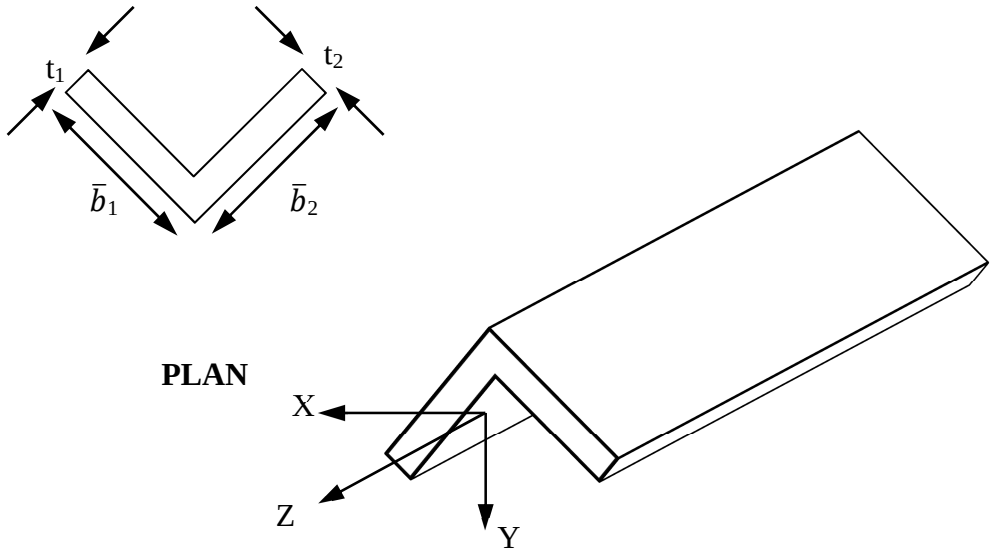

Figure 4.1- Angle specimen axis and dimension definitions

Table 4.1 also presents the maximum out-of-straightness, δ_o, measurements of all test specimens, which were measured using a theodolite. For specimens 36 in. in length and shorter the maximum out-of-straightness, δ_p, of each leg was measured with respect to a machinist table, as illustrated by Figure 4.2. For a given angle, the larger δ_p from its two legs is recorded in Table 4.2.

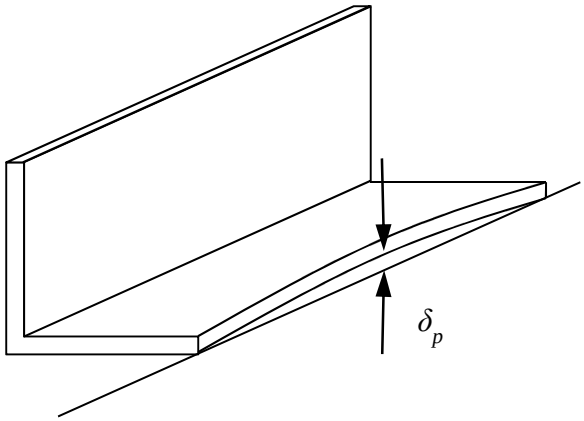

Figure 4.2- Leg out-of-straightness measurement (Zureick and Steffen 2000)

Table 4.2- Maximum plate out-of-straightness measurements

Specimen	L (in.)	δ_p (in.)	L/ δ_p
L2-18a	18	0.080	225
L2-18b	18	-0.020	-900
L3-18	18	0.008	2250
L2-24	24	0.005	4800
L3-24a	24	0.028	857
L3-24b	24	0.005	4800
L4-24	24	0.045	533
L2-36a	36	0.000	--
L2-36b	36	-0.013	-2769
L3-36	36	0.013	2769
L4-36a	36	0.002	18000
L4-36b	36	0.020	1800

4.2 TEST SETUP

Columns were supported vertically between a concrete strong floor and a steel load frame with adjustable beam height and tested with end fixtures simulating pinned boundary conditions about the minor principal axis of the single angles. An overview of

the test set-up is shown in Figure 4.3. Two sets of end fixtures were used: knife-edges for slender columns whose predicted strengths were less than 50 kip and roller end fixtures for columns whose predicted strengths exceeded 50 kips. Load was applied using a hydraulic ram mounted to the load frame, to which the top end fixture was mounted.

Instrumentation

The following instrumentation was used in testing:

1. Four string potentiometers (SPs) to measure midheight lateral deflections
2. Two strain gages mounted back-to-back on each leg at midheight (Figure 4.4) to detect the onset of local buckling and to assess accidental eccentricities resulting from loading
3. One string potentiometer (SP) to measure column shortening
4. A pair of linear variable differential transformers (LVDTs) to measure the slope of the column at its ends
5. A load cell

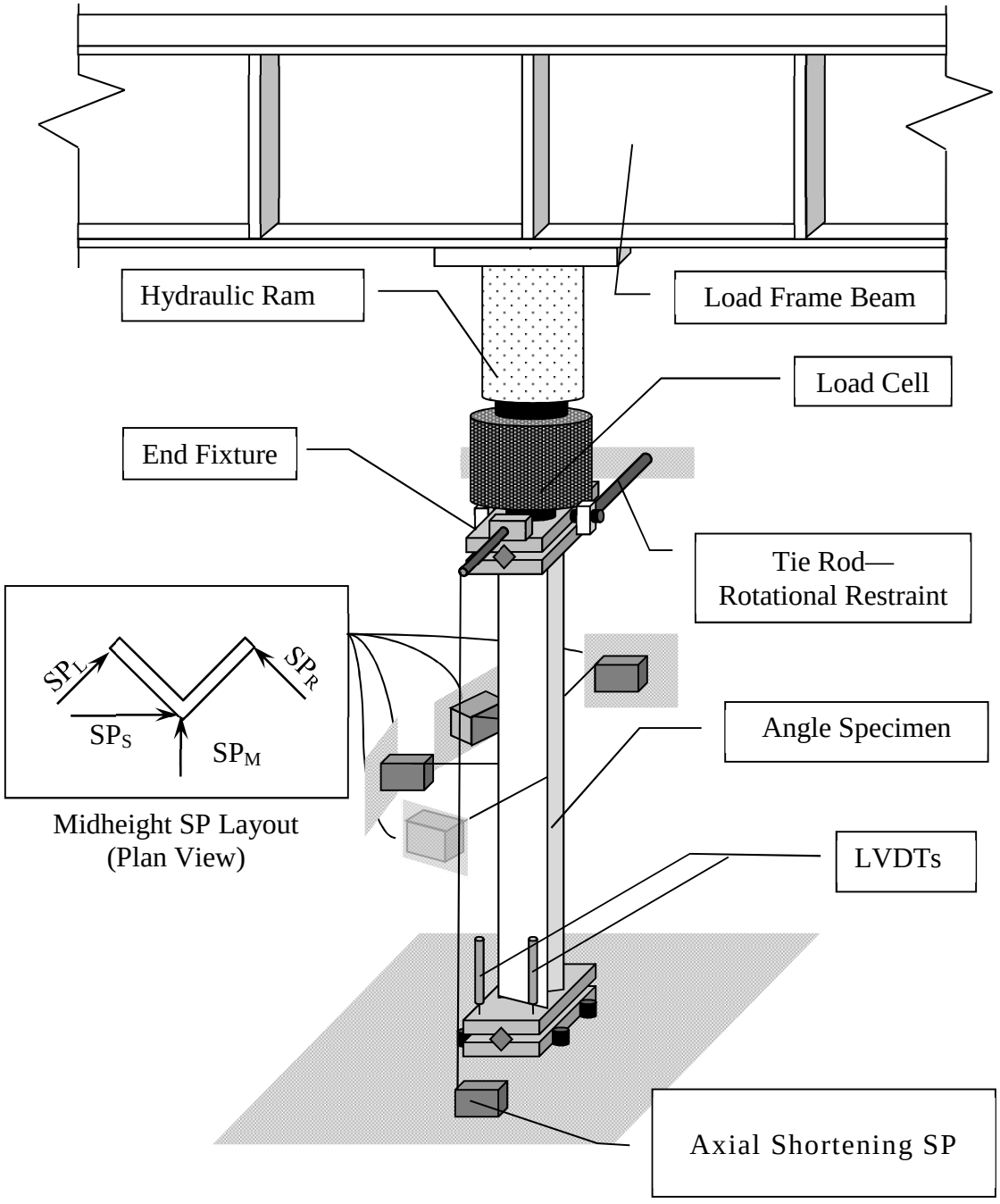

Figure 4.3- Test setup

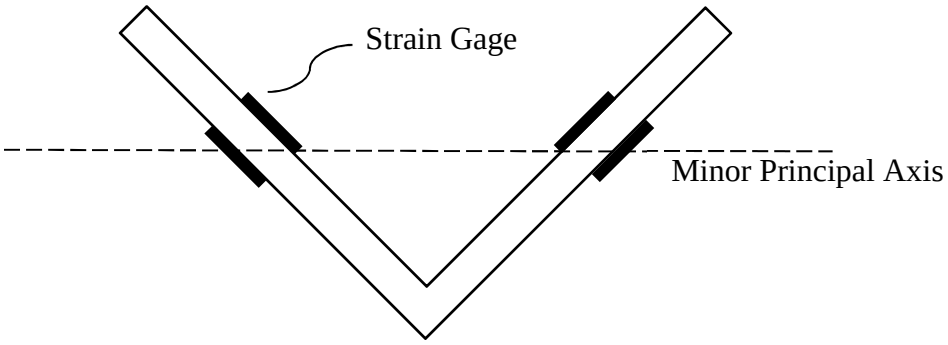

Figure 4.4- Strain gage locations

End Fixtures

Two types of end fixtures, shown in Figure 4.5, were used to test columns—knife-edge and roller end fixtures. These end fixtures approximated torsionally restrained, minor-axis pinned, major-axis fixed, and warping restrained boundary conditions. The top end fixtures were attached to safety chains which safeguarded against the end fixtures' falling if the angle snapped out of the test setup; however, enough slack was included to ensure the chains did not interfere with the rotational movement of the end fixtures as seen in Figure 4.6

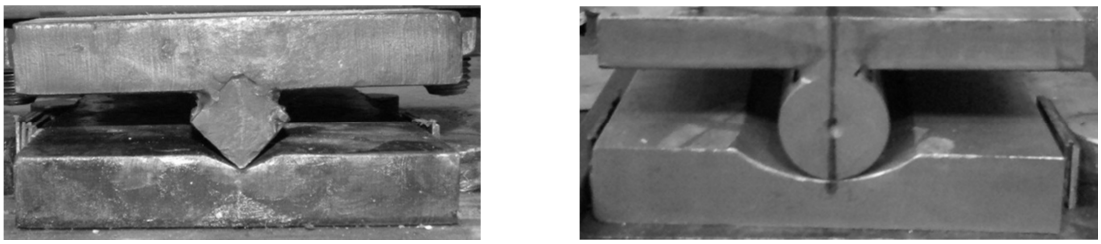

Figure 4.5- End Fixtures: Knife-edge end fixture (left); Roller end fixture (right)

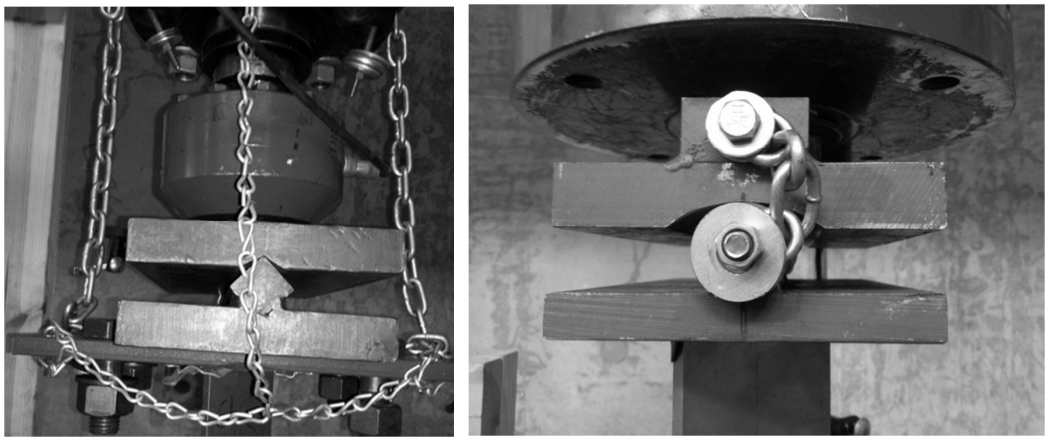

Figure 4.6- End fixture safety chains

Knife-Edge End Fixtures

Each knife edge consisted of a 1 in. x 1 in. square hardened carbon steel bar situated between of two grooved steel plates, one with a 130° grove and the other with a 90° to which it was welded. A malleable $^{1}/_{16}$ in. lead plate was placed between each end of the column specimen and the bearing plate to level possible unevenness of the contact surface. The knife-edge end fixtures added 5.323 in. to the length of the column.

Roller End Fixtures

Each roller end fixture consisted of a $1^{3}/_{8}$ in. Ø cylindrical rod welded situated between two steel plates—one with a 4 in. Ø cylindrical groove and the other ¾ in. thick plate to which it was welded. The end fixtures added 4.160 inches to the length of the column.

Twisting of the top end fixtures was restrained using anchored tie rods that prevented twist but allowed vertical displacement (Figure 4.7). The tie rods were

anchored to a strong wall adjacent to the test setup. Twisting of the bottom end fixtures was restrained by anchor bolts protruding from the strong floor.

To keep columns from becoming misaligned during flexural-torsional buckling, $^{5}/_{16}$ in. thick S32003 endplates were welded to the ends of the stocky columns and bolted to the end fixtures, as shown in Figure 4.8. These welded endplates also better imposed both fixed conditions for rotation about the major principal axis and warping restrained conditions.

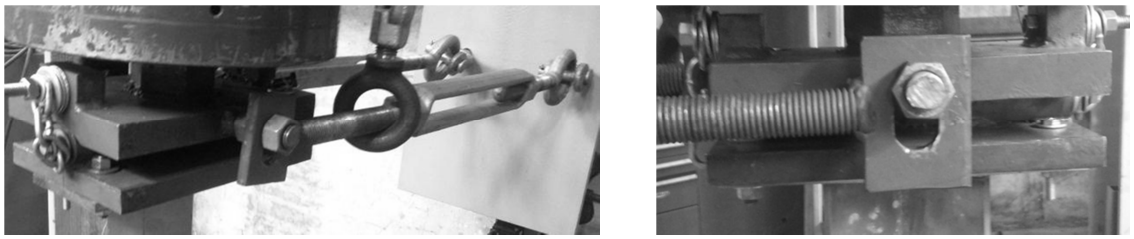

Figure 4.7- Tie rod torsional restraint anchoring scheme (left), slotted hole detail (right)

Figure 4.8- Angle endplate weld

Examination of End Fixtures' Rotational Restraint

Prior to testing the S32003 stainless steel sections, a series of buckling tests were performed on mild steel angles using these end fixtures to determine the rotational-restraint the fixtures imposed. In comparing the predicted Euler buckling load against the load determined from the Southwell plot, an effective length factor was determined for the end fixtures used in that test. For the knife-edge end fixtures, the effective length factor was calculated to be approximately 1.00 based on the results of an 8ft L3 x 3 x $^{5}/_{16}$ $\left(\frac{L_{actual}}{min} = 174\right)$ carbon steel angle. Similarly, the effective length factor value of approximately 0.95 was calculated for the roller end fixture from results of tests on a 7ft L4 x 4 x ½ $\left(\frac{L_{actual}}{min} = 113\right)$ angle, a 6 ft L3 x 3 x $^{5}/_{16}$ $\left(\frac{L_{actual}}{min} = 130\right)$ angle, and a 5ft L3 x 3 x $^{5}/_{16}$ $\left(\frac{L_{actual}}{min} = 110\right)$. These effective length factors are reflected in values of L_e, reported in Table 4.3.

4.3 TESTING PROCEDURE

The experimental procedure was guided by "Technical Memorandum B.4" of *Guide to Stability Design Criteria for Metal Structures* (Ziemian 2006). Each column was mounted between the end fixtures so that its minor principal axis coincided with the axis of the knife edge, and its centroidal axis coincided with the axis of the ram. Prior to loading, angles in this study were loaded to 40% of their predicted strengths and unloaded several times to shake down the test specimens in the fixtures.

Each column was loaded monotonically until a maximum force was observed and the force had dropped off about 10%. Measurements were continuously recorded using data acquisition software. After testing, the distortion of the section was examined by

manually measuring the distance between the toes at midheight with digital calipers and comparing it to the distance measured prior to testing.

4.4 BEHAVIOR OF ANGLE SPECIMENS

The results of the experimental buckling tests are shown in Figure 4.9 along with the flexural buckling stress curves calculated using both E_t and E_o. The strength, P_{exp}, of each test specimen was determined based on the peak load reached during testing. It is convenient to normalize strength with respect to cross-sectional area ($\sigma_{exp} = P_{exp}/A$), in order to provide insight into the buckling of various cross-sections. Buckling modes were identified using the midheight deflections; typical load-deflection curves plots for flexural buckling and flexural-torsional buckling can be seen in Figure 4.10 and Figure 4.11, respectively.

Of the 33 specimens tested, 28 angle specimens experienced minor-axis flexural buckling (Figure 4.12) while the remaining 5 experienced flexural-torsional buckling (Figure 4.13). No local buckling was observed in any of the angle specimens and plate bending was only detected in specimens that underwent flexural-torsional buckling. The midheight deflections of specimen L4-60a, which underwent flexural buckling, were in the direction of its heel, subjecting its toes to increased compression. This eventually caused the specimen to suddenly twist in the post-buckling range. Cross-sectional distortion was only observed in the post-buckling range in L2-18a whose midheight deflections were also toward its heel.

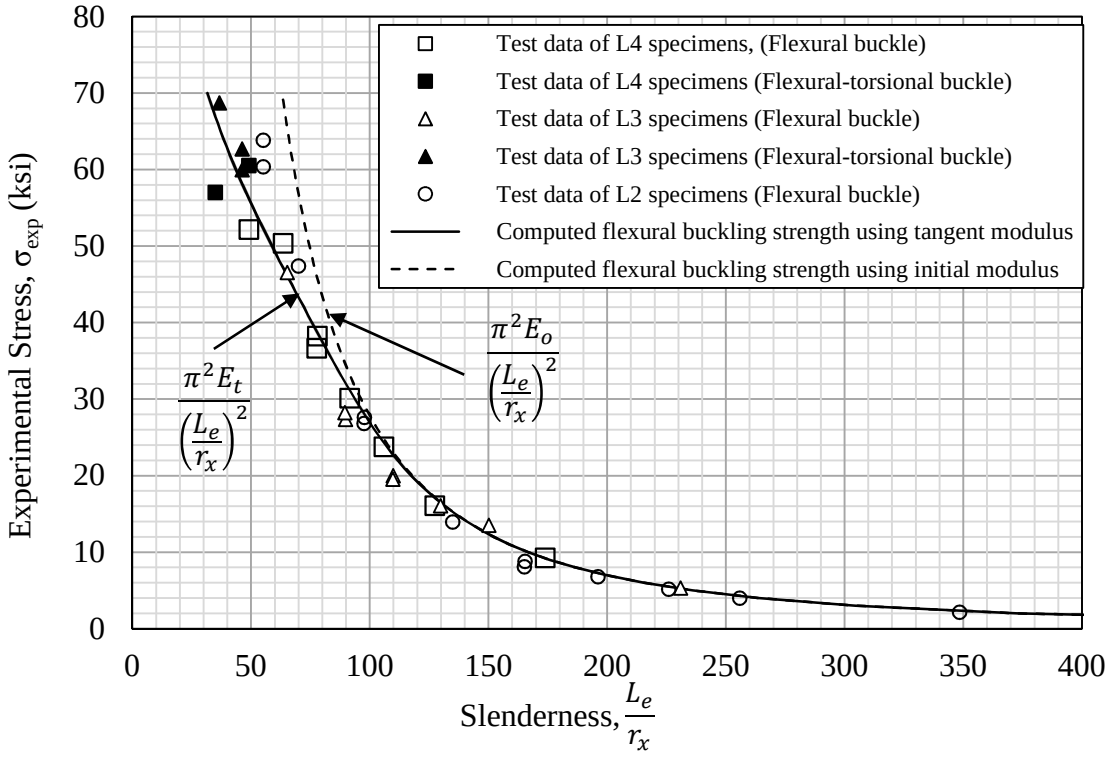

Figure 4.9- Experimental column curve for S32003 equal-leg angles

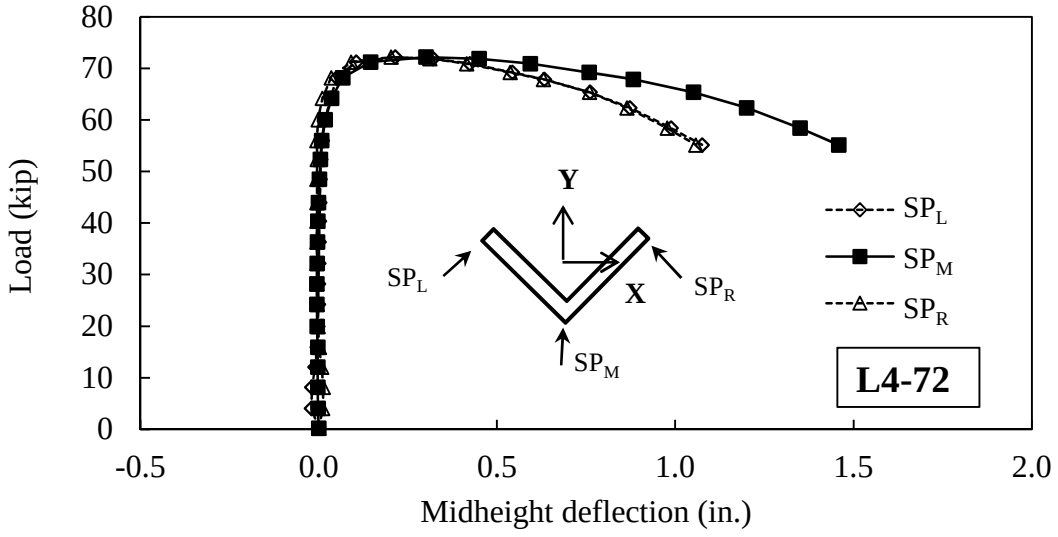

Figure 4.10-Typical load-deflection curves test specimens exhibiting flexural buckling

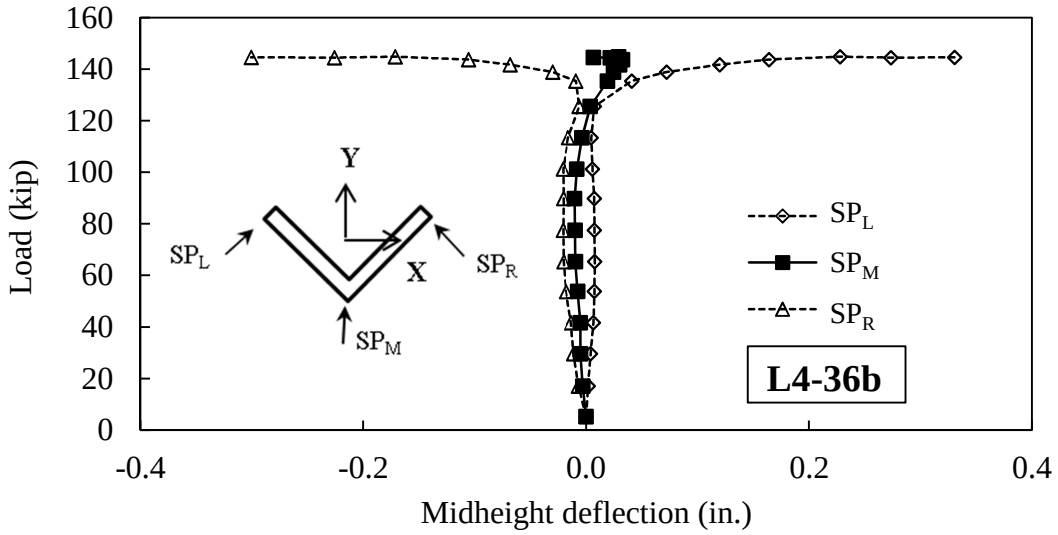

Figure 4.11- Typical load-deflection curves test specimens exhibiting flexural-torsional buckling

Figure 4.12- Flexural buckling specimens

Figure 4.13- Flexural-torsional buckling specimens

Analysis of the Column Curve

The data closely follows the flexural buckling curve that was calculated using the tangent modulus as shown in Figure 4.9. For reference, the flexural buckling curve that was calculated using the initial modulus of elasticity is also plotted to give indication of the deviation of the data from linear material behavior. Trends for the flexural-torsional data in Figure 4.9 could not be analyzed due to the limited number of specimens which buckled in this mode; further investigation is needed to evaluate this limit state.

Although the columns strengths of duplicate specimens generally show agreement with each other, the difference in strength between some duplicate test specimens can be attributed to experimental error related to loading eccentricity. Most notably, L4-36a underwent flexural buckling while L4-36b underwent flexural-torsional buckling. For this reason L4-36a is considered an outlier and will not be considered in subsequent analysis.

Load-deformation behavior

Flexural buckling

The influence of nonlinear material behavior can be seen by looking at the post-buckling behavior of flexural buckling specimens. The post-buckling load loss associated with increased lateral deflection occurred at a greater rate for stockier sections than slender sections, as shown in Figure 4.14. This is attributable to the fact that slender columns buckle at low stresses, which correspond to higher tangent moduli, whereas stockier columns are associated with reduced material stiffness.

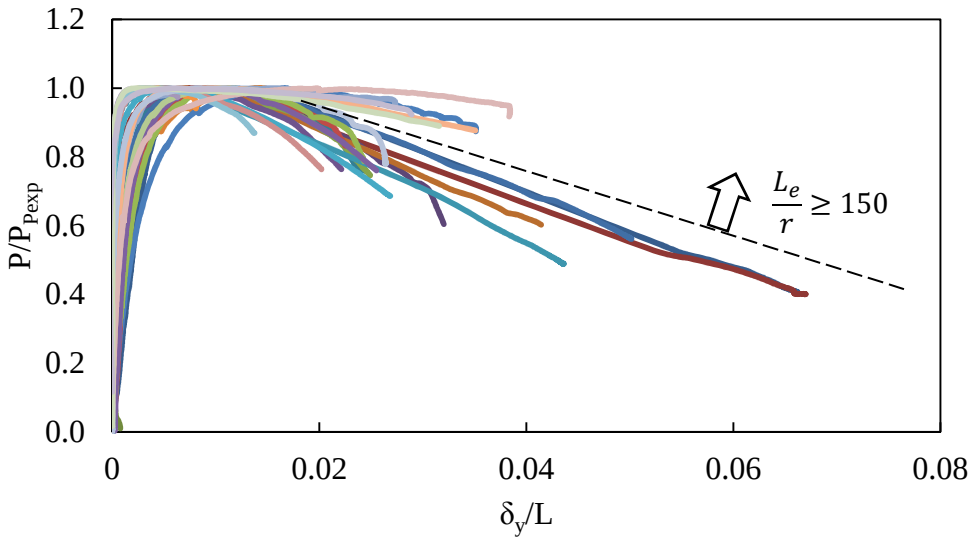

Figure 4.14- Normalized load-deflection curves

The influence of material nonlinearity on column deformation can also be seen by examining the deformed shape. For linear elastic material behavior, the deformed shape of a concentrically loaded prismatic pinned column is sinusoidal (Euler buckling), based on the solution to the equilibrium differential equation. For nonlinear material behavior, the extreme case is the formation of a plastic hinge, which causes the deformed shape to

be triangular for a pinned prismatic column. These two deformed shapes represent bounds between which the deformed shape of all pinned prismatic columns will lie. The midheight deflections of these bounds, shown in Figure 4.15, can be defined in terms of the slope, θ, of the deformed column at its ends.

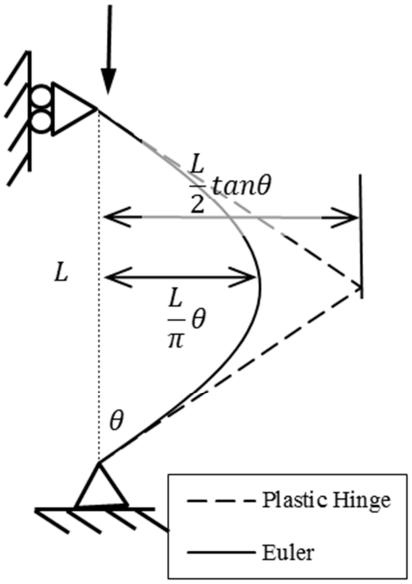

Figure 4.15- Deformed shape bounds and associated midheight deflections

Having experimentally measured the slope at the ends of the columns, the progression of material nonlinearity was examined by comparing the midheight deflection, δ_y, against the two bounds described in Figure 4.15. The resulting plot is shown in Figure 4.16. The peak loads are seen to occur near the sinusoidal bound, after which the material nonlinearity increases. Slender specimens, which are associated with lower buckling stresses closely follow the linear bound, even in the post buckling range. Shorter columns, which correspond to higher average stresses and material nonlinearity, exhibited greater deviation from the Euler buckling curve with increased base rotation.

The most apparent nonlinear behavior can be seen in specimen L2-18a, which approaches the plastic hinge bound immediately following its peak load. This apparent difference in deformed shape can be seen by visual comparison of its deformed shape to one following the Euler bound (L3-132), in Figure 4.17.

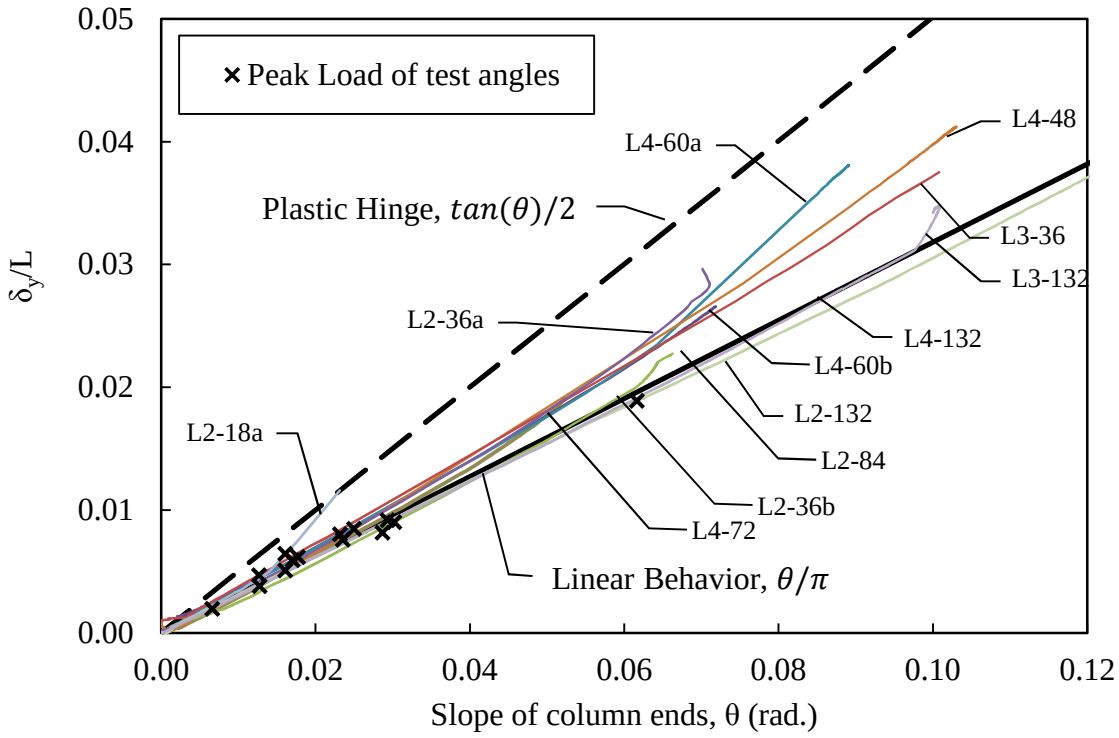

Figure 4.16- Experimental deformed shape plots for flexural buckling specimens

Figure 4.17- Deformed flexual-buckling specimens: L2-18a (left), L3-132 (right)

Flexural-torsional buckling

Flexural-torsional buckling was characterized by sudden twist, as seen in the time-stamped video frames shown in Figure 4.18. There was no evidence to suggest that cross-sectional distortion occurred during flexural-torsional buckling; thus the cross-sectional rotation at midheight could be determined numerically using deflection measurements. The midheight twist angle of the five specimens that underwent flexural-torsional buckling prior to reaching their peak loads is shown in Figure 4.19. Post-peak twisting behavior could not be analyzed due instrumentation failure. It can be seen that

for most specimens, the cross-section rotated approximately 0.07-0.09 rad. (4-5 degrees) at which point the load carried by the specimens dropped.

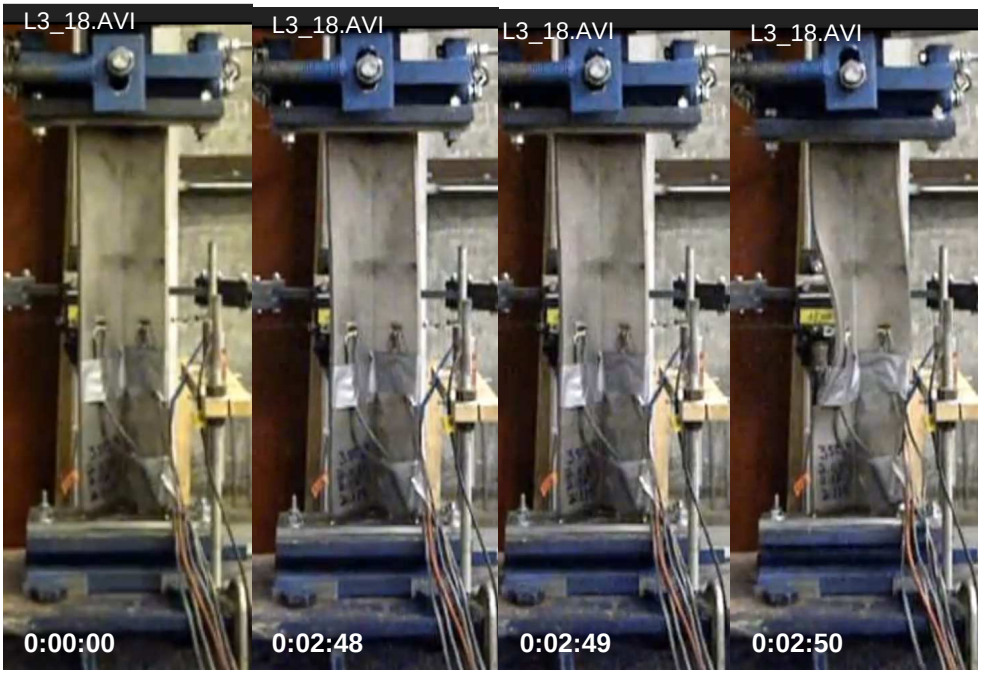

Figure 4.18- Progression of flexural-torsional buckling mode

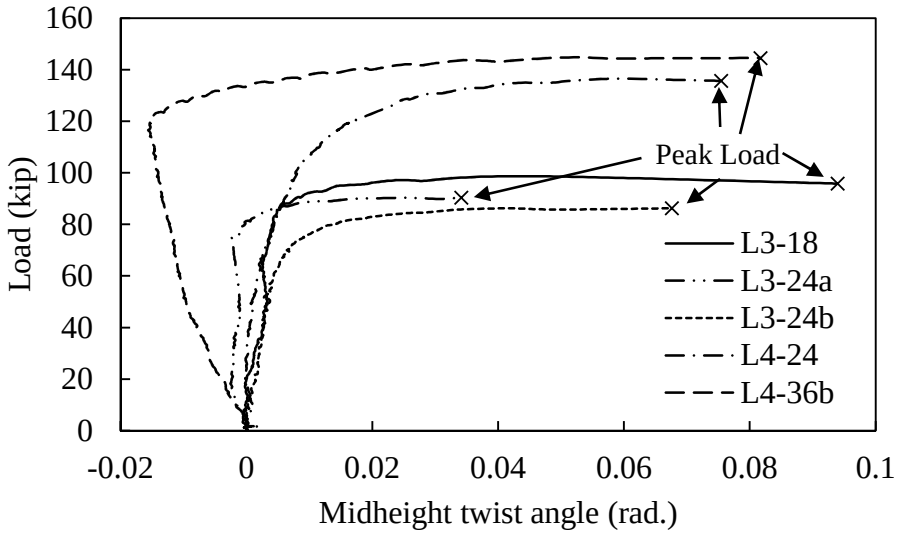

Figure 4.19- Midheight cross-sectional rotation for flexural-torsional buckling specimens

Southwell Plots

Although the Southwell plotting procedure was derived assuming linear material behavior (Southwell 1932), its applicability to inelastic column data was demonstrated by Wang (1948) and Singer (1989). Based on their survey of literature, the strengths determined from Southwell plots exceeded the tangent modulus buckling loads by 8% on average.

Southwell plots were prepared for specimens that buckled in the flexural mode using the axial force and midheight deflection data. A typical Southwell plot for a S32003 angle specimen (L3-48a) can be seen in Figure 4.20. Southwell plots were linear prior to buckling, but became nonlinear in the post-buckling range. Data for constructing the Southwell plots were taken in the range from approximately 70% of the peak load up to the peak load, since this region corresponded to the flexural rigidity present at the time of buckling. Data for each specimen is given in Table 4.3, and raw plots can be seen in Appendix B.

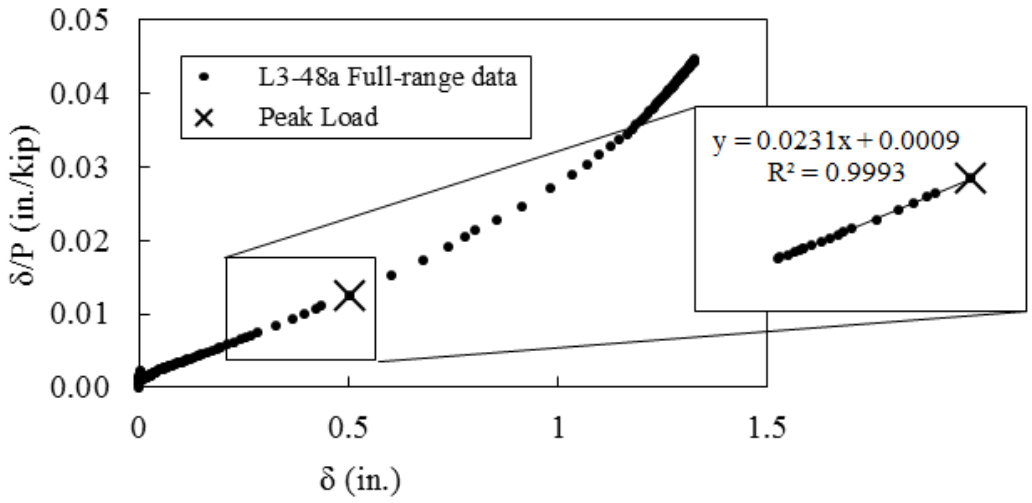

Figure 4.20- Typical Southwell plot (L3-48a)

Table 4.3- Southwell plot results and tangent modulus calculations

Specimen	$P_{Southwell}$ (kips)	$\frac{P_{exp}}{P_{Southwell}}$	$\frac{P_{Southwell}}{P_t}$	$\delta_o + \frac{4e}{\pi}$ (in.)	$\frac{L_e}{\delta_o + \frac{4e}{\pi}}$
L2-18a	61.05	0.928	1.245	0.014	1609
L2-18b	60.99	0.982	1.243	0.003	6237
L2-24	47.18	0.939	1.164	0.015	1491
L2-36a	27.79	0.896	1.065	0.038	721
L2-36b	26.41	0.969	1.016	0.018	1530
L2-48	14.26	0.922	0.993	0.061	626
L2-60a	8.59	0.895	0.886	0.104	373
L2-60b	8.77	0.947	0.914	0.056	952
L2-72	6.55	0.974	0.965	0.039	1695
L2-84	5.07	0.959	0.982	0.064	964
L2-96	4.02	0.943	0.995	0.052	1478
L2-132	2.12	0.960	0.975	0.105	847
L3-36	69.15	0.966	1.044	0.010	2744
L3-48a	45.77	0.863	0.986	0.055	696
L3-48b	42.40	0.962	0.912	0.017	2353
L3-60a	31.64	0.913	0.964	0.058	913
L3-60b	31.45	0.899	0.956	0.068	788
L3-72	24.04	0.964	1.012	0.012	5439
L3-84	18.83	1.036	1.060	0.008	7526
L3-132	7.76	0.989	1.029	0.004	21751
L4-36a	131.15	0.947	0.980	0.018	1571
L4-48	121.51	0.982	1.087	0.004	8647
L4-60a	94.19	0.930	1.013	0.043	1183
L4-60b	90.06	1.013	0.974	0.018	3690
L4-72	73.49	0.983	0.982	0.005	12702
L4-84	58.43	0.976	1.001	0.006	13702
L4-96	41.59	0.942	0.997	0.043	1693
L4-132	23.49	0.946	1.062	0.010	8686
AVERAGE	--	0.953	1.016		

4.5 DESIGN OF CONCENTRICALLY LOADED ANGLE STRUTS

The strengths of the experimental specimens were compared to the predicted strengths computed from existing stainless steel standards and design rules including *Design Manual for Structural Stainless Steel(Euro-Inox)* (SCI and Euro-Inox 2006), *Eurcode3 Part 1-4: General Rules – Supplementary rules for Stainless Steels (EC3, 1-4)*, the *SEI/ASCE 8-02: Specification for the Design of Cold-formed Stainless Steel Structural Members (SEI/ASCE 8-02), AS/NZS 4673:2001 Cold-formed Stainless Steel Structures(AS/NZS 4673)*, and *AISC Design Guide: Structural Stainless Steel (AISC 2012)*. From each standard or design rule, the strength was calculated using its provisions for concentrically loaded compression members, effective cross-sectional area (for unstiffened/outstand elements), and welded built-up sections (if applicable). The ratios of the experimental strengths of the specimens to their calculated strengths were used to in a first-order reliability analyses to calculate resistance factors for design.

It is noted that the following effective length factors were used in computing the buckling stresses (where applicable) to reflect the test boundary conditions for the angle specimens: K_x=1.0, K_y=0.5, and K_t=0.5. Additionally, it should be pointed out that because the legs of the angle were welded to base plates, the plate boundary conditions of each leg were rotationally restrained at the top and bottom instead of simply supported. The elastic torsional buckling stress, $F_{t,e}$, associated with these boundary conditions is given by Eq. (4-1) (Thomas 1941) and was used in computing the elastic torsional buckling stress in the stainless steel design standards (where applicable).

$$F_{t,e} = \frac{1}{A_g r_o^2}\left(GJ + 4\frac{\pi^2 E C_w}{(K_t L_t)^2}\right) \quad (4\text{-}1)$$

Design Manual for Structural Stainless Steel and EC3 1.4 (European)

Eurocode 3, Part 1.4 adopted the design formulations for concentrically loaded columns and effective area provisions found in the *Design Manual for Structural Stainless Steel.* The rules extend to non-cold-formed stainless steel structures, including the design of built-up welded members. These design formulations are explicit and were calibrated to test data, but do not consider the Ramberg-Osgood hardening parameter, *n*, in any formulations (Eurocode 3 2006; SCI and Euro-Inox 2006).

Effective Area

For welded sections, effective cross-sectional areas must be used if Eq. (4-2) is satisfied; the effective area is computed on the basis of the effective width method. The effective width, $\bar{b}_{eff}$, of each leg is calculated using Eq. (4-3).

$$\frac{\bar{b}}{t} > 0.30\sqrt{\frac{E}{F_y}} \quad (4\text{-}2)$$

$$\bar{b}_{eff} = \frac{\bar{b}\left(1 - \frac{0.242}{\lambda_p}\right)}{\lambda_p} \leq \bar{b} \quad (4\text{-}3)$$

Where

$$\lambda_p = \frac{1.053}{\sqrt{k_\sigma}} \frac{\bar{b}}{t} \sqrt{\frac{F_y}{E}} \tag{4-4}$$

$\bar{b}$ = leg width measured from heel to toe

E = Initial modulus of elasticity

F_y = Yield stress (0.2% proof stress)

t = leg thickness

k_σ = 0.43

Member strength

The strengths of the flexural and flexural-torsional buckling limit states are calculated using Eq. (4-5).

$$P_n = \chi A_e F_y \tag{4-5}$$

Where

$$\chi = \frac{1}{\varphi + \sqrt{\varphi^2 - \lambda^2}} \leq 1 \tag{4-6}$$

$$\varphi = \frac{1}{2}[1 + \alpha(\lambda - \lambda_o) + \lambda^2] \tag{4-7}$$

$$\lambda = \sqrt{\frac{F_y A_e}{P_{cr,e}}} \tag{4-8}$$

A_e = the effective cross-sectional area

P_{cr} = the critical elastic buckling force, (either $P_{fx,e}$, or $P_{ft,e}$)

α, λ_o = Parameters that depend on the buckling mode

For flexural buckling

$$P_{cr,,e} = \frac{\pi^2 E I_x}{(K_x L_x)^2} \tag{4-9}$$

α = 0.76

λ_o = 0.20

For flexural-torsional buckling

$$P_{cr,e} = \frac{P_{fy,e}}{2\beta}\left[\left(1 + \frac{P_{t,e}}{P_{fy,e}}\right) - \sqrt{\left(1 + \frac{P_{t,e}}{P_{fy,e}}\right)^2 - \frac{4\beta P_{t,e}}{P_{fy,e}}}\right] \tag{4-10}$$

$$P_{fy,e} = \frac{\pi^2 E I_y}{\left(K_y L_y\right)^2} \tag{4-11}$$

$$\beta = 1 - \left(\frac{y_o}{r_o}\right)^2 \tag{4-12}$$

$$P_{t,e} = F_{t,e} A_g \tag{4-13}$$

Where

α = 0.34

λ_o = 0.20

y_o = distance from the centroid to the shear center

r_o =polar radius of gyration about the shear center

$F_{t,e}$ = Given by Eq. (4-1)

SEI/ASCE 8-02

This design standard applies to cold-formed stainless steel members. The Ramberg-Osgood parameters for select austenitic and ferritic grades are listed in the appendices; however, the strengths of the angle specimens were calculated using the *SEI/ASCE 8-02* formulations with the Ramberg-Osgood properties for S32003 determined in Chapter 3 (SEI/ASCE 8-02 2002).

Effective Area

The *SEI/ASCE 8-02* standard uses the effective width approach to compute the effective cross-sectional area of a concentrically loaded column if Eq. (4-14) is satisfied. It is of interest to note that this is the same threshold for a slender unstiffened element in Section E7.1 of the *AISC Steel Construction Manual (13th Ed.)* for carbon steel when *f* is taken as the yield stress. The effective width, $\bar{b}_{eff}$, of each leg is computed using Eq. (4-15). In *SEI/ASCE 8-02*, $\bar{b}$ is defined as the width of the flat portion of the outstanding element, which implies that the curved region caused by the cold-forming process need not be included. Because built-up angles had no curved section, $\bar{b}$ was taken as the width of the leg measured from the heel to the toe (as in *EC3, 1-4* and *AISC* (carbon) *Steel Construction Manual*).

$$\frac{\bar{b}}{t} > 0.45\sqrt{\frac{E}{f}} \qquad (4\text{-}14)$$

$$\bar{b}_{eff} = \frac{\bar{b}\left(1 - \frac{0.22}{\lambda_p}\right)}{\lambda_p} \leq \bar{b} \tag{4-15}$$

Where

$$\lambda_p = \frac{1.053}{\sqrt{k_\sigma}} \frac{\bar{b}}{t} \sqrt{\frac{F_y}{E}} \tag{4-16}$$

f = Minimum of the nonlinear flexural buckling stress Eq. (4-18) and nonlinear flexural-torsional buckling stress Eq. (4-19)

t = leg thickness

k_σ = 0.5

Member strength

The design strength Eq. (4-17) of concentrically loaded, singly-symmetric compression members is taken as the effective cross-sectional area multiplied by the lesser of the minor-axis flexural buckling stress and the flexural-torsional buckling stress. The *SEI/ASCE 8-02* formulations are linear elastic buckling equations multiplied by the tangent modulus reduction factor, $\frac{E_t}{E_o}$, which is tantamount to assuming that the shear modulus remains proportional to the longitudinal modulus for increased nonlinearity.

$$P_n = A_e \min\left(F_{fx}, F_{ft}\right) \tag{4-17}$$

Where

$$F_{fx} = \frac{\pi^2 E_t}{\left(\frac{K_x L_x}{r_x}\right)^2} \tag{4-18}$$

$$F_{ft} = \frac{1}{2\beta}\left[\left(F_{fy} + F_t\right) - \sqrt{\left(F_{fy} + F_t\right)^2 - 4\beta F_t F_{fy}}\right] \tag{4-19}$$

$$F_{fy} = \frac{\pi^2 E_t}{\left(\frac{K_y L_y}{r_y}\right)^2} \tag{4-20}$$

$$F_t = \frac{1}{A_g r_o^2}\left(G_o J + 4\frac{\pi^2 E_o C_w}{(K_t L_t)^2}\right)\left(\frac{E_t}{E_o}\right) \tag{4-21}$$

AS/NZS 4673

AS/NZS 4673 is a similar design standard to *SEI/ASCE 8-02*. In addition to also being limited to cold-formed sections, *AS/NZS 4673* computes the effective cross-sectional areas and flexural and flexural-torsional buckling stresses using the same formulations as *SEI/ASCE 8-02*. It does, however, offer an alternative, explicit approach for calculating the flexural-buckling stress of a concentrically loaded column. This explicit approach utilizes the Perry-Robertson formulation, given by Eq. (4-22), which is similar to the Perry-Robertson formulation given by the European design rules; however, unlike *EC3, 1-4*, which does not account for nonlinear material behavior, *AS/NZS 4673* accounts for nonlinear material behavior by using the parameters α, β, λ_0, and λ_1 in Eq. (4-25), which were calibrated for various values of modified-Ramberg-Osgood parameters by Rasmussen and Rondal (1997b), (AS/NZS 4673).

$$F_{fx} = \frac{F_y}{\varphi + \sqrt{\varphi^2 - \lambda^2}} \leq F_y \tag{4-22}$$

Where

$$\varphi = \frac{1}{2}(1 + \eta + \lambda^2) \tag{4-23}$$

$$\lambda = \frac{1}{\pi}\frac{K_x L}{r_x}\sqrt{\frac{F_y}{E_o}} \tag{4-24}$$

$$\eta = \alpha\left[(\lambda - \lambda_1)^{\beta} - \lambda_0\right] \tag{4-25}$$

For the *AS/NZS 4673* standard, the predicted flexural-torsional buckling stresses were calculated using Eq. (4-19)-(4-21), and the predicted flexural buckling stresses were computed using the explicit formulation given by Eq. (4-22)-(4-25). In *AS/NZS 4673* the parameters α, β, λ_0, and λ_1 are tabulated for select grades. In this study, these parameters were computed for S32003 using the formulations, Eq. (4-26)-(4-30), given by (Rasmussen and Rondal 1997a). The parameters for S32002 are presented in Table 4.4.

$$\alpha = \frac{1.5}{(e^{0.6} + 0.03)\left[n^{(0.0048e^{-0.55}+1.4)} + 13\right]} + \frac{0.002}{e^{0.6}} \tag{4-26}$$

$$\beta = \frac{0.36\exp(-n)}{e^{0.45} + 0.007} + \tanh\left(\frac{n}{180} + \frac{6E - 6}{e^{1.4}} + 0.04\right) \tag{4-27}$$

$$\lambda_0 = 0.82\left(\frac{e}{e + 0.0004} - 0.01n\right) \geq 0.2 \tag{4-28}$$

$$\lambda_1 = 0.8\frac{e}{e + 0.0018}\left[1 - \left(\frac{n - 5.5}{n + \frac{6e - 0.0054}{e + 0.0015}}\right)^{1.2}\right] \tag{4-29}$$

$$e = \frac{F_y}{E_o} \tag{4-30}$$

n = Ramberg-Osgood Hardening Parameter

Table 4.4- AS/NZS explicit design parameters, S32003

AS/NZS Perry Curve Parameter	Values
α	1.009
β	0.111
λ_0	0.667
λ_1	0.473

AISC Design Guide: Structural Stainless Steel

The (draft) *AISC Design Guide* for structural stainless steel applies to hot-rolled and built-up stainless steel sections whose plate thicknesses exceed ⅛ in. The design formations are similar to those in (AISC 2005).

Effective Area

The *Q*-reduction factor approach is used to account for slender elements. For equal-leg angles, slender column formulas must be used to calculate column strength if Eq. (4-31) is satisfied.

$$\frac{\bar{b}}{t} > 0.38\sqrt{\frac{E}{F_y}} \tag{4-31}$$

For equal-leg angles, the Q-reduction factor is equal to the reduction factor for slender unstiffened elements, Q_s, since there are no stiffened elements, $Q = Q_s$, which was calculated used on Eq. (4-32). It is noted that there is an inconsistency in this formulation in comparison to Eq. (4-31)—there is a range $\left(0.38\sqrt{\frac{E}{F_y}} \leq \frac{\bar{b}}{t} \leq 0.47\sqrt{\frac{E}{F_y}}\right)$ in which an angle is considered slender but no reductions are made. Despite this assumed error, Q was calculated based on Eq. (4-32)

$$Q = \begin{cases} 1.0, \quad if \quad \dfrac{\bar{b}}{t} \le 0.47\sqrt{\dfrac{E}{F_y}} \\ 1.498 - 1.06\left(\dfrac{\bar{b}}{t}\right)\sqrt{\dfrac{F_y}{E}}, \quad if \quad 0.47\sqrt{\dfrac{E}{F_y}} < \dfrac{\bar{b}}{t} \le 0.90\sqrt{\dfrac{E}{F_y}} \\ \dfrac{0.44E}{F_y\left(\dfrac{\bar{b}}{t}\right)^2}, \quad if \quad \dfrac{\bar{b}}{t} > 0.90\sqrt{\dfrac{E}{F_y}} \end{cases} \tag{4-32}$$

Member Strength

For singly-symmetric compression members with slender elements in uniform compression, the nominal compressive strength is taken as the lowest value of the flexural and flexural-torsional buckling limit states.

$$P_n = A_g \min\left(F_{cr,fx}, F_{cr,ft}\right) \tag{4-33}$$

Flexural buckling

$$F_{cr,fx} = \begin{cases} Q\left[0.50^{\frac{QF_y}{F_e}}\right]F_y, \quad if \quad \dfrac{K_x L_x}{r_x} \le 3.77\sqrt{\dfrac{E}{QF_y}} \\ 0.531F_e, \quad if \quad \dfrac{K_x L_x}{r_x} > 3.77\sqrt{\dfrac{E}{QF_y}} \end{cases} \tag{4-34}$$

Where

$$F_e = \frac{\pi^2 E_o}{\left(\dfrac{K_x L_x}{r_x}\right)^2} \tag{4-35}$$

Flexural-torsional buckling

$$F_{cr,ft} = \begin{cases} Q\left[0.50^{\frac{QF_y}{F_e}}\right]F_y, \quad if \quad \dfrac{QF_y}{F_e} \le 1.44 \\ 0.531F_e, \quad if \quad \dfrac{QF_y}{F_e} > 1.44 \end{cases} \tag{4-36}$$

Where

$$F_e = \frac{F_{fy,e}}{2\beta}\left[\left(1+\frac{F_{t,e}}{F_{fy,e}}\right) - \sqrt{\left(1+\frac{F_{t,e}}{F_{fy,e}}\right)^2 - \frac{4\beta F_{t,e}}{F_{fy,e}}}\right] \quad (4\text{-}37)$$

$$F_e = \frac{\pi^2 E_o}{\left(\frac{K_y L_y}{r_y}\right)^2} \quad (4\text{-}38)$$

$F_{t,e}$ = Given by Eq. (4-1)

Computed Strength Comparison

The computed strengths for flexural and flexural-torsional buckling are reported in Table 4.5 and Table 4.6, respectively. It can be seen that strength predictions from *SEI/ASCE 8-02, AS/NZS 4673,* and *AISC Design Guide* all predicted the buckling mode that was observed during experimental tests. The *EC3, 1-4* predicted flexural buckling for all 32 angles, including those which underwent flexural-torsional buckling during the experimental buckling tests. It should be noted that *EC3, 1-4,* and *AISC Design Guide,* which do not take into account the nonlinear behavior specific to S32003, give very conservative load predictions in comparison to the strengths computed using the *SEI/ASCE 8-02* and *AS/NZS 4673,* both of which took into account the nonlinear behavior of S32003, resulting in closer strength predictions. Additionally, the *SEI/ASCE 8-02* and *AS/NZS 4673* design formulations for the flexural-torsional buckling mode give more conservative strength predictions than for the flexural-buckling mode.

Table 4.5- Flexural-buckling experimental/calculated strength ratios

	Experiment				SEI/ASCE 8-02		AS/NZS 4673		EC3, Part 1-4		AISC Stainless Steel	
	$\frac{\bar{b}}{t}$	$\frac{L_x}{r_x}$	L_x	P_{exp} (kips)	P_{ASCE} (kips)	$\frac{P_{exp}}{P_{ASCE}}$	$P_{AS/NZS}$ (kips)	$\frac{P_{exp}}{P_{AS/NZS}}$	P_{EC3} (kips)	$\frac{P_{exp}}{P_{EC3}}$	P_{AISC} (kips)	$\frac{P_{exp}}{P_{AISC}}$
L2-18a	8.15	55	21.8	56.6	49.0	1.16	46.2	1.23	35.6	1.59	40.0	1.42
L2-18b	8.15	55	21.7	59.9	49.0	1.22	46.2	1.30	35.6	1.68	40.0	1.50
L2-24	8.17	70	27.5	44.3	40.5	1.09	36.5	1.21	27.4	1.62	28.1	1.58
L2-36a	8.27	98	38.3	24.9	26.1	0.95	22.6	1.10	17.3	1.44	14.4	1.73
L2-36b	8.32	98	38.4	25.6	26.0	0.98	22.5	1.14	17.2	1.49	14.3	1.78
L2-48	8.20	135	53.3	13.1	14.4	0.92	13.1	1.00	10.5	1.26	7.6	1.72
L2-60a	8.09	165	65.3	7.7	9.7	0.79	9.1	0.85	7.5	1.03	5.1	1.49
L2-60b	8.11	165	65.3	8.3	9.6	0.87	9.0	0.92	7.4	1.12	5.1	1.63
L2-72	8.19	196	77.3	6.4	6.8	0.94	6.5	0.98	5.5	1.17	3.6	1.77
L2-84	8.14	226	89.3	4.9	5.2	0.94	5.0	0.98	4.3	1.14	2.7	1.77
L2-96	8.10	256	101.3	3.8	4.0	0.94	3.9	0.97	3.4	1.11	2.1	1.77
L2-132	8.06	349	137.3	2.0	2.2	0.94	2.1	0.95	1.9	1.06	1.2	1.76
L3-36	12.07	65	38.8	66.8	63.3	1.06	59.4	1.13	40.8	1.64	46.3	1.44
L3-48a	12.13	90	53.3	39.5	46.4	0.85	40.1	0.98	28.3	1.40	26.5	1.49
L3-48b	12.11	90	53.3	40.8	46.5	0.88	40.2	1.01	28.3	1.44	26.6	1.53
L3-60a	12.09	110	65.3	28.9	32.8	0.88	28.9	1.00	21.2	1.36	17.7	1.63
L3-60b	12.16	110	65.3	28.3	32.9	0.86	29.0	0.98	21.2	1.33	17.7	1.59
L3-72	12.13	130	77.3	23.2	23.7	0.98	21.5	1.08	16.3	1.42	12.7	1.83
L3-84	12.15	150	89.3	19.5	17.8	1.10	16.5	1.19	12.9	1.52	9.4	2.07
L3-132	12.07	231	137.3	7.7	7.5	1.02	7.3	1.05	67.4	1.77	4.0	1.92
L4-48	13.15	63	50.3	119.4	101.6	1.17	96.0	1.24	55.0	1.59	77.2	1.55
L4-60a	13.04	78	61.6	87.6	89.9	0.97	81.7	1.07	54.7	1.67	58.2	1.51
L4-60b	12.96	78	61.8	91.3	89.5	1.02	81.2	1.12	45.0	1.61	57.7	1.58
L4-72	12.88	91	72.4	72.2	74.8	0.97	64.7	1.12	36.7	1.55	42.3	1.71
L4-84	12.83	106	83.8	57.0	58.4	0.98	51.1	1.12	28.2	1.39	31.6	1.80
L4-96	12.75	127	101.3	39.2	41.7	0.94	37.7	1.04	16.6	1.34	22.2	1.76
L4-132	12.74	174	137.3	22.3	22.1	1.01	20.9	1.07	67.4	1.77	11.7	1.90
				Average		0.98		1.07		1.41		1.68
				COV		0.11		0.10		0.15		0.10
				φ_f		0.70		0.77		0.94		1.21

Table 4.6- Flexural-torsional buckling experimental/calculated strength ratios

	Experiment				SEI/ASCE 8-02		AS/NZS 4673		EC3, Part 1-4		AISC Stainless Steel	
	$\frac{\bar{b}}{t}$	$\frac{L_y}{r_y}$	L_y (in.)	P_{exp} (kips)	P_{ASCE} (kips)	$\frac{P_{exp}}{P_{ASCE}}$	$P_{AS/NZS}$ (kips)	$\frac{P_{exp}}{P_{AS/NZS}}$	P_{EC3} (kips)	$\frac{P_{exp}}{P_{EC3}}$	P_{AISC} (kips)	$\frac{P_{exp}}{P_{AISC}}$
L3-18	12.15	15.7	18.5	98.7	75.1	1.31	75.1	1.31	61.8*	--	65.8	1.50
L3-24a	12.12	20.8	24.6	90.4	72.4	1.25	72.4	1.25	54.6*	--	61.1	1.48
L3-24b	12.10	20.8	24.6	86.3	71.9	1.20	71.9	1.20	54.3*	--	60.8	1.42
L4-24	12.81	15.7	24.6	136.6	118.3	1.15	118.3	1.15	102.3*	--	102.8	1.33
L4-36b	12.93	23.3	36.6	144.6	109.8	1.32	109.8	1.32	84.1*	--	89.6	1.61
				Average		1.25		1.25		--		1.47
				COV		0.06		0.06		--		0.07
				φ_{ft}		0.92		0.92		--		1.06

*Flexural buckling predicted as limit state

4.6 RELIABILITY ANALYSIS

The strength of each angle section was divided by the strength predicted by each standard and design rule. These strength ratios were then used to calculate a resistance factor for design based on that design method. Flexural-torsional buckling was not considered for *EC3, 1-4* since it failed to predict that buckling mode. Using first-order reliability, the resistance factor can be computed from Eq. (4-39) (SEI/ASCE 8-02 2002).

$$\varphi = \frac{\left(\frac{1.2D_n}{L_n} + 1.6\right)}{\left(\frac{1.05D_n}{L_n} + 1\right)} M_m F_m P_m e^{\left(-\beta_o \sqrt{V_M^2 + V_F^2 + V_q^2 + C_P V_P^2}\right)} \tag{4-39}$$

$$V_Q = \frac{\sqrt{\left[\left(\frac{1.05D_n}{L_n}\right)^2 V_D^2 + V_L^2\right]}}{\left(\frac{1.05D_n}{L_n} + 1\right)} \tag{4-40}$$

For a nominal live-to-dead load ratio L_n/D_n =3, which is used in (AISC 2005), Eq. (4-39) becomes Eq. (4-41). Additionally, knowing V_L=0.25 vs. V_D=0.1 (SEI/ASCE 8-02 2002), V_Q is calculated to be 0.19.

$$\varphi = 1.481 M_m F_m P_m e^{\left(-\beta_o \sqrt{V_M^2 + V_F^2 + V_q^2 + C_P V_P^2}\right)} \tag{4-41}$$

Using the average, P_m, and coefficient of variation, V_P, experimental/computed strength ratios of each standard or design rule and buckling mode, the resistance factor was computed with the following parameters.

1. Target reliability index, β_o, was selected to be a value of 3.0.

2. Material factor mean, M_m, was taken as 1.0 since the strengths were computed using the stress-strain relationship resulting from stub column tests. The coefficient of variation in the material factor, V_m, was taken 0.10 from (SEI/ASCE 8-02 2002).
3. The values of the fabrication statistical parameters, F_m and $V_{F,}$ were taken from (SEI/ASCE 8-02 2002); they are 1.0 and 0.05, respectively.
4. The sample size correction factor, C_p , given by Eq. (4-42), was taken from Eq. 6.2-3 of (SEI/ASCE 8-02 2002) (n=27 for flexural buckling, and n=5 for flexural-torsional buckling).

$$C_p = \frac{n-1}{n-3} \tag{4-42}$$

The computed resistance factors are listed in Tables 4.5-6 along with the design standard and mode they accompany. It is noted that the *AISC Design Guide* is unduly conservative for both the flexural and flexural-torsional buckling modes, due to its resistance factors being nearly 150%. This suggests that the model adopted does not reflect the behavior of axially loaded columns, and alternative formulations should be used. The resistance factor associated with flexural buckling design by *EC3, 1-4* was calculated to be 0.94; however, *EC3, 1-4* was unable to predict flexural-torsional buckling as limit state for the angles tested. Since the flexural-torsional buckling formulation is identical for both *SEI/ASCE 8-02* and *AS/NZS 4673*, and each design standard predicted the same as the other (0.92), the resistance factor for flexural-torsional buckling was the same for both standards. For flexural buckling, *AS/NZS 4673* gives

more conservative strength predictions than *SEI/ASCE 8-02*, resulting in higher resistance factors. This was reflected by the S32003 angle data, and has been similarly observed elsewhere (Baddoo 2003; Rasmussen and Rondal 1997a).

4.7 CONCLUSIONS

Based on a test series that involved full-scale testing of 33 equal-leg angles, nonlinear material behavior becomes increasingly apparent, both in terms of column strength and deformation for stockier columns. Stocky columns were also more susceptible to flexural-torsional buckling, particular for angles with larger *b/t* ratios.

The results were used to evaluate existing design standards and design rules. This evaluation revealed that design rules such as *EC3, 1-4* and the *AISC Design Guide* which do not reflect the stress-strain behavior of a column either predicted the incorrect limit state or were unduly conservative. The cold-formed standards, *SEI/ASCE 8-02* and *AS/NZS 4673*, which do consider the nonlinear stress-strain behavior, were shown to closely predict both the buckling mode and strengths of the tested angle specimens. Therefore it is concluded that the mechanics-based strength formulations rated to concentrically loaded columns in the American and Australian cold-formed stainless steel standards can be used to predict the strength of built-up stainless steel sections.

CHAPTER 5

NUMERICAL ANALYSES

This chapter presents a series of finite element analyses that were used to model the buckling behavior of concentrically loaded S32003 stainless steel single equal-leg angles. The modeling procedure was validated from experimental results and then used as a computational tool to generate additional data from which recommendations could be made for design purposes. The effects of material anisotropy, boundary conditions, and out-of-straightness on column strength were also investigated.

5.1 NUMERICAL EXPERIMENTATION

Overview of Wempner-Riks Method

As described in Chapter 2, numerical experimentation using the finite element method has previously been employed as a cost-effective computational tool to simulate the compressive behavior of stainless steel sections. One of the algorithms used for such analysis is the Wempner-Riks procedure. This incremental procedure, which traces the static equilibrium path of a discrete formulation (i.e. finite element model) in the load-displacement space, can be used to determine member strength while incorporating second-order effects and nonlinear material behavior. The magnitude, λ, of the load pattern, P^N, applied to the structure is unknown, but it remains proportional from increment to increment.

This procedure was first developed by Wempner (1971) and subsequently modified by Crisfield (1981); Riks (1972). The loading increments are sized on the basis of arc length, which enables the equilibrium path of events like snap-through buckling

and post-buckling, where the load and displacements do not have a monotonic relationship, to be traced. Convergence is achieved for each increment using the Newton-Raphson method.

Commercial finite element software, *ABAQUS,* includes a Wempner-Riks arc-length algorithm (called STATIC, RIKS). The initial load increment at the beginning of analysis is based on user-defined arc-length input and is calculated automatically for subsequent increment steps so that regions of high-curvature are traced with small increments and near-linear regions are traced with larger increments. Within each increment, potential solution points are limited by the plane orthogonal to the previous iteration's tangent stiffness, K_{i-1}^{NM}, and passing through the previous potential solution point, A^{i-1} (ABAQUS 2011). This procedure is summarized in Figure 5.1 and is seen visually in Figure 5.2. Furthermore, it should be noted that *ABAQUS* also scales the solution space so that the load magnitude parameter, λ, and displacements, u^N, are approximately the same magnitude for each increment, which is not reflected in either figure.

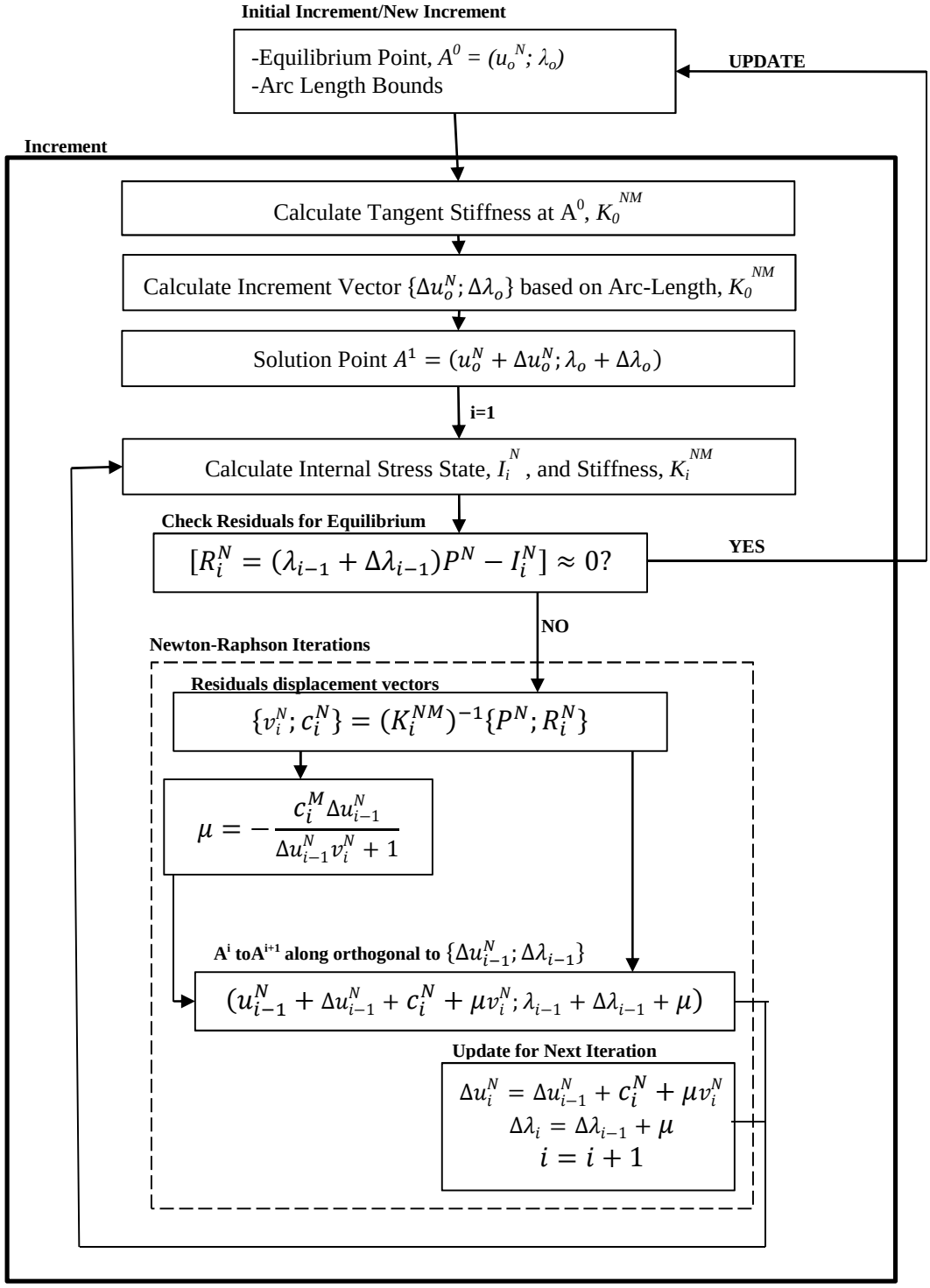

Figure 5.1- *ABAQUS* Wempner-Riks increment and iteration procedure

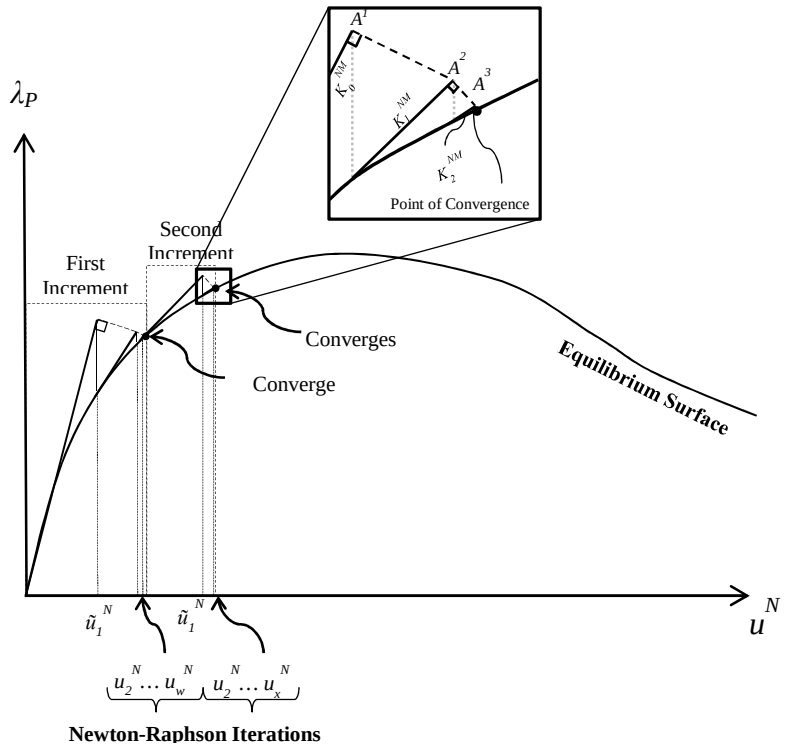

Figure 5.2- Equilibrium surface tracing according to Wempner-Riks method in *ABAQUS*

Aims of Numerical Experimentation in Present Study

Due to the limited number of full-scale compression tests conducted on S32003 single equal-leg angles, it was deemed necessary to conduct numerical experiments for the purpose of generating additional data. Of interest is the effect of out-standing leg slenderness (*b/t*) ratios on column strength. This is an important aspect of column strength to address since relatively little work has been devoted to the flexural-torsional buckling strength of stainless steel columns, and only a very narrow range of leg slenderness ratios were experimentally tested and reported in Chapter 4. A finite element study was thus undertaken to expand upon the experimental data and to evaluate the strength of angle sections based on outstanding leg-slenderness ratios.

5.2 MODELING PROCEDURE

All numerical buckling analyses were conducted using commercial finite element software, *ABAQUS v.6.12-1*. A consistent unit system was established for the modeling procedure, relying on base units which included pounds-force, inches, and seconds.

Model Geometry

Each angle was modeled and positioned such that its centroidal axis coincided with the global Z axis, and the cross-sectional principal axes coincided with the global X and Y axes, as shown in Figure 5.3. This figure also shows the orientation of the element coordinate axes. Angles were modeled using two-dimensional shells positioned mid-thickness of the actual cross-section, as shown in Figure 5.4.

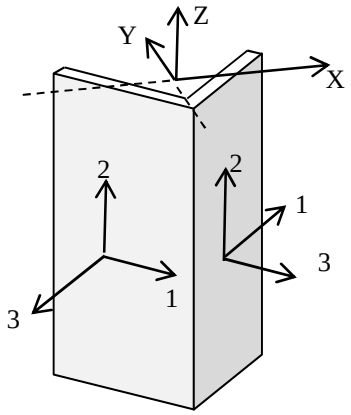

Figure 5.3- Element and global coordinate systems of finite element models

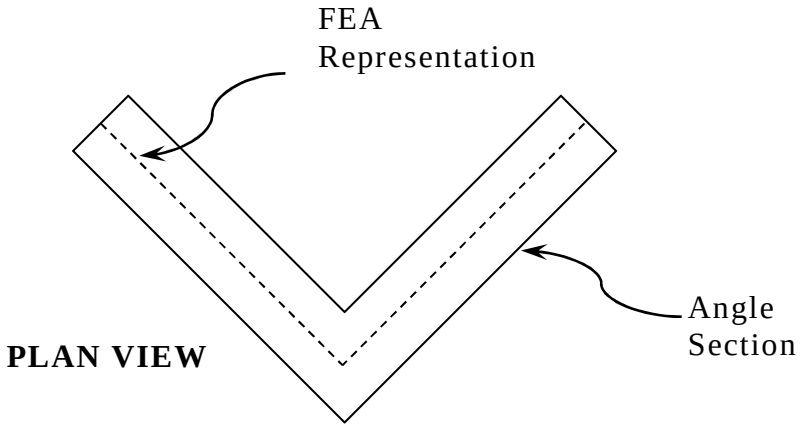

Figure 5.4- Cross-sectional representation of angle

Modeling Procedure

The angle sections were modeled with the S4R general purpose shell element. The S4R consists of four nodes with 6 degrees of freedom per node. It utilizes reduced integrations with hour-glass control (ABAQUS 2011). The integration through the thickness of the shell sections was executed using Simpson's rule, which was the program default; the number of through-thickness integration points was determined through a sensitivity study. Previous numerical studies have used this element in modeling the structural response of cold-formed stainless steel members to compressive loading (Becque and Rasmussen 2009c; Becque and Rasmussen 2009d; Ellobody 2007; Ellobody and Young 2005; Theofanous and Gardner 2009).

Each end fixture was modeled using two R3D3 rigid triangular shell elements, which transferred loads between the boundary conditions and the deformable S4R shell elements, as shown in Figure 5.5. Interaction between the S4R and R3D3 elements was

defined using a tied slave-master (respectively) surface relationship. With respect to plate behavior of the legs of the angles, this interaction simulates fixed rotational boundary conditions at the top and bottom edges of the plate to correspond to the boundary conditions imposed by the welded end plates on the test specimens. The desired boundary conditions were defined at the nodes labeled as the "Top Support Node" and "Base Support Node" in Figure 5.5. The loading pattern consisted of a unit point-load oriented in the negative Z-direction, which was applied at the "Top Support Node."

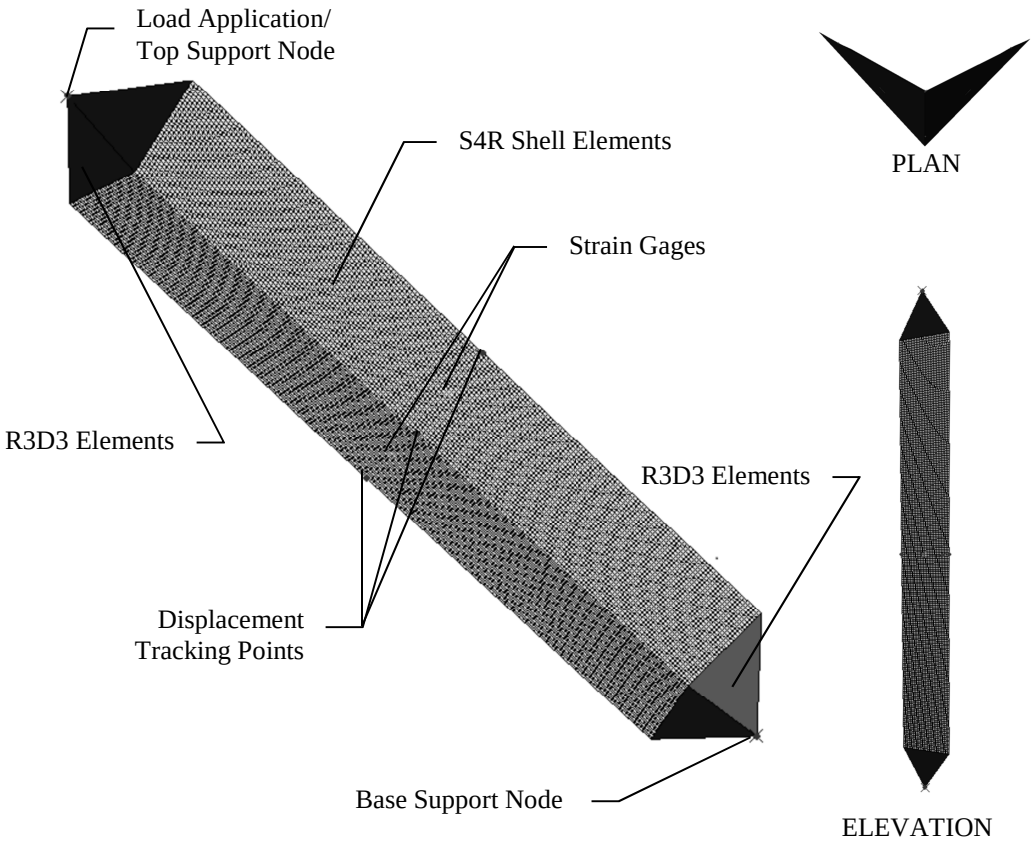

Figure 5.5- Finite element model components

Material Model

The material model used in the finite element models was based on the typical stress-strain relationship developed in Chapter 3. The material model was constructed summoning both the *ELASTIC command, to describe the linear material behavior, and the *PLASTIC command, to describe the nonlinear material behavior. Within *ELASTIC the LAMINA suboption was selected. This treats the shell elements as orthotropic plates under plane stress conditions whose behavior is governed using five material constants, E_1, E_2, v, G_{12}, G_{23}, and G_{31} (ABAQUS 2011). The LAMINA suboption was selected rather than the default isotropic case to include the in-plane shear modulus determined in Chapter 3. E_2, G_{23}, and G_{31} were not experimentally determined, but were instead set equal to the longitudinal and in-plane values that were determined for E_1 and G_{12}. This is summarized below in Table 5.1.

Table 5.1- Elastic material model parameters

E_1 (psi)	E_2 (psi)	v	G_{12} (psi)	G_{23} (psi)	G_{31} (psi)
28.2E+6	28.2E+6	0.24	9.83E+6	9.83E+6	9.83E+6

The nonlinear material behavior was described using a multi-linear representation of the typical stress-strain curve within the *PLASTIC option. This option utilizes an associated flow rule with isotropic hardening (ABAQUS 2011). The multi-linear curve used in the material model consisted of 100 points, which were distributed in proportion to the curvature of the stress-strain curve, as suggested by Theofanous and Gardner (2009). The input syntax required that stress-strain data be converted to true stress-true plastic strain forms, which were calculated using Eq. (5-1) and Eq. (5-2). Plastic

behavior was specified to initiate at the first point datum, 23.3 ksi, rather than the 0.2% proof stress, 75.6 ksi to capture early nonlinear material behavior. The resulting experimental model can be seen in Figure 5.6.

$$\varepsilon_t^{pl.} = \ln(1+\varepsilon) - \frac{\sigma_t}{E_o} \tag{5-1}$$

$$\sigma_t = \sigma(1+\varepsilon) \tag{5-2}$$

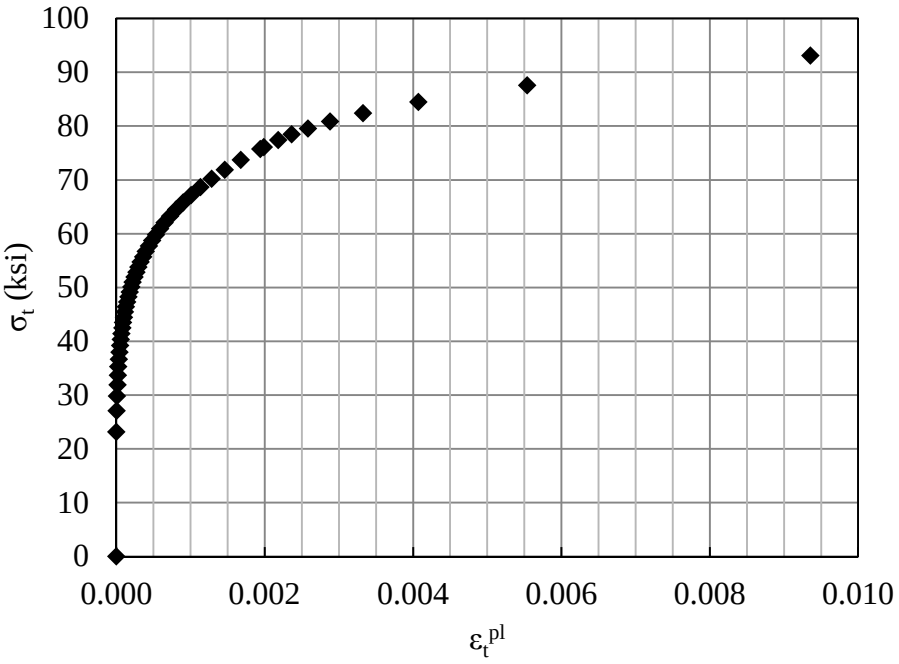

Figure 5.6- Finite element material model for S32003

Analysis Procedure

A two-step analysis procedure was followed that was similar to those used by Becque and Rasmussen (2009c); Becque and Rasmussen (2009d); Ellobody (2007); and Ellobody and Young (2005). In the first step, a linear eigenvalue buckling analysis was

performed on a defect-free model with linear material behavior to determine the nodal displacements associated with various buckling modes. In the second step, geometric imperfections were imposed on the model using the *IMPERFECTION command, which scales the nodal displacements determined from the first step. This was done for the sake of simplicity in imposing out-of-straightness and plate imperfections with desired magnitudes; however, it is to be noted that this assumes that the initial imperfections are proportional to the elastic buckled shape. A nonlinear analysis was performed. The *NLGEOM option was enabled to consider second-order effects. Analyses were terminated when the axial displacement of the top support node reached a threshold value.

History Output Requests

Certain nodes and elements, shown in Figure 5.5, were flagged during the creation of the model to track their movement throughout analysis. This data could then be compared against experimentally recorded data. These include the displacements of toes and heel of the angle at midheight, which were tracked experimentally with string potentiometers. Vertical (Z) displacement at the point of load application was tracked and compared to the axial shortening which was measured using a potentiometer during experimental testing. The strain was tracked for the elements whose locations coincided with the location of the strain gages on the test specimens.

Modeling Sensitivity Analyses

Prior to conducting numerical experiments, the modeling procedure was evaluated to ensure that the models were not artificially strong/weak due to the modeling methodology. These checks included convergence studies to determine adequate mesh

size, arc-length increment sensitivity studies to determine its effect on peak load, and a sensitivity study to determine the effect of the number of through-thickness points on peak load. These checks were performed in this order to ensure that only one aspect of modeling was considered at a time. Additionally, the sensitivity of the strength of the models to changes in the material model was investigated.

Convergence Study

The proper element mesh density was examined to ensure that the models were not artificially stiff or computationally expensive. Convergence studies were conducted on five models to examine the influence of element size on strength and computation time. Models were meshed such that the elements were approximately square. Five models were constructed and subjected to eigenvalue buckling analyses. From the convergence analyses, whose results can be seen in further detail in Appendix C, it was decided at least 8 elements were necessary to model the width of each leg in order to obtain the converged strength.

Arc-Length Sensitivity

Although the arc-length solving procedure in *ABAQUS* will determine the arc-length for each increment based on the curvature of the equilibrium path, user-defined bounds will limit what arc-length the auto-incrementation script can calculate. It is desirable to maintain small arc-length increments to prevent significant deviation from the equilibrium path; however, small-arc length increments are computationally expensive. Large arc-length increments result in coarse traces of equilibrium paths, which may underestimate the strength of the model, despite their computational efficiency.

To determine the effect of the specified maximum arc-length on model strength, four models were subject to sensitivity analyses—a 18 in. long L2 x 2 x ¼, a 132 in. long L2 x 2 x ¼ , a 24 in. long L4 x 4 x $^{5}/_{16}$, and a 60 in. long L4 x 4 x $^{5}/_{16}$. The sections were selected to evaluate the effect of arc-length on various load levels and buckling modes. Two different maximum arc-length increments were compared for each of the models: 1,000,000 and 10,000. Although no specimen ever reached loads near 1,000,000, this maximum arc-length was specified as an arbitrarily large bound for the auto-incrementation calculations. It was observed that specifying maximum arc-length increments smaller than 10,000 caused some of the analyses to become unstable. The results of this study, which can be found in Appendix C, indicate that model strength is not sensitive to the maximum specified arc-length with the maximum difference being 1.6% between the two cases. It was ultimately decided to use an arc-length of 20,000, which produced refined traces of the equilibrium path while still reducing the computation time.

Through-thickness integration points

A sensitivity study was conducted to select the proper number of through-thickness integration points to use in the S4R elements for Simpson's rule. The number of integration points must be, inclusively, an odd number between 3 and 99. Because flexural-torsional buckling involves plate bending in addition to flexure, the strength of a 24 in. long L4 x 4 x $^{5}/_{16}$ model was analyzed using varying through-thickness integration points. From the results, which are summarized in Appendix C, it was decided to use seven through-thickness integration points for Simpson's rule.

Material Model Sensitivity

The sensitivity of the models to changes in material parameters was investigated in order to determine the validity of the findings of these analyses to angles with different material parameters. Specifically, the influences of the initial shear modulus and of Poisson's ratio on the strength of the angles were investigated. Two models were used in this investigation, a 26 in. long L3¼ x 3¼ x ¼ angle and a 71.75 in. long L5⅛ x 5⅛ x ¼ angle. The strengths of these two models, using the material model previously described, were determined based on a full nonlinear analysis and served for comparison when material parameters were varied.

Three cases were considered for comparison. Firstly, both models were reexamined when Poisson's ratio was set equal to 0.31. Secondly, both models were examined when the material model was assumed to be isotropic with Poisson's ratio set equal to 0.31, rather than orthotropic under plane stress conditions. Lastly, both models were examined when orthotropic material behavior under plane stress conditions were assumed along with a Poisson's ratio equal to 0.24, but with the shear modulus equal to 10,800 ksi, which corresponds to the shear modulus computed using isotropic material relationships and a Poisson's ratio of 0.3. The strengths of the two models under each condition are given in Appendix C. From these three cases, it can be seen that the model strengths are most sensitive to the value of the shear modulus, which caused the strengths to vary by up to 9% based on the values considered. Varying only Poisson's ratio caused the strengths to increase by approximately 0.1%. Assuming isotropic material behavior rather than orthotropic/plane stress material behavior caused negligible change in the model strengths. Thus, the models showed little sensitivity to changes in Poisson's ratio,

and the findings of subsequent analyses, whose models use a Poisson's ratio of 0.24, are valid for angles with similar shear properties, but with different values of Poisson's ratio.

5.3 VALIDATION OF MODELING PROCEDURE

Prior to using finite element analyses to generate additional data, the modeling procedure was validated by comparing its results to the results from the experimental tests described in Chapter 4. Each of the 33 test specimens was modeled and loaded using *ABAQUS*.

Modeling Considerations

To match the boundary conditions of the experiments, the support nodes were specified to permit rotation about the minor principal axis as well as axial deformation while all other degrees of freedom at the support nodes were restrained. To incorporate the rotational restraint imposed on the test specimens by the experimental end fixtures, the depth of the R3D3 end fixture elements was adjusted so that the length between the support nodes matched the effective length of the column given in Chapter 4.

Angles that underwent flexural buckling during experimental testing were modeled to have out-of-straightness magnitudes equal to those determined from their Southwell plots in Chapter 4; angles that underwent flexural-torsional buckling were modeled to have out-of-straightness magnitudes equal to the out-of-straightness measured with a theodolite. Flexural-torsional imperfections were scaled by the plate out-of-straightness determined in Chapter 4; however, flexural-torsional imperfections were not included for specimens longer than 36 in.

Comparison of Experimental and Numerical Behavior

Results from the finite element analyses were compared to the experimental results. For each angle, Table 5.2 lists the peak load and buckling mode determined from numerical analyses and experimental testing. From this table it can be seen that this modeling procedure is able to predict the strength within 4% on average and the corresponding buckling mode (including L4-36a, which buckled in the flexural mode during experimental testing). Based on the load-deflection curves (for specimens that underwent flexural buckling) and on the load-twist curves (for the angles that underwent flexural-torsional buckling), deformational behavior of the analytical models was also seen to closely match experiments. Typical load-deflection and load–twist curves can be seen in Figure 5.7 and Figure 5.8. Load-deflection and load-twist curves for each angle can be found in Appendix C. Additionally, it can be seen in Figure 5.9 that this finite element procedure is able to capture the complex buckled shapes of each of the buckling modes, including the post-buckling torsion that was observed for L4-60a.

It can be seen in Table 5.2 that the strengths of the stockiest L2 angles do not match the experimentally determined strengths. This is attributable to the effective length used in the analysis. In Chapter 4, an effective length factor of 0.95 was determined based on tests of slender carbon steel columns. The rotational restraint that the end fixtures impose on stocky columns was not tested. Based on the observed strength in comparison to the tangent modulus predictions, it can be inferred that the effective length factor is actually less than 0.95 for the stockiest columns. Based on agreement with specimen test strength for other angles, it is concluded that this procedure can be used to model S32003 single equal-leg angles for numerical experiments.

Table 5.2- Experimental/Finite element comparison

Specimen	Experimental		Finite Element		$\frac{P_{exp}}{P_{FEM}}$
	P_{exp} (kip)	Mode	P_{FEM} (kip)	Mode	
L2-18a	56.6	F	48.4	F	1.17
L2-18b	59.9	F	49.4	F	1.21
L2-24	44.3	F	38.2	F	1.16
L2-36a	24.9	F	23.3	F	1.07
L2-36b	25.6	F	25.1	F	1.02
L2-48	13.1	F	12.4	F	1.06
L2-60a	7.7	F	8.4	F	0.92
L2-60b	8.3	F	8.6	F	0.96
L2-72	6.4	F	6.3	F	1.00
L2-84	4.9	F	4.8	F	1.02
L2-96	3.8	F	3.8	F	1.00
L2-132	2.0	F	2.0	F	1.00
L3-18	98.7	FT	88.5	FT	1.11
L3-24a	90.4	FT	86.2	FT	1.05
L3-24b	86.3	FT	84.9	FT	1.02
L3-36	66.8	F	66.3	F	1.01
L3-48a	39.5	F	39.1	F	1.01
L3-48b	40.8	F	42.5	F	0.96
L3-60a	28.9	F	28.4	F	1.02
L3-60b	28.3	F	28.1	F	1.00
L3-72	23.2	F	22.8	F	1.02
L3-84	19.5	F	17.3	F	1.13
L3-132	7.7	F	7.4	F	1.04
L4-24	136.6	FT	119.8	FT	1.14
L4-36a	124.3	F	134.6	F	0.92
L4-36b	144.6	FT	121.1	FT	1.19
L4-48	119.4	F	109.0	F	1.09
L4-60a	87.6	F	87.2	F	1.00
L4-60b	91.3	F	91.0	F	1.00
L4-72	72.2	F	77.1	F	0.94
L4-84	57.0	F	55.7	F	1.02
L4-96	39.2	F	38.6	F	1.01
L4-132	22.3	F	21.6	F	1.03
				AVERAGE	1.04

F-Flexural Buckling

FT-Flexural-torsional Buckling

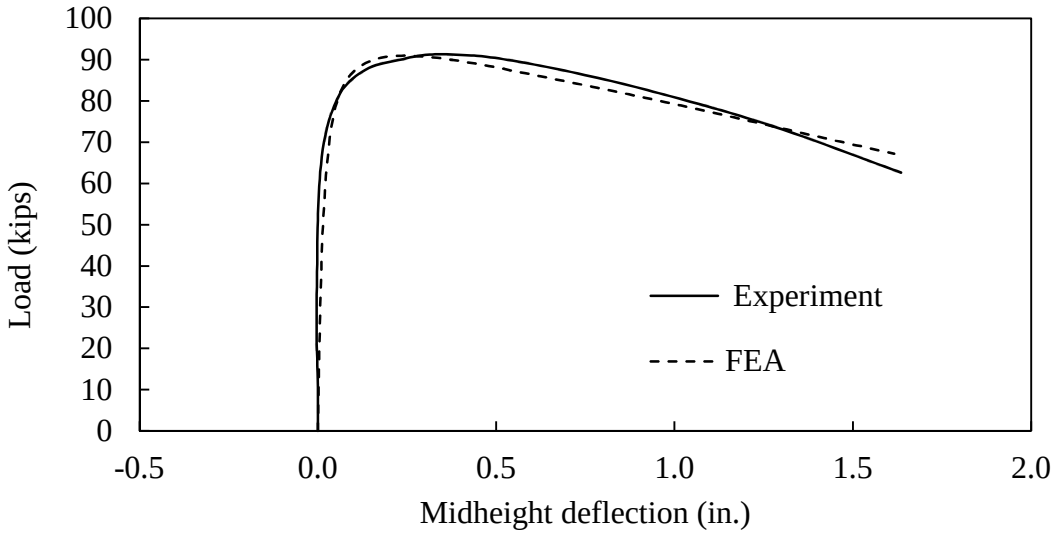

Figure 5.7- Experimental/numerical comparison of load-deflection curves for flexural buckling (L4-60b)

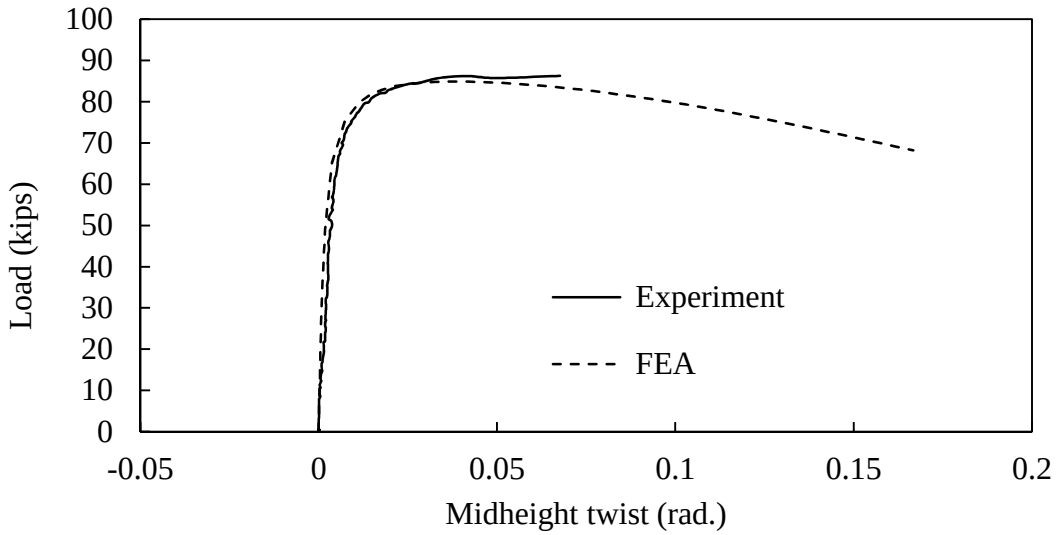

Figure 5.8- Experimental/numerical comparison of load-twist curves for flexural-torsional buckling (L3-24a)

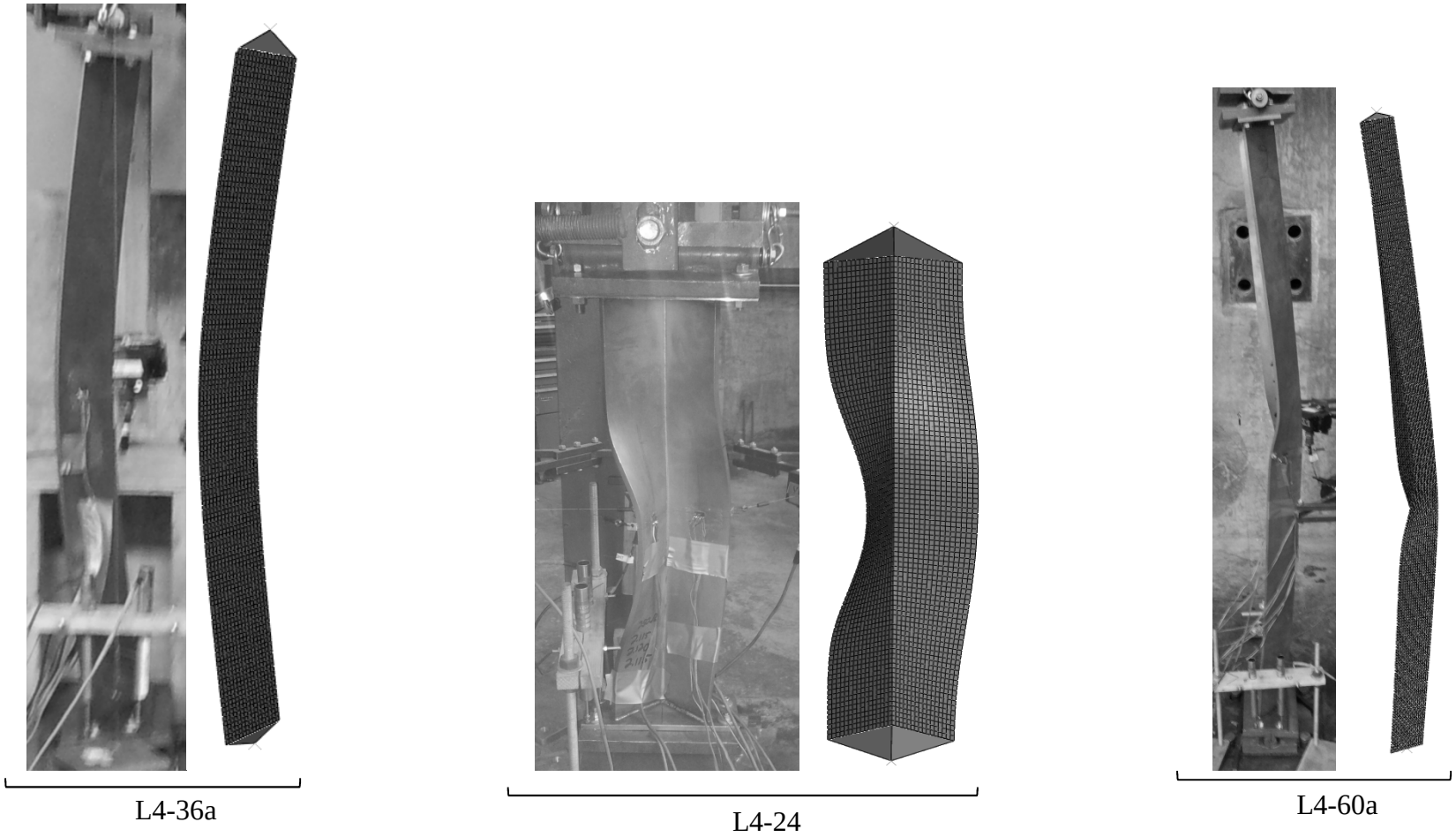

Figure 5.9- Comparison of finite element buckled shapes to buckled shapes from experiments

5.4 PARAMETRIC STUDY

The validated numerical testing procedure was subsequently used as a computational tool to perform numerical experiments. These analyses evaluated the strength angles across various leg slenderness and overall member slenderness ratios. Additionally, it was used to examine the effect of several design parameters on column strength.

Modeling procedure

In subsequent analyses, the following modeling procedures were standardized so the effect of individual parameters could be investigated between corresponding angles.

Boundary conditions

Boundary conditions were again modeled using R3D3 elements; however, the end-fixtures thickness was set equal to zero, as shown in Figure 5.10. Rotational boundary conditions about the principal axes could still be controlled by changing the constraints at the support nodes. Additionally, these boundary conditions still restrained warping at the S4R and R3D3 interfaces and imposed the same boundary conditions to the edges of the shells as described in Section 5.2. Except where noted, numerical analyses were conducted under pinned conditions for both major and minor axis bending.

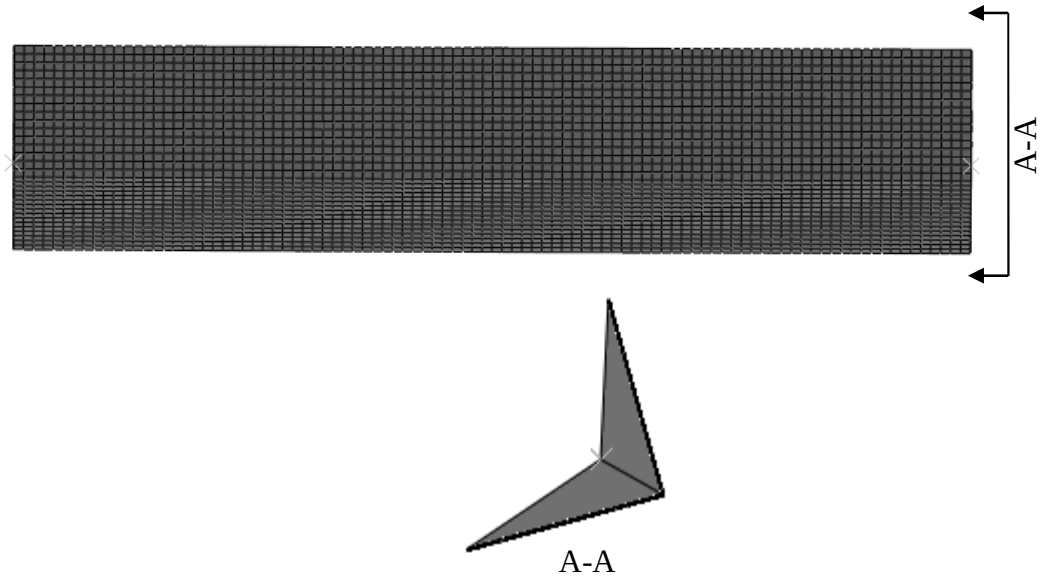

Figure 5.10- Parametric study end fixtures

Column Imperfections

For most of the analyses, it was decided to standardize the magnitude of column out-of-straightness as L/1500 based on the average out-of-straightness reported by Bjorhovde (1972) on his survey of carbon steel columns. Preliminary analyses indicated that out-of-straightness in the negative Y-direction resulted in lower strengths than when out-of-straightness was specified in the positive Y-direction. Subsequent analyses included out-of-straightness in the negative Y-direction.

The magnitudes by which the flexural-torsional imperfections were scaled were based on sensitivity analyses. The strengths of a 24 in. long L3x3x24 angle and a 30 in. long L$5^{1}/_{8}$ x $5^{1}/_{8}$ x ¼ angle were determined based on variation in the magnitude of the flexural-torsional imperfections. It was decided to scale flexural-torsional nodal

imperfections by 1% of the thickness, which corresponded to 0.01% and 1.6% drops in strength, respectively, for the two models in comparison to the strengths of comparable modes with imperfections equal to 0.1% of the thickness. When flexural-torsional imperfections were scaled by less than 0.1% of the thickness, models exhibited distortional buckling rather than flexural-torsional buckling.

Leg-Slenderness Parametric Study

The leg slenderness (b/t) ratio of hot-rolled carbon steel equal-leg angles vary between 4.5 and 18.7, where b is defined as the distance from the shear center to the toe. Based on the increased susceptibility to flexural-torsional buckling for increased leg slenderness, a parametric study was conducted for all-realistic ranges of $\bar{b}/t$ ratios to determine their effect on column strength and buckling mode.

Six cross-sections were selected to correspond to six different leg slenderness ratios—L2 x 2 x ¼ (b/t=7.5), L$2^{5}/_{8}$ x $2^{5}/_{8}$ x ¼ (b/t=10), L3¼ x 3¼ x ¼ (b/t=12.5), L$3^{7}/_{8}$ x $3^{7}/_{8}$ x ¼ (b/t=15), L4½ x 4½ x ¼ (b/t=17.5), and L$5^{1}/_{8}$ x $5^{1}/_{8}$ x ¼ (b/t=20). It was decided to use a plate thickness of 0.25 in. for all models since this was the plate thickness used in most of the experimental tests. The strength of each cross-section was determined across all practical column lengths—(L/r_x) =30 to 200. The peak load normalized by cross-sectional area for each of the major axis pinned cases is plotted in Figure 5.11. For validation of these results, the flexural buckling stresses for S32003 that were calculated using the explicit formulation given in Section 3.4.2 of the *AS/NZS 4673* are also plotted in Figure 5.11; this formulation was developed based on finite element analyses of imperfect columns made of nonlinear materials whose out-of-straightness magnitudes

were also L/1500 (Rasmussen and Rondal 1997b). The tangent modulus formulation presented by *SEI/ASCE 8-02* is plotted for reference.

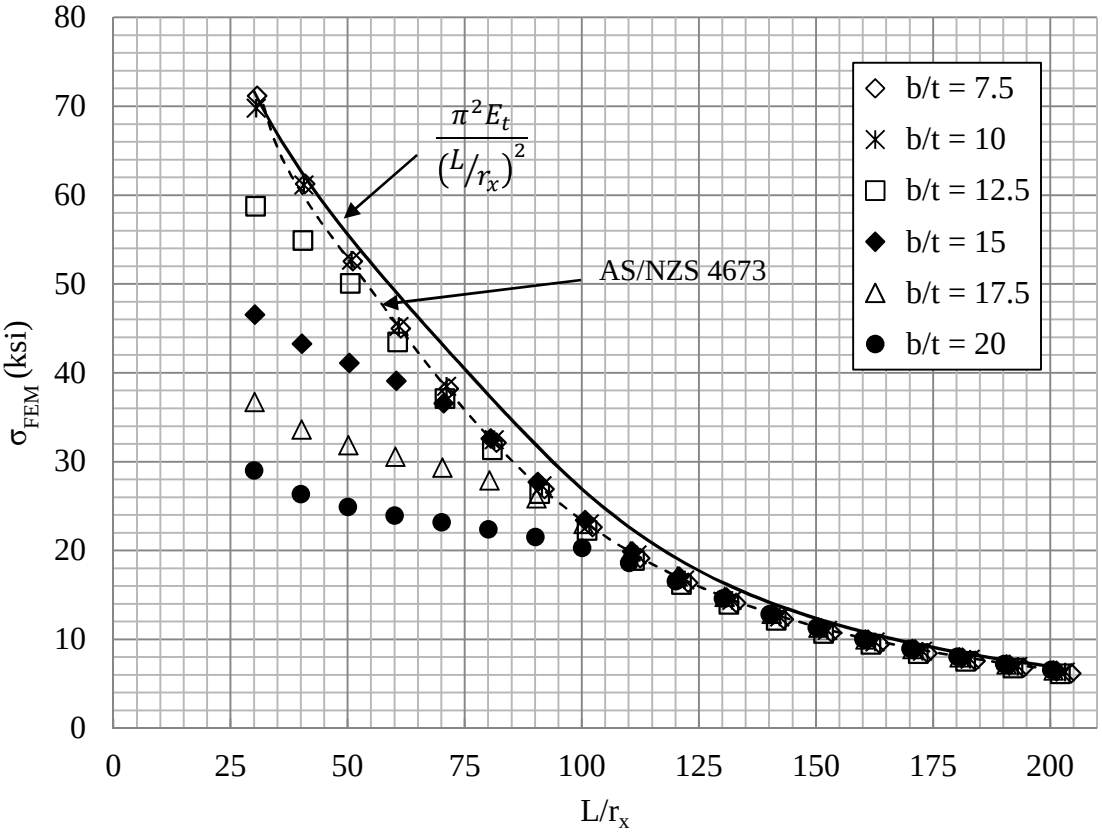

Figure 5.11- Column curves for various equal-leg angle cross-sections

It can be clearly seen that the column curves consist of two sections, which are labeled in Figure 5.12—one which corresponds to flexural-torsional buckling for stockier angles and one which corresponds to minor-axis flexural buckling for slender angles. No distinct point exists at which flexural buckling transitions to flexural-torsional buckling; rather, the column curves also include a transitional region, which will be defined as the concave down portion of the column curve. The transition point was defined using the

top-of-the-knee method, as illustrated in Figure 5.12. Additionally, the transition point will be defined as the point determined using the top-of-the-knee method.

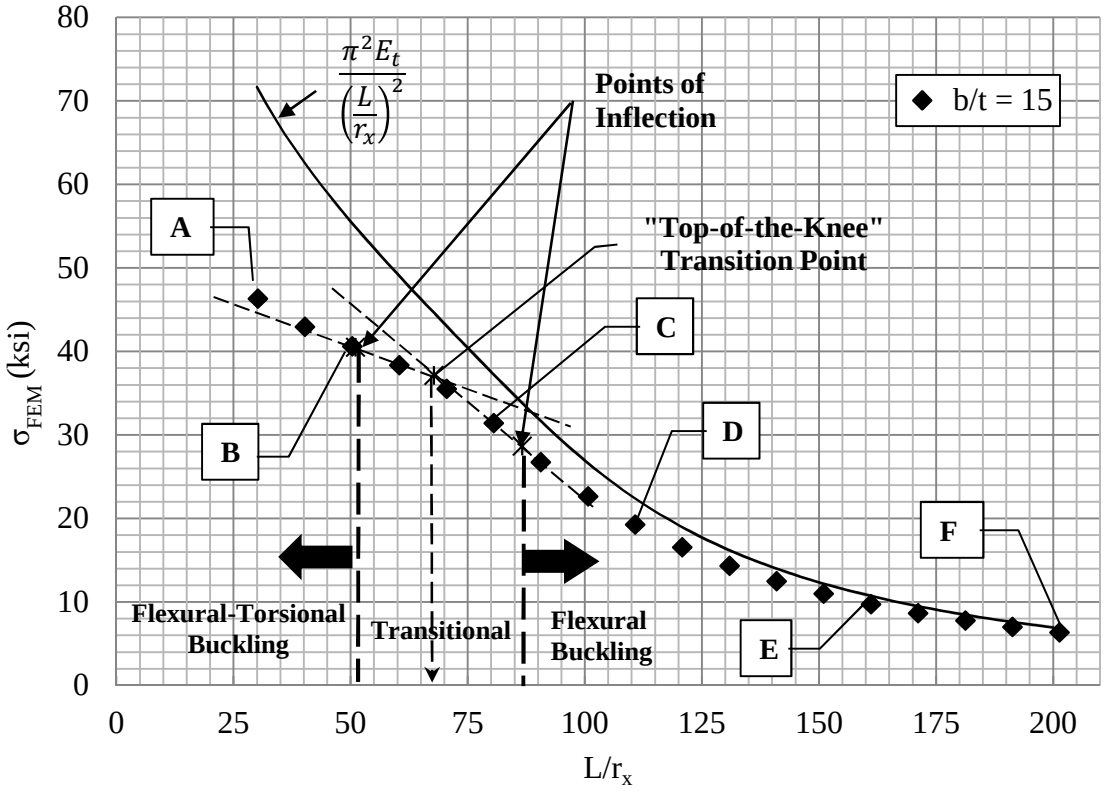

Figure 5.12- Characterization of the column curves for a single equal-leg angle

The characteristics of deformation at different points along the column curve can be seen in Figure 5.13, which references Figure 5.12. The midheight load-deflection curves and cross-sectional load-rotation curves for six points along the column curves are shown; the horizontal scale for each of the load-deflection and load-rotation plots is the same. At point A, which falls along the flexural-torsional buckling portion of the column curve, deformation is characterized by increased twist as loading reaches the peak load

and continues into the post-buckling range; little lateral deflection occurs even in the post-buckling range. Point B, which falls along the flexural-torsional buckling portion of the column curve near the transition region, shares similar deformation characteristics with Point A. Deformation at Point C, which falls inside the transition region, is characterized by flexural bending followed by a sudden drop in the carried load. The sudden drop in the carried load corresponds to the onset of twist at midheight. The suddenness of the torsion can be seen by visually comparing the sharpness of the knee in the load-twist curve for C against those for A or B.

The load-deflection curves for Points D and E, both of which fall in the flexural buckling region, follow the pattern of a column undergoing flexural buckling; however, a drop in load similar to C can be seen in the post-buckling range corresponding to cross-sectional twist at midheight. The buckling behavior at C differs from the behavior at D or E due to the onset of torsional deformation almost immediately upon reaching the peak load; D and E experienced torsional deformation in the post-buckling region of the flexural load-deflection curve. Additionally, it should be noted that the angle at point E, which has a higher slenderness than at D, is able to undergo further post-buckling flexural deformation before the onset of torsion than D. Similarly, F, which is more slender than E, did not ever exhibit torsional deformation and only exhibits flexural buckling behavior.

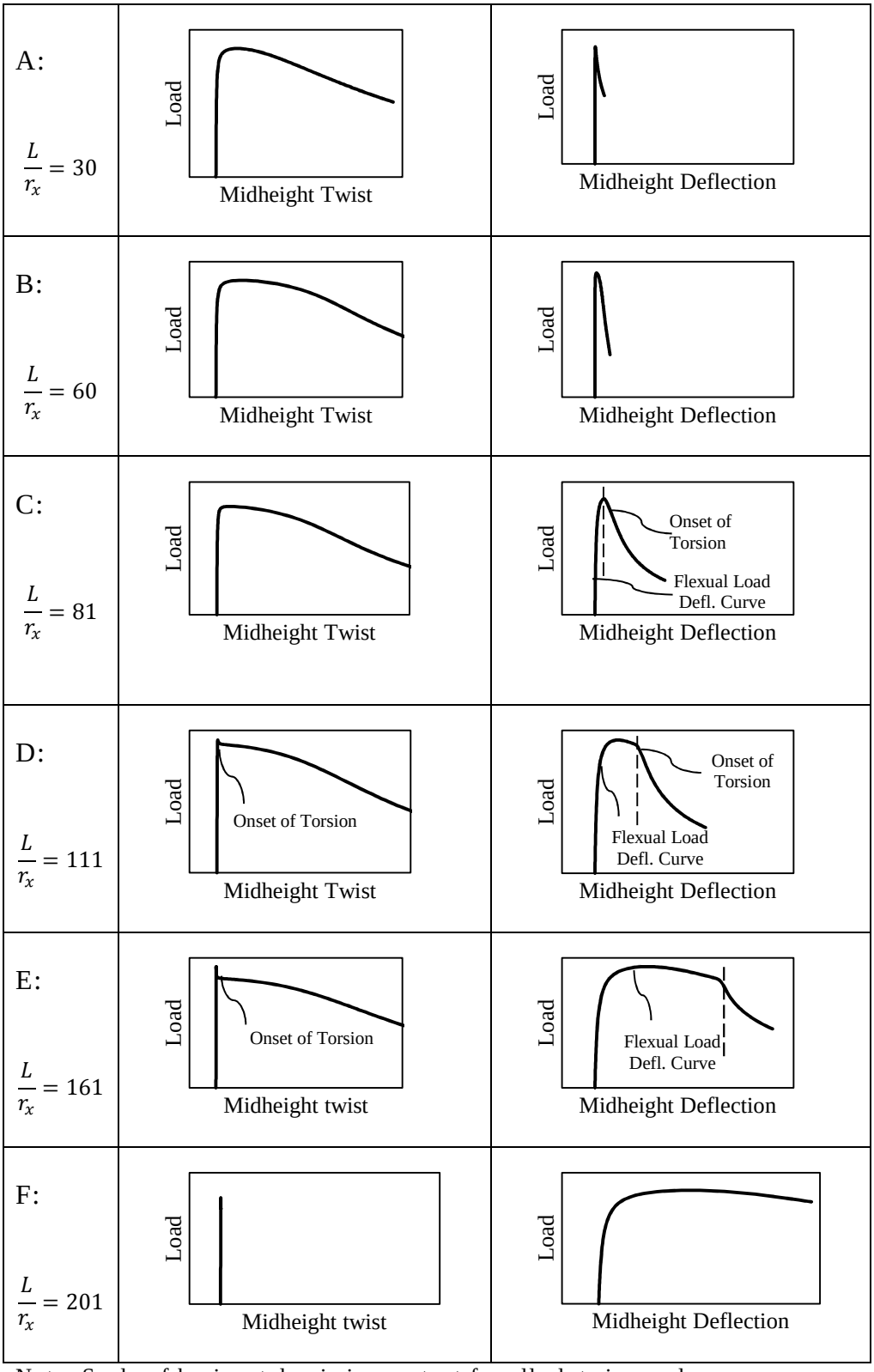

Note: Scale of horizontal axis is constant for all plots in a column.

Figure 5.13- Characterization of load-deflection/twist behavior at various points along the column curve (*b/t*=15)

Influence of Major Axis Rotational Fixity

Having previously evaluated the strength of the columns when rotation about the major principal axes was unrestrained (pinned), angle strength was examined when rotation about the major principal axes was restrained (fixed) for evaluation of the experimental test results. The same models were analyzed by restraining major axis rotation at the top and bottom support nodes. The resulting strengths from the fixed cases are plotted along with the strengths determined for the pinned cases in Figure 5.14. Strengths are reported in Appendix C. The strengths for corresponding columns from the two series show close agreement for the two cases— there is a slight strength increase in the flexural-torsional buckling arm of the column curve for angles with low *b/t* ratios and little to no difference everywhere else. The maximum strength increase was approximately 1%, which occurred for the L3¼ x 3¼ x ¼ (*b/t*=12.5) and L$3^{7}/_{8}$ x $3^{7}/_{8}$ x ¼ (*b/t*=15) sections. It is concluded that major axis fixity is not an important design parameter to consider in determining the flexural-torsional buckling strength of a concentrically-loaded duplex stainless steel angle, and thus the experimental results obtained using the end fixtures described in Chapter 4 may be compared to the results of numerical buckling experiments.

When the flexural-torsional buckling strengths are computed for the major axis pinned and fixed cases using the flexural-torsional buckling formulation presented by *AS/NZS 4673* and *SEI/ASCE 8-02*, the difference can vary by as much as 4% if effective cross-sectional area provisions are used and 9% if gross cross-section areas are used. For the purposes of design, the major axis fixity factor should be conservatively taken as one.

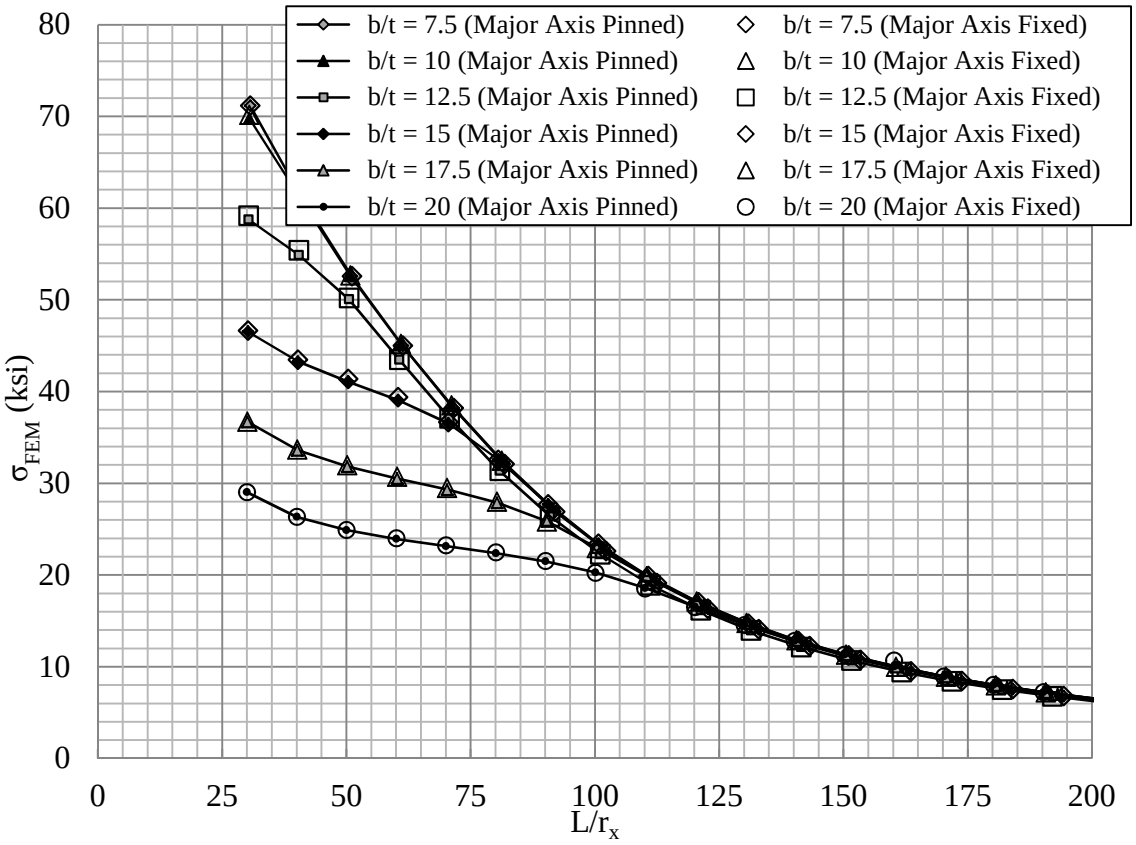

Figure 5.14- Column curve comparison—major axis rotationally pinned and fixed

Anisotropic Yielding

Material anisotropy is often introduced to the material as a result of the manufacturing rolling process. The series of simulations were performed to determine if anisotropic yielding would reduce the strength of concentrically loaded single equal-leg angles. In *ABAQUS*, anisotropic yielding was considered using Hill's anisotropic yield criterion, given by Eq. (5-3) and summoned with the *POTENTIAL command.

$$f(\sigma) = F(\sigma_{22} - \sigma_{33})^2 + G(\sigma_{11} - \sigma_{33})^2 + H(\sigma_{22} - \sigma_{11})^2 + 2(L\sigma_{23}^2 + M\sigma_{31}^2 + N\sigma_{12}^2) = 1 \quad (5\text{-}3)$$

F, *G*, *H*, *L*, *M*, and *N* are material constants that are determined from tests on different material orientations. These constants are defined in *ABAQUS* using the anisotropic yield stress ratios, R_{11}, R_{22}, R_{33}, R_{23}, R_{31}, and R_{12}, using the relations Eq. (5-4) through Eq. (5-10) (ABAQUS 2011).

$$F = \frac{1}{2}\left(\frac{1}{R_{33}^2} + \frac{1}{R_{22}^2} - \frac{1}{R_{11}^2}\right) \quad (5\text{-}4)$$

$$G = \frac{1}{2}\left(\frac{1}{R_{33}^2} + \frac{1}{R_{11}^2} - \frac{1}{R_{22}^2}\right) \quad (5\text{-}5)$$

$$H = \frac{1}{2}\left(\frac{1}{R_{22}^2} + \frac{1}{R_{11}^2} - \frac{1}{R_{33}^2}\right) \quad (5\text{-}6)$$

$$L = \frac{3}{2}\left(\frac{1}{R_{23}^2}\right) \quad (5\text{-}7)$$

$$M = \frac{3}{2}\left(\frac{1}{R_{31}^2}\right) \quad (5\text{-}8)$$

$$L = \frac{3}{2}\left(\frac{1}{R_{12}^2}\right) \quad (5\text{-}9)$$

Where

$$R_{11} = \frac{\bar{\sigma}_{11}}{\sigma^0}; R_{22} = \frac{\bar{\sigma}_{22}}{\sigma^0}; R_{33} = \frac{\bar{\sigma}_{33}}{\sigma^0}; R_{23} = \sqrt{3}\frac{\bar{\sigma}_{23}}{\sigma^0}; R_{31} = \sqrt{3}\frac{\bar{\sigma}_{31}}{\sigma^0}; R_{12} = \sqrt{3}\frac{\bar{\sigma}_{12}}{\sigma^0} \quad (5\text{-}10)$$

σ^0 = the user-defined reference yield stress.

$\bar{\sigma}$ = the yield stresses for different material orientations.

Rather than perform 6 material tests, a parametric study was performed to determine the parameters necessary to define anisotropic yielding for the present loading conditions. The loading conditions were idealized as a plate uniformly loaded along opposite edges under plane stress conditions whose material coordinate axes coincide with the geometric coordinate axes, as shown in Figure 5.15. Under such conditions Eq. (5-3) simplifies to Eq. (5-11).

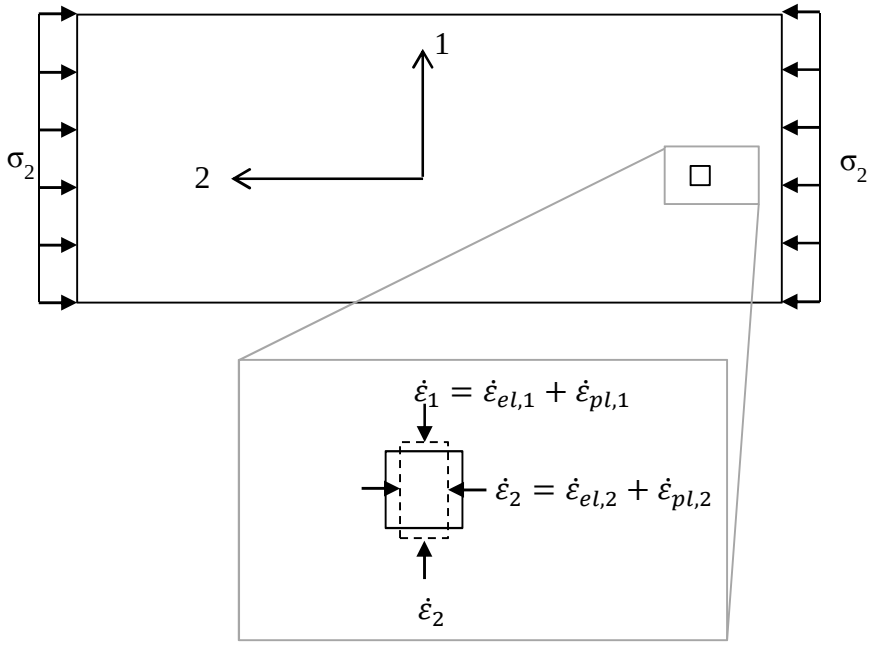

Figure 5.15- Idealized loading

$$f(\sigma) = F\sigma_{22}^2 + G\sigma_{11}^2 + H(\sigma_{22} - \sigma_{11})^2 = 1 \tag{5-11}$$

The plastic strain increment ratio, κ, given by Eq. (5-12), can be determined based on the direction of the normal to the yield surface (for associated flow rules) at the point

corresponding to that state of stress $(0,\bar{\sigma}_{22})$. Rewritten using the *ABAQUS* anisotropic input parameters, Eq. (5-12) becomes Eq. (5-13).

$$\kappa = \frac{\dot{\varepsilon}_{pl,2}}{\dot{\varepsilon}_{pl,1}} = -\left.\frac{{df}/{d\sigma_{11}}}{{df}/{d\sigma_{22}}}\right|_{\sigma_{11}=0} = -\frac{H}{F+H} \tag{5-12}$$

$$\kappa = -\frac{1}{2}\left(1 + \frac{1}{R_{11}^2} - \frac{1}{R_{33}^2}\right) \tag{5-13}$$

For the isotropic case, $\bar{\sigma}_{11} = \bar{\sigma}_{22} = \bar{\sigma}_{33} = \sigma^0$ Eq. (5-13) becomes κ=-0.5, which corresponds to the plastic strain increment ratio associated with the von Mises yield criterion. For the anisotropic case, no data was available for the yield stress along non-longitudinal plate orientations for the S32003 plates used in Chapter 3; instead, a survey of literature was conducted concerning the inelastic anisotropic behavior of stainless steel plates and is summarized in Table 5.3. The data indicates that the rolling process used to manufacture stainless steel plates induces anisotropic material behavior in the inelastic range (Becque and Rasmussen 2009a; Becque and Rasmussen 2009b; Kim 2010; Rasmussen et al. 2003). In these studies, the 0.2% proof stress was determined to be up to 17% higher in the direction oriented perpendicular to the rolling direction than parallel to the rolling direction for virgin plates. Since the longitudinal axis of structural shapes are normally parallel to the rolling direction, only cases where R_{11}>1 were examined. This is consistent with Section 5.1.3 of the *AS/NZS 4673*, which notes that duplex grades of stainless steel have a lower yield stress in the longitudinal direction.

Table 5.3- Stainless steel plate anisotropy in the inelastic range

Source	Tension/ Compression	Alloy	R_{11}
Rasmussen et al. (2003)	Tension	S31803	1.10
	Compression		1.17
Kim (2010)	Tension	S32003	1.06
Becque and Rasmussen (2009a)	Tension	S30400	1.02
	Compression		1.06
	Tension	S43000	1.05
	Compression		1.11
	Tension	S40900	1.03
	Compression		1.16
Becque and Rasmussen (2009b)	Tension	S30400	1.01
	Compression		1.03
	Tension	S40400	1.03
	Compression		1.12

To evaluate the effect of anisotropic yielding, it was decided to use R_{11} = 1.2 based on the maximum yield stress ratios observed from the review of literature. Substituting this into Eq. (5-13), κ will deviate most from its isotropic value when R_{33} = 1, which results in a value of κ=-0.35. This is shown graphically with respect to the isotropic and anisotropic yield surfaces in Figure 5.16.

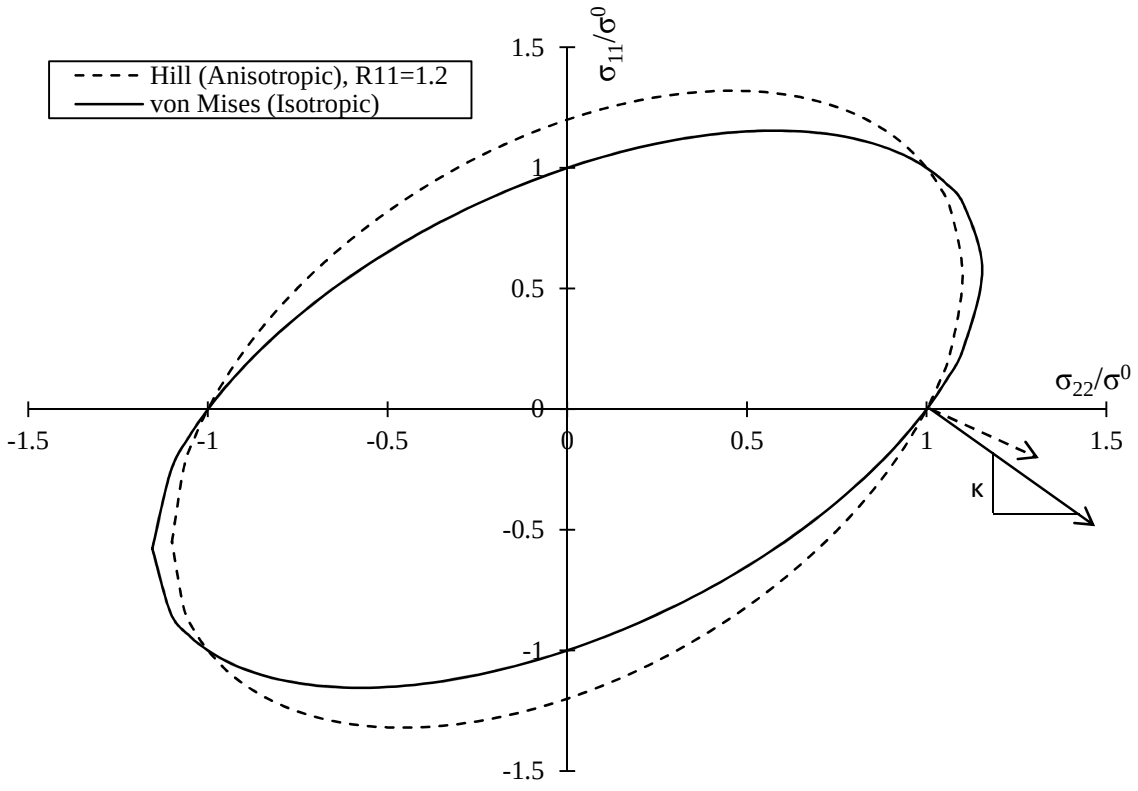

Figure 5.16- Plastic strain increment ratio for isotropic and anisotropic yielding

These yield stress ratios are listed in Table 5.4. The yield stress ratios for all the shear terms, as well as the through-thickness modulus, were taken as one. Additionally, it should be noted that the studies in Table 5.3 reported higher elastic moduli in the transverse direction, E_1, than in the longitudinal direction, E_2. Preliminary finite element analyses, which included reflected this ($E_1 = 1.1\ E_2$), showed strength increases in the models. Since the aim of investigating this property was to determine if anisotropic material behavior resulted in reduced strength, subsequent analyses did not include the elastic anisotropy, and only anisotropic yielding was modeled. The resulting column curves are plotted alongside the isotropic yielding case in Figure 5.17.

Table 5.4- Material model parameters for severe anisotropy case

Anisotropic Yielding	
R_{11}	1
R_{22}	1.2
R_{33}	1
R_{23}	1
R_{31}	1
R_{12}	1

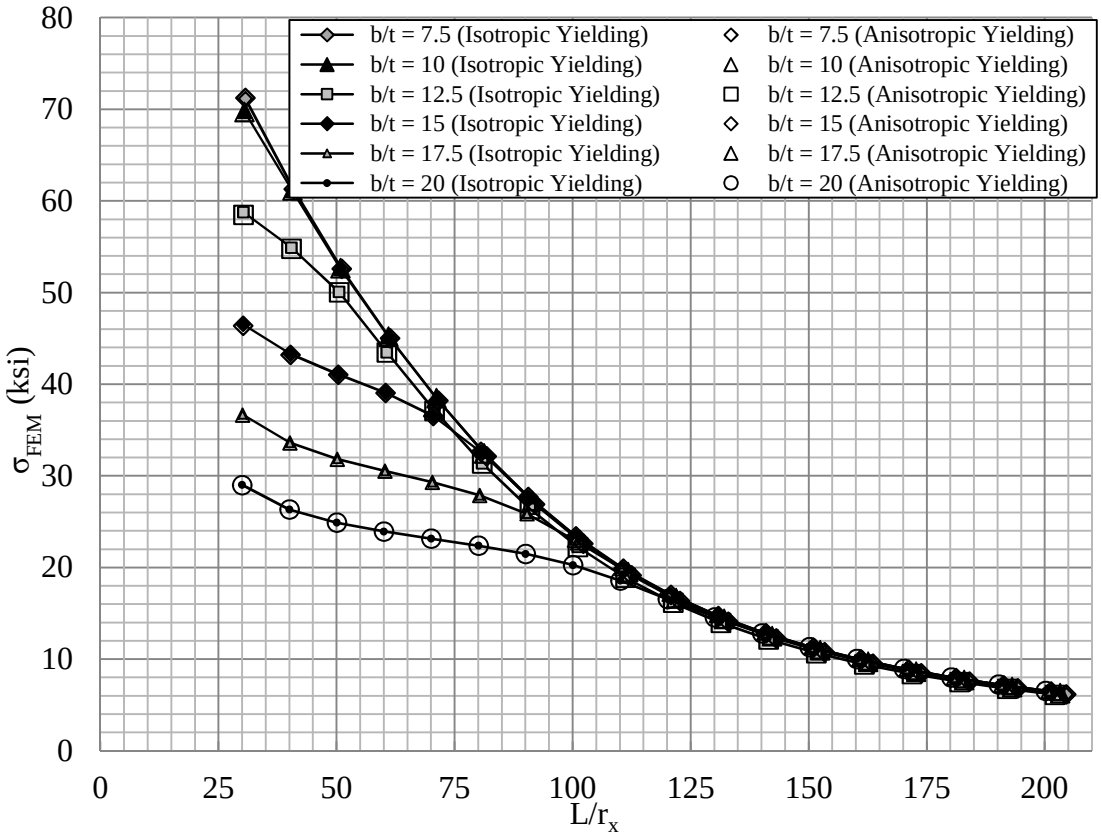

Figure 5.17- Column curve comparison--isotropic and anisotropic yielding

It is apparent from Figure 5.17 that anisotropic yielding does not contribute to a noticeable change in the strength of angles. A similar conclusion was made by Rasmussen et al. (2003) concerning the buckling of a simply supported S31803 duplex

plate when only perfectly plastic material models were considered. The ratio of the two strengths for each angle, which are listed in Appendix C, show that there is less than a 0.01% difference in strengths on average. This indicates that anisotropic yielding does not need to be considered in determining the strength of concentrically loaded single equal-leg stainless steel angles for the case where rolling direction of plates is oriented parallel to the longitudinal axis of the member in fabrication.

Out-of-straightness

Previous numerical analyses considered the case where column out-of-straightness was set equal to L/1500, for which most design column curves are calibrated; however, angles were also tested with out-of-straightness magnitude set equal to L/1000 to consider the sensitivity of strength based on the out-of-straightness limits specified in (ASTM A6-12). The resulting strengths are seen in Figure 5.18 and are reported in Appendix C.

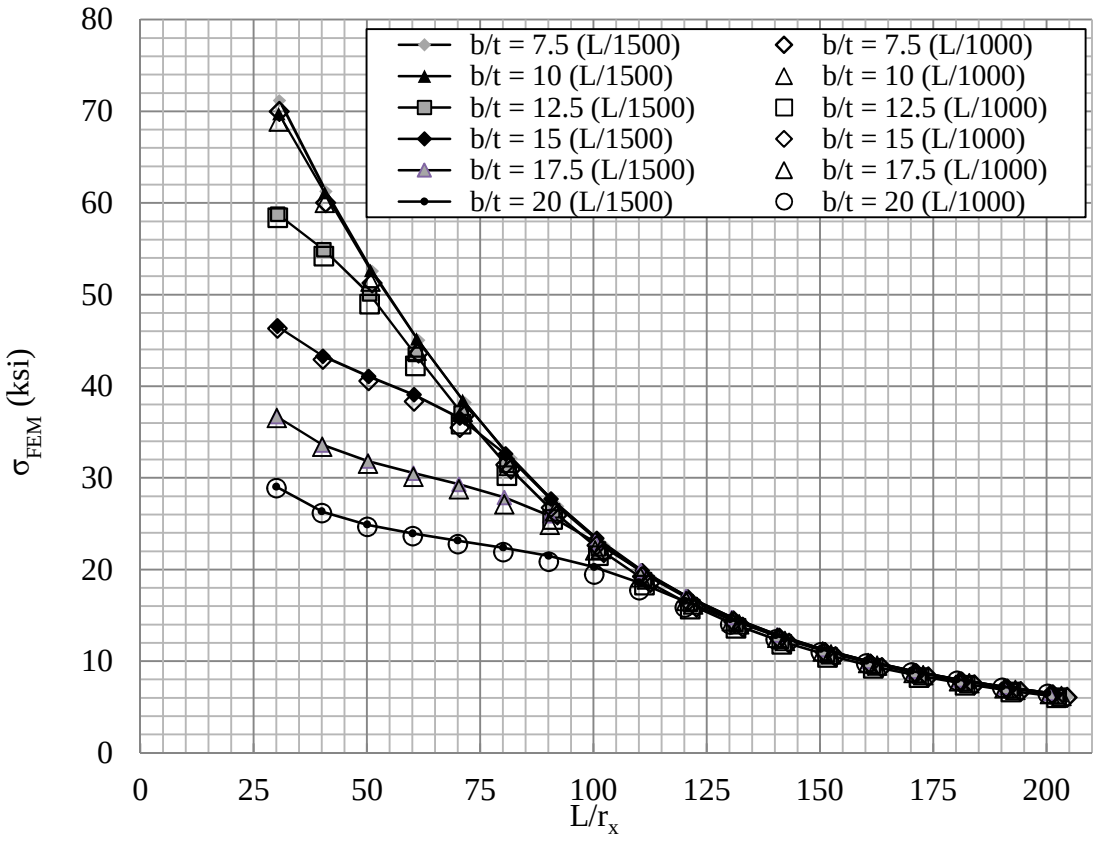

Figure 5.18- Effect of out-of-straightness on column strength

The increased out of straightness has limited effect on the member strength, as shown in Figure 5.18. In the flexural buckling region, the buckling stress decreases approximately 2% when the initial out-of-straightness increases from L/1500 to L/1000; however, the strength decreases less than 1% for members in the flexural-torsional buckling region of the column curve. The effect of initial out-of-straightness is greatest for columns which fall in the transitional region, wherein this change can result in up to a 5% drop in the buckling stress. Thus, while initial out-of-straightness has a greater effect on member strength than anisotropic yielding behavior or major axis fixity, the difference between these two cases is small enough to justify use of column curves based on an L/1500 out-of-straightness for duplex stainless steel single equal-leg angles.

5.5 COMPARISON TO DESIGN FORMULATIONS

Results from the L/1500 out-of-straightness finite element study and the mechanistic-based flexural and flexural-torsional buckling stresses in *SEI/ASCE 8-02* are plotted together in Figure 5.19. This figure indicates that larger *b/t* ratios cause a concentrically loaded single equal-leg angle strut to become susceptible to flexural-torsional buckling at higher member slenderness ratios. Additionally, it can be seen that flexural-torsional buckling stress formulation becomes less conservative for angles with *b/t*>12.5. As a result, the effective cross-sectional area must be performed in computing the predicted strengths.

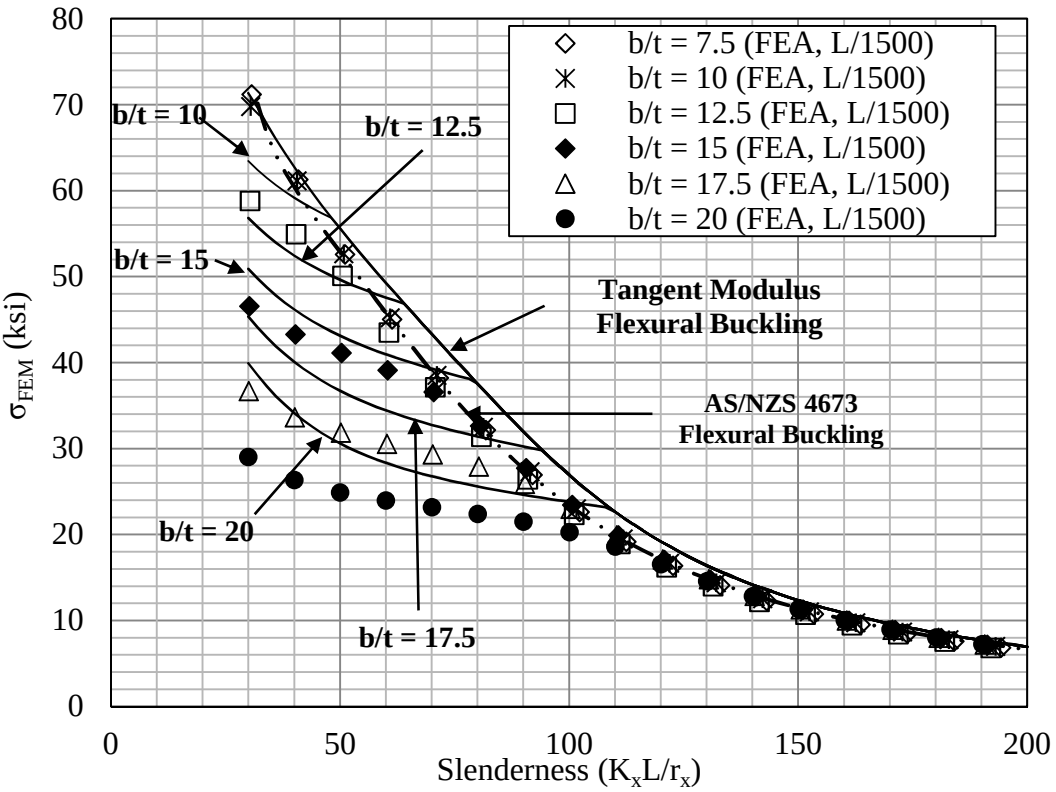

Figure 5.19- Calculated/FEA buckling stress comparison (gross cross-sectional area)

The strength of each angle was computed using *SEI/ASCE 8-02, AS/NZS 4673, EC3, 1-4/Euro-Inox,* and the *AISC Design Guide* (whose formulations are described in further detail in Chapter 4) and compared to the strengths determined from finite element analysis. The effective length factors were taken as K_x=1.0, K_y=1.0, K_t=0.5. Effective area calculations were computed using the full width of the leg, $\bar{b}$, as in Chapter 4, instead of *b* for consistency. Additionally, the strengths were computed using the *SEI/ASCE 8-02* and *AS/NZS 4673* design provisions (found in Section 3.4-3 and Section 3.4.1, respectively) for concentrically-loaded cold-formed stainless steel angles that requires consideration of a loading eccentricity of L/1000 toward the toes of the angle. The computed strength of each angle was divided by its gross cross-sectional area in order to compare different cross-sections and design standards (including effective area provisions) to the buckling stress determined from the finite element buckling experiments. The resulting comparisons are seen in Figures 5.20-5.25.

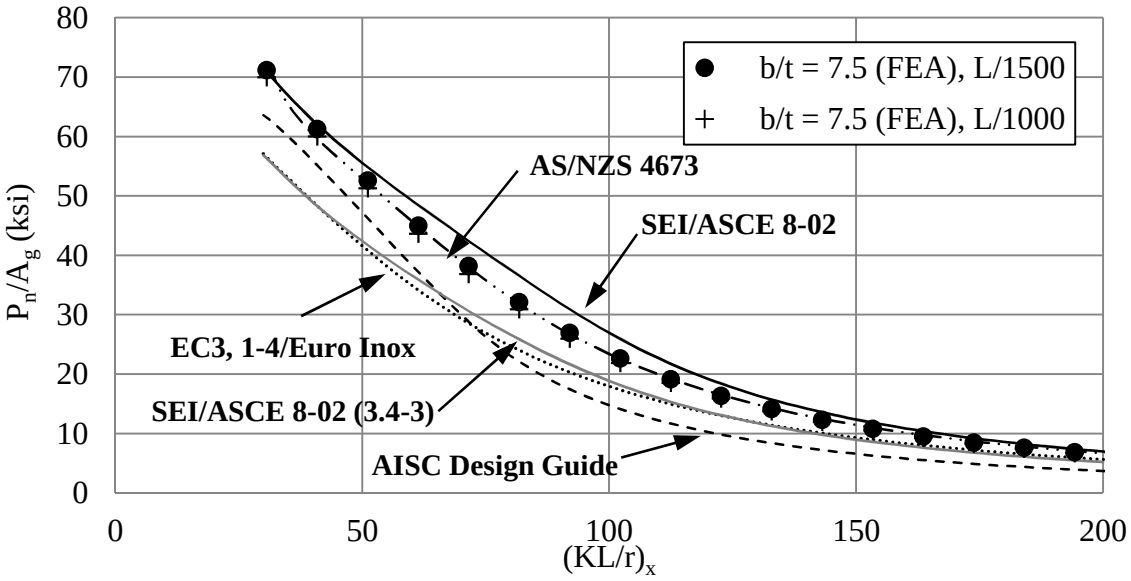

Figure 5.20- Predicted/FEA buckling stress comparison (*b/t* = 7.5)

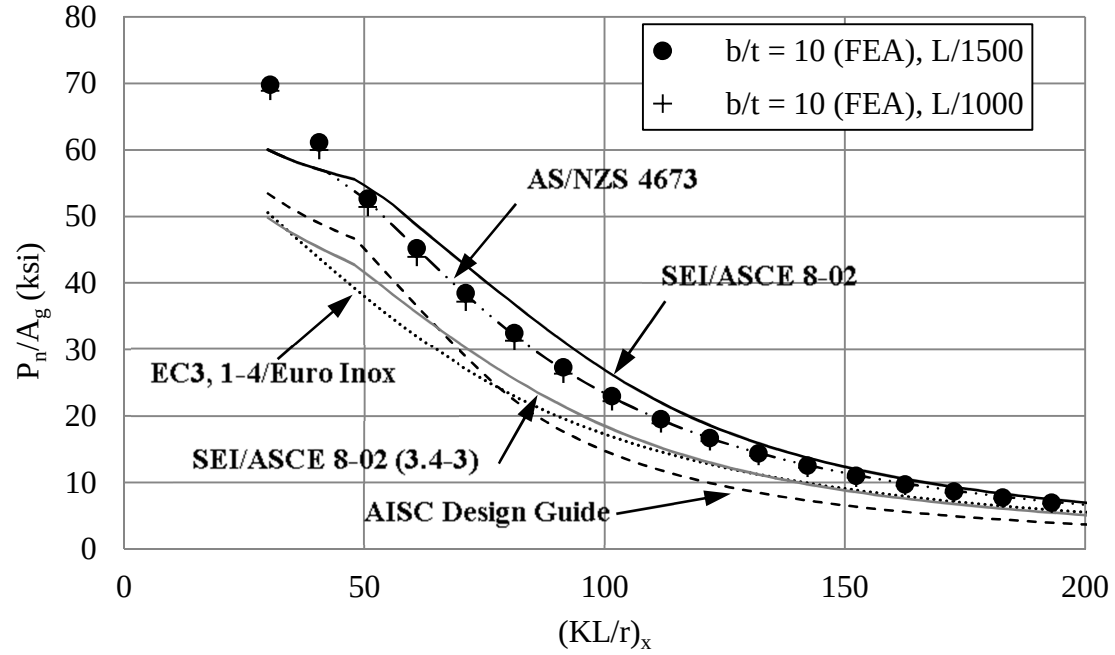

Figure 5.21- Predicted/FEA buckling stress comparison (*b/t* = 10)

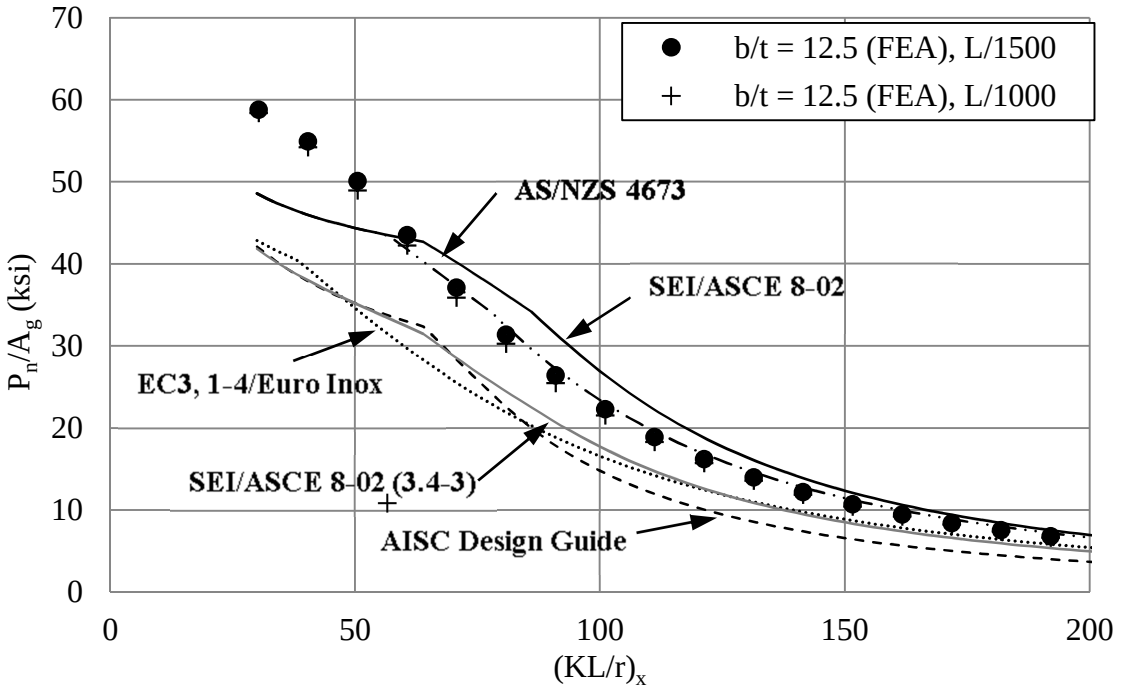

Figure 5.22- Predicted/FEA buckling stress comparison (*b/t* = 12.5)

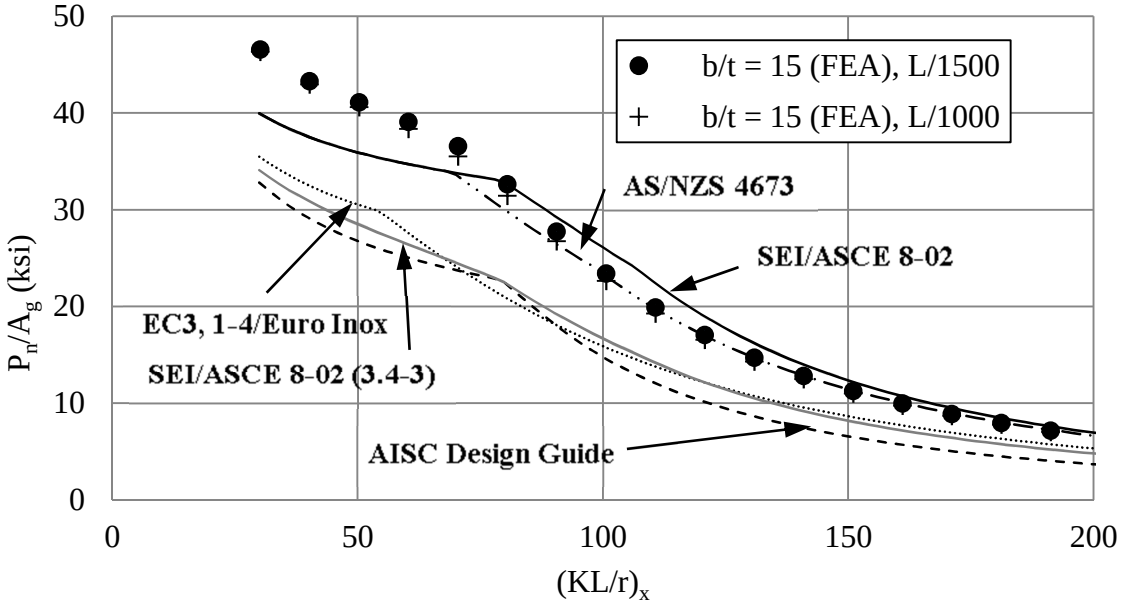

Figure 5.23- Predicted/FEA buckling stress comparison (*b/t* = 15)

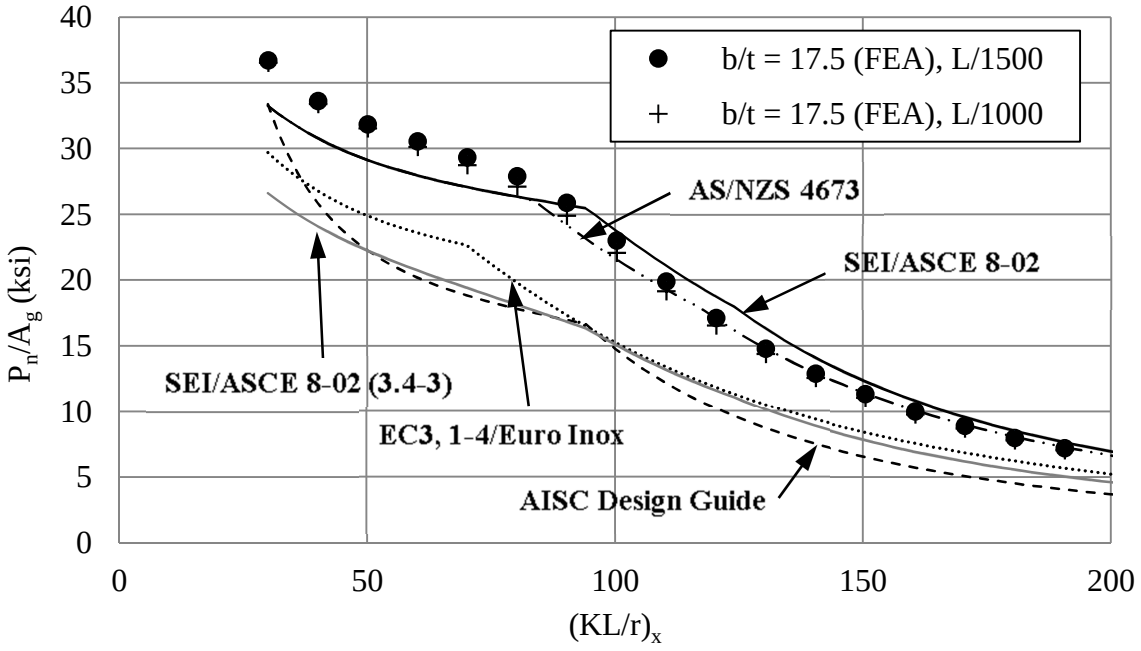

Figure 5.24- Predicted/FEA buckling stress comparison (*b/t* = 17.5)

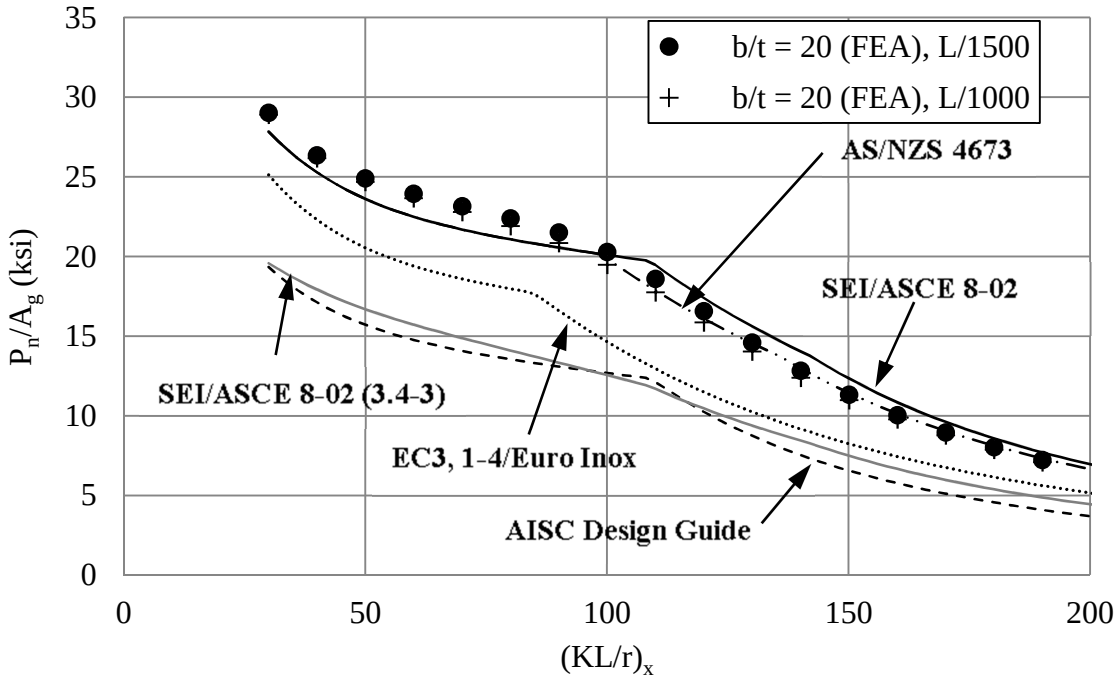

Figure 5.25- Predicted/FEA buckling stress comparison (*b/t* = 20)

From Figures 5.20-25, it can be seen that the buckling stresses predicted using cold-formed stainless steel standards, *AS/NZS 4673* and *SEI/ASCE 8-02*, closely follow the finite element data along the flexural buckling arm of the column curve. The flexural-torsional buckling formulation, which is identical for both standards, closely predicts the intersection of the buckling modes. The flexural-torsional buckling stress predicted by this formulation becomes increasingly conservative for stockier angles. It can also be noted that while both *SEI/ASCE 8-02* and *AS/NZS 4673* overestimate the flexural buckling stress determined from the finite element data, *SEI/ASCE 8-02* does so more. The maximum difference between predicted and actual stress was approximately 17%, which occurred at a slenderness ratio around 90 for the L2 x 2 x ¼ (b/t=7.5) cross-section. This tendency to overestimate the buckling stress is attributable to the initially-straight assumption inherent in tangent-modulus buckling theory.

The buckling stresses predicted using *EC3, 1-4* and the *AISC Design Guide*, neither of which incorporate the nonlinear stress-strain behavior of a particular grade of stainless steel in their formulations, can be seen to be very conservative for all slenderness values. This supports the findings in Chapter 4, wherein the resistance factors for the *AISC Design Guide* were seen to exceed 1 for both buckling modes. This indicates that this design formulation is overly conservative and would result in inefficient design.

Figures 5.20-25 also indicate that the different design rules predict different slenderness ratios for the point at which the flexural buckling stress is equal to the flexural-torsional buckling stress (buckling mode transition point). This is an important design consideration given that different buckling modes may have different resistance

factors. *EC3, 1-4* is seen to predict the buckling mode transition point at lower slenderness ratios than was seen in the finite element data, whereas *SEI/ASCE 8-02* and *AISC Design Guide* predict that this transition occurs at a slenderness ratio higher than is reflected by the data. It is of interest to note that in assuming that the shear modulus remains proportional to the longitudinal modulus of elasticity $\left(\text{i. e. } G_t = G_o \frac{E_t}{E_o}\right)$ the buckling mode transition point will be the same for both linear and nonlinear materials; thus, the *AISC Design Guide* predicts the same buckling mode transition point as *SEI/ASCE 8-02* despite underestimating the buckling stresses. The slenderness ratios at the buckling mode transition point are summarized in Table 5.5.

Table 5.5- Buckling mode transition slenderness ratio $(KL/r)_x$

Method	*b/t*				
	10	12.5	15	17.5	20
FEA_{1000}	--	44.2	67.8	80.9	94.2
FEA_{1500}	--	45.8	69.3	83.3	97.3
SEI/ASCE 8-02	48.1	64.0	79.3	94.2	108.9
AS/NZS 4673	42.5	56.6	69.4	83.4	98.8
EC3, 1-4	24.4	38.6	67.7	70.0	84.9
AISC	48.1	64.0	79.3	94.2	108.9

Based on the extreme conservatism seen in the *AISC Design Guide* and *EC3, 1-4,* only *AS/NZS 4673* and *SEI/ASCE 8-02* will be considered in the remainder of the discussion. The fact that the *AS/NZS 4673* is able to more closely predict the slenderness ratio at the buckling mode transition point than *SEI/ASCE 8-02* highlights the shortcomings of the initially straight assumption of tangent modulus buckling theory. For finite element models with out-of-straightnesses equal to L/1500, the tangent modulus formulation over-predicted the strength. This causes the ratio of the flexural

buckling strength (P_{FEM}) to the calculated flexural buckling strength (P_n) to vary with the slenderness of the column, as shown in Figure 5.26a. In contrast, the *AS/NZS 4673* explicit formulation resulted in more precise strength predictions, as shown in Figure 5.26b.

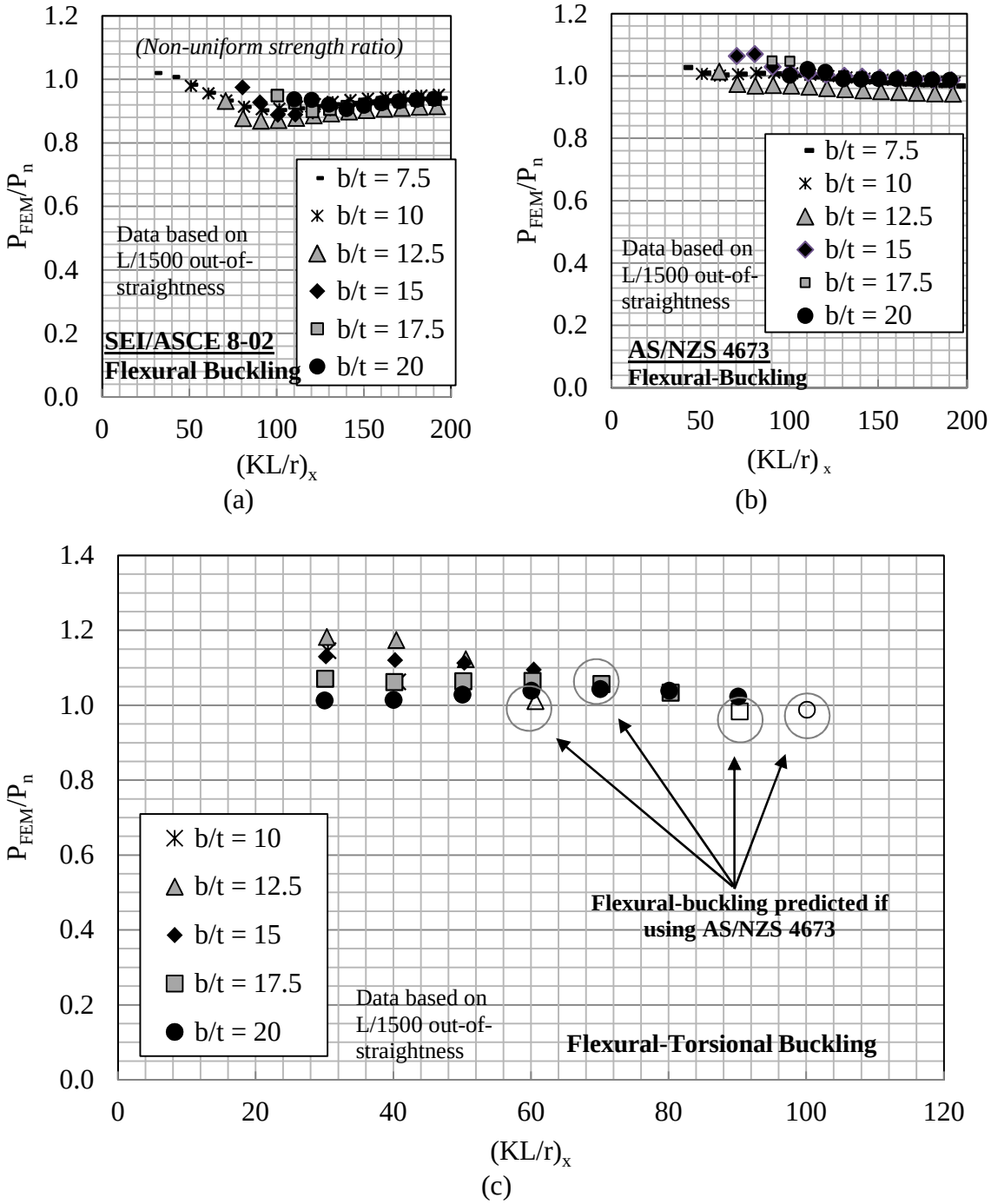

Figure 5.26- Strength ratio comparison for flexural buckling (a) *SEI/ASCE 8-02*, (b) *AS/NZS 4673*, and (c) flexural-torsional buckling

The ratio of the flexural-torsional buckling strength (P_{FEM}) to the predicted flexural-torsional buckling strength (P_n) computed using the formulation of *AS/NZS 4673* and *SEI/ASCE 8-02* is shown in Figure 5.26c. As noted in the figure, different flexural buckling stress formulations cause some data near the buckling mode transition point to be included for the *SEI/ASCE 8-02* standard, but not for the *AS/NZS 4673* standard. It can be seen that this flexural-torsional buckling formulation becomes less conservative for larger *b/t* ratios. Experimental flexural-torsional buckling data from Chapter 4 (*b/t* ratios of 11.7 and 12.3 and $(KL/r)_x$ between 35 and 50) are geometrically closest to the *b/t*=12.5 models. In Figure 5.26c, the *b/t*=12.5 flexural-torsional buckling data is the most conservative; thus, the resistance factor (φ_{ft}=0.92) computed in Chapter 4 for the flexural-torsional buckling mode may high due to the sampled data. Further experimental investigation is necessary to determine if this resistance factor needs to be reduced for larger *b/t* ratios.

5.6 CONCLUSIONS

A modeling procedure, which was validated against experimental test data, was used to perform numerical experiments for concentrically loaded S32003 single equal-leg angle struts. The strengths and buckling modes were determined for all practical cross-sections across all ranges of column slenderness. Rotational fixity about the major principal axis and material anisotropy were determined to have negligible effect on the strength of angles and therefore do not need to be considered in design. These are important design considerations which can simplify the design of duplex stainless steel single equal-leg angles. In the case of anisotropic hardening, no transverse material testing is necessary, and the longitudinal stress-strain relationship can be conservatively

used in calculating column strength, assuming that the longitudinal direction corresponds to the plate rolling direction. Initial column out-of-straightness was seen to have the greatest influence on column strength, particularly in the transitional regions where columns are susceptible to either flexural or flexural-torsional buckling.

A comparison of the strengths determined from the finite element tests to the strengths predicted using different stainless steel design rules reveals that consideration of the nonlinear stress-strain relationship of a particular grade of stainless steel leads to more precise column strength predictions than design rules that generalize the stress-strain relationship of all stainless steels. This latter approach gives overly-conservative strength predictions. This indicates that the mechanistic-based design formulations for the flexural and flexural-torsional buckling modes of concentrically loaded columns found in the cold-formed standards, *AS/NZS 4673* and *SEI/ASCE 8-02*, can be applied to built-up stainless steel sections as a method of calculating more realistic column strength.

Comparison of predicted column strengths calculated using tangent modulus flexural formulation of *SEI/ASCE 8-02* and the explicit formulation of *AS/NZS 4673* highlights the limitations of tangent modulus theory in determining the flexural buckling strength. In overestimating column strength, the initially straight assumption of tangent modulus theory can cause the incorrect buckling mode to be predicted. The explicit formulation used in *AS/NZS 4673* predicts strengths closer to those determined from the finite element analyses, and corresponds more closely with the observed buckling modes. The ideal limit-state design provisions to use for design are those of *AS/NZS 4673*; however, if the *SEI/ASCE 8-02* provisions are used in design, caution should be exercised by designers near the buckling mode transition point.

CHAPTER 6

SUMMARY, CONCLUSIONS, AND FUTURE WORK

This chapter summarizes the major accomplishments of this dissertation while highlighting its important conclusions. The summary and conclusions are followed by ideas for possible future work, which were identified during the course of this research.

6.1 SUMMARY OF RESEARCH

This dissertation addresses the behavior of built-up laser-welded duplex stainless steel single equal-leg angles subject to concentric loading. The work is conducted by means of two complementary approaches, the first of which was experimental and consisted of conducting 33 full-scale buckling tests on S32003 duplex stainless steel single equal-leg angle components. Angle specimens had slenderness ratios ranging from 35 to 350 and leg width-to-thickness ratios of 7.5 to 12.3. In the second approach, finite element models that accounted for material nonlinearity, material anisotropy, and geometric out-of-straightness were developed and validated using the experimentally obtained test results. These models were subsequently used to perform numerical buckling experiments, which examined the influence of leg width-to-thickness ratios on buckling mode and strength.

Results from the full-scale tests and from the numerical models were shown to correlate well with the classical mechanics-based formulae for predicting flexural and flexural-torsional buckling strengths of singly-symmetric members made of nonlinear materials. Finally, a first-order reliability analysis was performed using the experimental test data to calculate resistance factors for design purposes.

6.2 CONCLUSIONS

Based on the results of this thesis, the following conclusions can be made:

1. The residual stress patterns of built-up duplex stainless steel angles are similar to those found for built-up carbon steel angles. The peak tensile stress was found to be approximately $0.5F_{y,c}$ at the site of the weld.
2. Duplex stainless steel single equal-leg angles loaded concentrically in compression exhibit increased nonlinear material behavior for decreased column slenderness, which can be seen in its experimental buckling load and deformed shape.
3. Duplex stainless steel equal-leg angles become increasingly susceptible to flexural-torsional buckling as the leg slenderness ratio increases. Strength predictions using gross cross-sectional area ceased to be conservative for *b/t* ratios exceeding 12.5, which require the use of effective area provisions.
4. The transition between flexural and flexural-torsional buckling does not occur at a specific slenderness ratio; rather a transitional region exists in which an angle will begin to deflect laterally, as in flexural buckling, followed by cross-sectional twist.
5. The mechanics-based flexural-torsional buckling strength formulation of *AS/NZS 4673* and *SEI/ASCE 8-02* closely predicts the flexural-torsional buckling strength of single equal-leg struts, as well as the buckling mode transition point.
6. The assumption of tangent modulus buckling theory that columns are perfectly straight causes the flexural buckling strength of imperfect columns

to be overestimated, particularly for columns with slenderness ratios around 100; instead, the explicit flexural buckling formulation used by *AS/NZS 4673* closely predicts the flexural buckling strength of imperfect columns across all ranges of slenderness, as well as the intersection of buckling modes on the column curve.

7. *EC3, 1-4/Euro-Inox* and *AISC Design Guide*, which generalize the nonlinearity of different grades of stainless steel, result in overly conservative design strengths. The European standards predict that the buckling mode transition point occurs at slenderness ratios lower than seen in the data.
8. Angles showed little sensitivity (<1%) to the major-axis rotational fixity in numerical buckling tests; however, the difference between major axis fixed and pinned cases for *AS/NZS 4673* and *SEI/ASCE 8-02* indicate greater sensitivity (~4%). The major axis effective length factor, K_y, should thus be conservatively taken as 1.0.
9. Anisotropic yielding was shown to have negligible effect on column strength. Since stainless steel had a higher modulus of elasticity in the transverse direction (which causes strength increase), column strength can be conservatively predicted using the longitudinal stress-strain relationship for cases where the longitudinal axis of the section coincides with the rolling direction.
10. Concentrically-loaded, laser-welded, built-up, single equal-leg angles composed of duplex stainless steel can be designed using the Load and

Resistance Factor Design (LRFD) criteria, given by $P_u \leq \varphi P_n$, where P_u is the factored load, P_n is the nominal strength, and φ can be taken as 0.70 when designing for the flexural buckling limit state using the *SEI/ASCE 8-02* tangent modulus formulation, as 0.75 when designing for the flexural buckling limit using the *AS/NZS 4673* explicit formulation, and (for single equal-leg angles that have *b/t* ratios less than 12.5) as 0.90 when using either standard to design for the flexural-torsional buckling limit state.

6.3 RECOMMENDATIONS FOR FUTURE WORK

Over the course of this research, a number of issues were identified on which future investigations should focus. Firstly, improvement can be made on the material characterization performed in Chapter 3. The stress-strain curve used for analysis was based on fabricated stub columns, which have different residual stress patterns than the angles tested in the buckling experiments. This stress-strain curve approximated the effects of residual stresses and assumed homogenous material behavior across the cross-section. The influence of residual stresses can be more realistically modeled by imposing the distribution of the magnitudes of the residual stresses onto the cross-section, which would be modeled with virgin material behavior. Additionally, Poisson's ratio requires further examination, despite have little influence on the strength of the analytical models.

Secondly, additional data is needed to address the flexural-torsional mode of buckling for stainless steel columns. Only five experimental specimens in the present study exhibited this buckling mode. Additionally, only one other study (van den Berg and van der Merwe 1988) has addressed the flexural-torsional buckling mode in stainless steel columns, which was limited to cold-formed hat sections; it represents 100% of the

flexural-torsional buckling data used to calculate the resistance factor in stainless steel design standards. Validation of the existing resistance factors is needed for other stainless steel cross-sections, particularly built-up sections. Ideally, such an investigation would consider not only unequal-leg angles, which always buckle in the flexural-torsional mode, but also singly-symmetric sections, such as T-sections, and equal-leg angles with highly slender legs. Tests on singly-symmetric sections would shed light on transition and interaction between buckling modes. The outcome of this study would be a flexural-torsional design formulation that has been validated across multiple cross-sections. One possible formulation that ought to be examined in such a study is using the secant modulus nonlinear reduction factor, $\frac{E_s}{E_o}$, instead of the tangent modulus nonlinear reduction factor, $\frac{E_t}{E_o}$, in calculating the torsional buckling stress. This was considered as an alternative to current design formulations because it is currently used as a nonlinear reduction factor in calculating plate buckling stresses of unstiffened elements. A comparison of the strength data from the finite element analyses performed in Chapter 5 to the flexural-torsional buckling strength calculated using this formulation gave indications of being more precise for different cross-sections; however, little experimental test data was available to validate it.

Thirdly, future work should also focus on the strength and behavior of eccentrically loaded single equal-leg angle sections. Such research is necessary to implement duplex stainless steel angles in construction since angles are usually connected and loaded through one of their legs. The strength of eccentrically loaded angles is notoriously complex to analyze. Empirical design formulations, such as the effective slenderness ratio method, which are used for the design of eccentrically loaded

carbon steel single angle sections, have not been validated for stainless steels to account for their nonlinear material behavior. This investigation would also address topics such as non-principal axis bending, which was not covered in the present study.

Lastly, work is also needed to address the way in which material variability is approached. Variation in material properties is currently only addressed in *SEI/ASCE 8-02*, *AS/NZS 4673*, and *AISC Design Guide* with statistical parameters relating to the 0.2% proof/yield stress. The nonlinear stress-strain relationship of stainless steels varies from grade to grade and depends on three material parameters; it is possible for two grades of stainless steel to have the same yield stress and initial modulus, but different stress-strain curves. In this way, the yield stress does not encompass variation in material behavior as it does for carbon steel. Since stability problems require understanding of the slope of the stress-strain curve, future investigations should develop effective statistical material parameters M_m and V_m, which take into account both n and the 0.2% proof stress.

APPENDIX A

MATERIAL DATA

Stub Colum Stress-Strain Curves and Extended Ramberg-Osgood Model

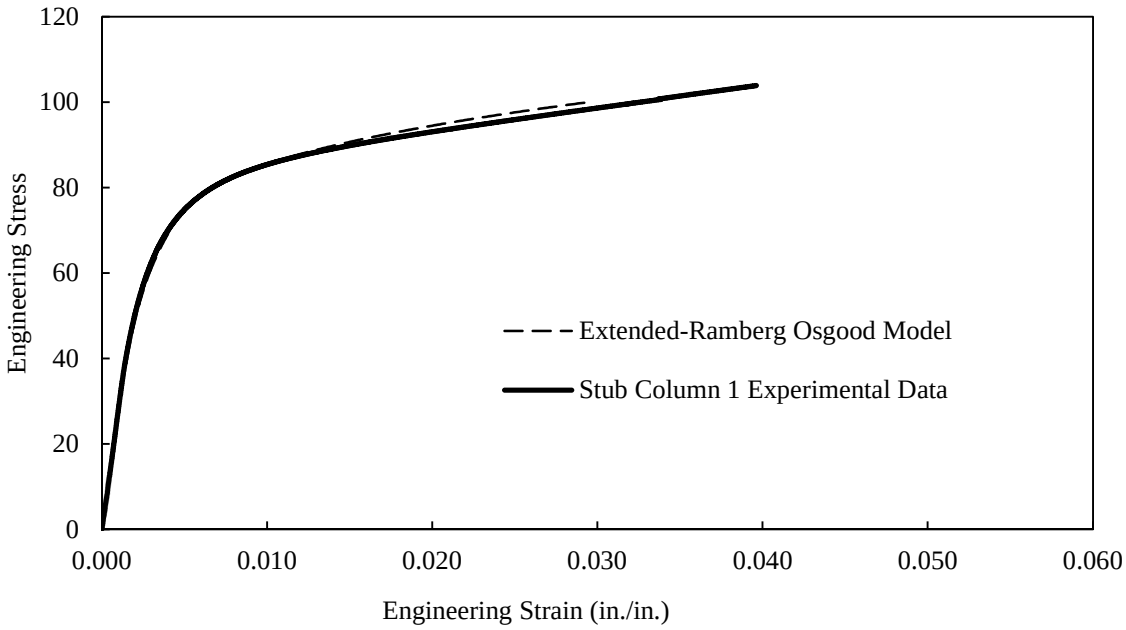

Figure A.1- Modeled/experimental stress-strain data, stub column 1

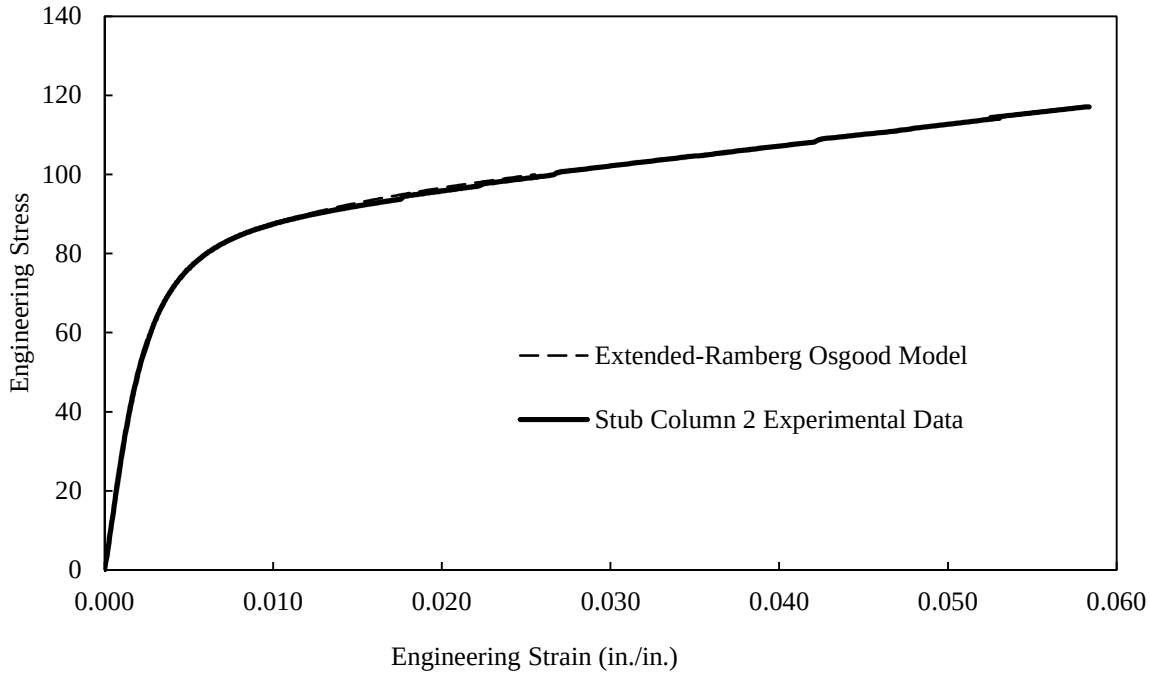

Figure A.2- Modeled/experimental stress-strain data, stub column 2

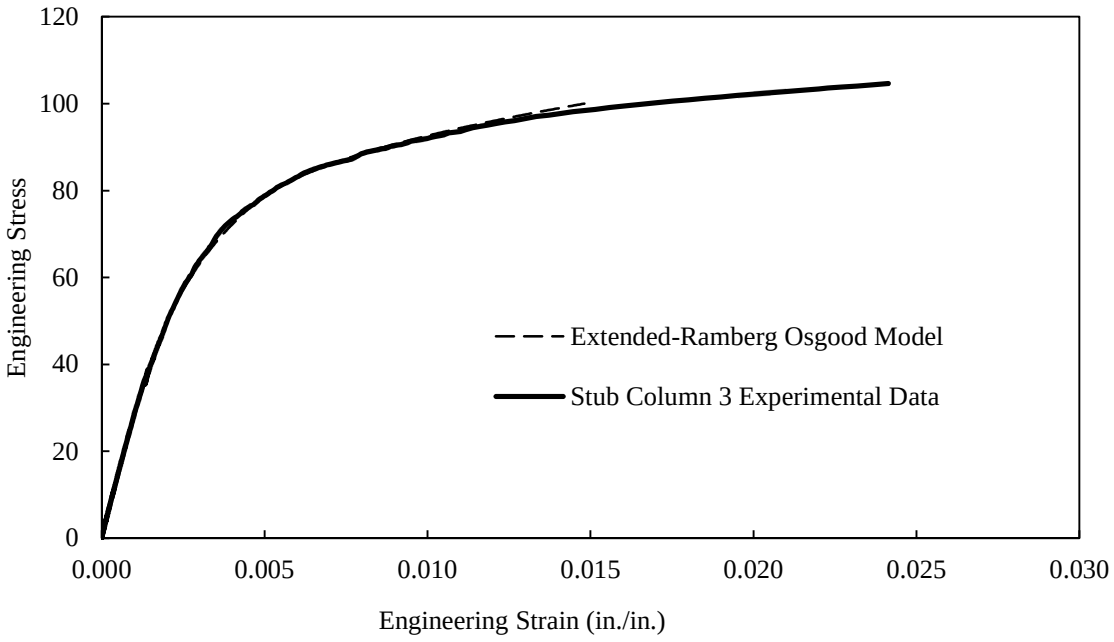

Figure A.3- Modeled/experimental stress-strain data, stub column 3

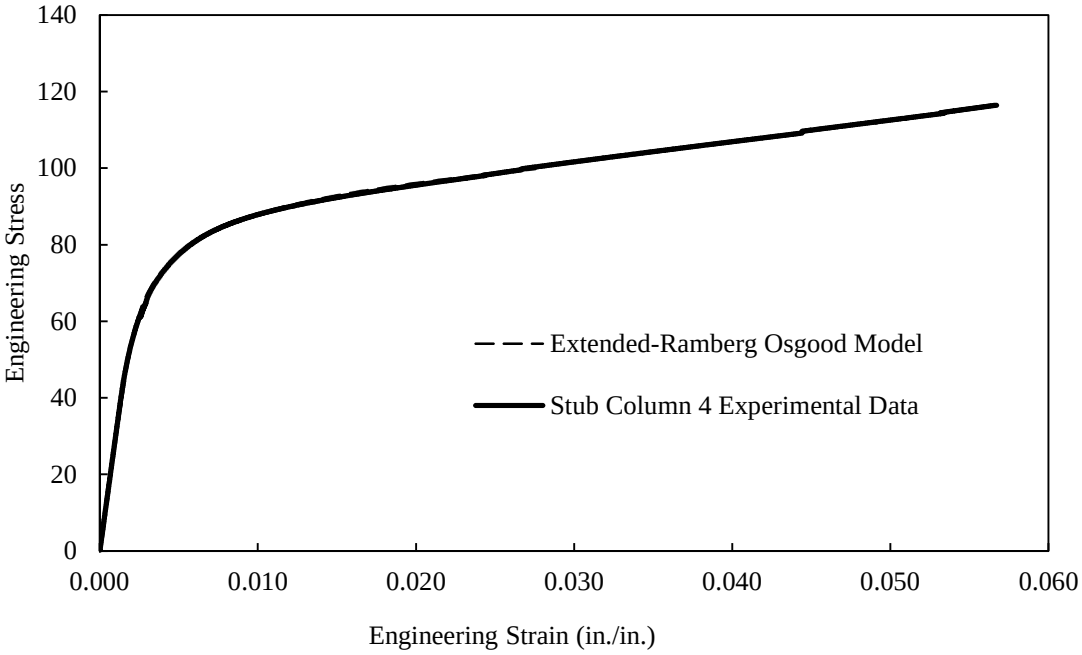

Figure A.4- Modeled/experimental stress-strain data, stub column 4

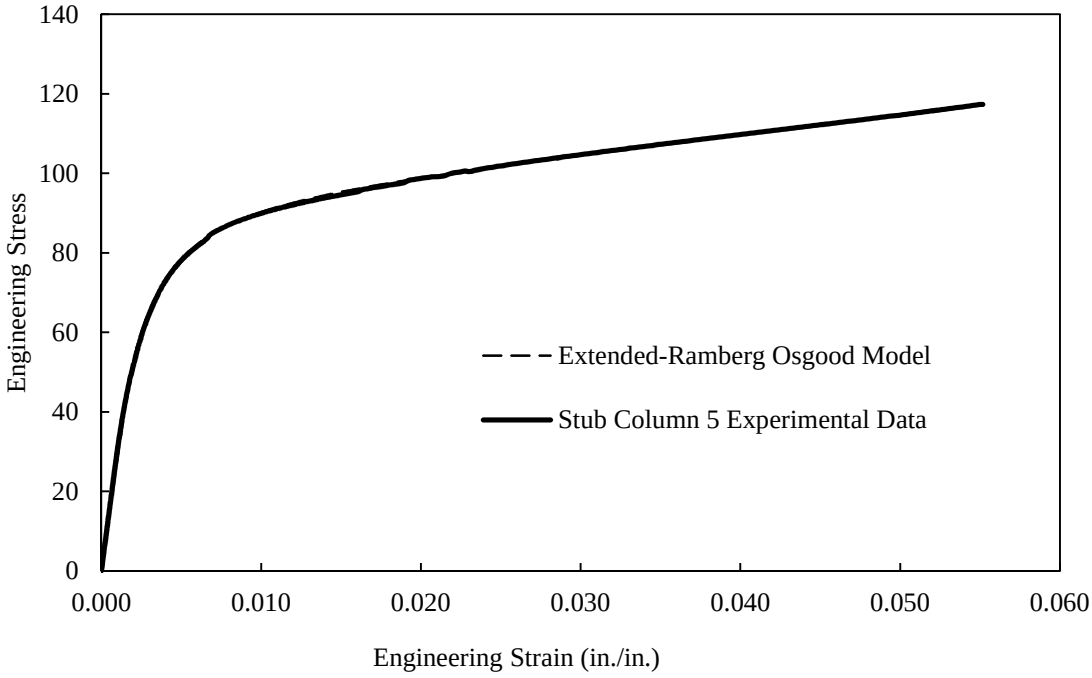

Figure A.5- Modeled/experimental stress-strain data, stub column 5

Four-point Asymmetric Loading Shear Test Results

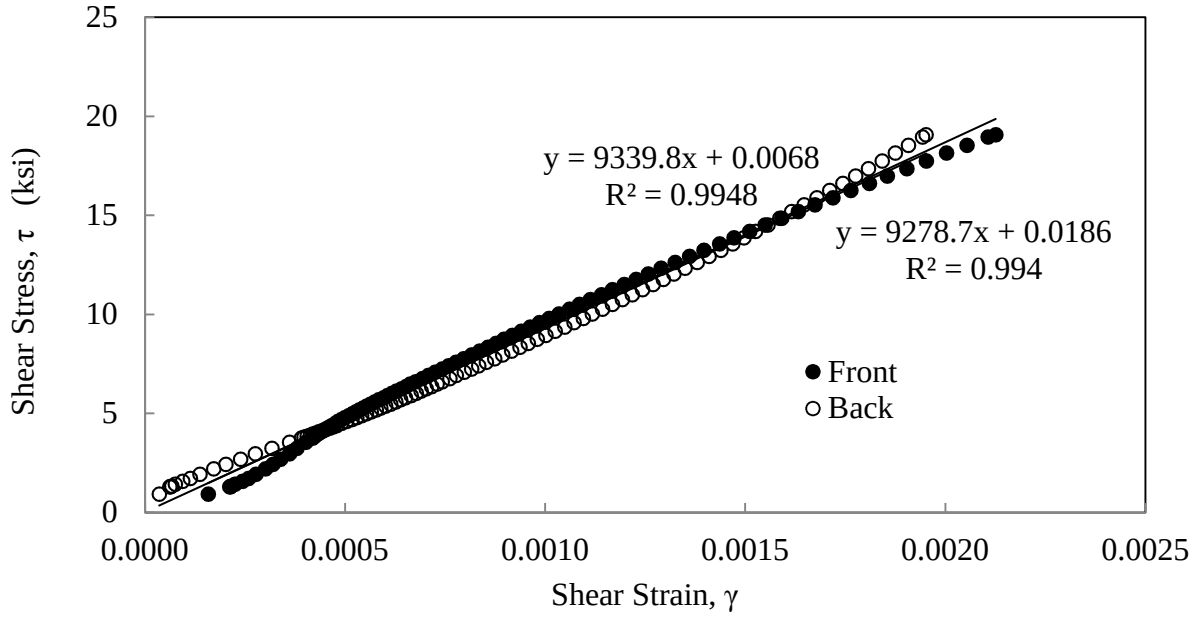

Figure A.6- Transverse specimen 1

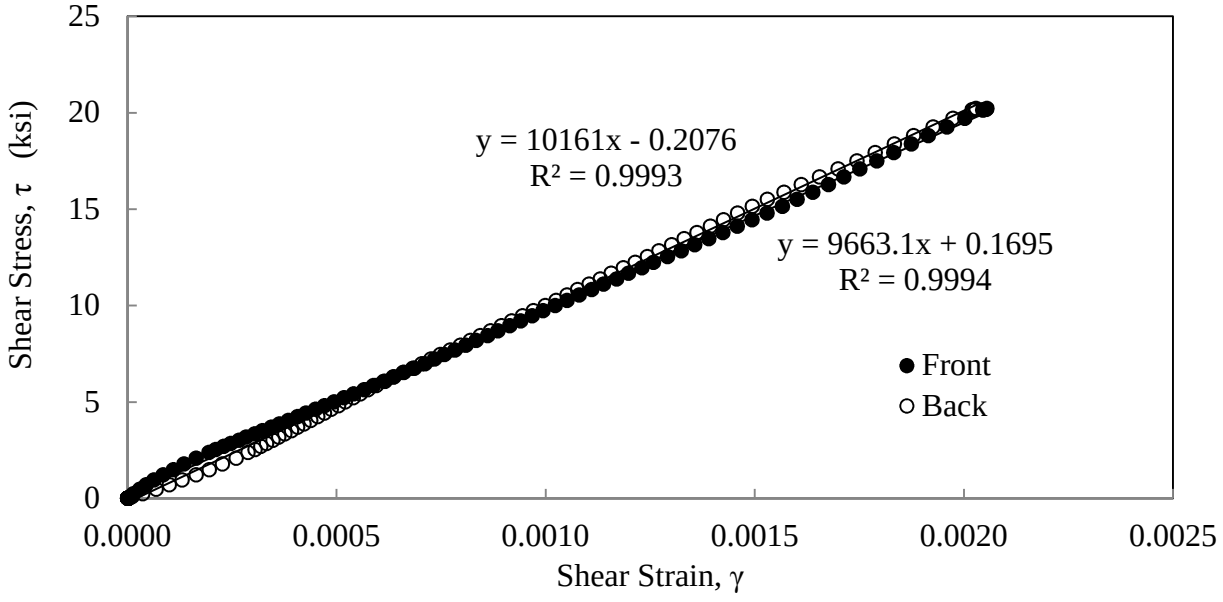

Figure A.7- Transverse specimen 2

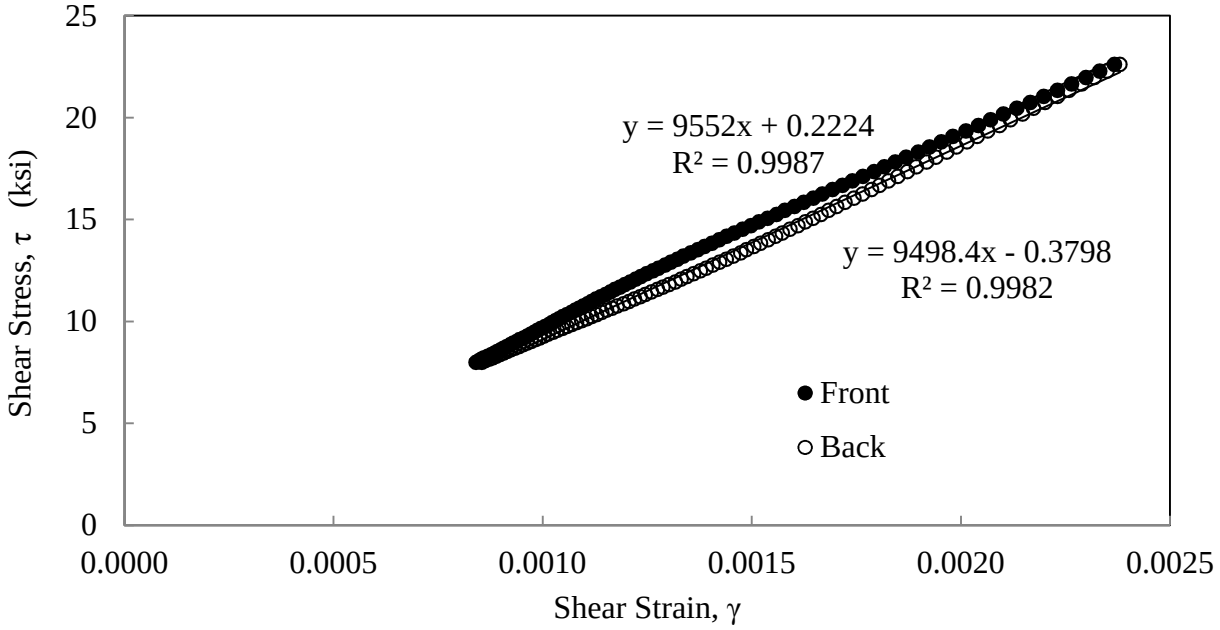

Figure A.8- Transverse specimen 3

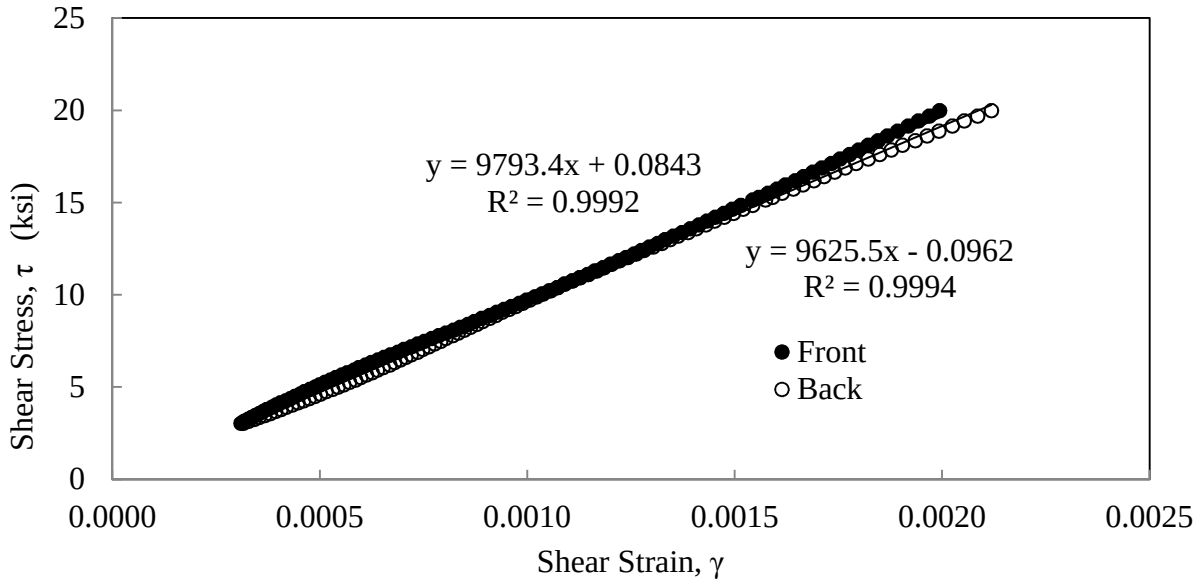

Figure A.9- Transverse specimen 4

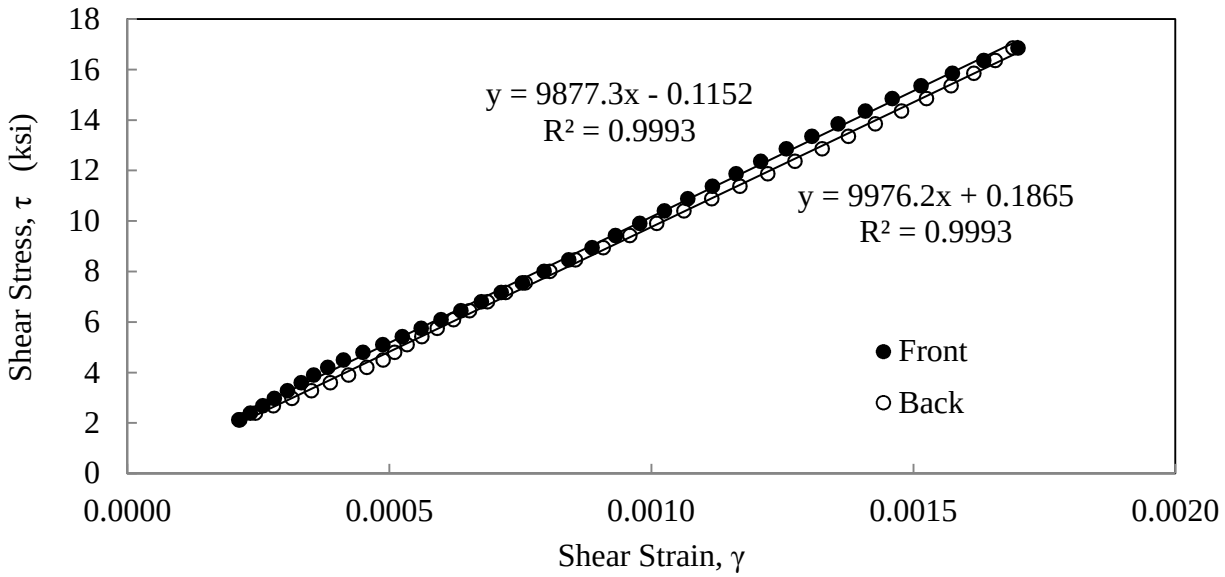

Figure A.10- Longitudinal specimen 1

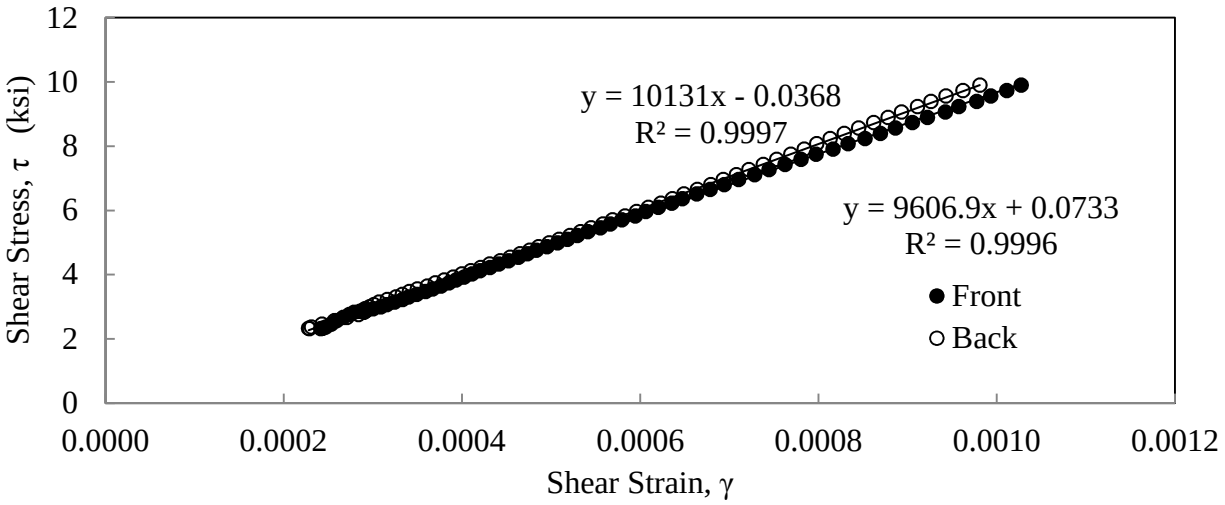

Figure A.11- Longitudinal specimen 2

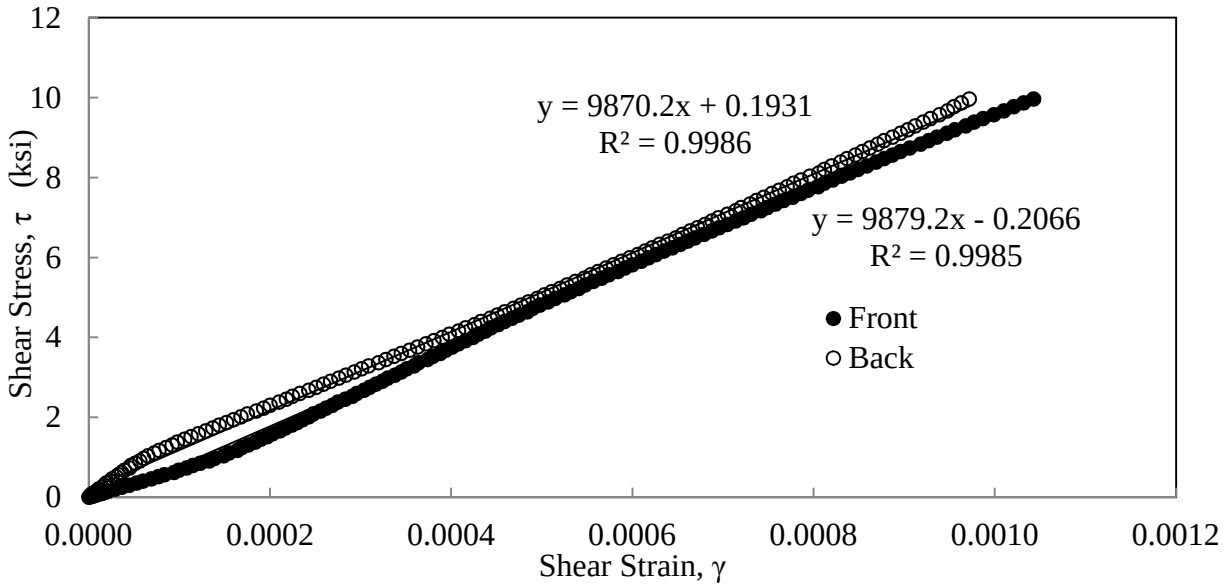

Figure A.12- Longitudinal specimen 3

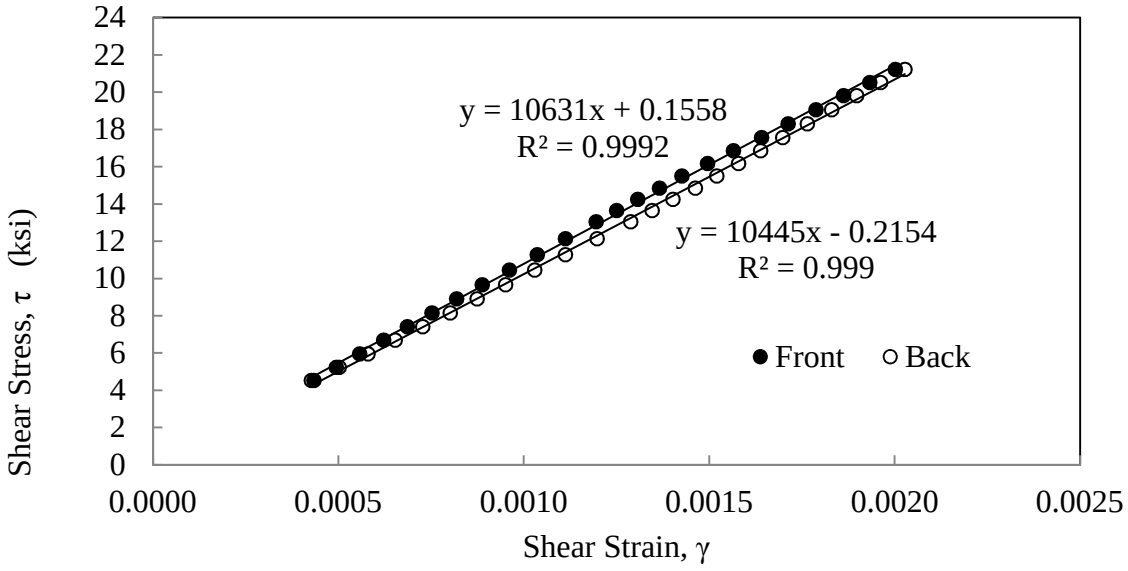

Figure A.13- Longitudinal specimen 4

APPENDIX B

EXPERIMENTAL BUCKLING TEST DATA

Load Deflection Curves

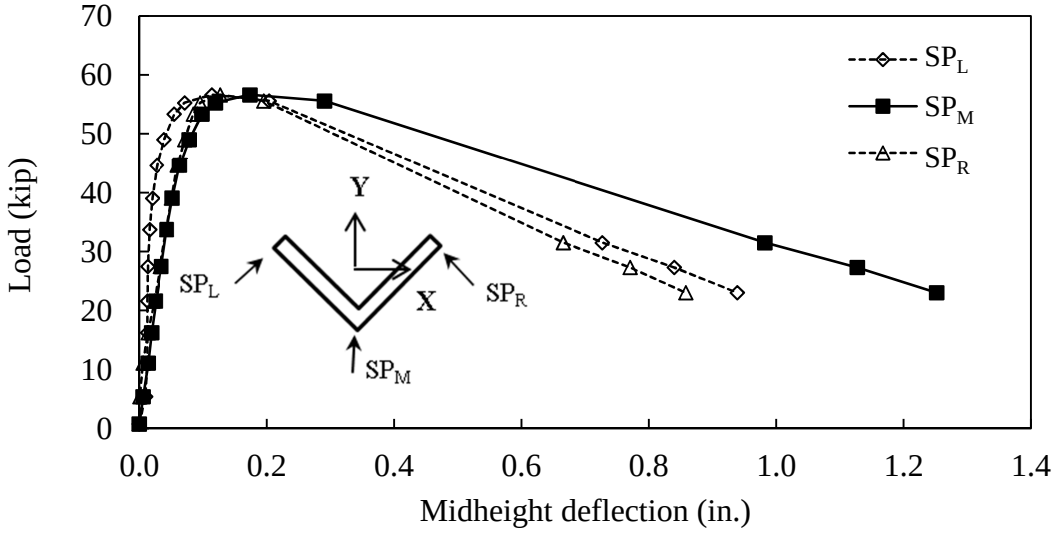

Figure B.1- Load-deflection curves, L2-18a

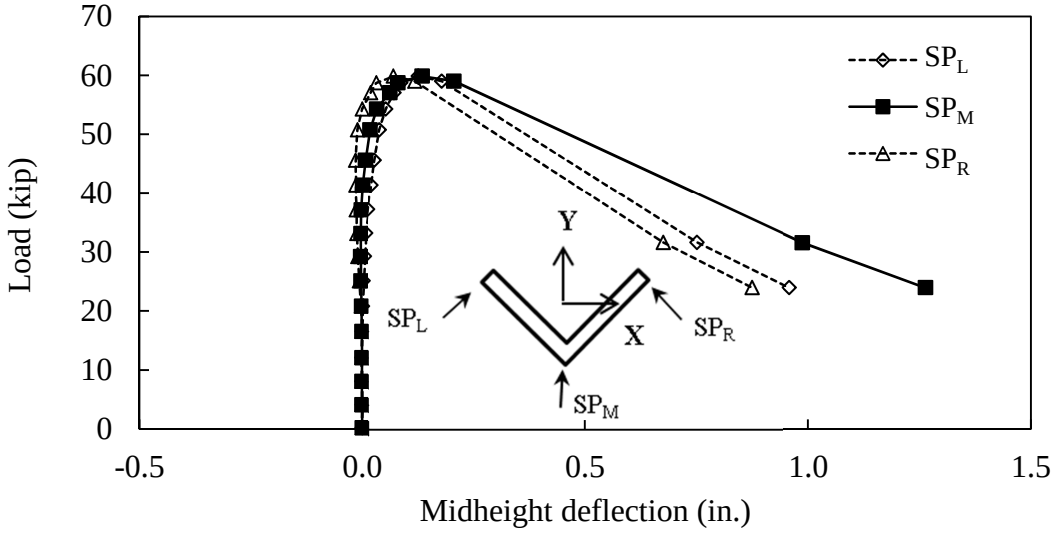

Figure B.2- Load-deflection curves, L2-18b

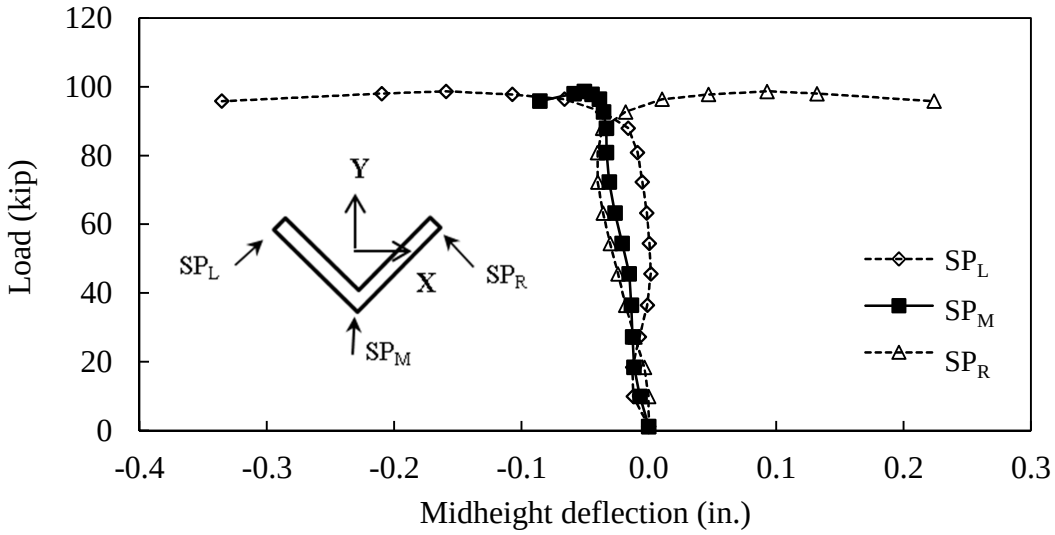

Figure B.3- Load-deflection curves, L3-18

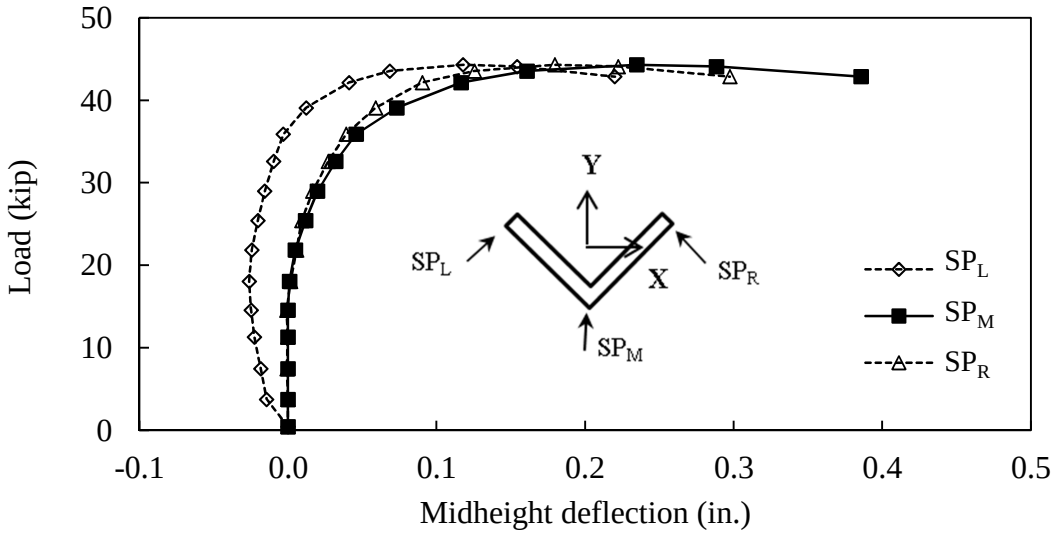

Figure B.4- Load-deflection curves, L2-24

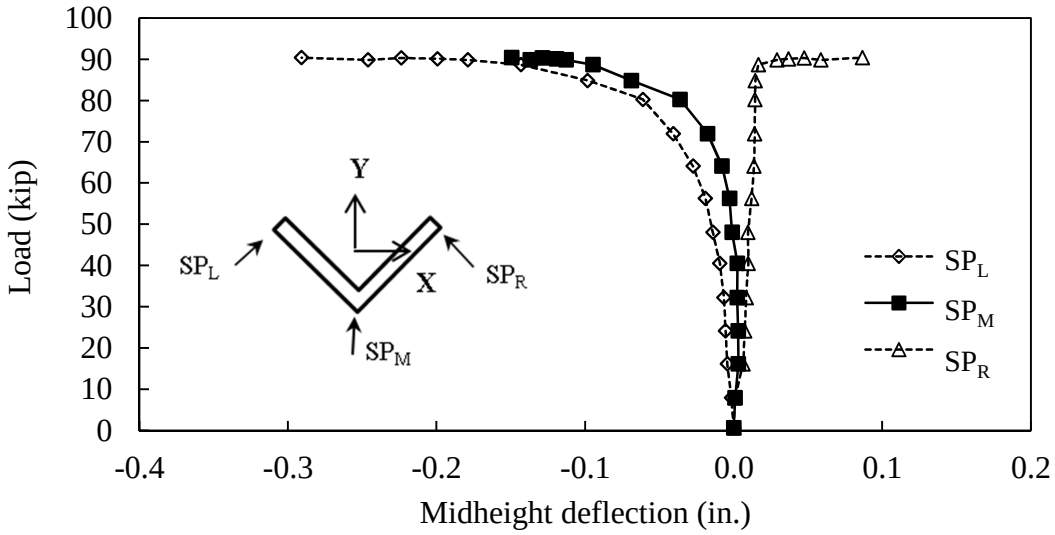

Figure B.5- Load-deflection curves, L3-24a

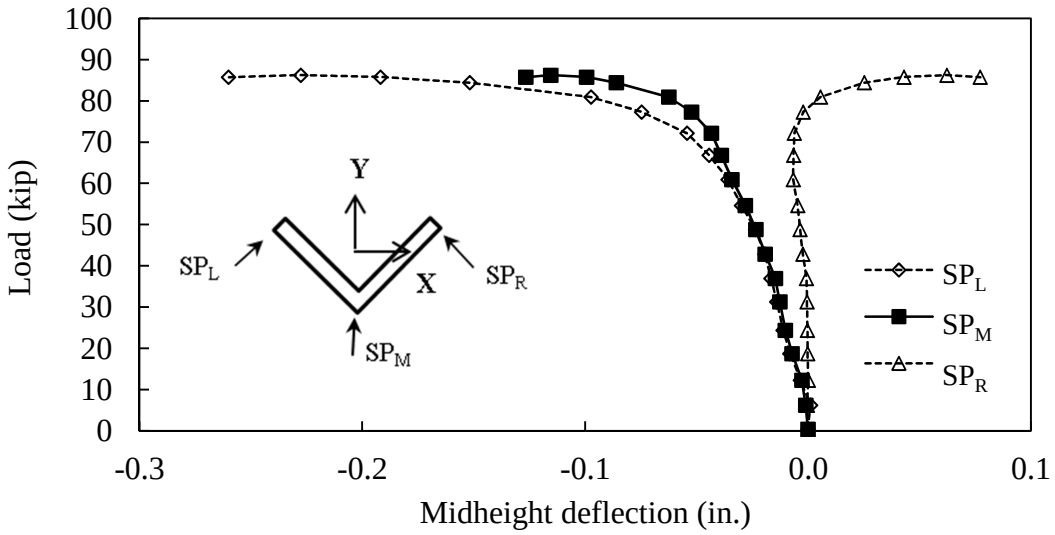

Figure B.6- Load-deflection curves, L3-24b

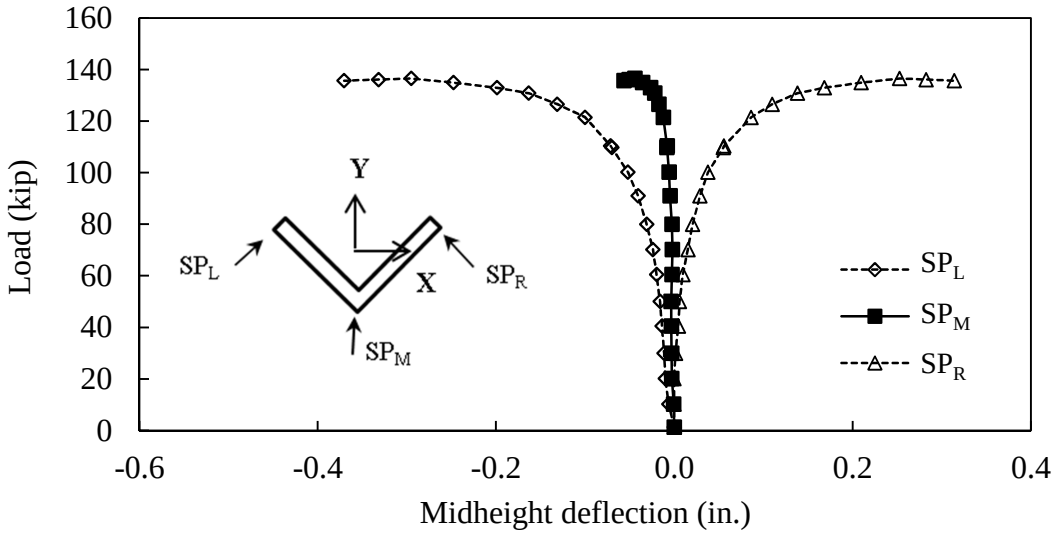

Figure B.7- Load-deflection curves, L4-24

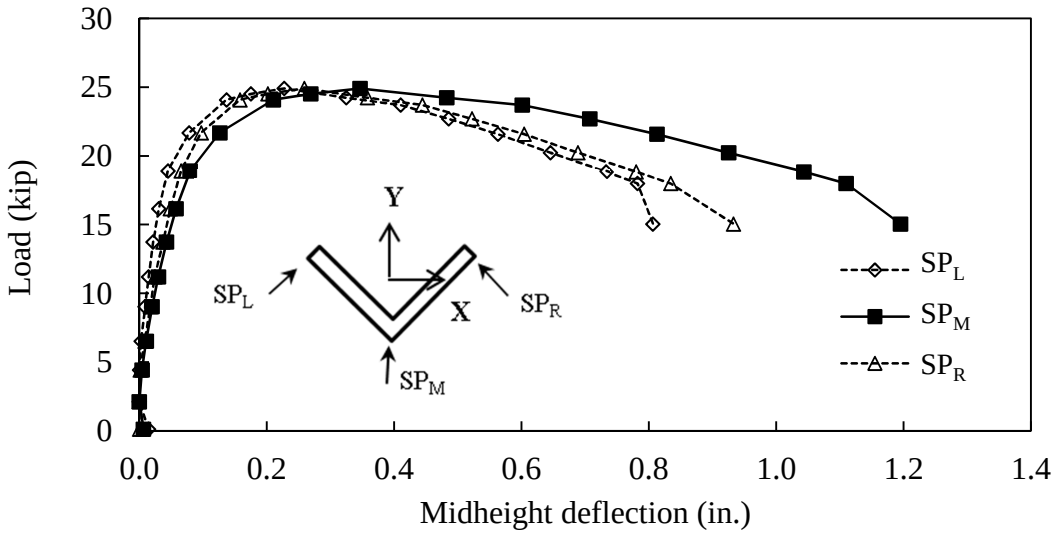

Figure B.8- Load-deflection curves, L2-36a

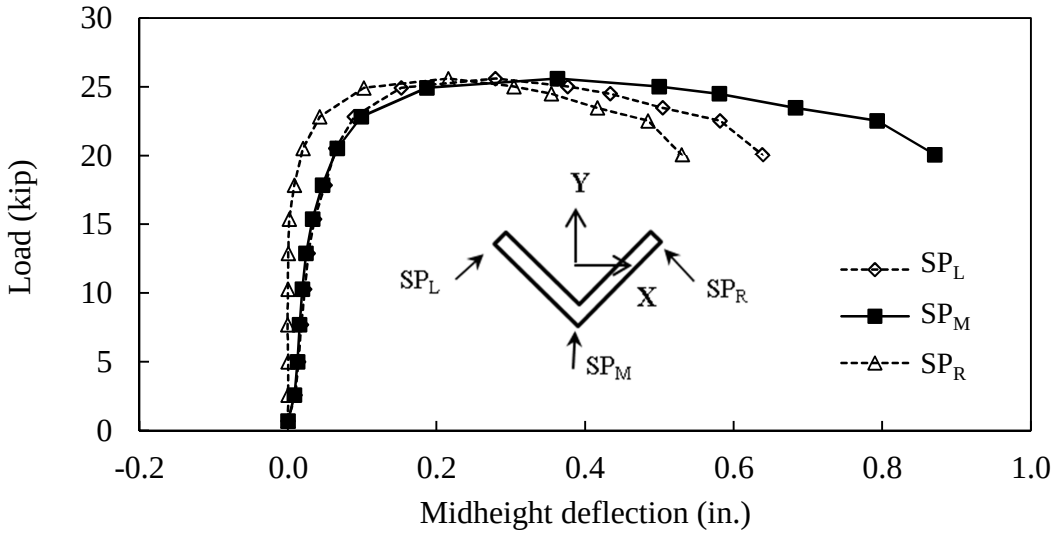

Figure B.9- Load-deflection curves, L2-36b

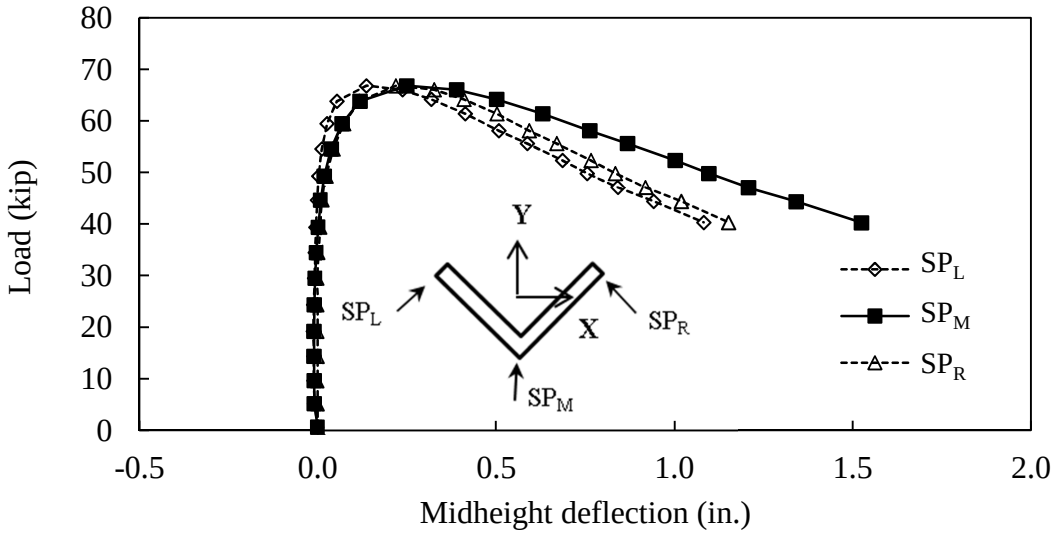

Figure B.10- Load-deflection curves, L3-36

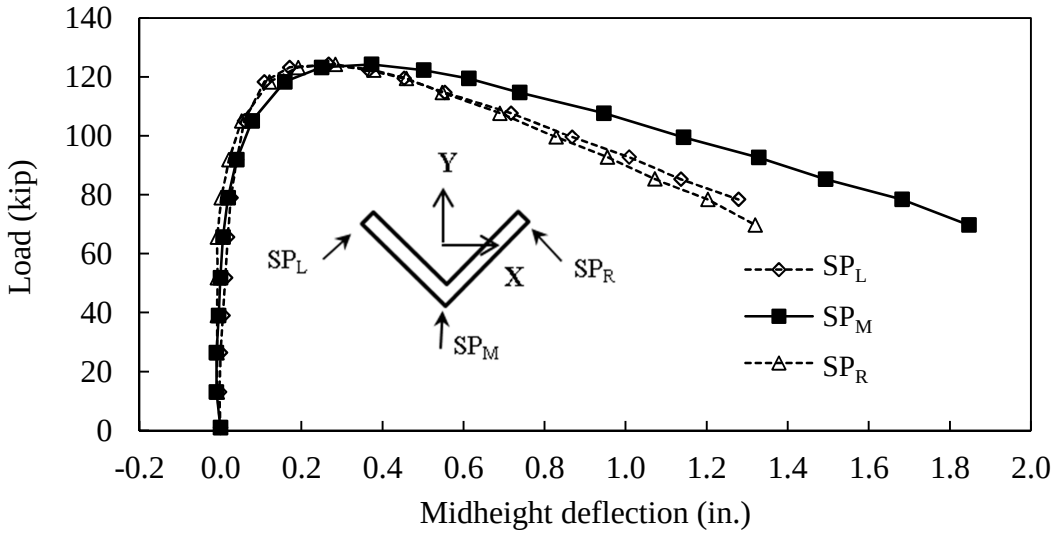

Figure B.11- Load-deflection curves, L4-36a

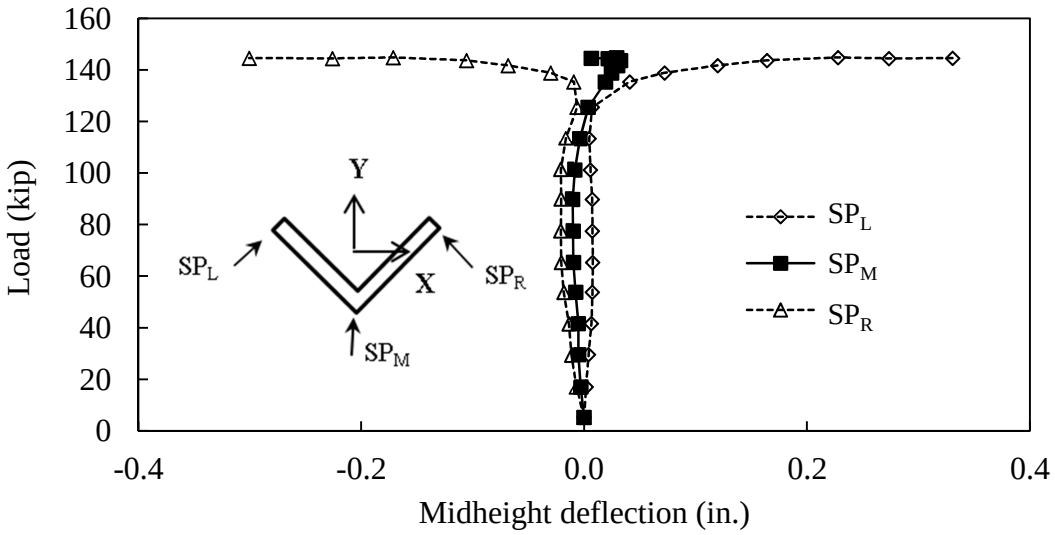

Figure B.12- Load-deflection curves, L4-36b

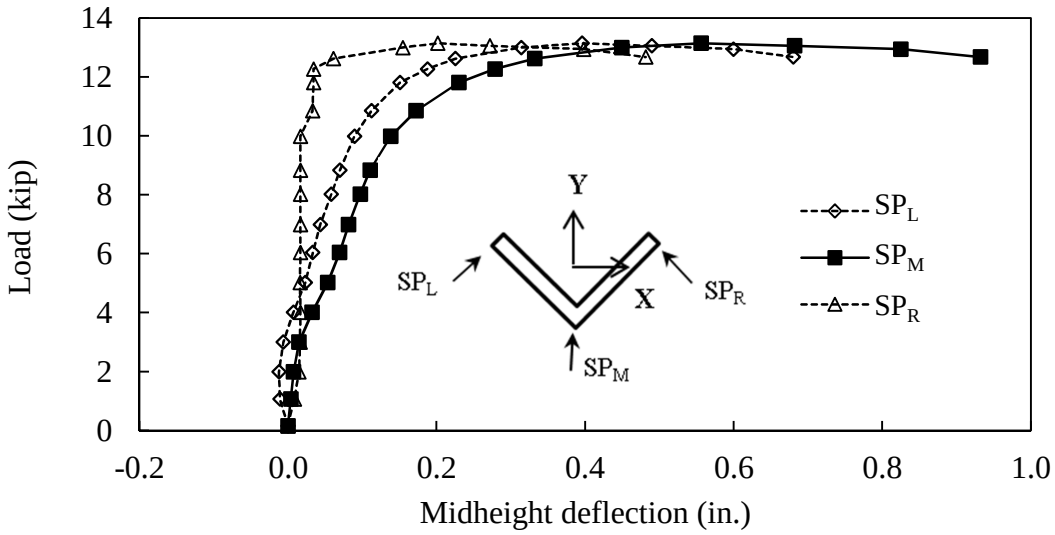

Figure B.13 Load-deflection curves, L2-48

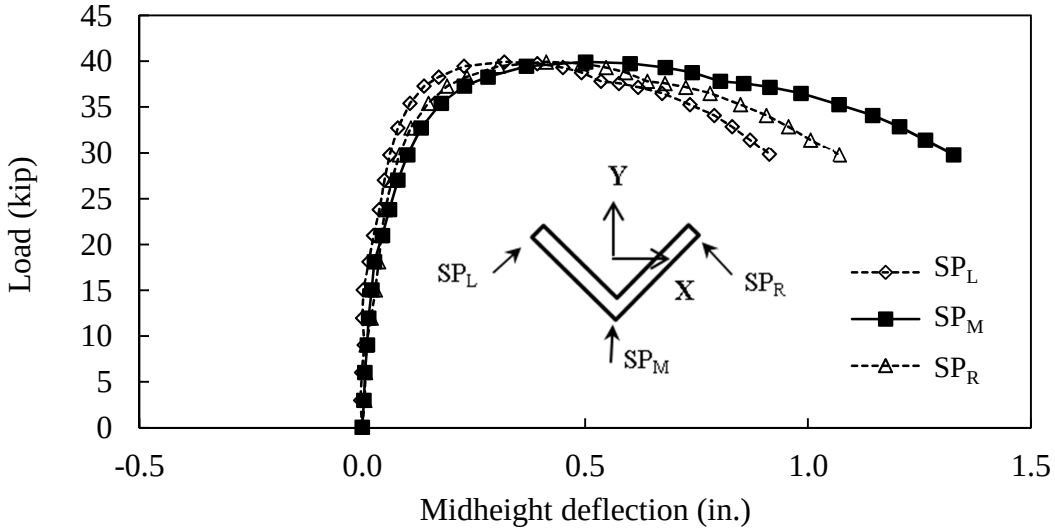

Figure B.14- Load-deflection curves, L3-48a

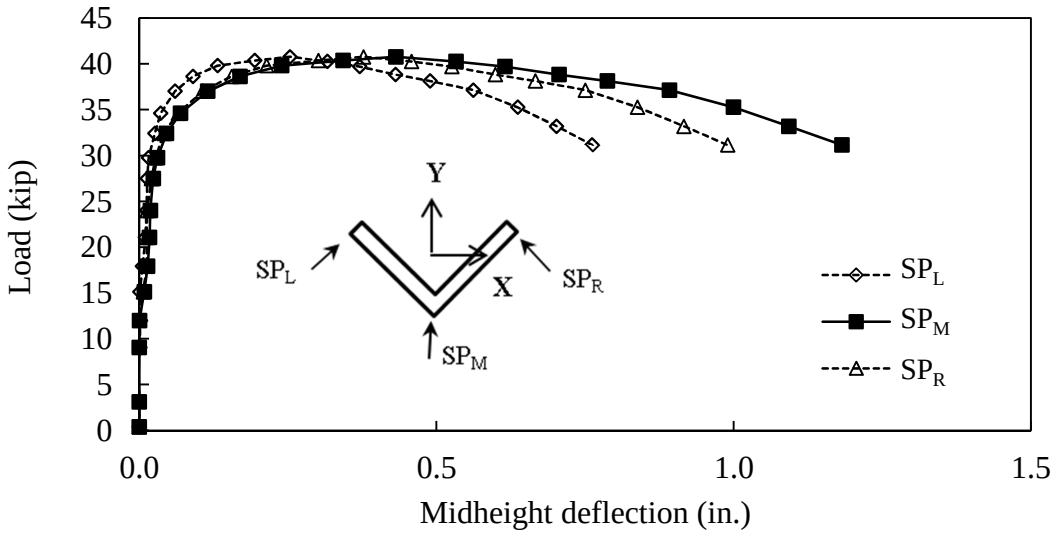

Figure B.15- Load-deflection curves, L3-48b

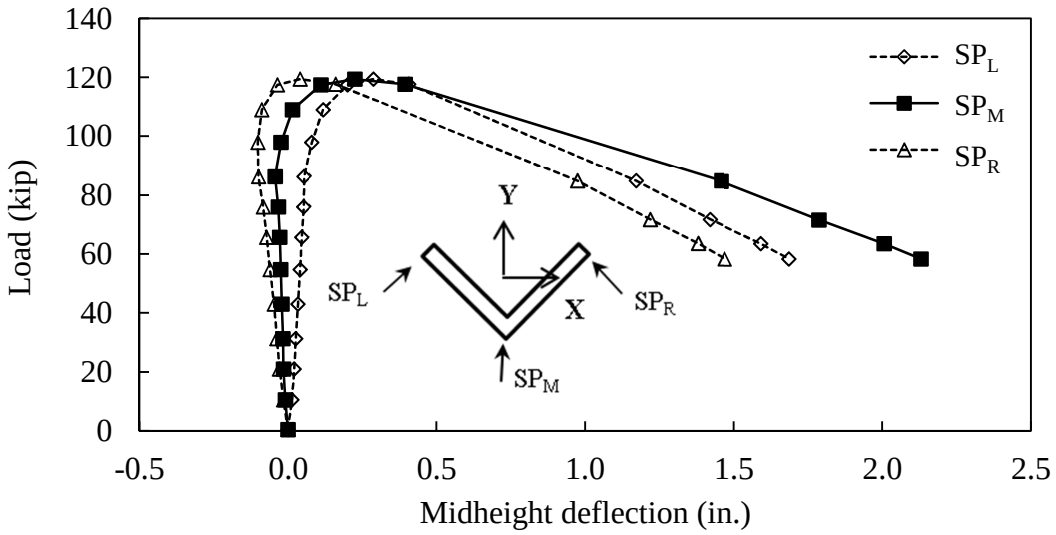

Figure B.16- Load-deflection curves, L4-48

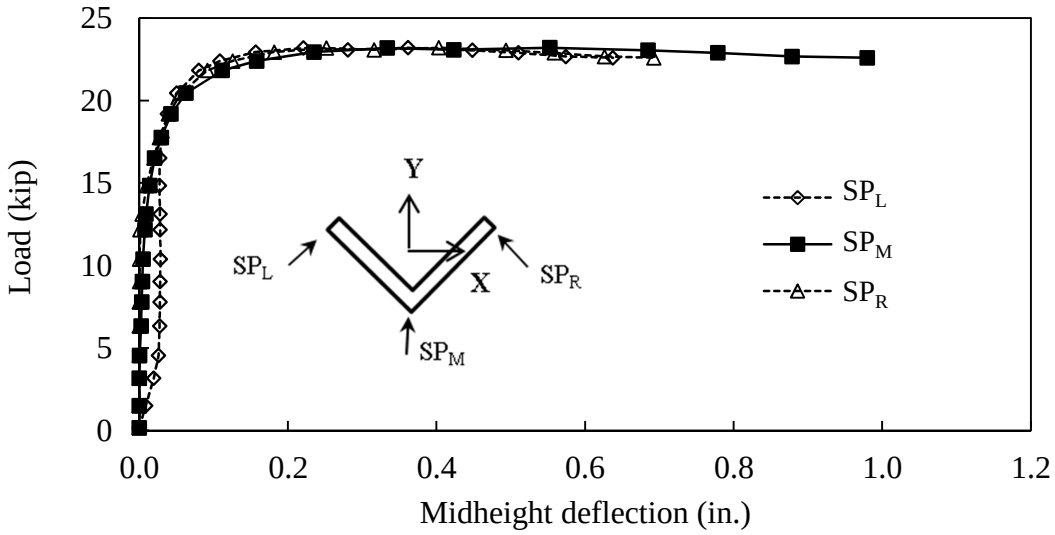

Figure B.17- Load-deflection curves, L2-60a

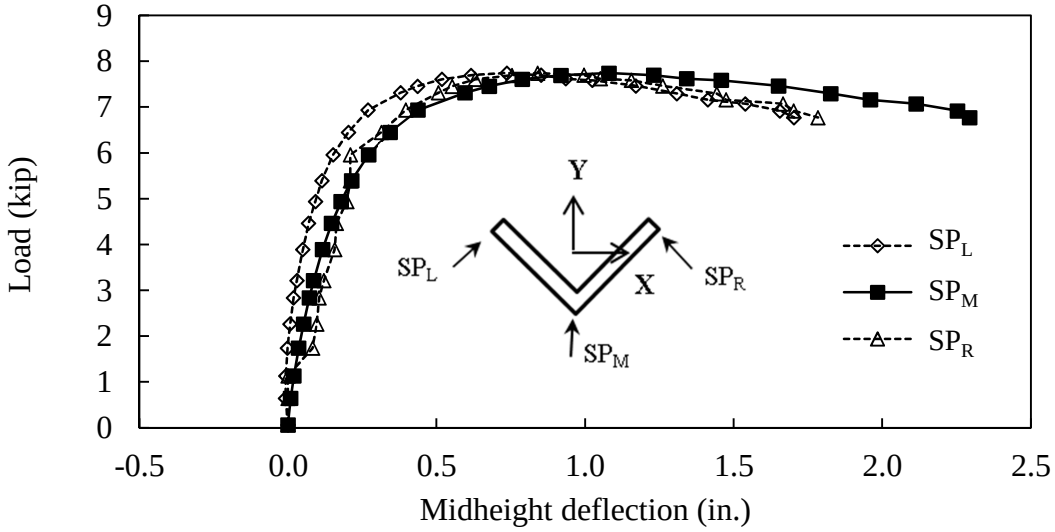

Figure B.18- Load-deflection curves, L2-60b

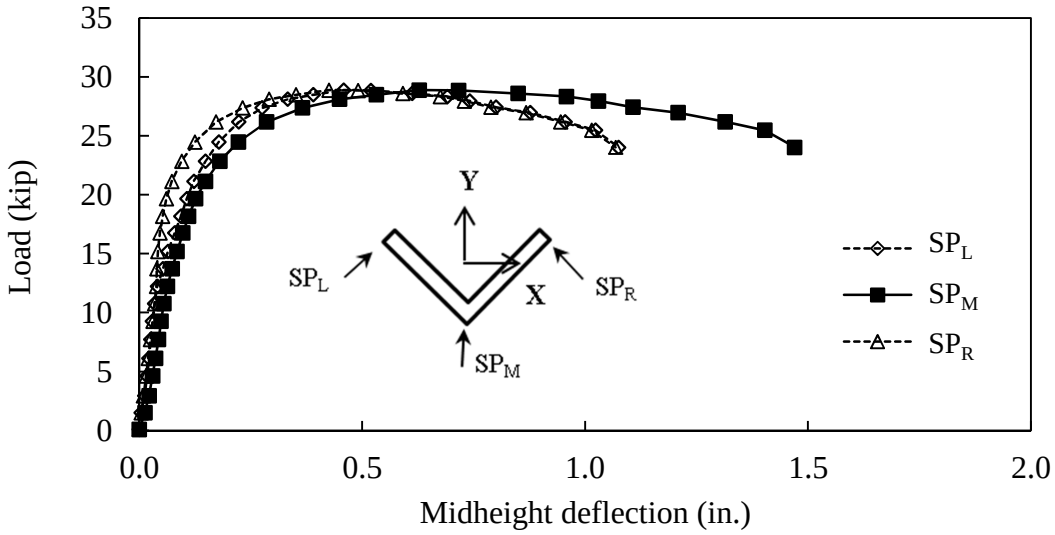

Figure B.19- Load-deflection curves, L3-60a

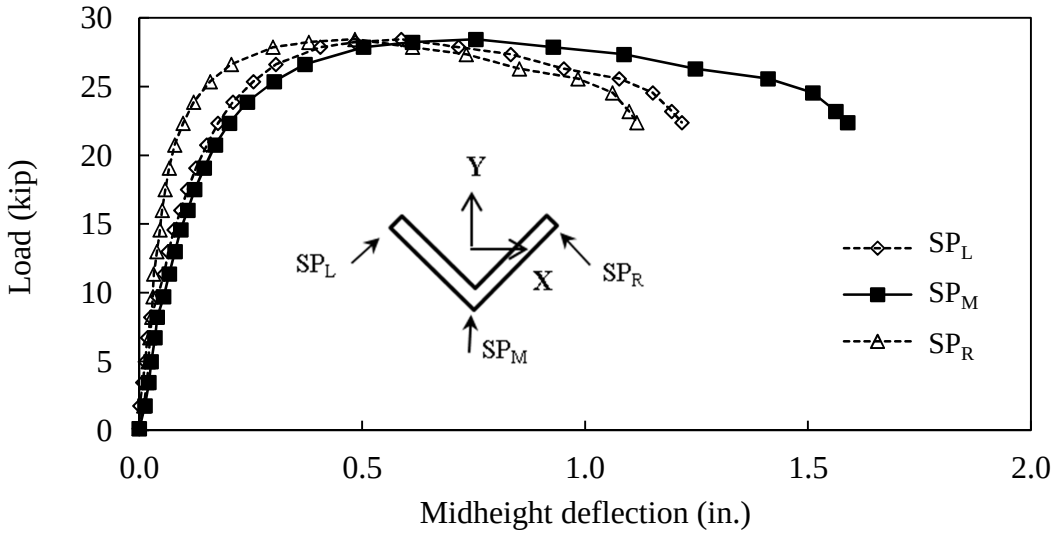

Figure B.20- Load-deflection curves, L3-60b

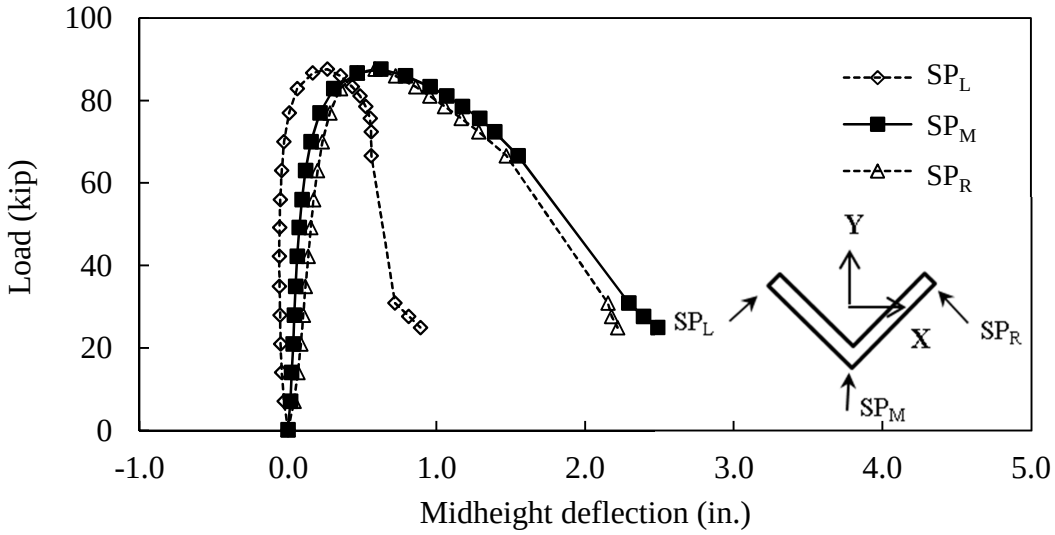

Figure B.21- Load-deflection curves, L4-60a

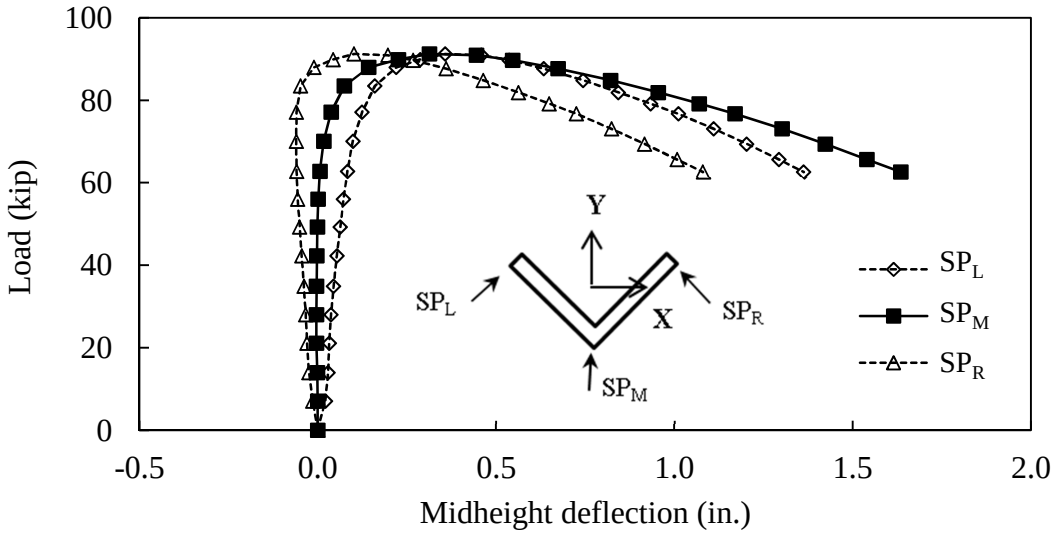

Figure B.22- Load-deflection curves, L4-60b

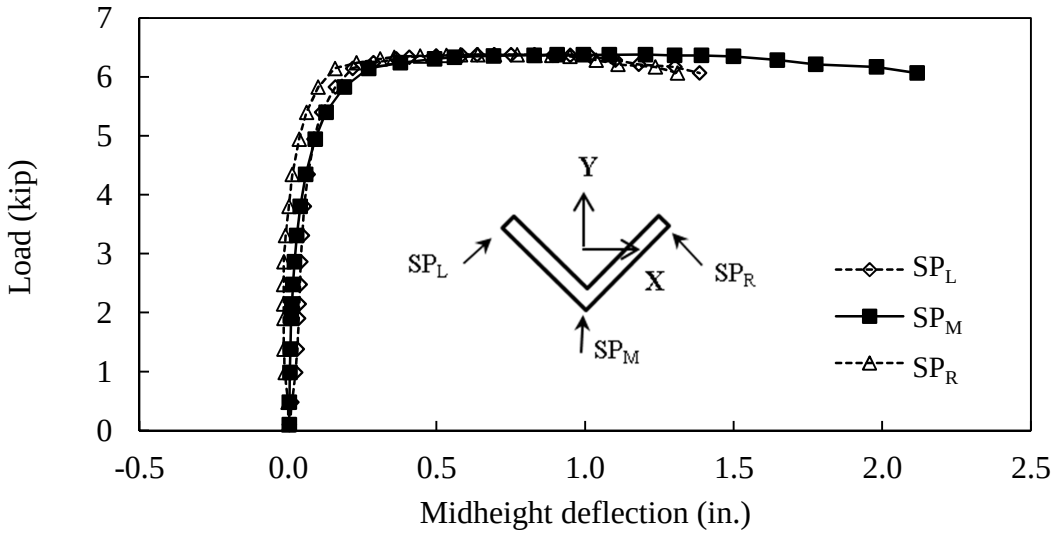

Figure B.23- Load-deflection curves, L2-72

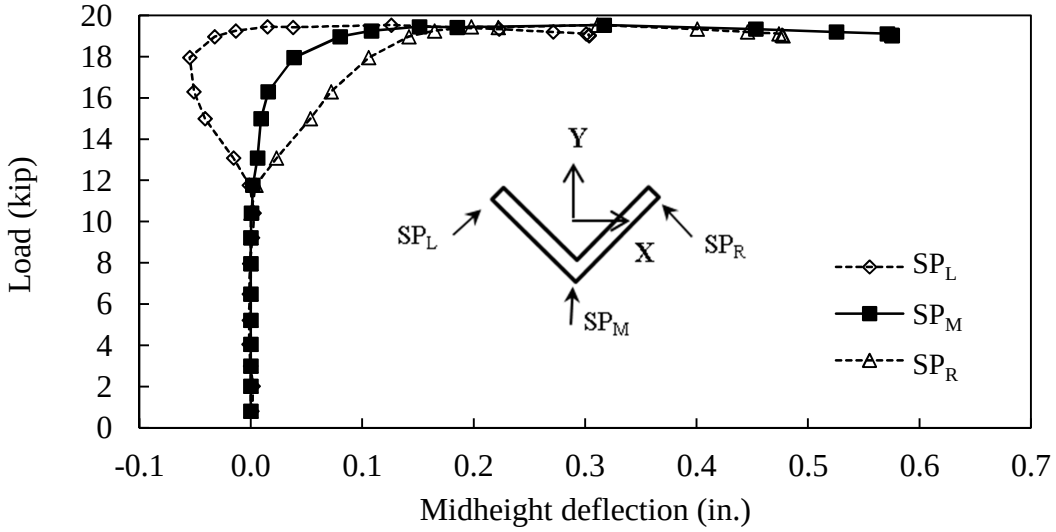

Figure B.24- Load-deflection curves, L3-72

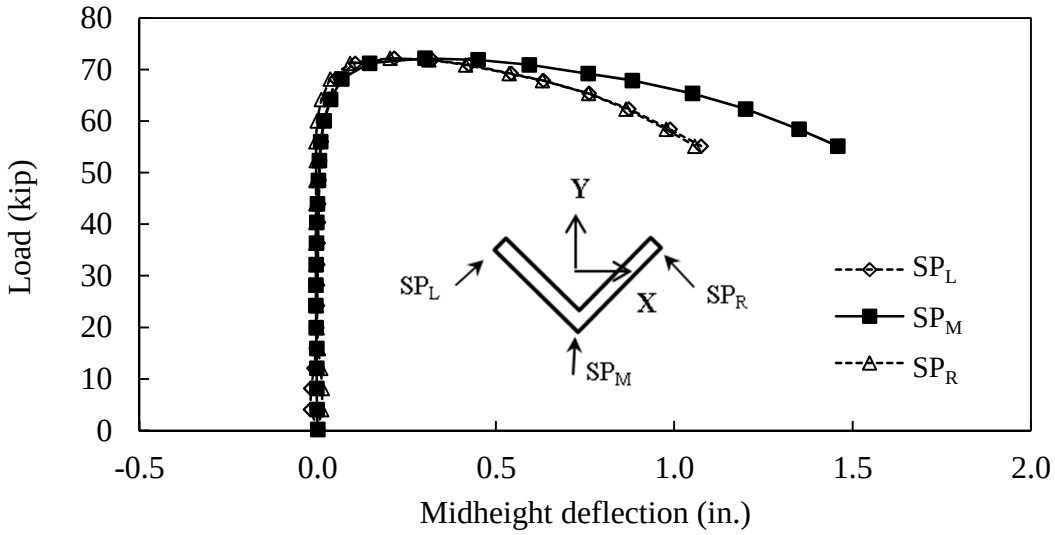

Figure B.25- Load-deflection curves, L4-72

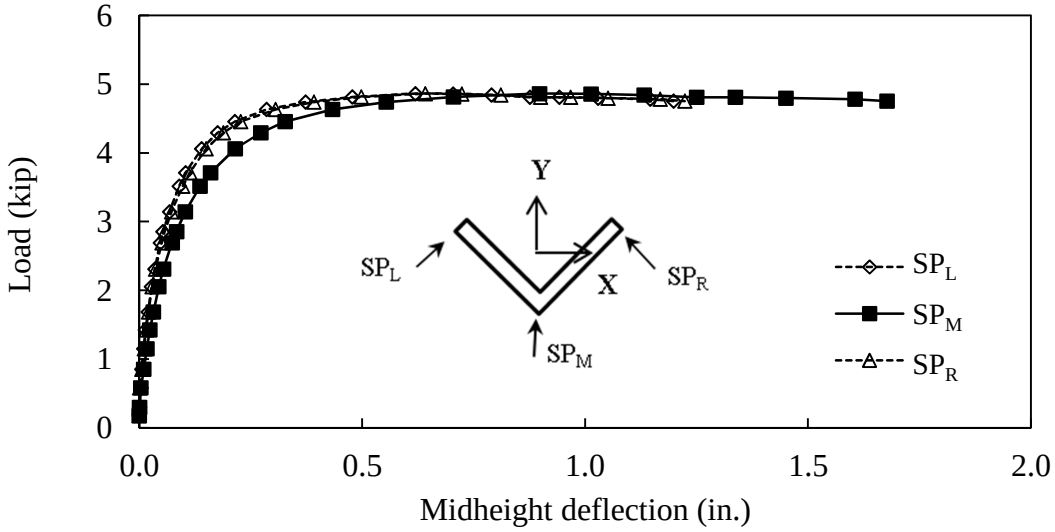

Figure B.26- Load-deflection curves, L2-84

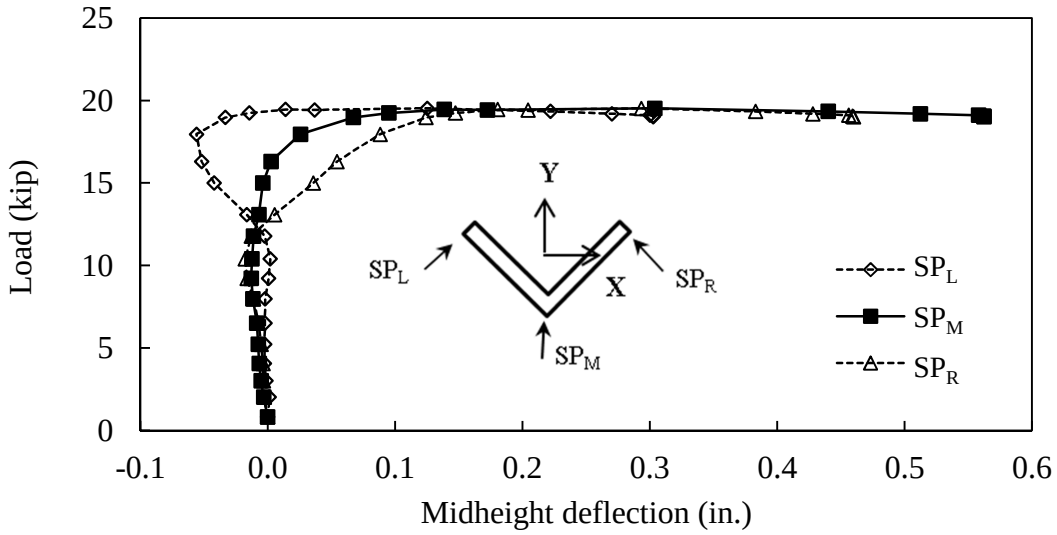

Figure B.27- Load-deflection curves, L3-84

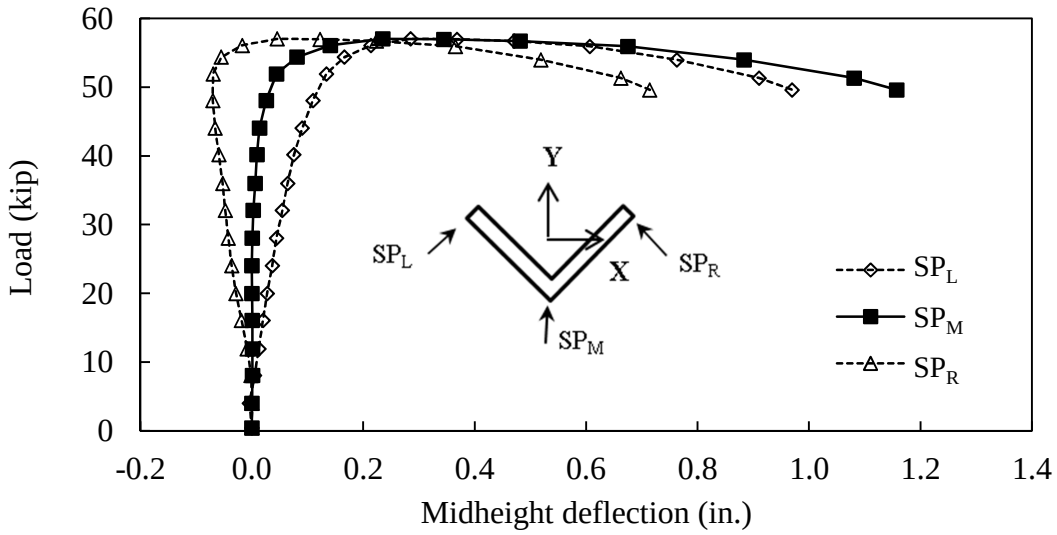

Figure B.28- Load-deflection curves, L4-84

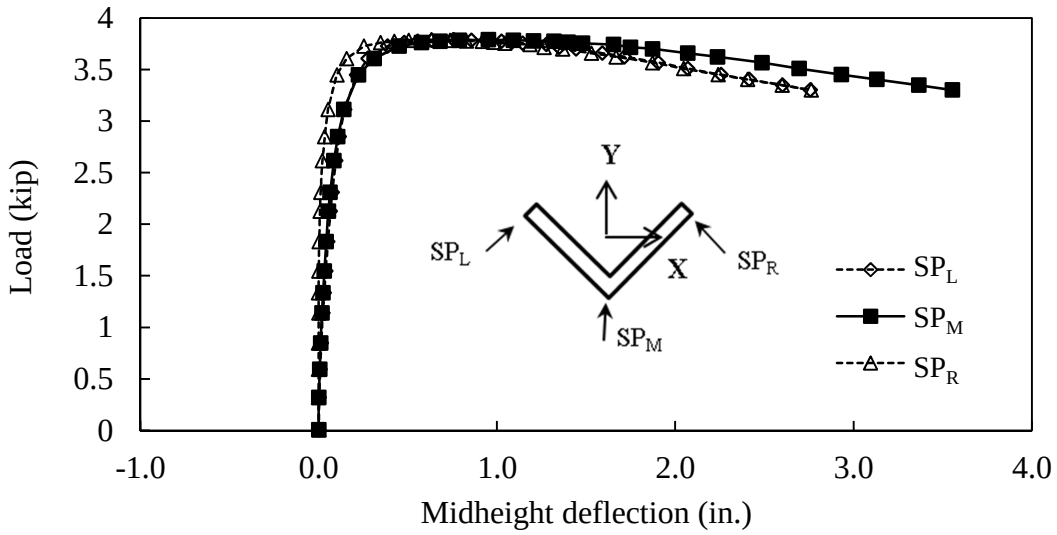

Figure B.29- Load-deflection curves, L2-96

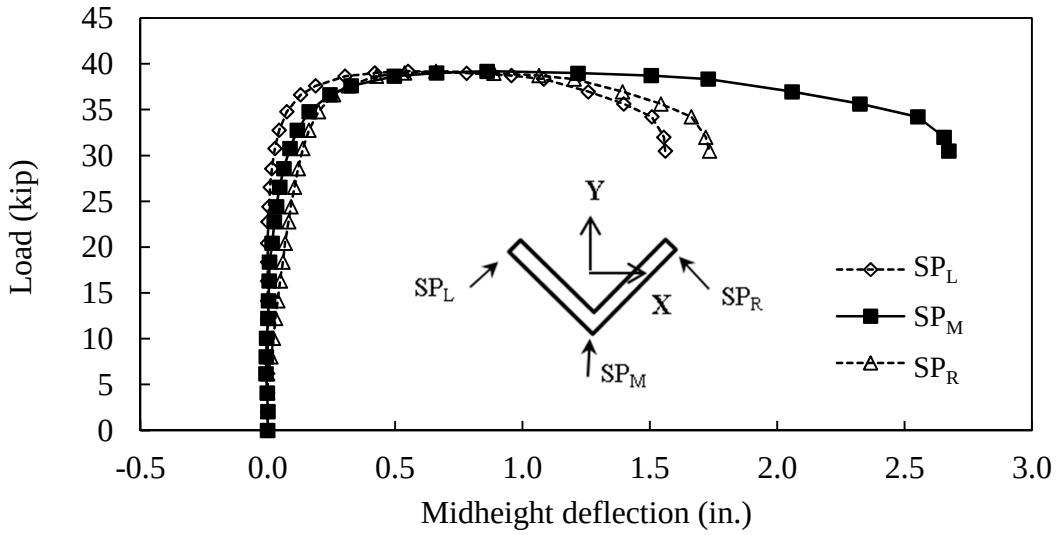

Figure B.30- Load-deflection curves, L4-96

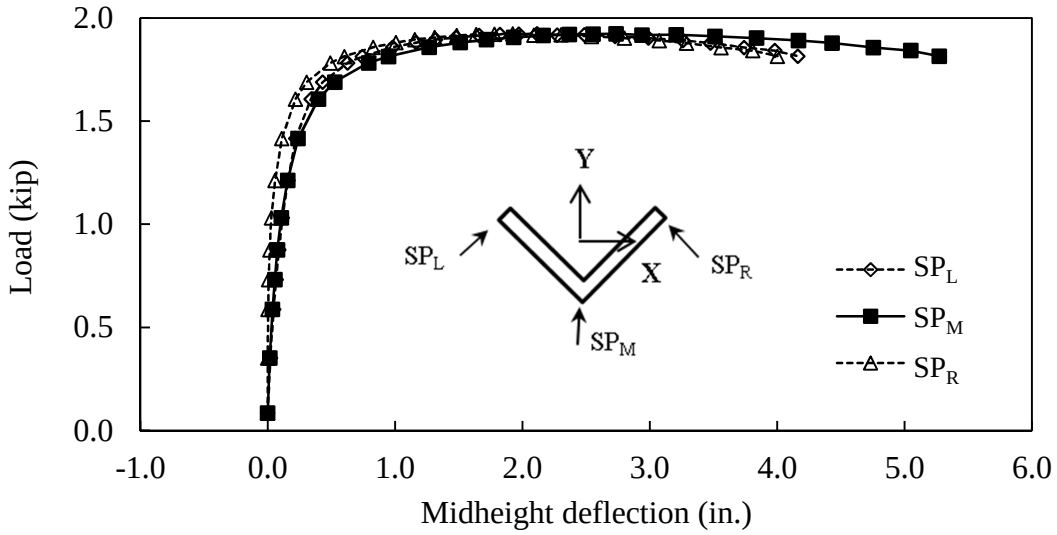

Figure B.31- Load-deflection curves, L2-132

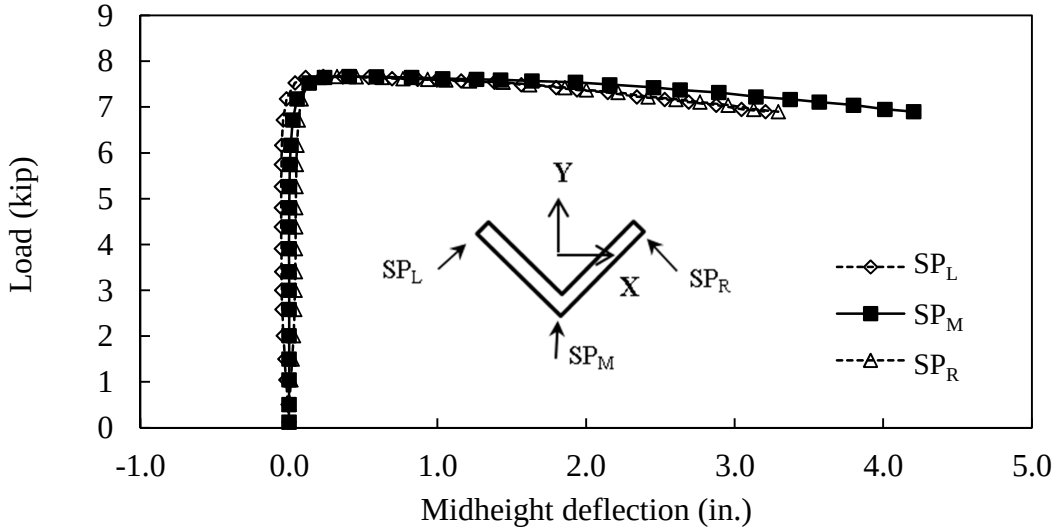

Figure B.32- Load-deflection curves, L3-132

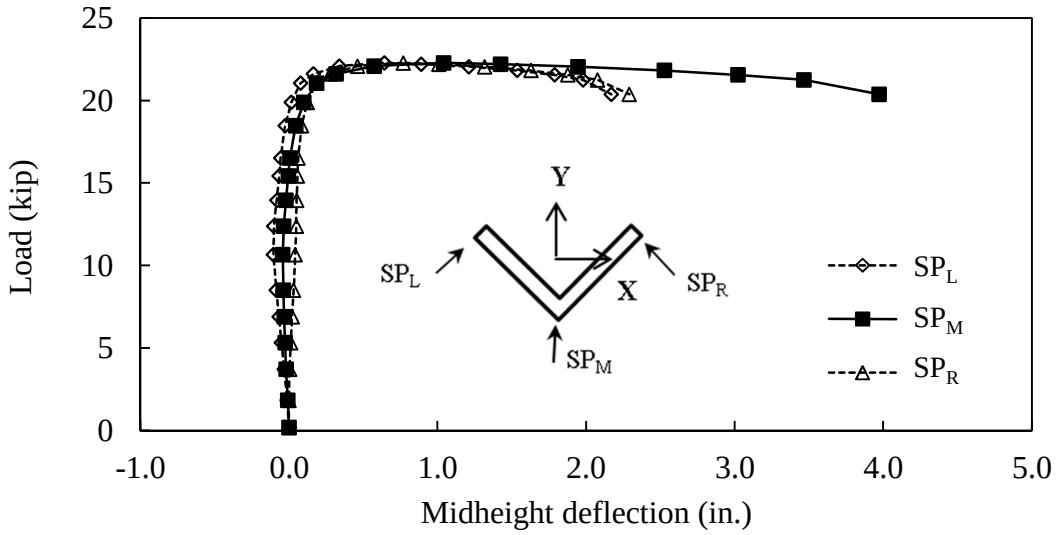

Figure B.33- Load-deflection curves, L4-132

Load-Shortening Data

NOTE: Load-shortening data for L2-18b, L3-24b, and L4-24 unavailable due to instrumentation malfunction.

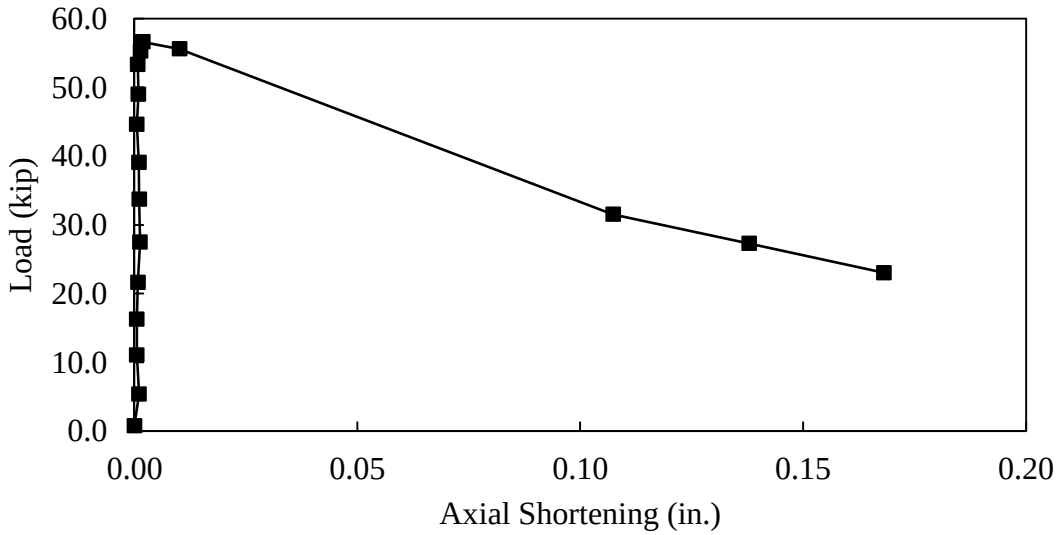

Figure B.1- Load-shortening curve, L2-18a

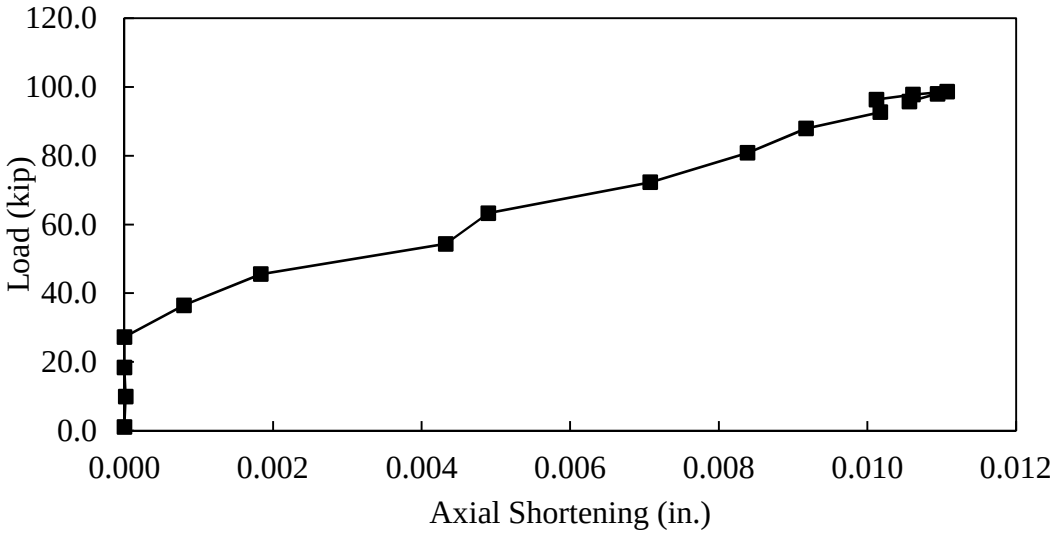

Figure B.2- Load-shortening curve, L3-18

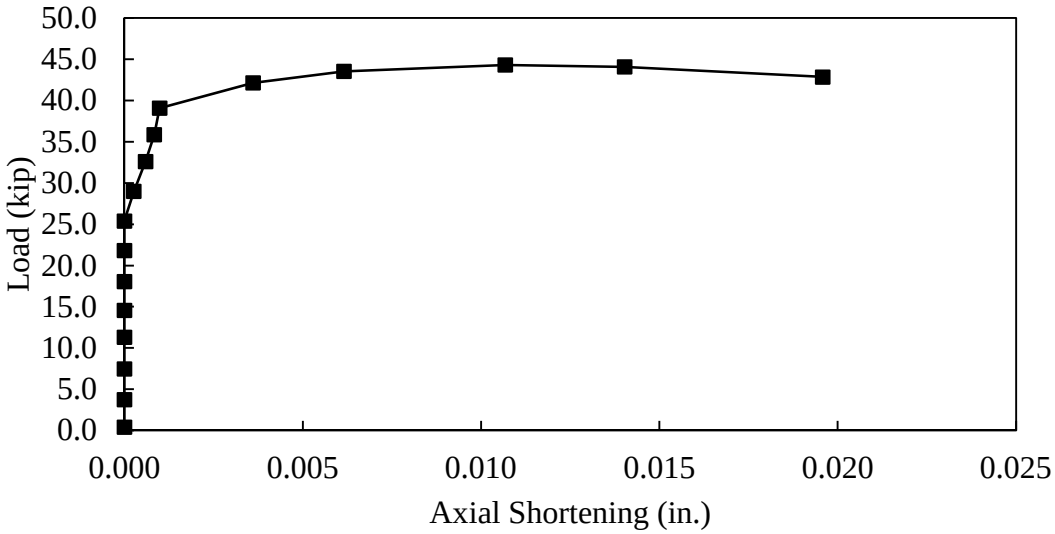

Figure B.3- Load-shortening curve, L2-24

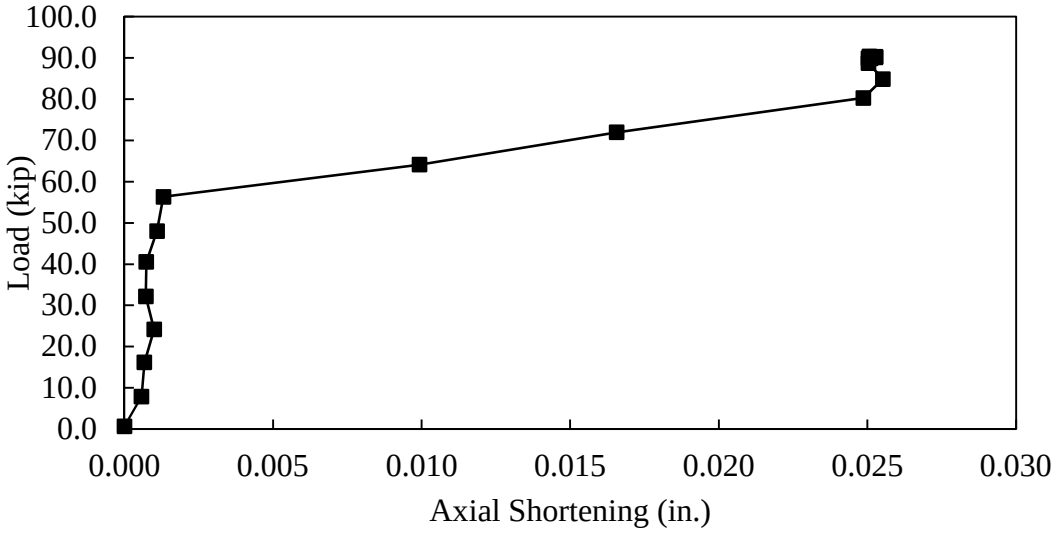

Figure B.4- Load-shortening curve, L2-36a

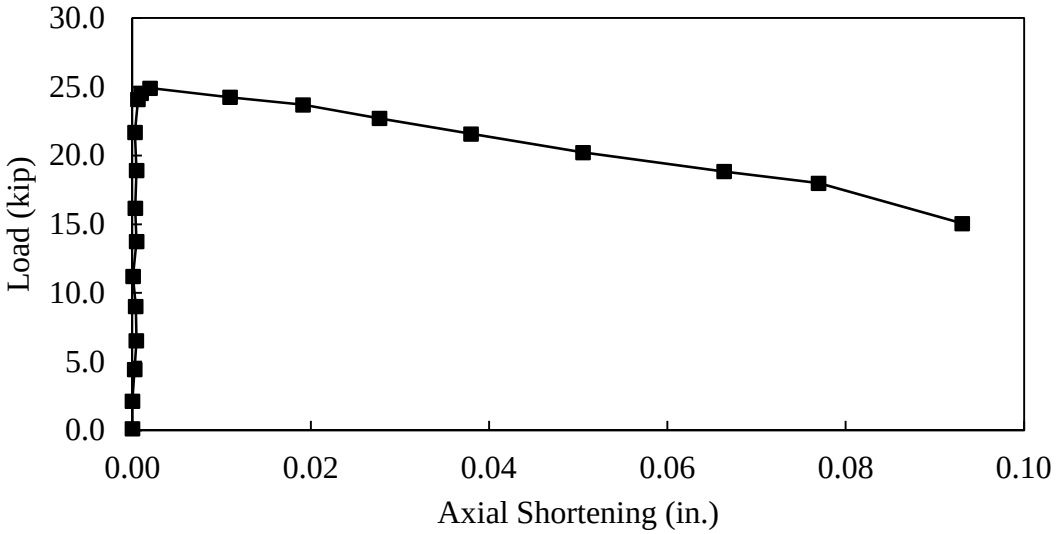

Figure B.5- Load-shortening curve, L2-36a

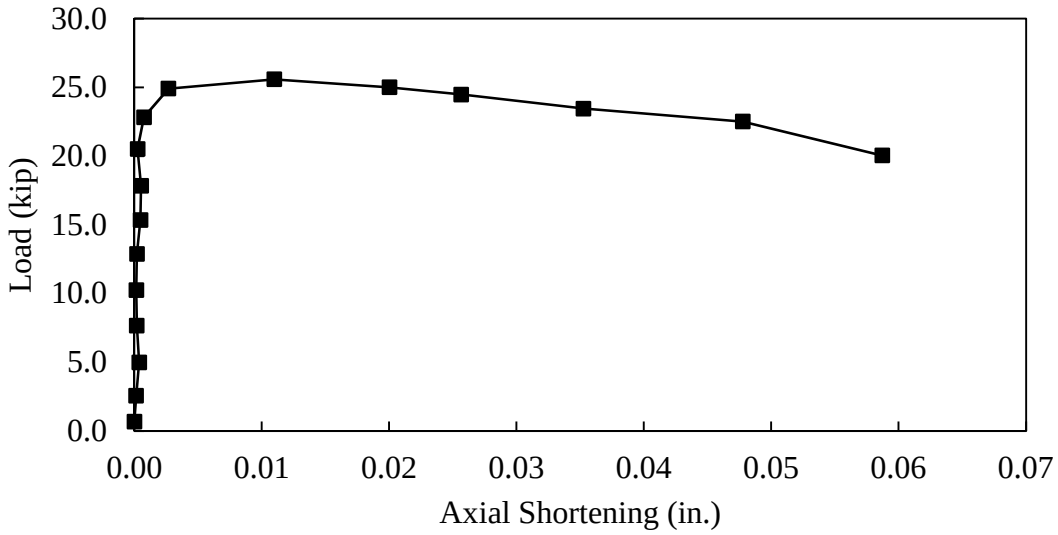

Figure B.6- Load-shortening curve, L2-36b

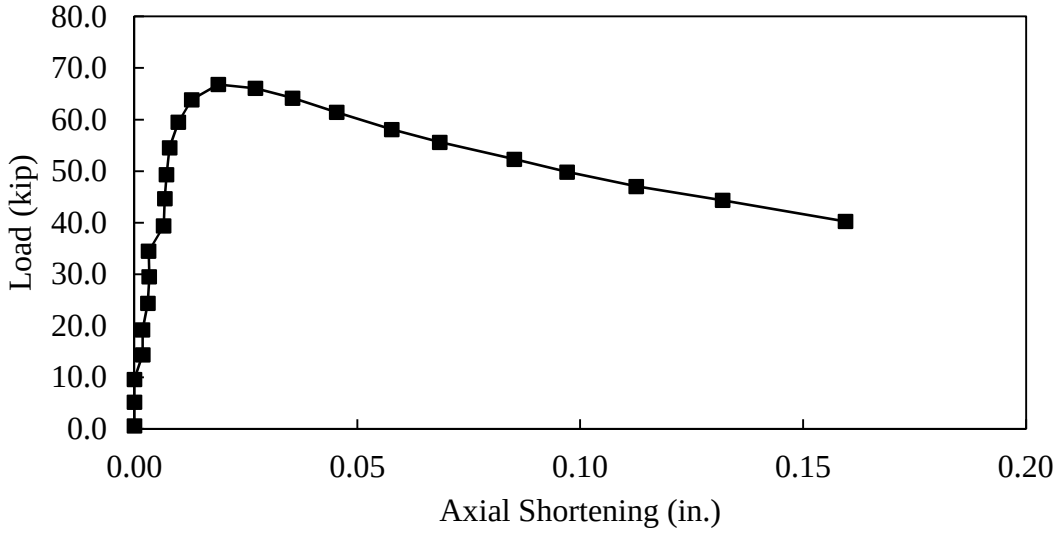

Figure B.7- Load-shortening curve, L3-36

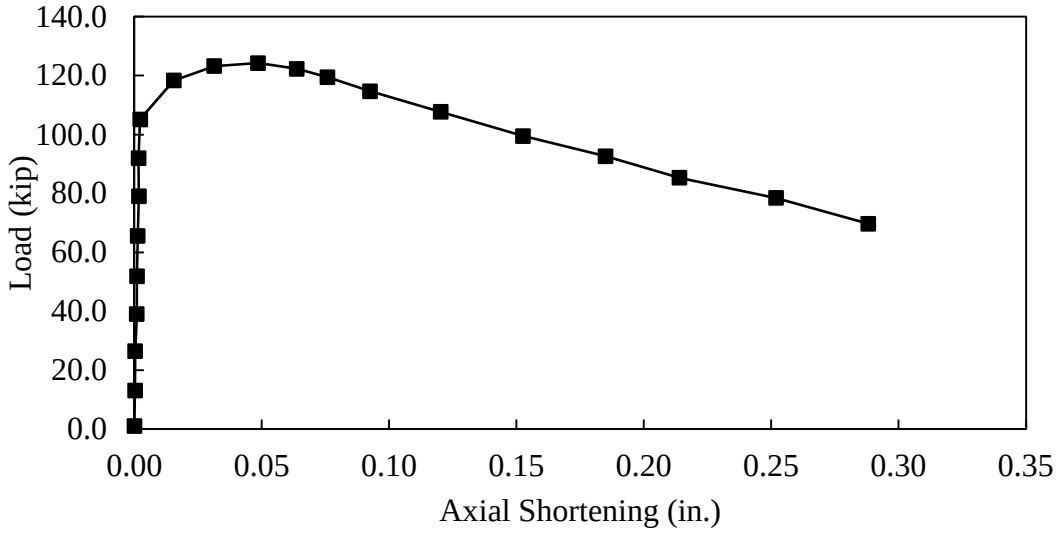

Figure B.8- Load-shortening curve, L4-36a

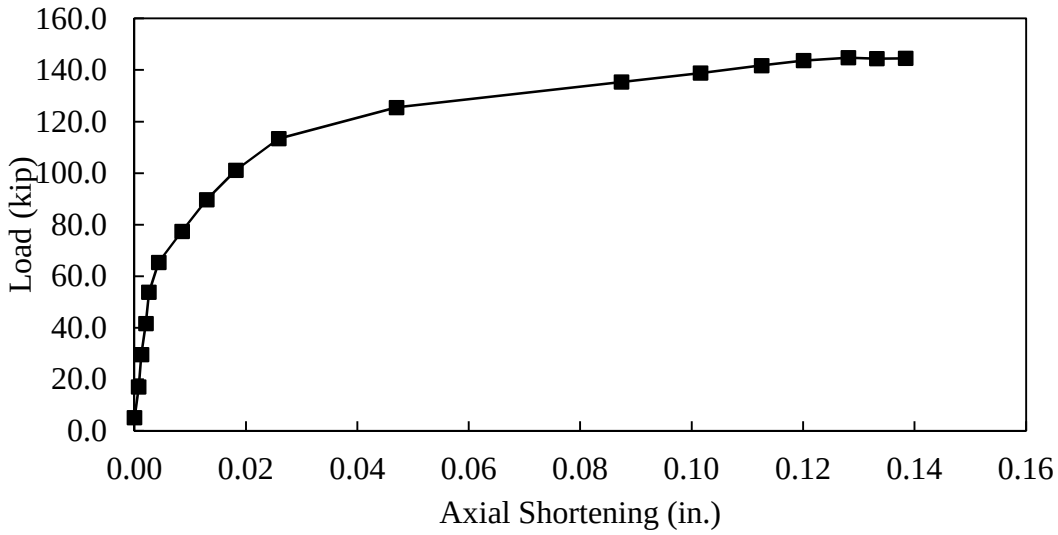

Figure B.9- Load-shortening curve, L4-36b

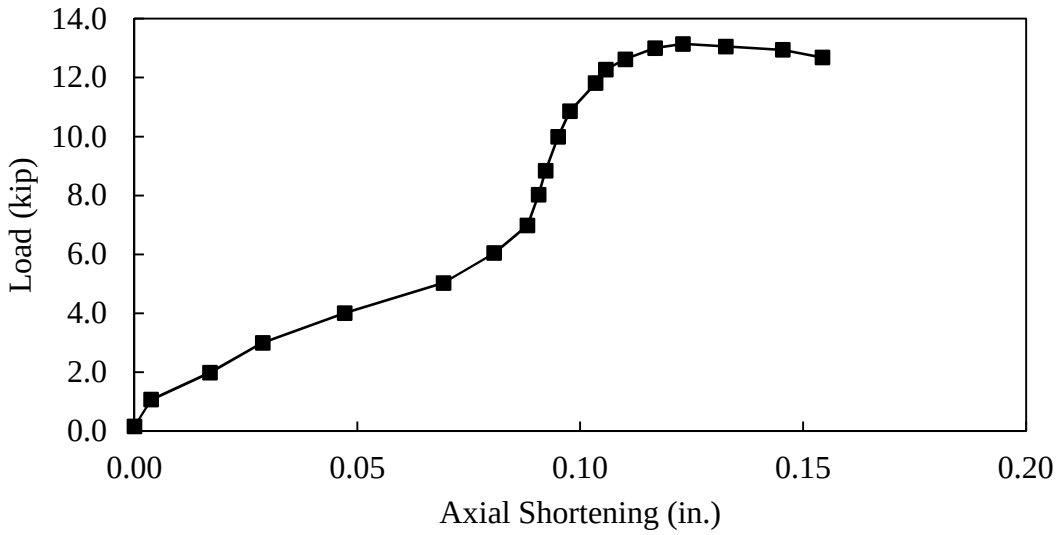

Figure B.10- Load-shortening curve, L2-48

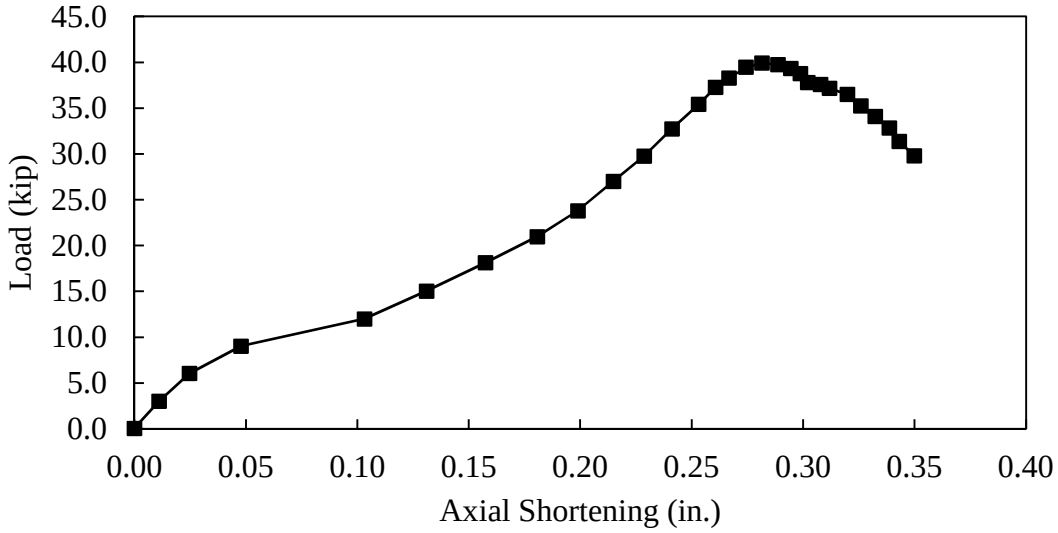

Figure B.11- Load-shortening curve, L3-48a

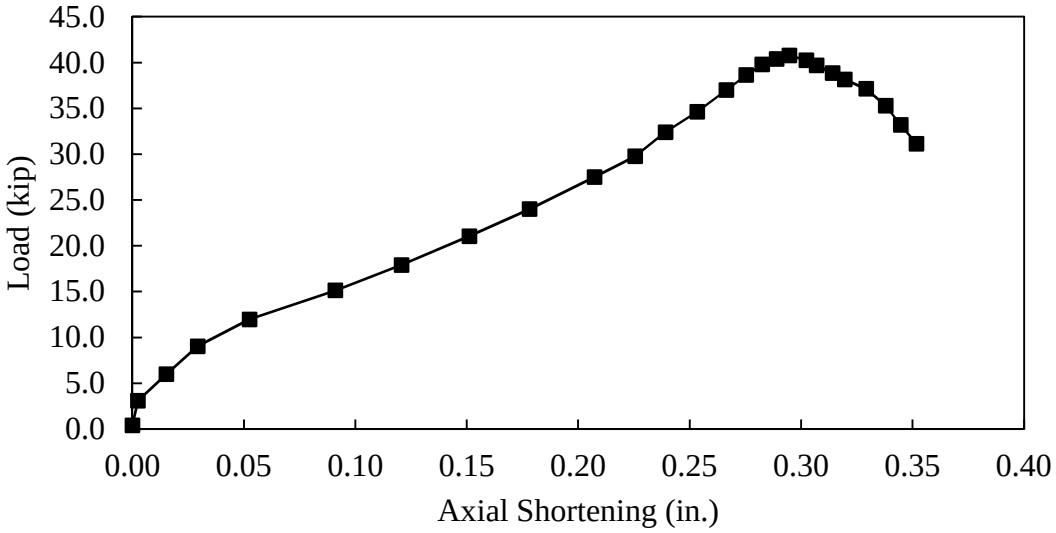

Figure B.12- Load-shortening curve, L3-48b

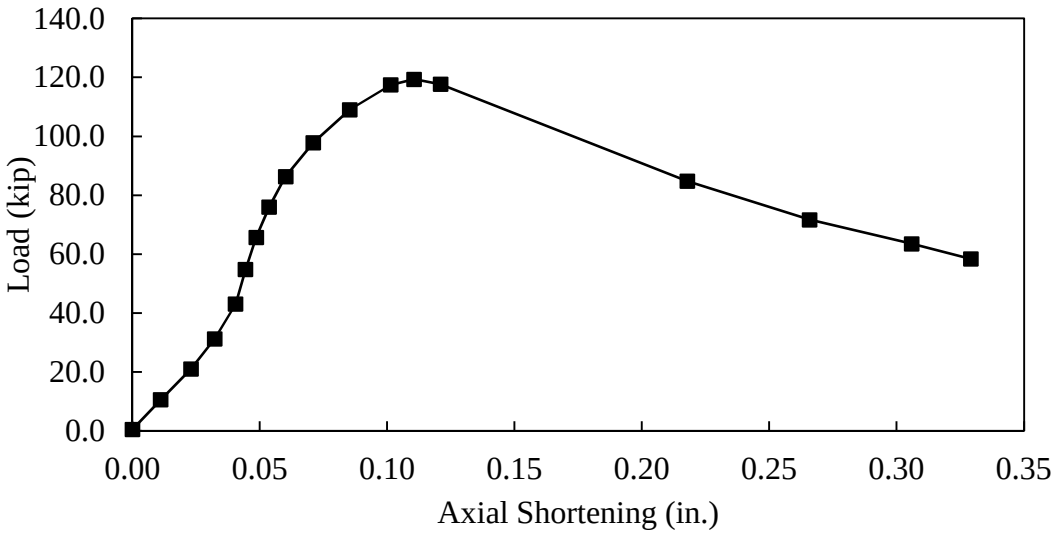

Figure B.13- Load-shortening curve, L4-48

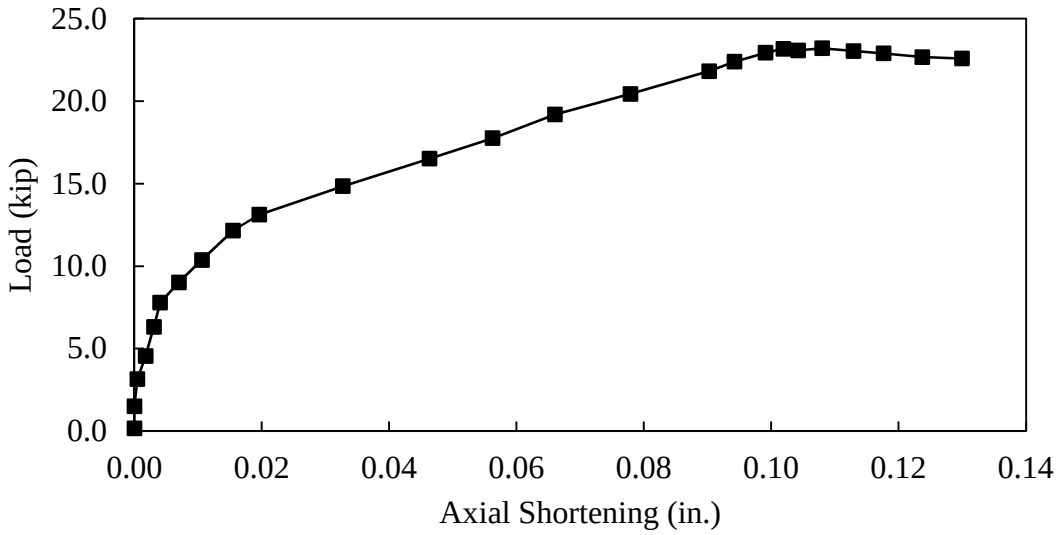

Figure B.14- Load-shortening curve, L2-60a

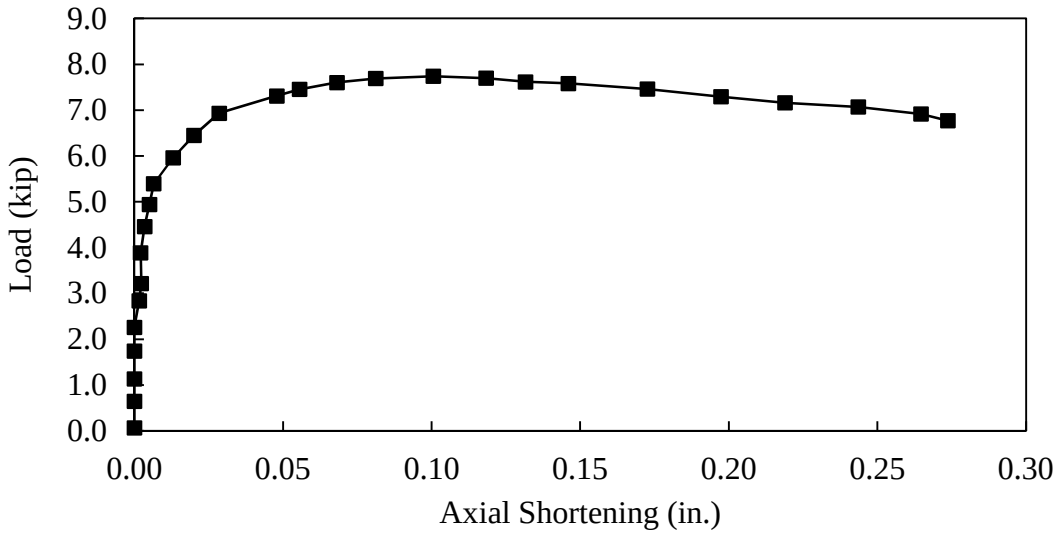

Figure B.15- Load-shortening curve, L2-60b

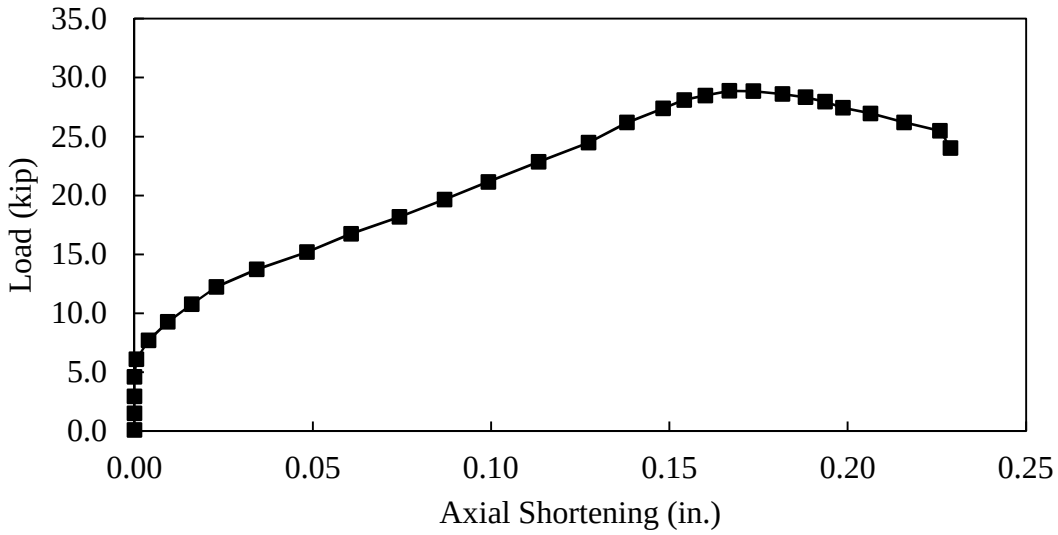

Figure B.16- Load-shortening curve, L3-60a

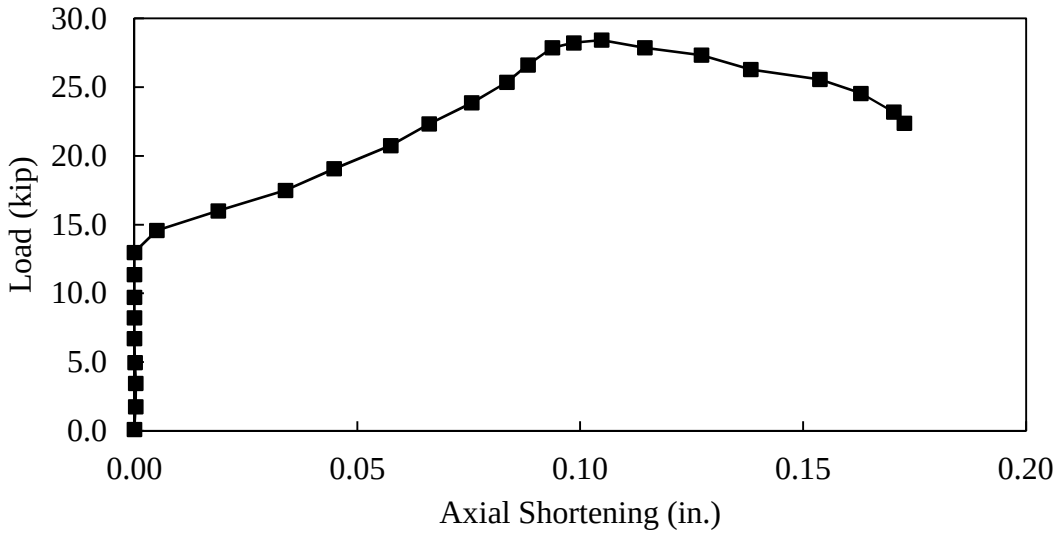

Figure B.17- Load-shortening curve, L3-60b

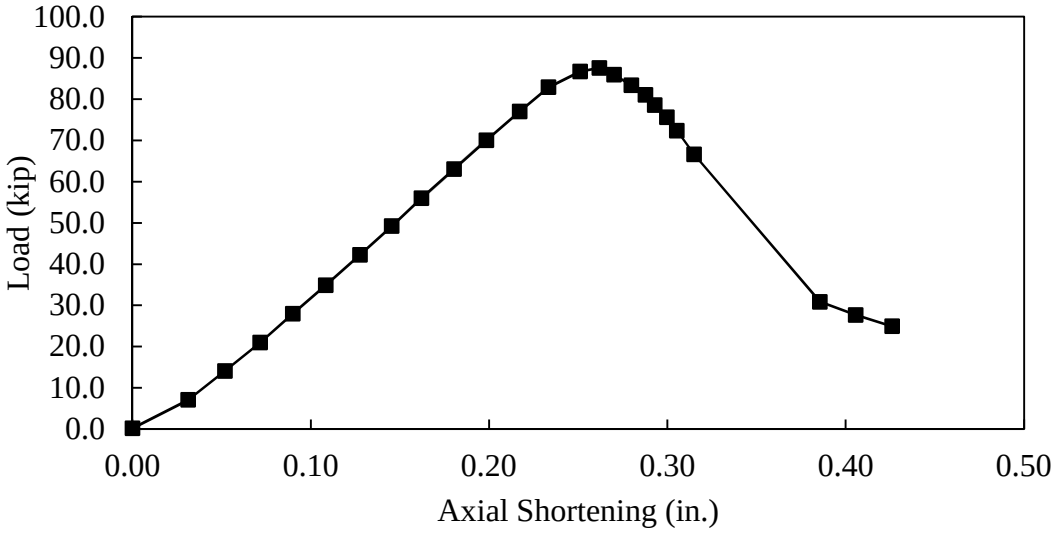

Figure B.18- Load-shortening curve, L4-60a

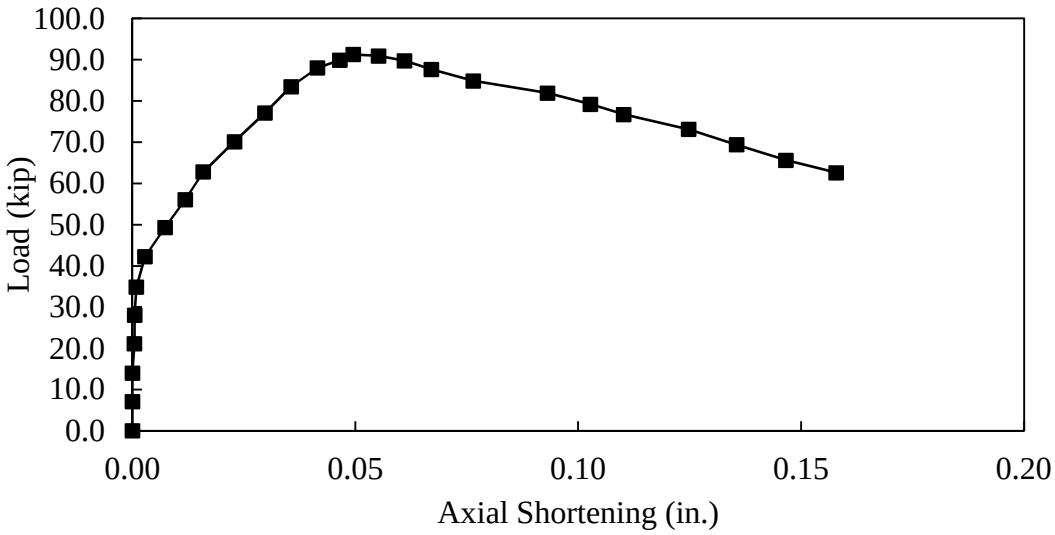

Figure B.19- Load-shortening curve, L4-60b

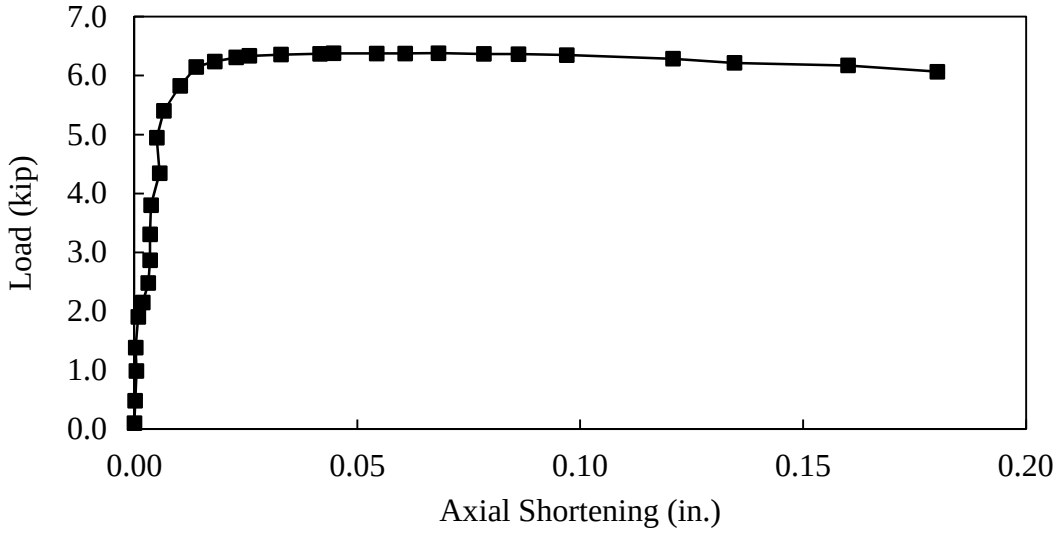

Figure B.20- Load-shortening curve, L2-72

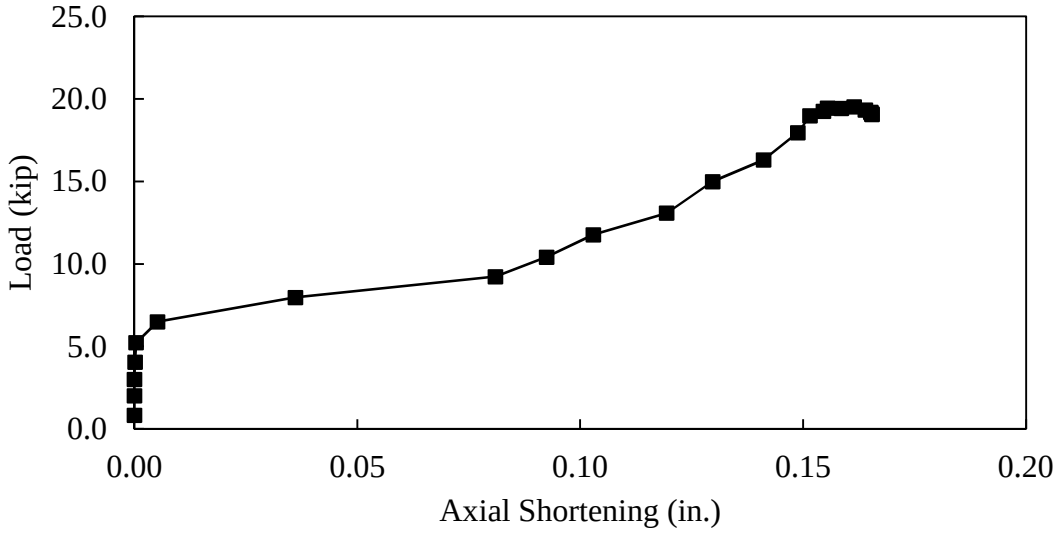

Figure B.21- Load-shortening curve, L3-72

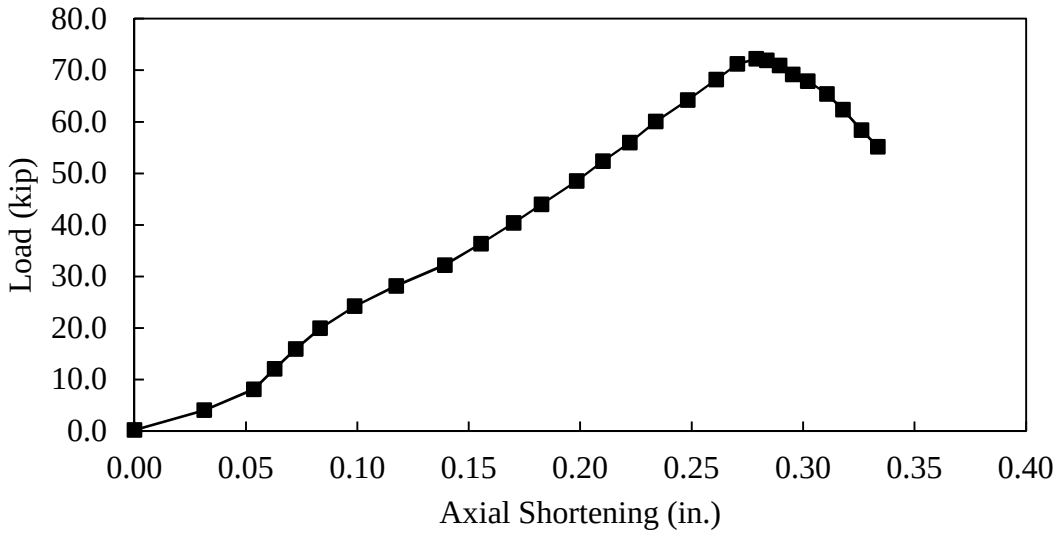

Figure B.22- Load-shortening curve, L4-72

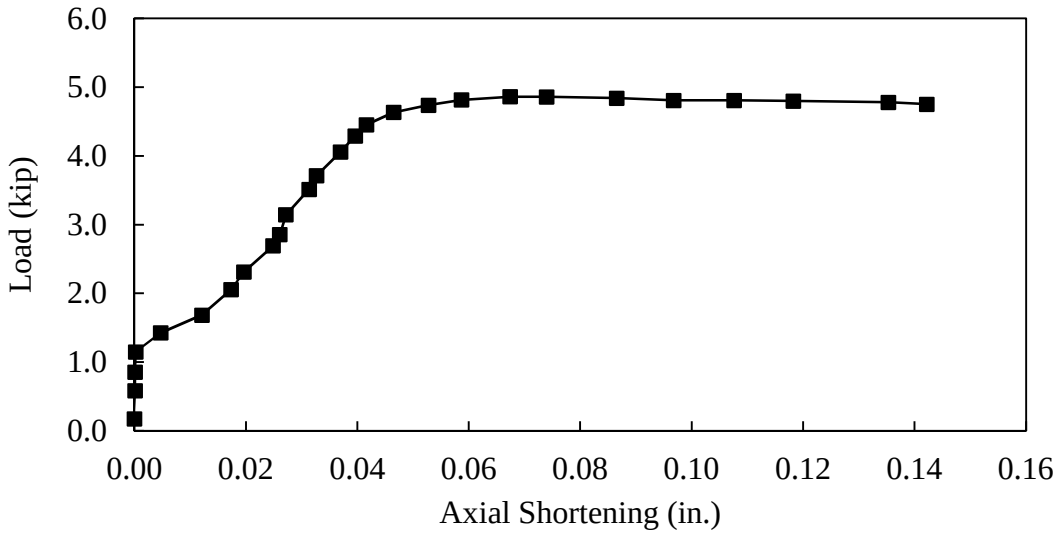

Figure B.23- Load-shortening curve, L2-84

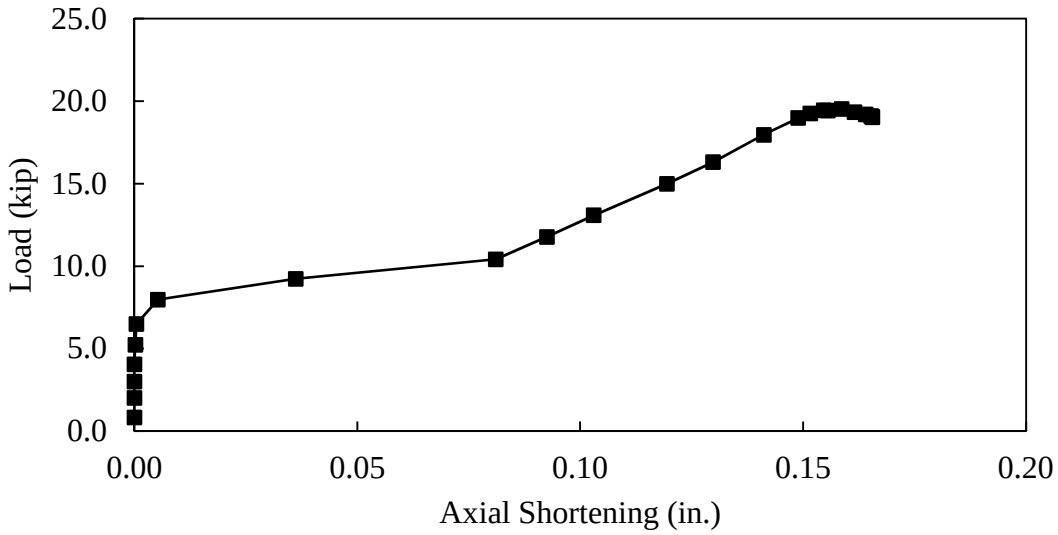

Figure B.24- Load-shortening curve, L3-84

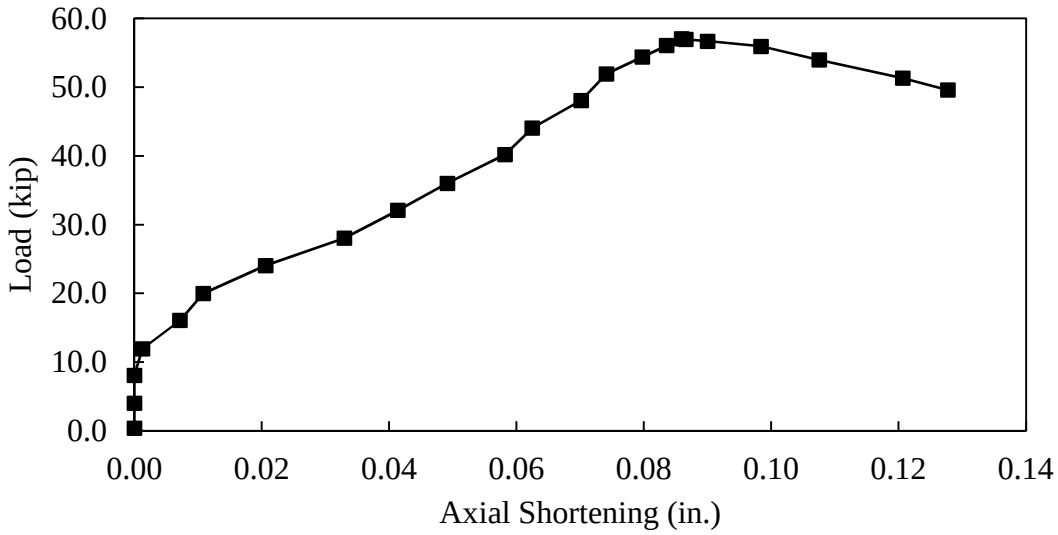

Figure B.25- Load-shortening curve, L4-84

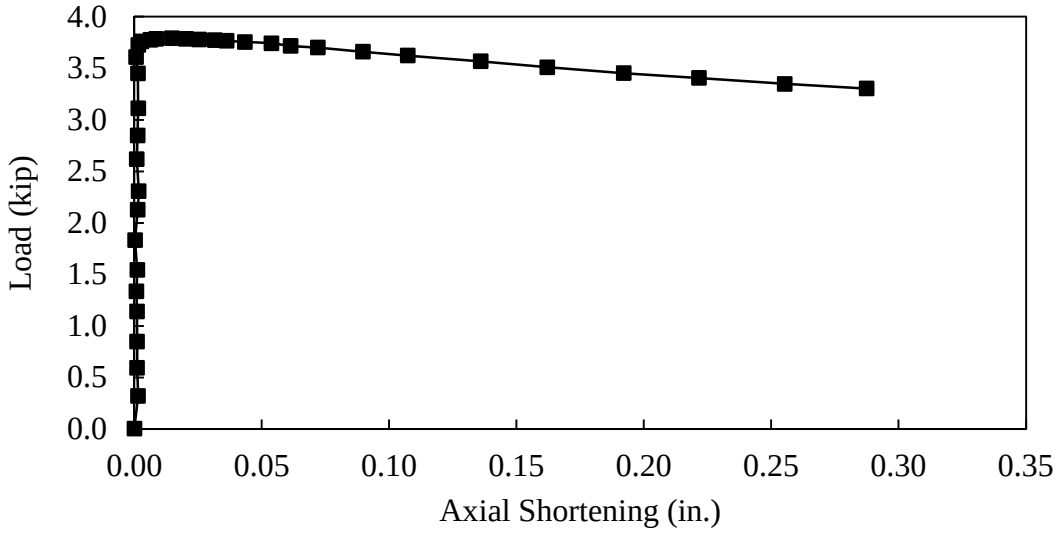

Figure B.26- Load-shortening curve, L2-96

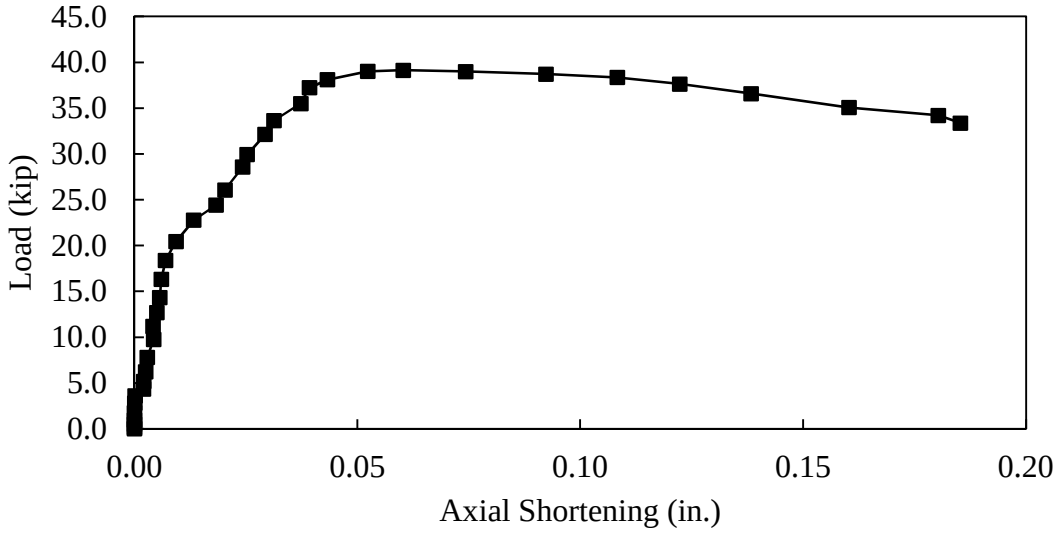

Figure B.27- Load-shortening curve, L4-96

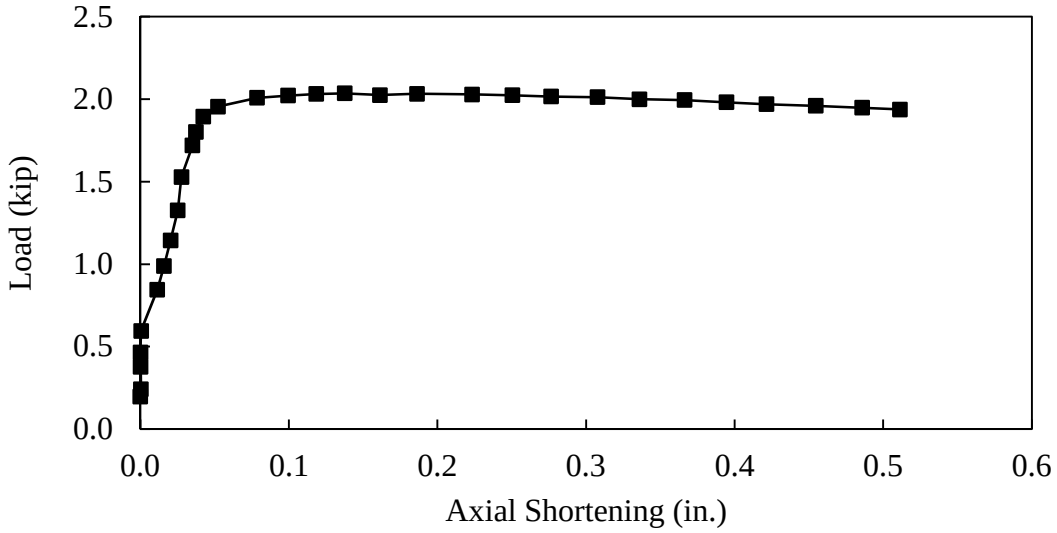

Figure B.28- Load-shortening curve, L2-132

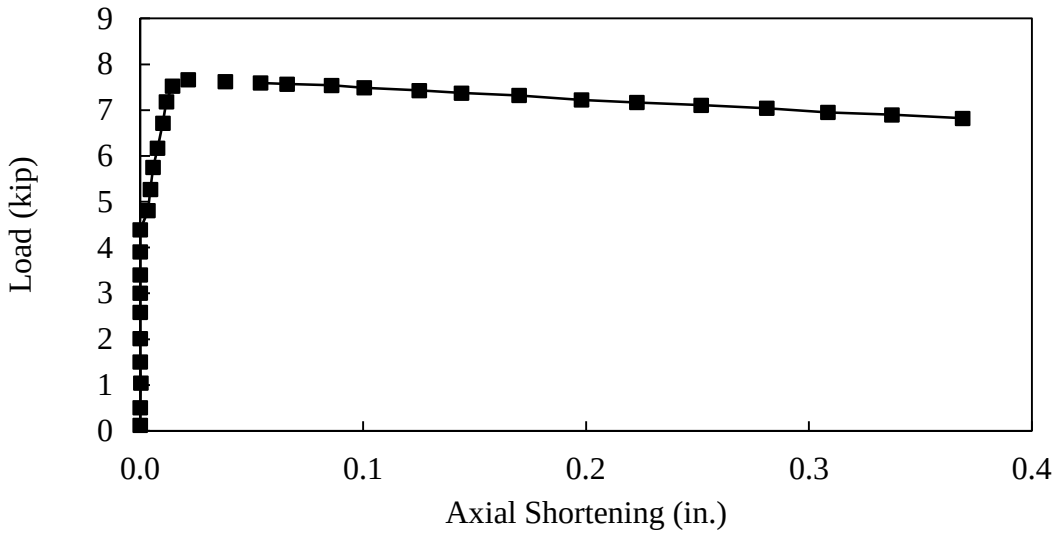

Figure B.29- Load-shortening curve, L3-132

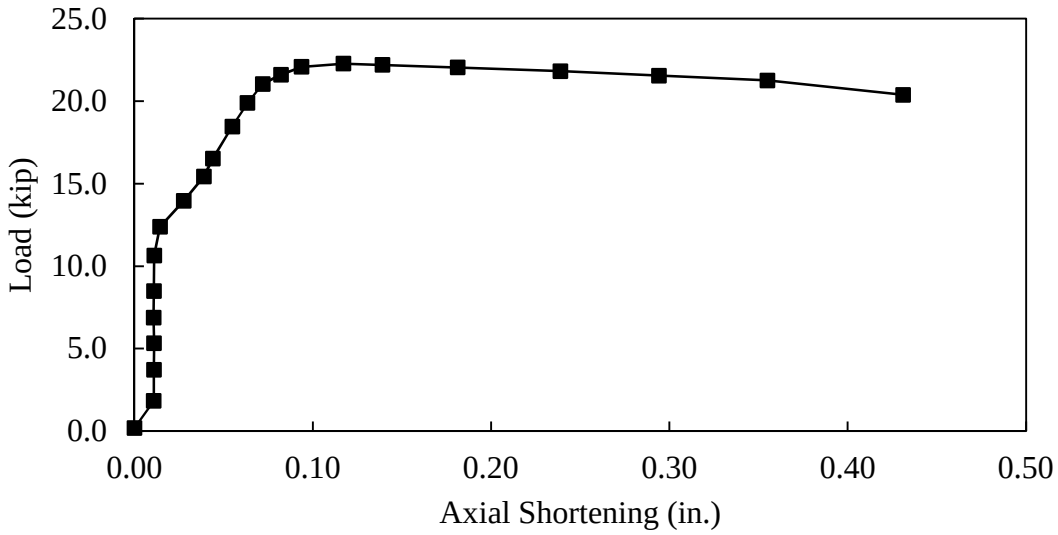

Figure B.30- Load-shortening curve, L4-132

Southwell Plots

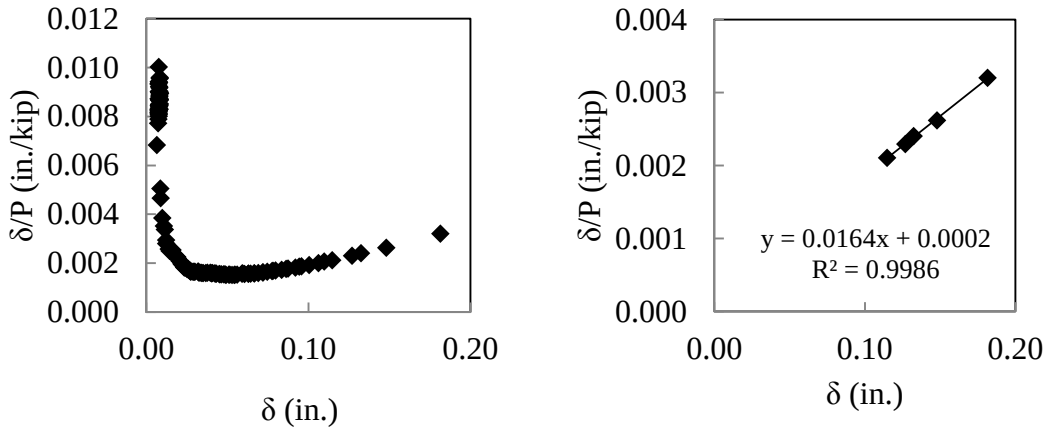

Figure B.1- Southwell-plot, L2-18a; Prebuckling data (left), Regression data (right)

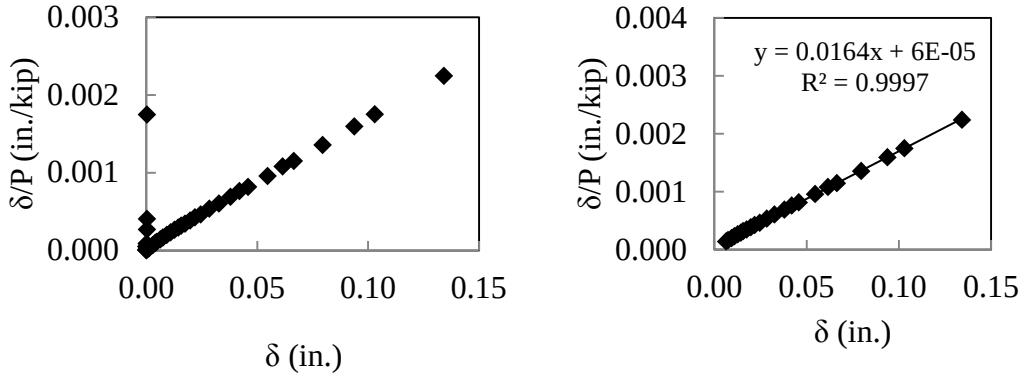

Figure B.2- Southwell-plot, L2-18b; Prebuckling data (left), Regression data (right)

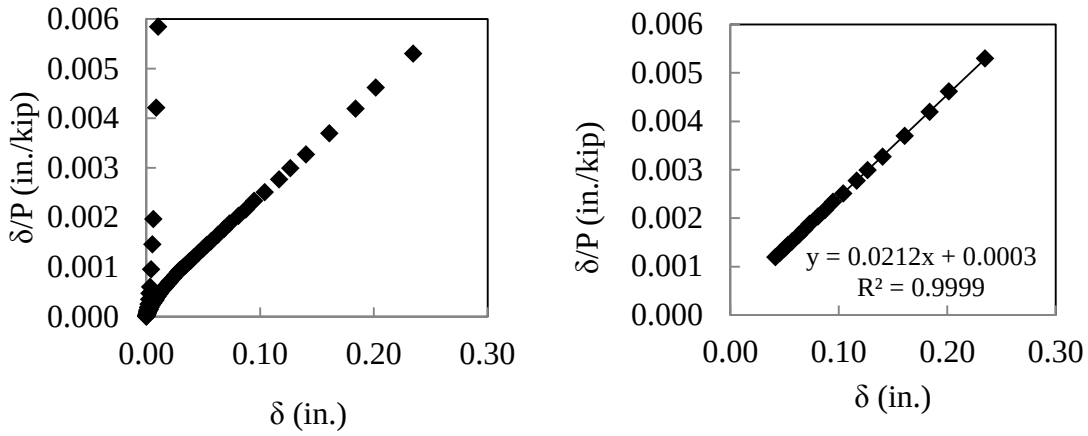

Figure B.3- Southwell-plot, L2-24; Prebuckling data (left), Regression data (right)

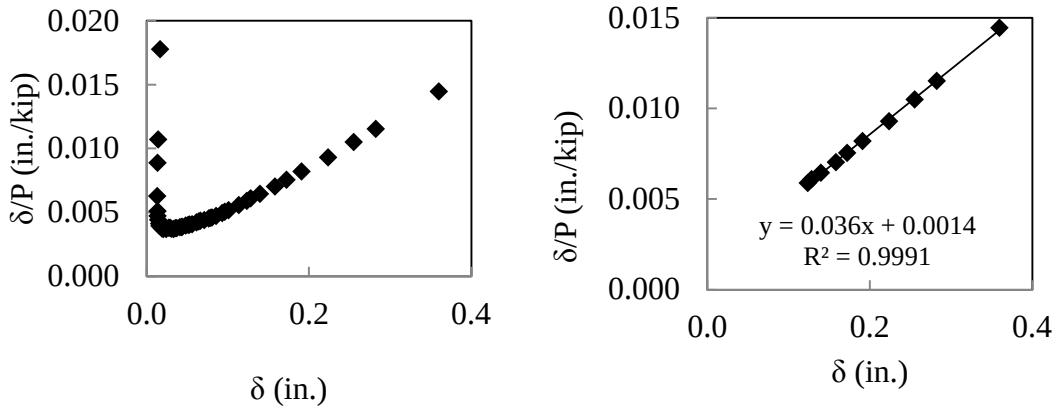

Figure B.4- Southwell-plot, L2-36a; Prebuckling data (left), Regression data (right)

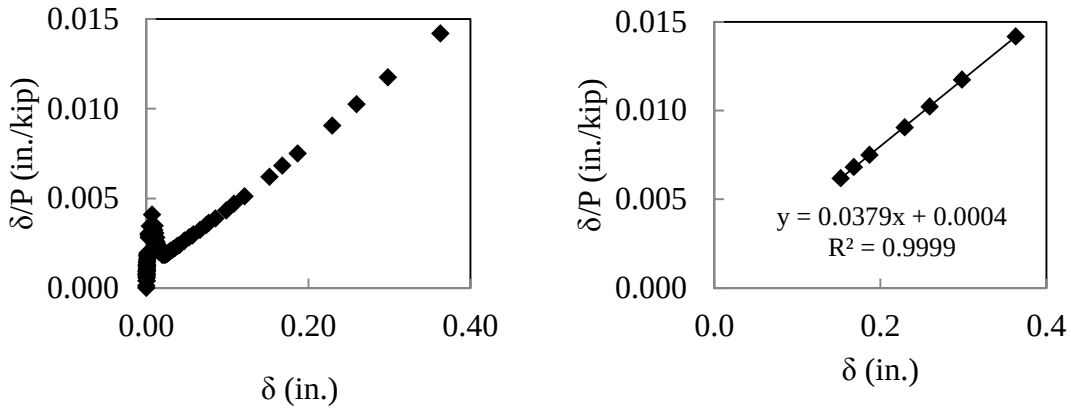

Figure B.5- Southwell-plot, L2-36b; Prebuckling data (left), Regression data (right)

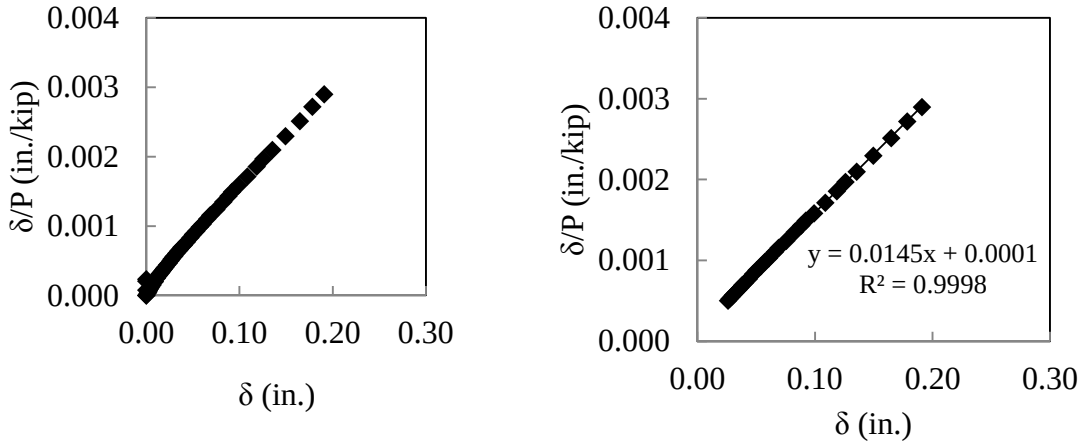

Figure B.6- Southwell-plot, L3-36; Prebuckling data (left), Regression data (right)

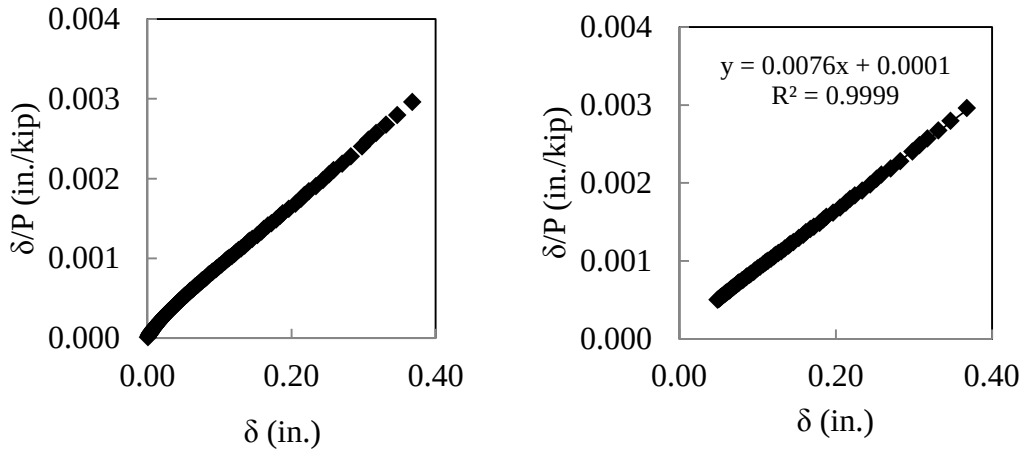

Figure B.7- Southwell-plot, L4-36a; Prebuckling data (left), Regression data (right)

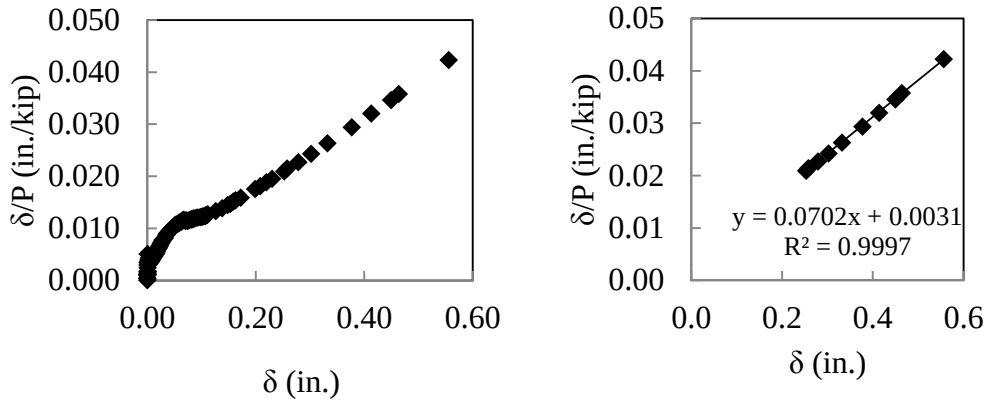

Figure B.8- Southwell-plot, L2-48; Prebuckling data (left), Regression data (right)

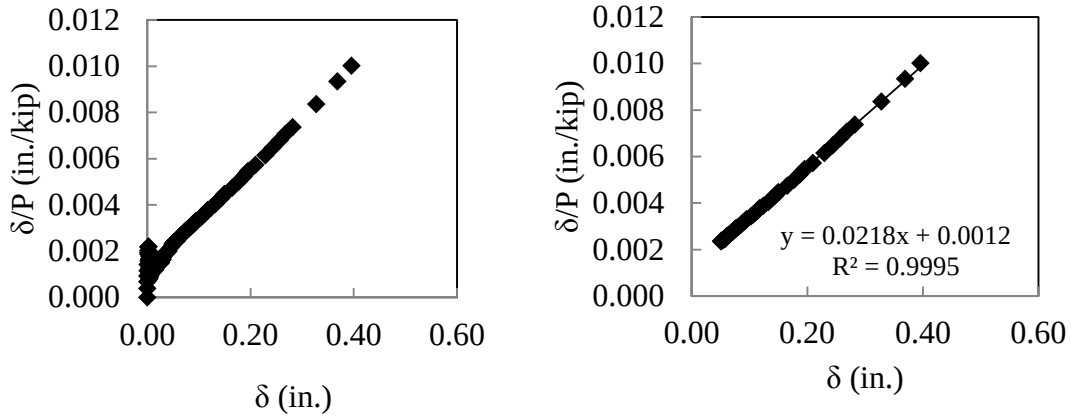

Figure B.9- Southwell-plot, L3-48a; Prebuckling data (left), Regression data (right)

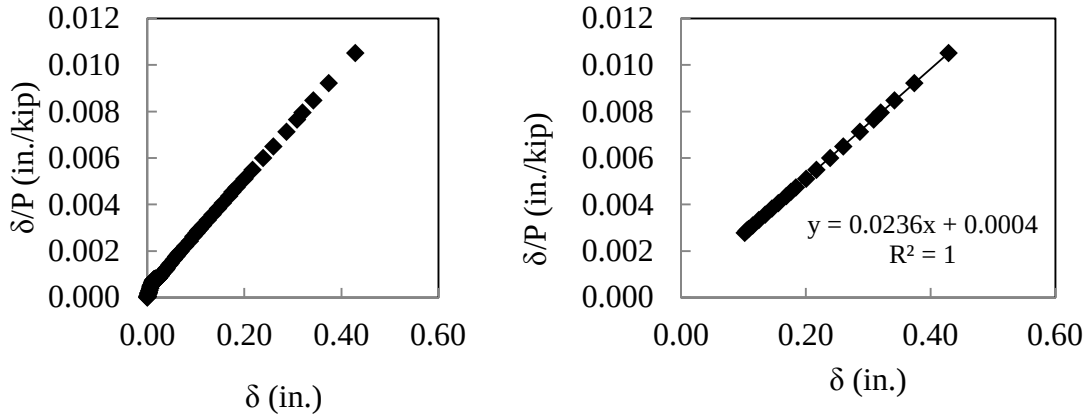

Figure B.10- Southwell-plot, L3-48b; Prebuckling data (left), Regression data (right)

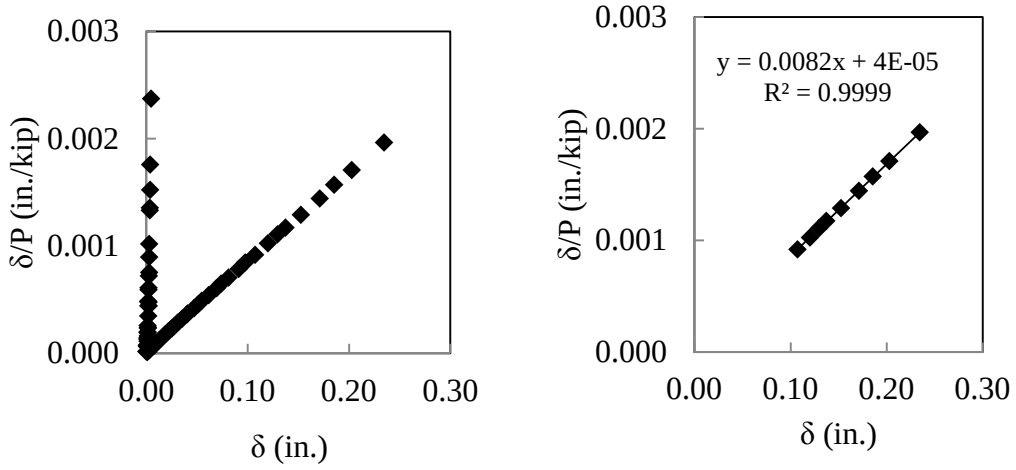

Figure B.11- Southwell-plot, L4-48; Prebuckling data (left), Regression data (right)

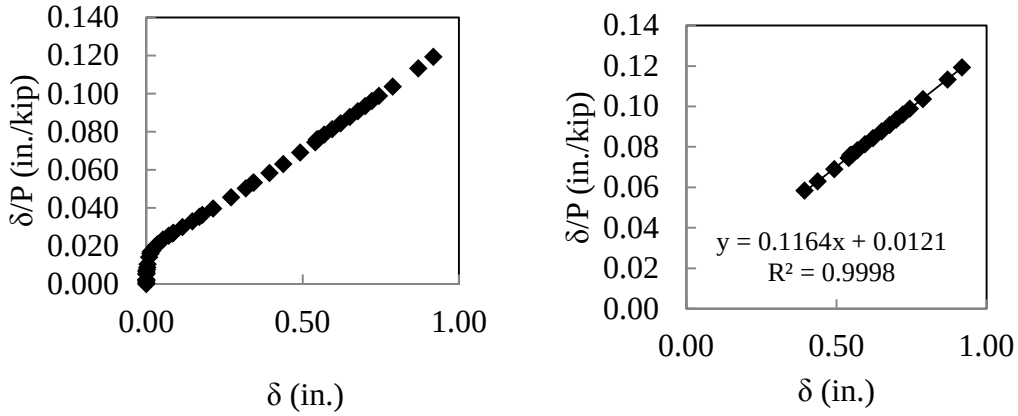

Figure B.12- Southwell-plot, L2-60a; Prebuckling data (left), Regression data (right)

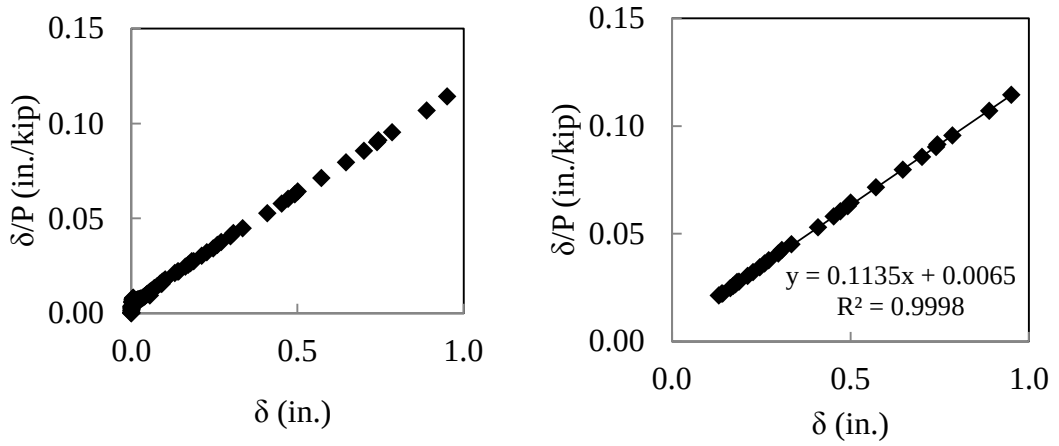

Figure B.13- Southwell-plot, L2-60b; Prebuckling data (left), Regression data (right)

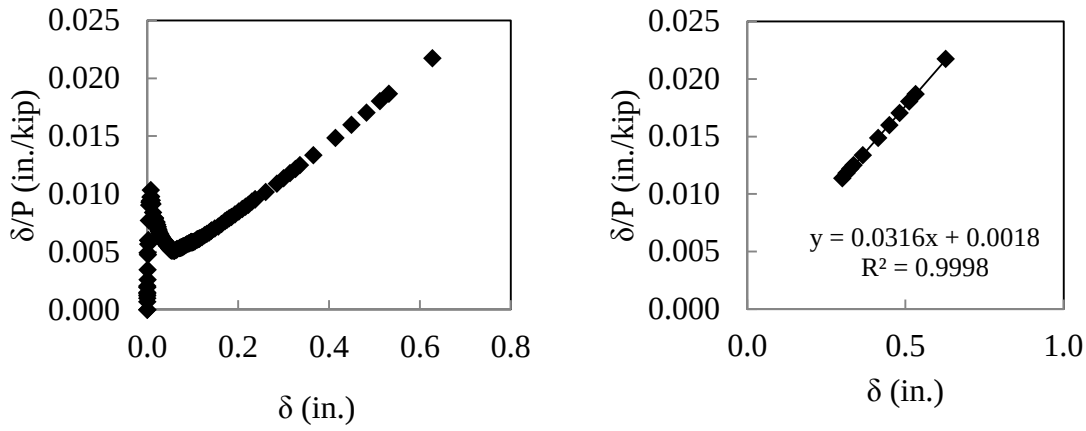

Figure B.14- Southwell-plot, L3-60a; Prebuckling data (left), Regression data (right)

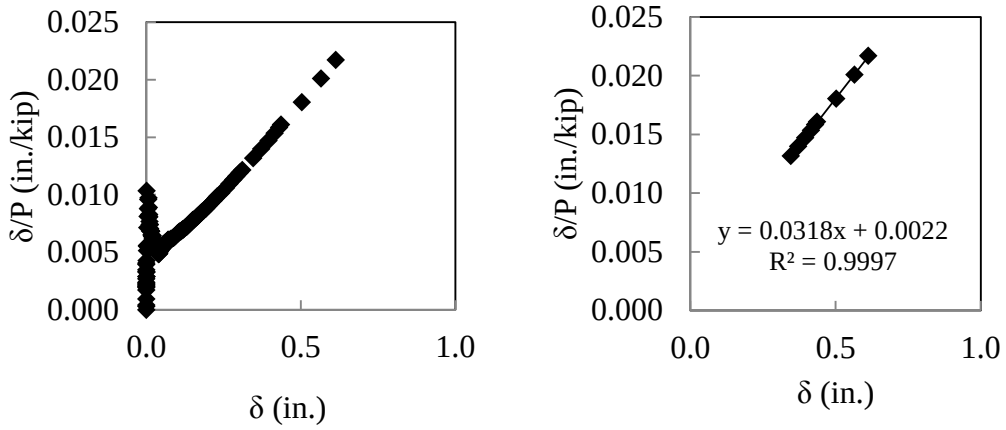

Figure B.15- Southwell-plot, L3-60b; Prebuckling data (left), Regression data (right)

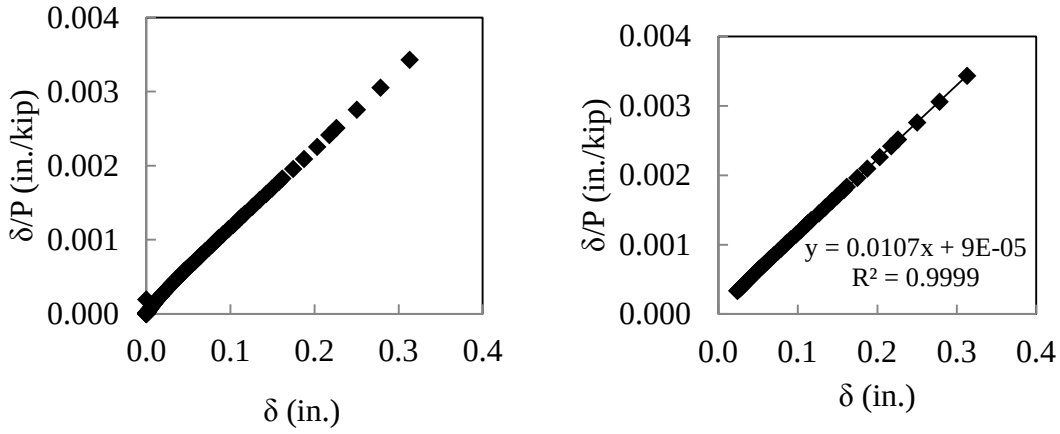

Figure B.16- Southwell-plot, L4-60a; Prebuckling data (left), Regression data (right)

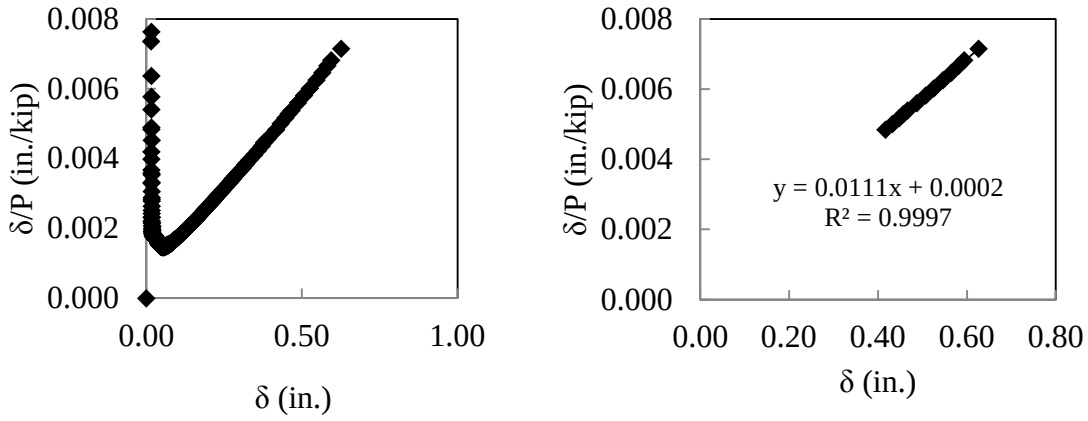

Figure B.17- Southwell-plot, L4-60b; Prebuckling data (left), Regression data (right)

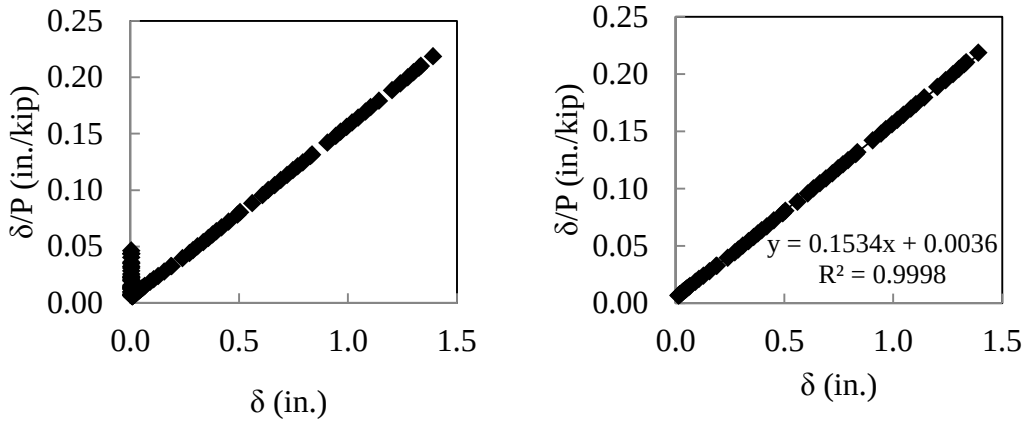

Figure B.18- Southwell-plot, L2-72; Prebuckling data (left), Regression data (right)

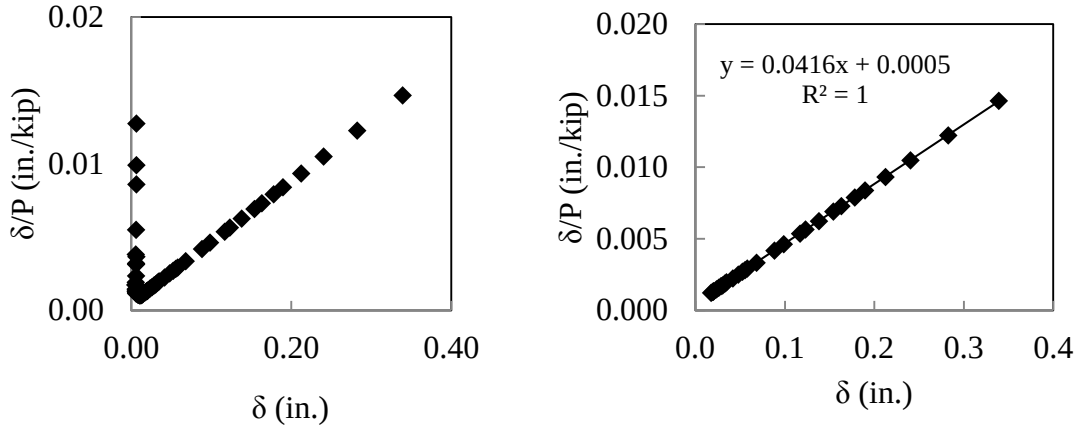

Figure B.19- Southwell-plot, L3-72; Prebuckling data (left), Regression data (right)

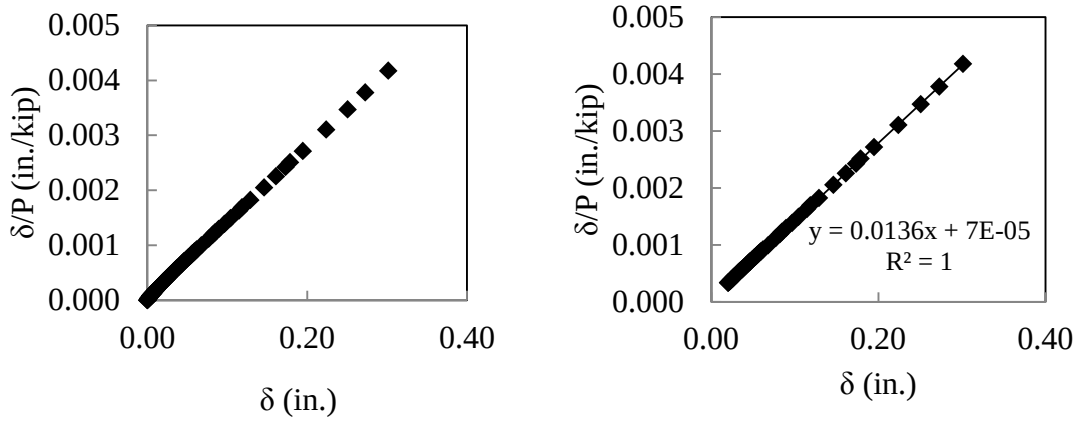

Figure B.20- Southwell-plot, L4-72; Prebuckling data (left), Regression data (right)

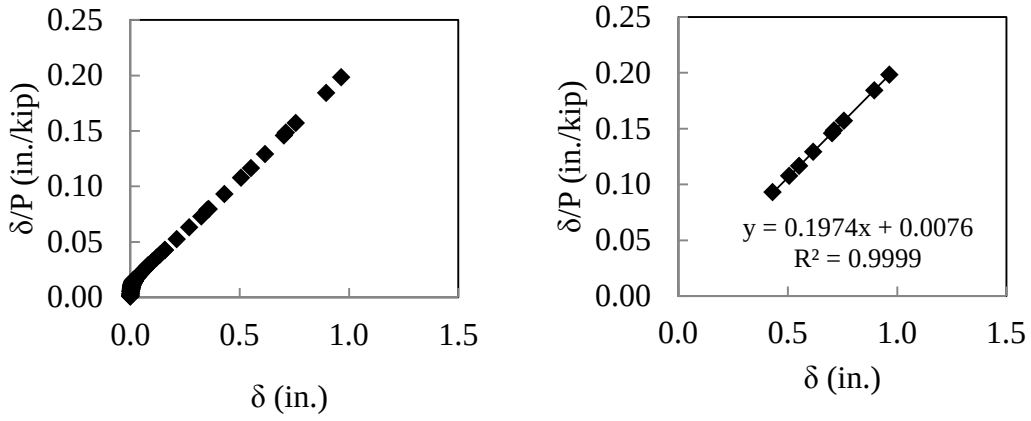

Figure B.21- Southwell-plot, L2-84; Prebuckling data (left), Regression data (right)

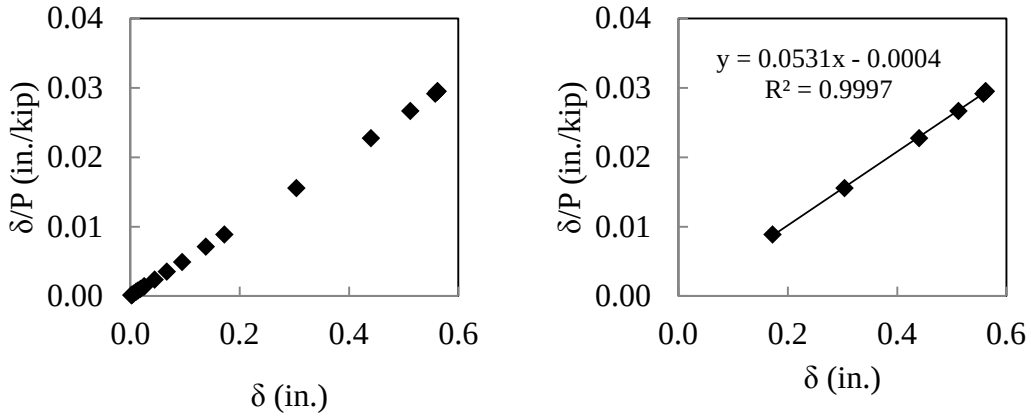

Figure B.22- Southwell-plot, L3-84; Prebuckling data (left), Regression data (right)

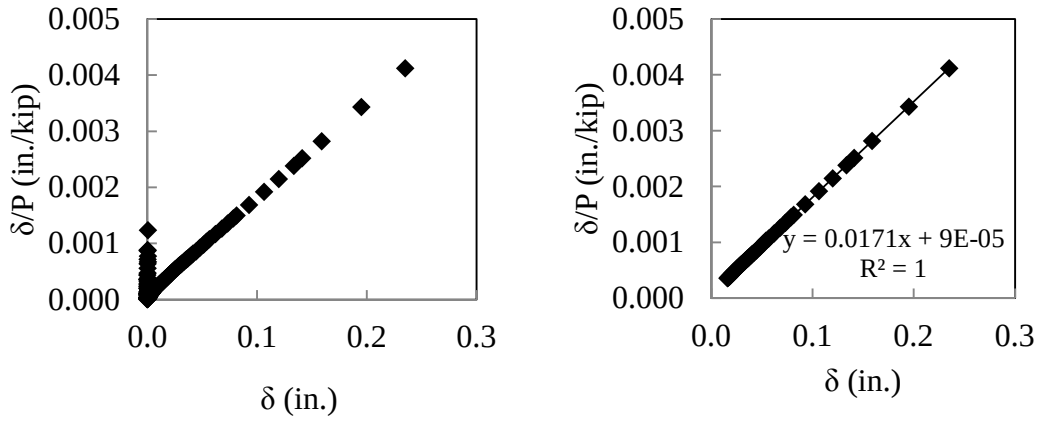

Figure B.23- Southwell-plot, L4-84; Prebuckling data (left), Regression data (right)

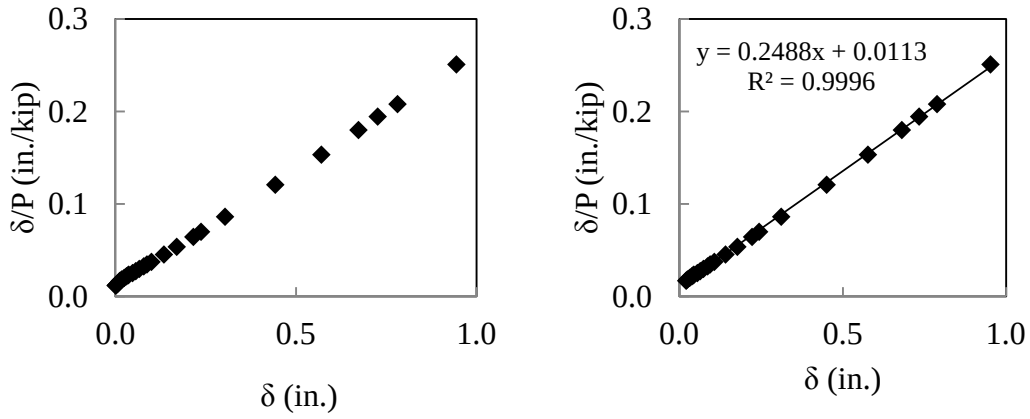

Figure B.24- Southwell-plot, L2-96; Prebuckling data (left), Regression data (right)

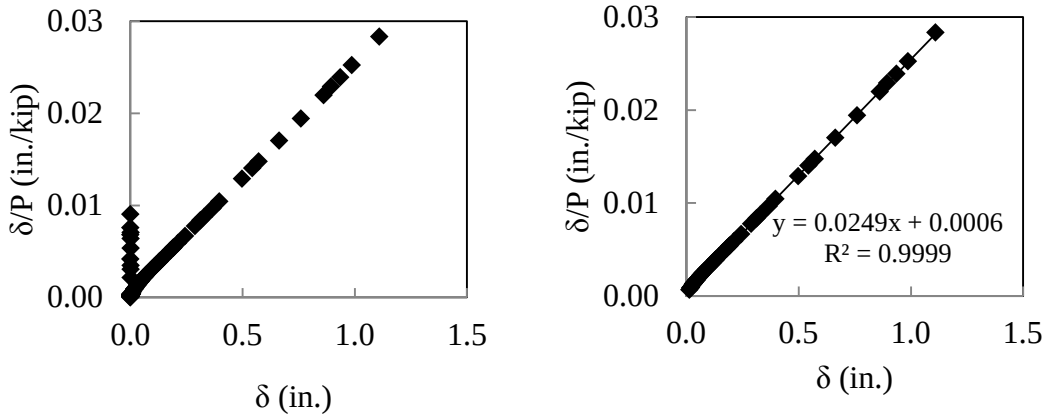

Figure B.25- Southwell-plot, L4-96; Prebuckling data (left), Regression data (right)

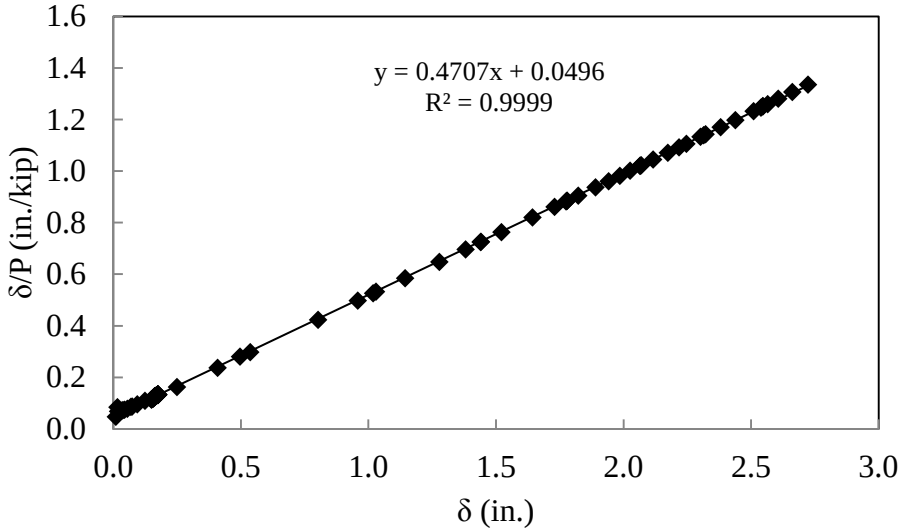

Figure B.26- Southwell-plot, L2-132

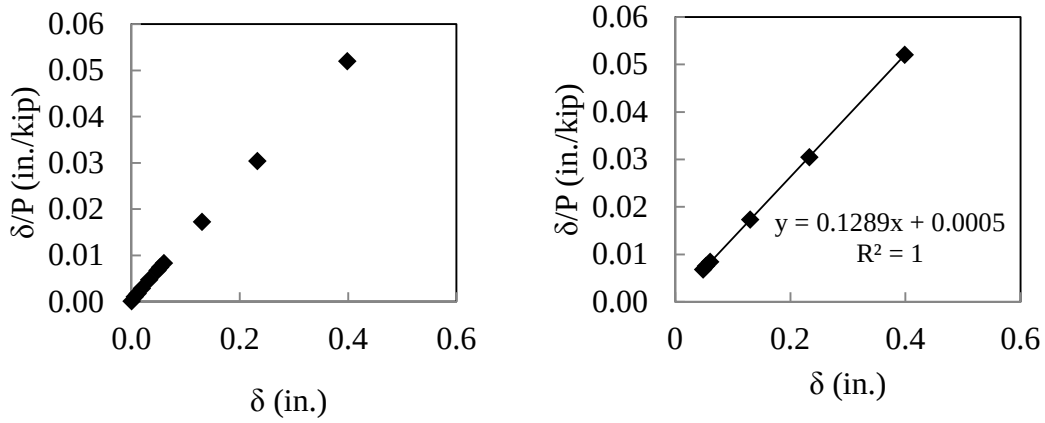

Figure B.27- Southwell-plot, L3-132; Prebuckling data (left), Regression data (right)

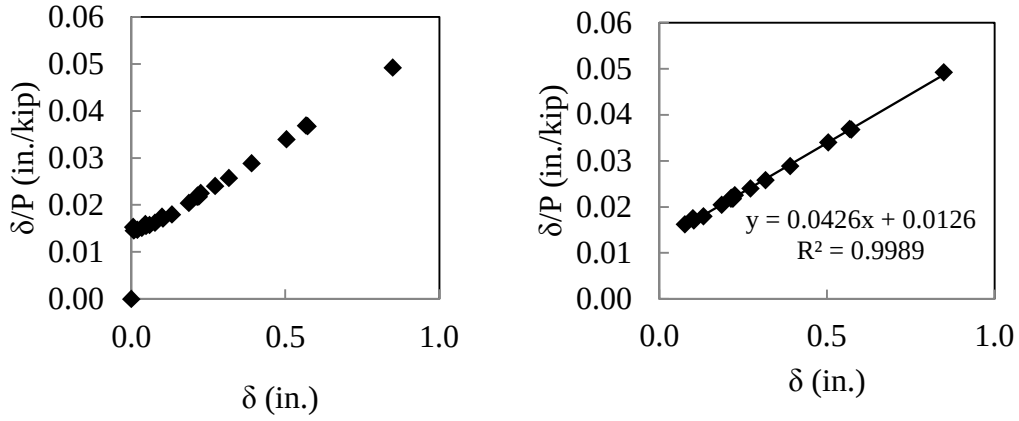

Figure B.28- Southwell-plot, L4-132; Prebuckling data (left), Regression data (right)

APPENDIX C

FINITE ELEMENT ANALYSES

Modeling Sensitivity Studies

Convergence

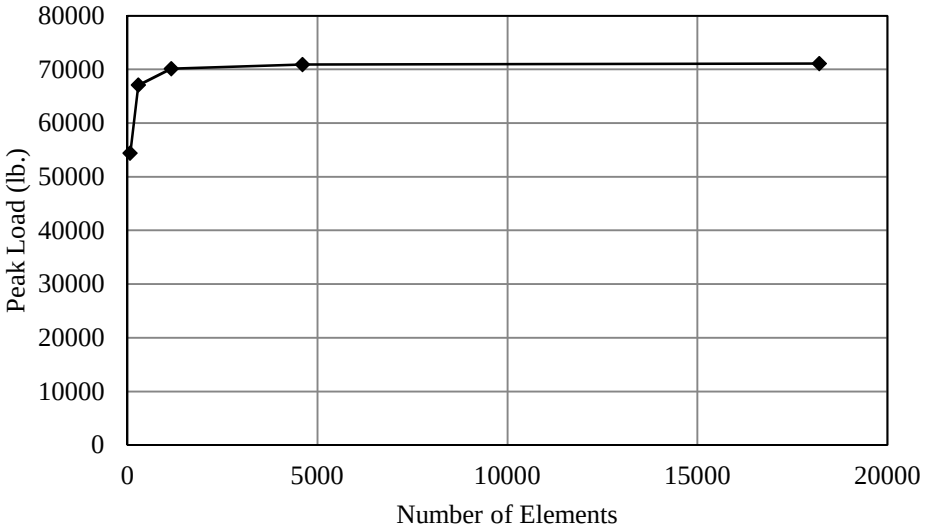

Figure C.1- Convergence study for L2-18 (Eigenvalue)

Table C.1- Convergence study for L2-18 (Eigenvalue)

Maximum Element Size (in.)	Number of Elements	Peak Load (lb.)	CPU Time (sec.)
1	72	54391	0.3
0.5	288	67059	0.7
0.25	1152	70137	2.2
0.125	4608	70896	9.6
0.0625	18205	71080	38.5

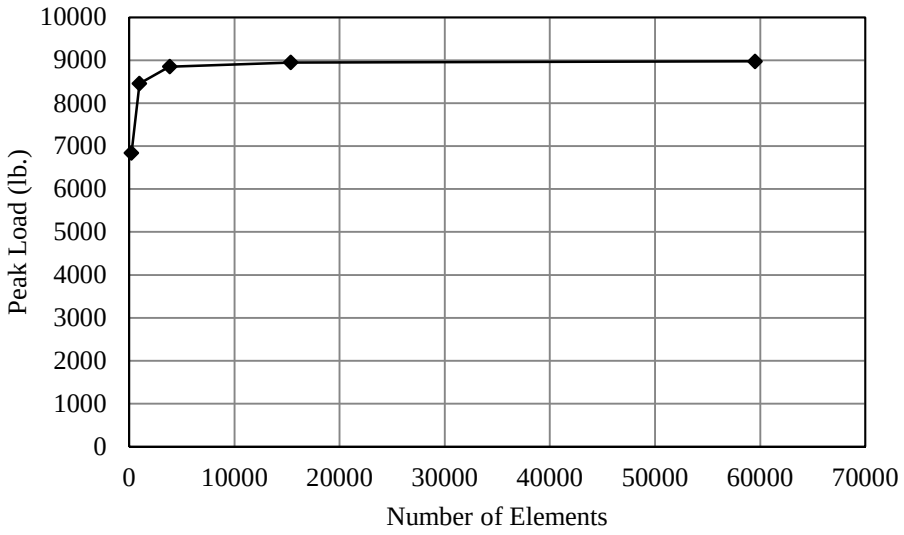

Figure C.2- Convergence study for L2-60 (Eigenvalue)

Table C.2- Convergence Study for L2-60 (Eigenvalue)

Maximum Element Size (in.)	Number of Elements	Peak Load (lb.)	CPU Time (sec.)
1	204	6839	0.6
0.5	960	8457	2.3
0.25	3840	8852	7.8
0.125	15360	8949	32.1
0.0625	59520	8973	132.3

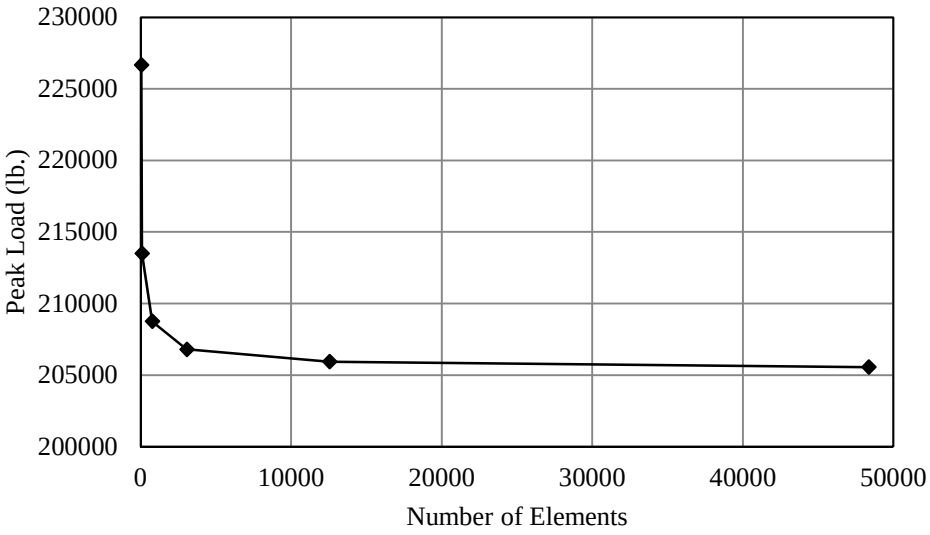

Figure C.3- Convergence study for L4-24 (Eigenvalue)

Table C.3- Convergence Study for L4-24 (Eigenvalue)

Maximum Element Size (in.)	Number of Elements	Peak Load (lb.)	CPU Time (sec.)
2	48	226675	0.3
1	96	213501	0.4
0.5	768	208757	1.5
0.25	3072	206802	5.6
0.125	12545	205934	27.0
0.0625	48384	205559	106.7

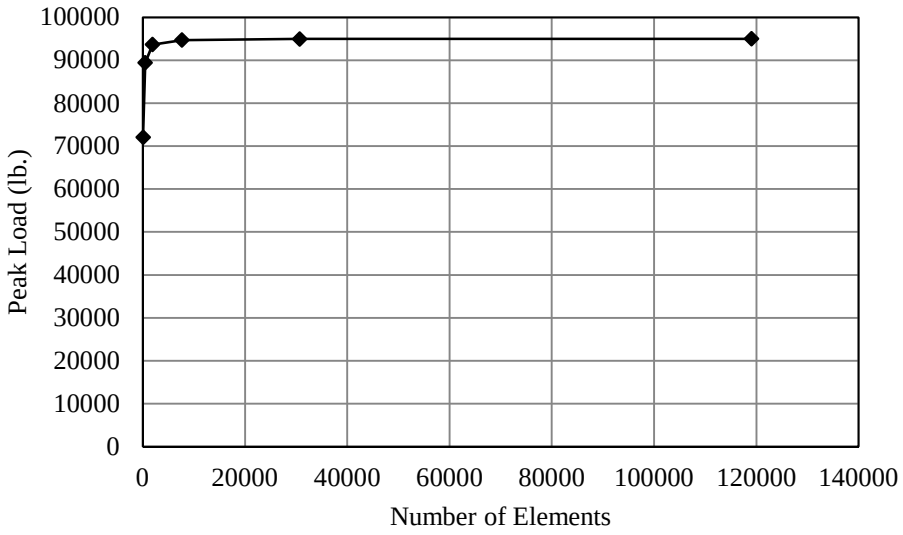

Figure C.4- Convergence study for L4-60 (Eigenvalue)

Table C.4- Convergence Study for L4-60 (Eigenvalue)

Maximum Element Size (in.)	Number of Elements	Peak Load (lb.)	CPU Time (sec.)
2	96	72028	0.5
1	480	89400	1.2
0.5	1920	93654	3.9
0.25	7680	94694	14.4
0.125	30720	94951	77.4
0.0625	119040	95015	350.4

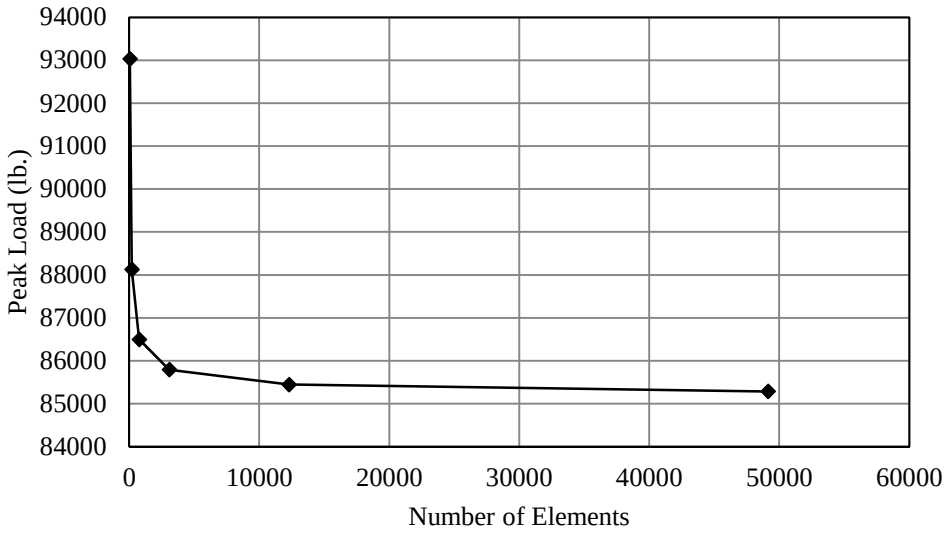

Figure C.5- Convergence study for L5-30 (Eigenvalue)

Table C.5- Convergence Study for L5-30 (Eigenvalue)

Maximum Element Size (in.)	Number of Elements	Peak Load (lb.)	CPU Time (sec.)
2.5	48	93030	0.3
1.25	192	88126	0.6
0.625	768	86496	2.5
0.3125	3072	85791	6.8
0.15625	12288	85445	30.8
0.078125	49152	85286	115.8

Arc-length sensitivity studies

Table C.6- Maximum arc-length sensitivity studies

Max.Arc-Length Increment	L2-18		L2-132		L4-24		L4-60	
	P_{Peak} (lb.)	CPU Time (s)	P_{Peak} (lb.)	CPU Time (s)	P_{Peak} (lb.)	CPU Time (s)	P_{Peak} (lb.)	CPU Time (s)
100,000	43239.9	264.4	1973.32	1242.6	134880	121.8	76519	317.8
10,000	43240.8	880.8	1973.32	1235.3	132727	1126.1	76538.2	3066.8

Through-thickness integration points

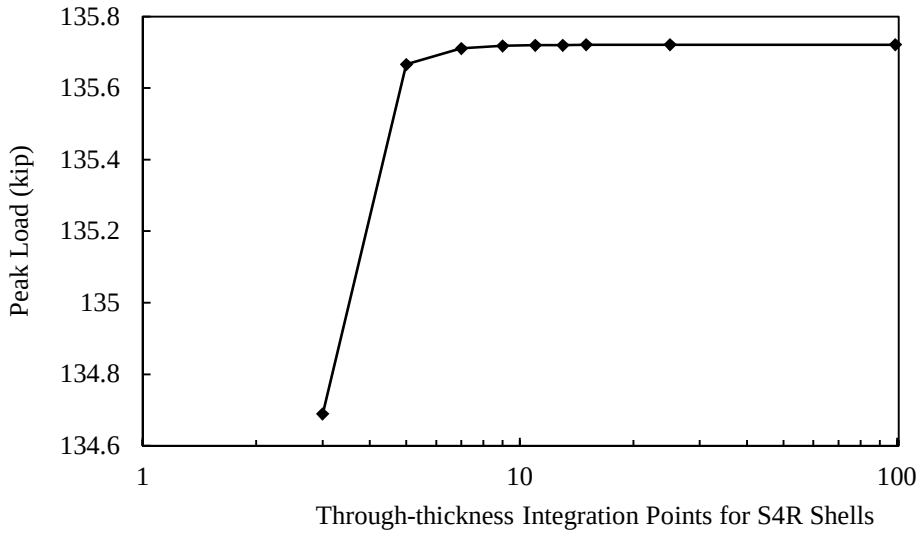

Figure C.6- Though-thickness integration points sensitivity study (L4-24)

Table C.7- Though-thickness integration points sensitivity study (L4-24)

No. of Through-thickness Integration Points	Peak Load (lb.)	CPU Time (sec.)
3	134.689	208.9
5	135.666	240.8
7	135.711	220.1
9	135.718	228.8
11	135.72	240.8
13	135.72	264.2
15	135.721	271.6
25	135.721	346.4
99	135.721	856.4

Table C.8- Material model sensitivity studies for L3¼ x 3¼ x ¼ (26 in.)

Material Model	Strength (kip)	Change in Strength
Orthotropic/Plane Stress, ν=0.24, G_o = 9830 ksi	85.77	--
Orthotropic/Plane Stress, ν=0.31, G_o = 9830 ksi	85.82	0.06%
Isotropic, ν=0.31	88.44	3.02%
Orthotropic/Plane Stress, ν=0.24, G_o = 10800 ksi	87.77	2.28%

Table C.9- Material model sensitivity studies for a L5⅛ x 5⅛ x ¼ (71.75 in.)

Material Model	Strength (kip)	Change in Strength
Orthotropic/Plane Stress, ν=0.24, G_o = 9830 ksi	57.87	--
Orthotropic/Plane Stress, ν=0.31, G_o = 9830 ksi	57.94	0.12%
Isotropic, ν=0.31	62.72	8.38%
Orthotropic/Plane Stress, ν=0.24, G_o = 10800 ksi	63.08	9.00%

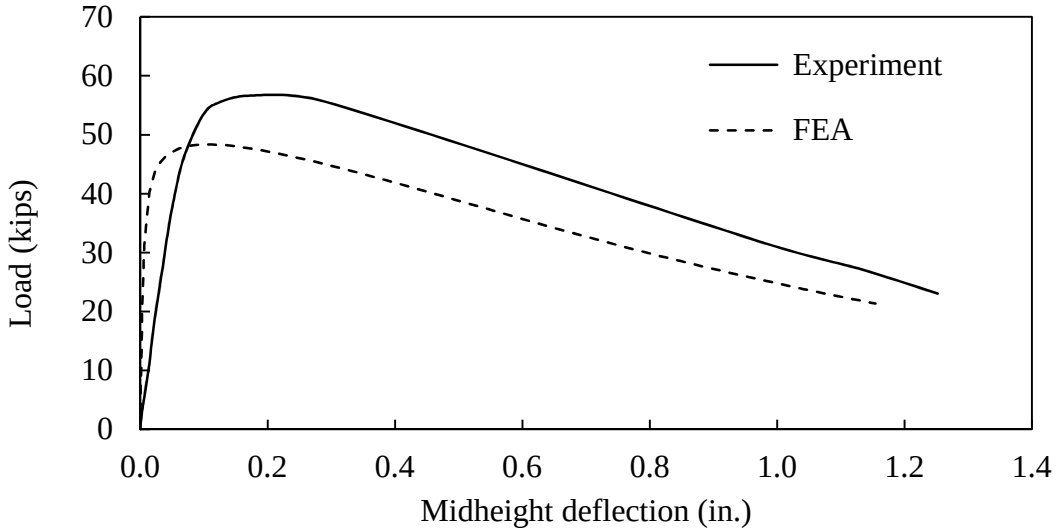

Figure C.7- Load-deflection comparison of experimental and numerical tests (L2-18a)

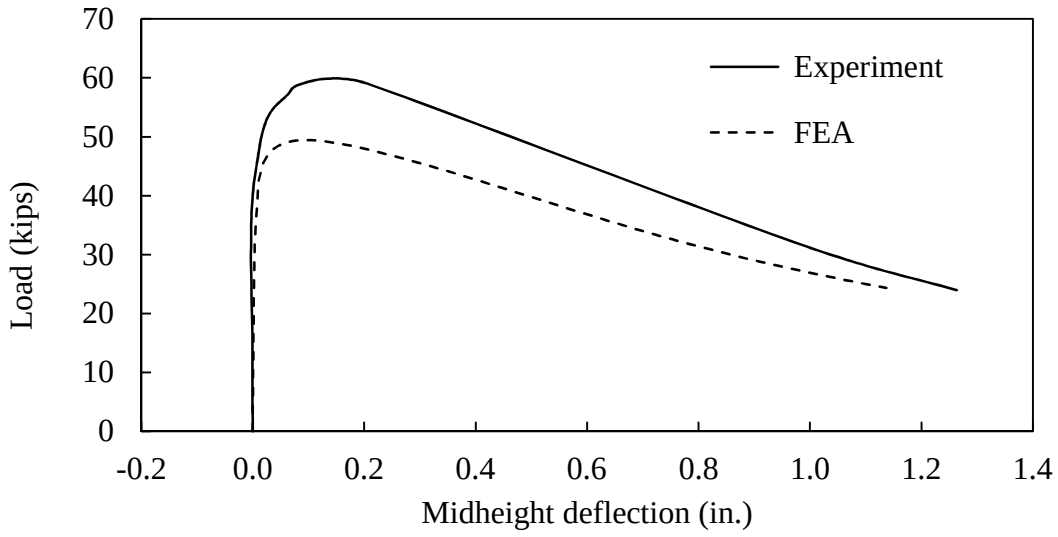

Figure C.8- Load-deflection comparison of experimental and numerical tests (L2-18b)

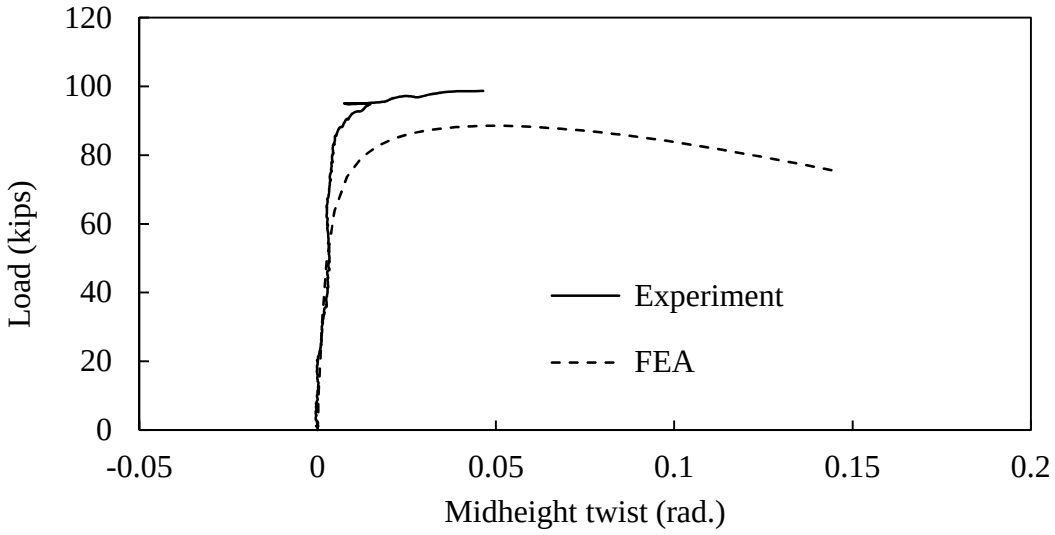

Figure C.9- Load-twist comparison of experimental and numerical tests (L3-18)

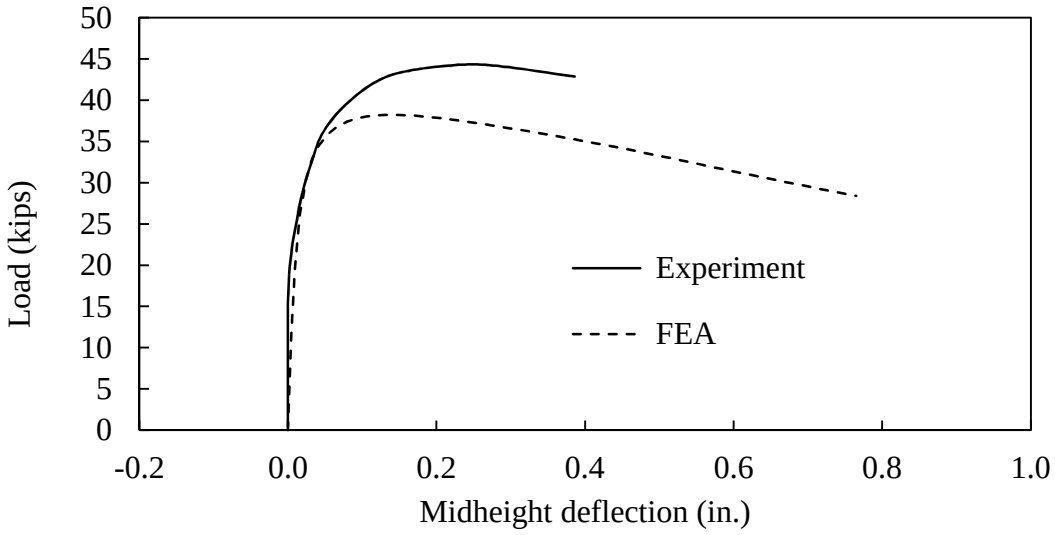

Figure C.10- Load-deflection comparison of experimental and numerical tests (L2-24)

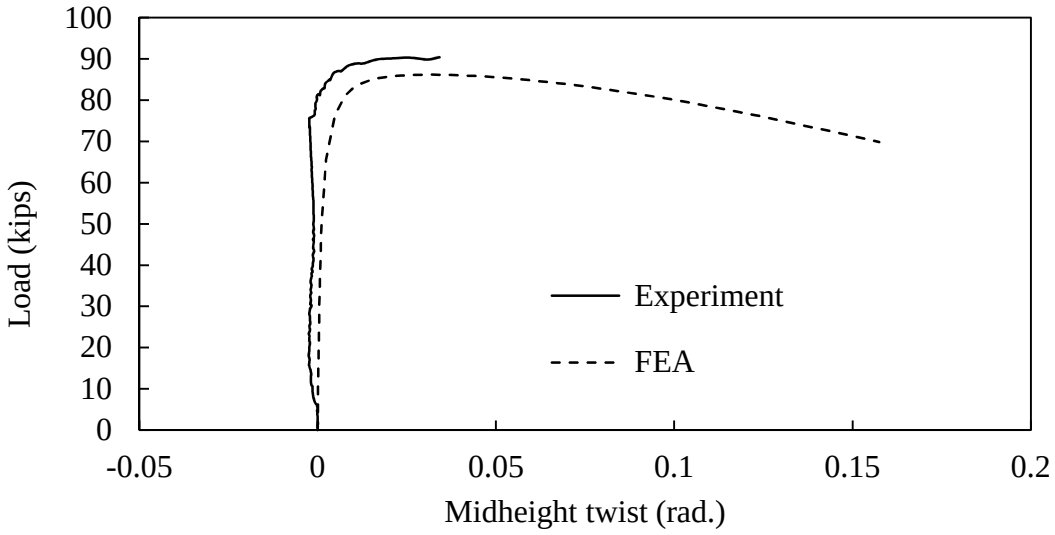

Figure C.11- Load-twist comparison of experimental and numerical tests (L3-24a)

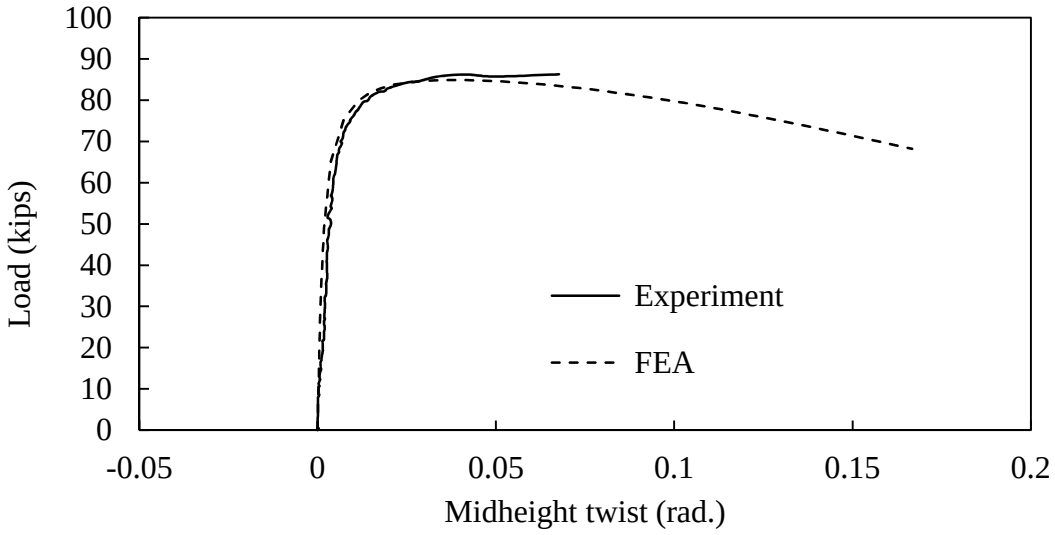

Figure C.13- Load-twist comparison of experimental and numerical tests (L3-24b)

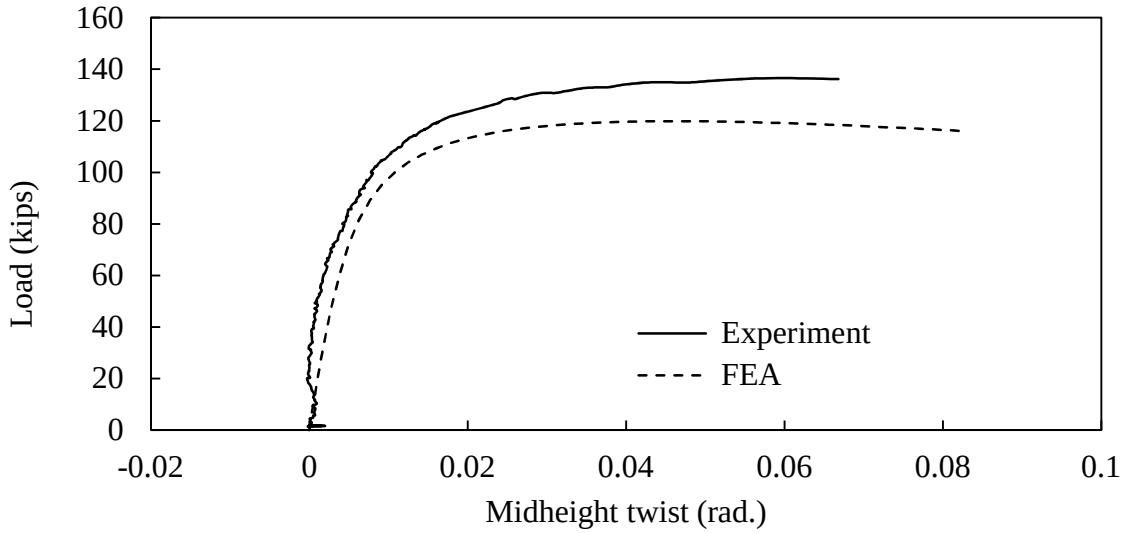

Figure C.14- Load-twist comparison of experimental and numerical tests (L4-24)

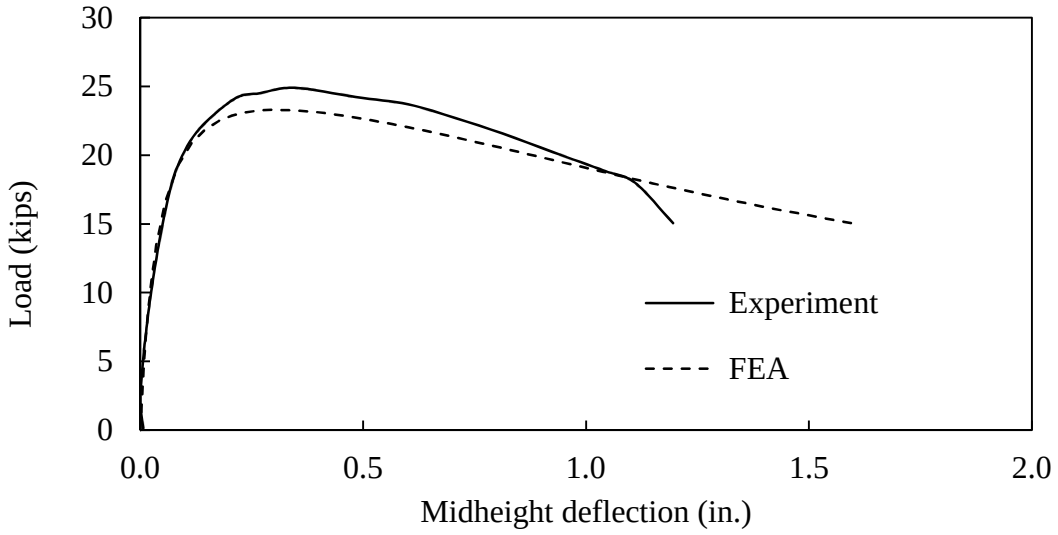

Figure C.15- Load-deflection comparison of experimental and numerical tests (L2-36a)

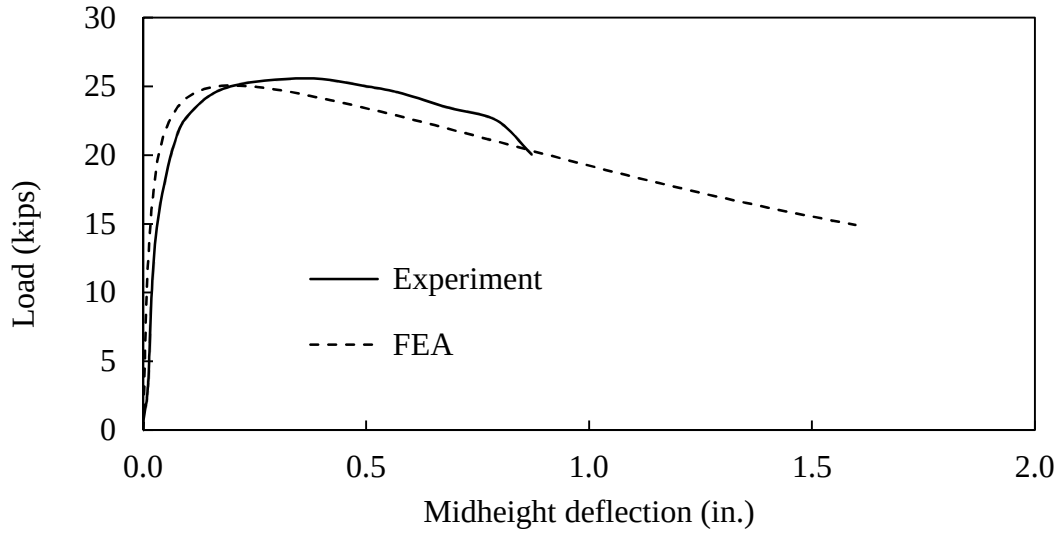

Figure C.16- Load-deflection comparison of experimental and numerical tests (L2-36b)

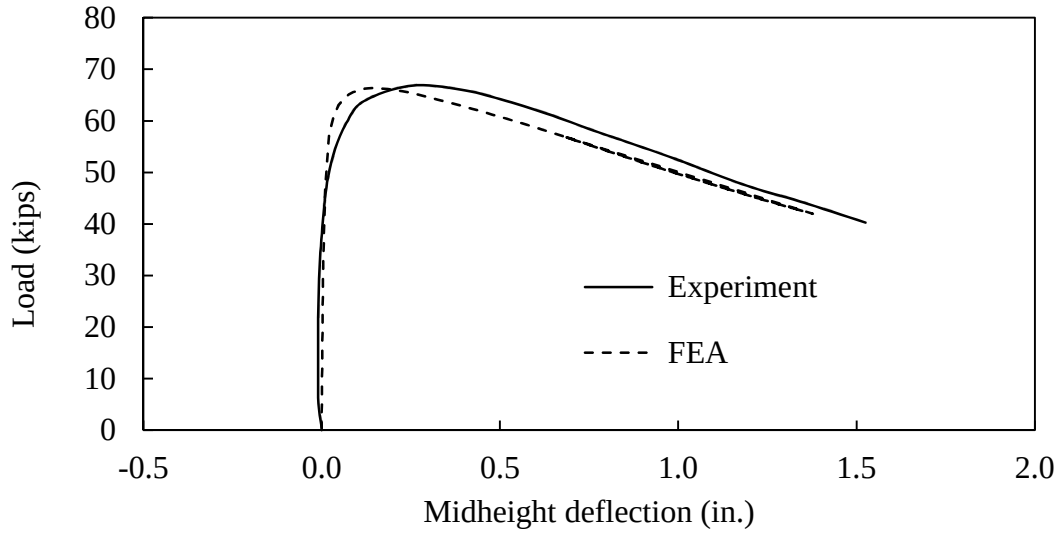

Figure C.17- Load-deflection comparison of experimental and numerical tests (L3-36)

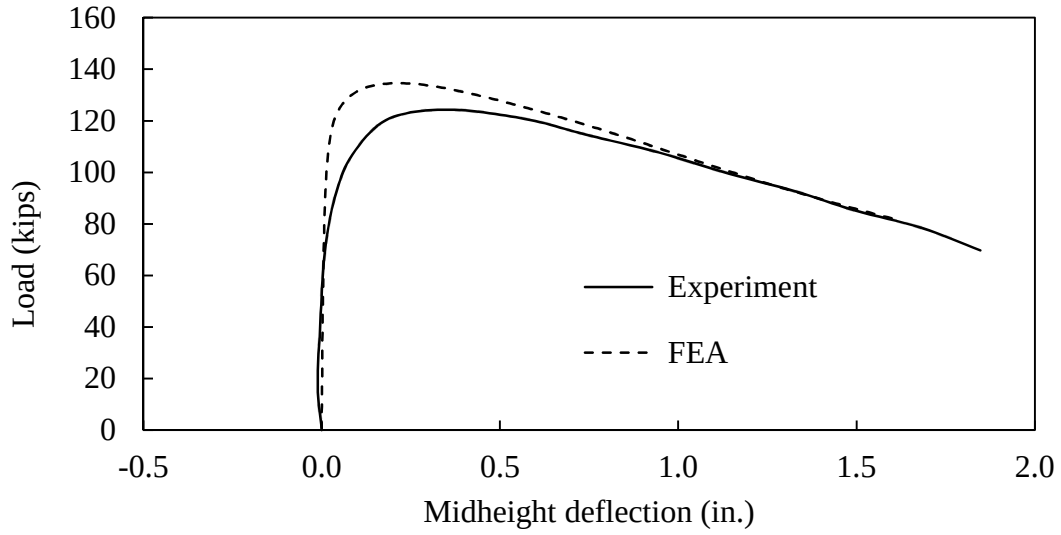

Figure C.18- Load-deflection comparison of experimental and numerical tests (L4-36a)

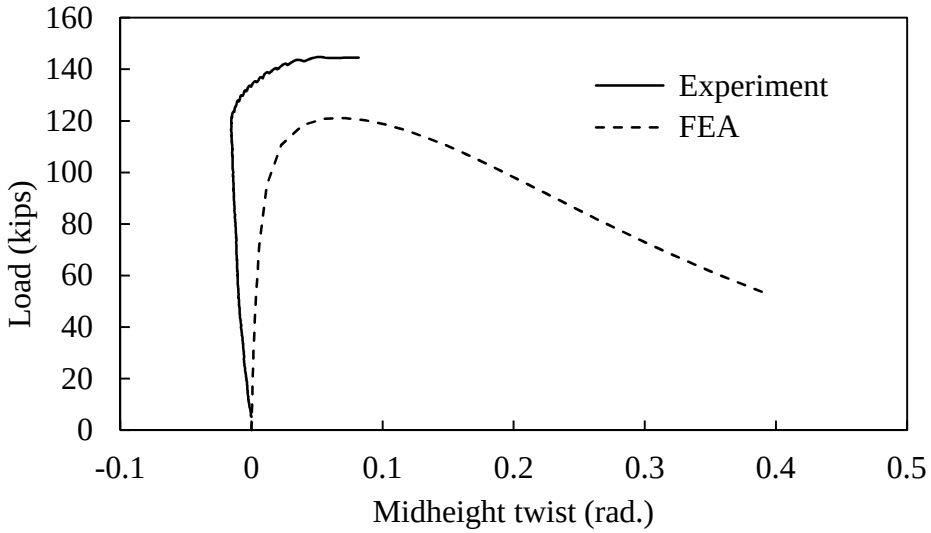

Figure C.19- Load-twist comparison of experimental and numerical tests (L4-36b)

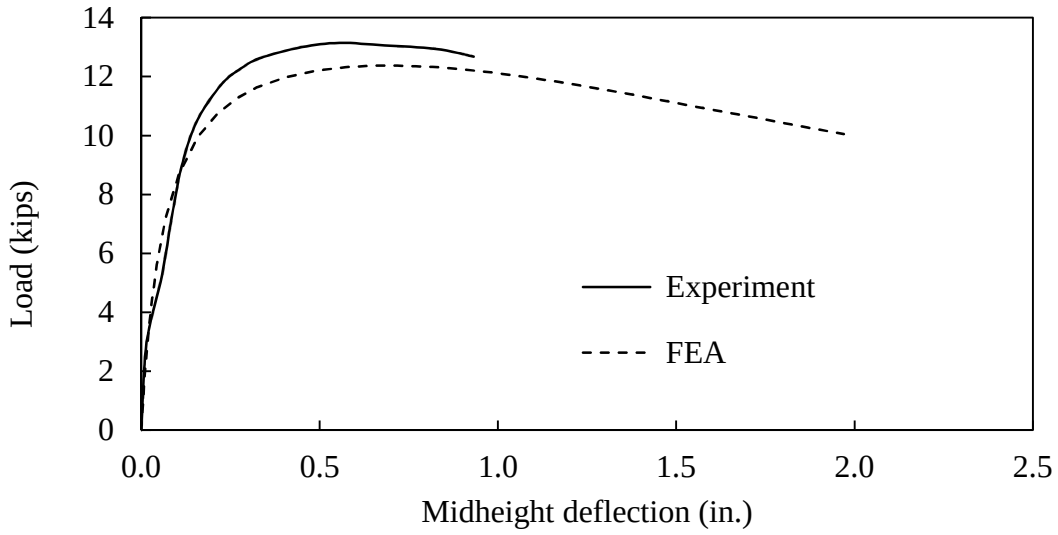

Figure C.20- Load-deflection comparison of experimental and numerical tests (L2-48)

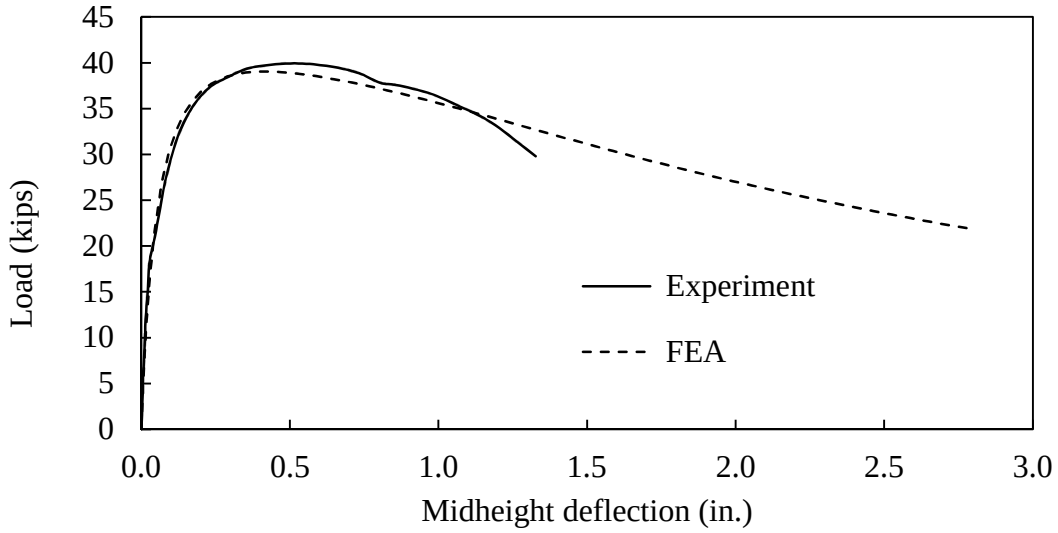

Figure C.21- Load-deflection comparison of experimental and numerical tests (L3-48a)

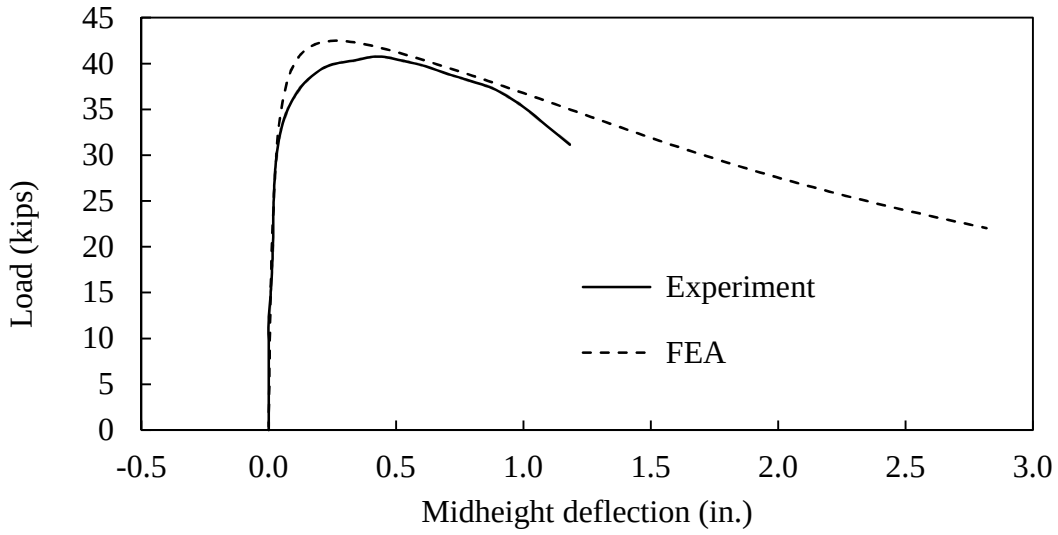

Figure C.22- Load-deflection comparison of experimental and numerical tests (L3-48b)

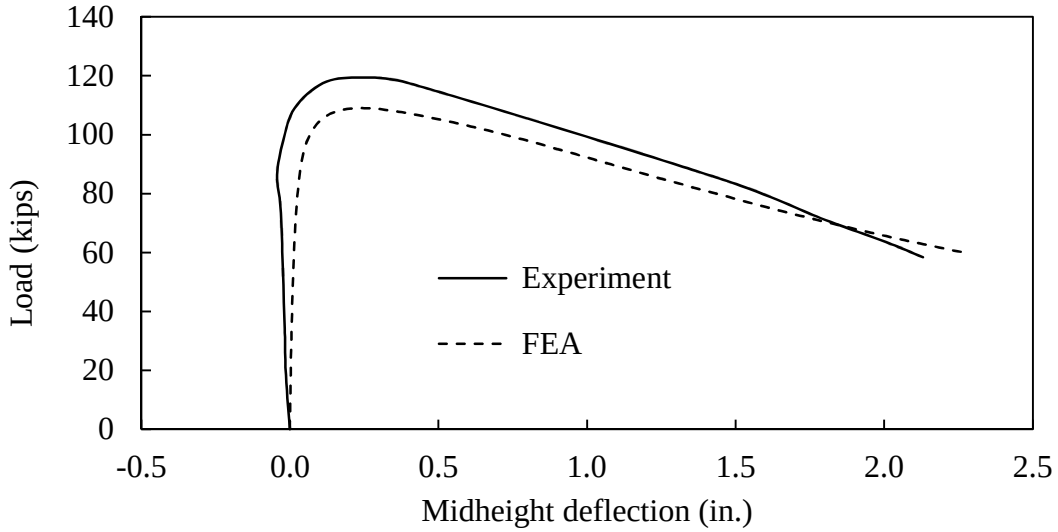

Figure C.23- Load-deflection comparison of experimental and numerical tests (L4-48)

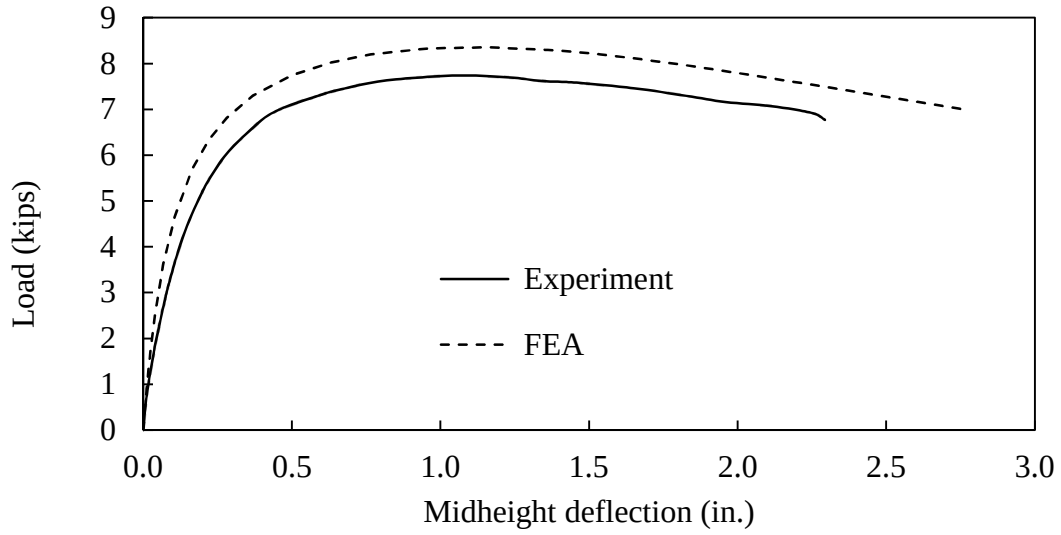

Figure C.24- Load-deflection comparison of experimental and numerical tests (L2-60a)

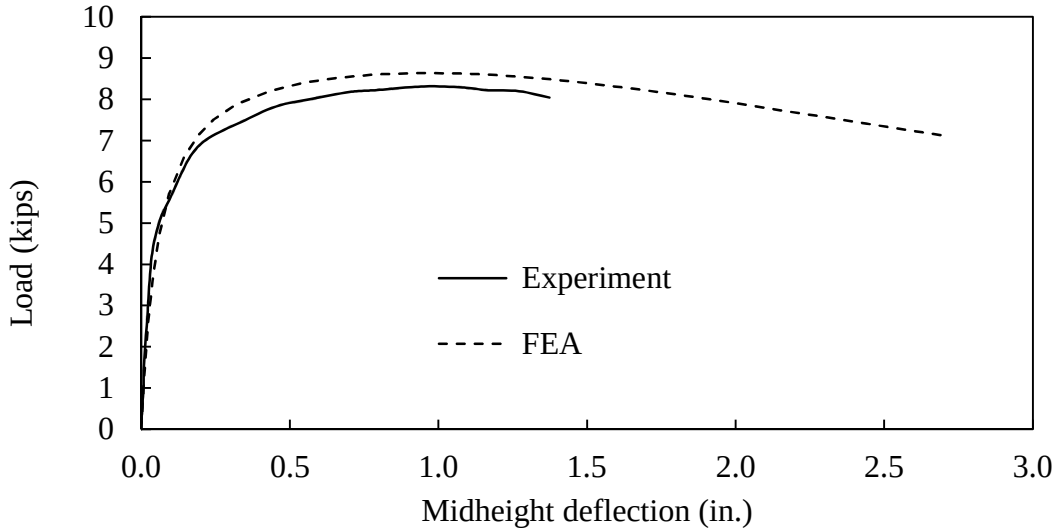

Figure C.25- Load-deflection comparison of experimental and numerical tests (L2-60b)

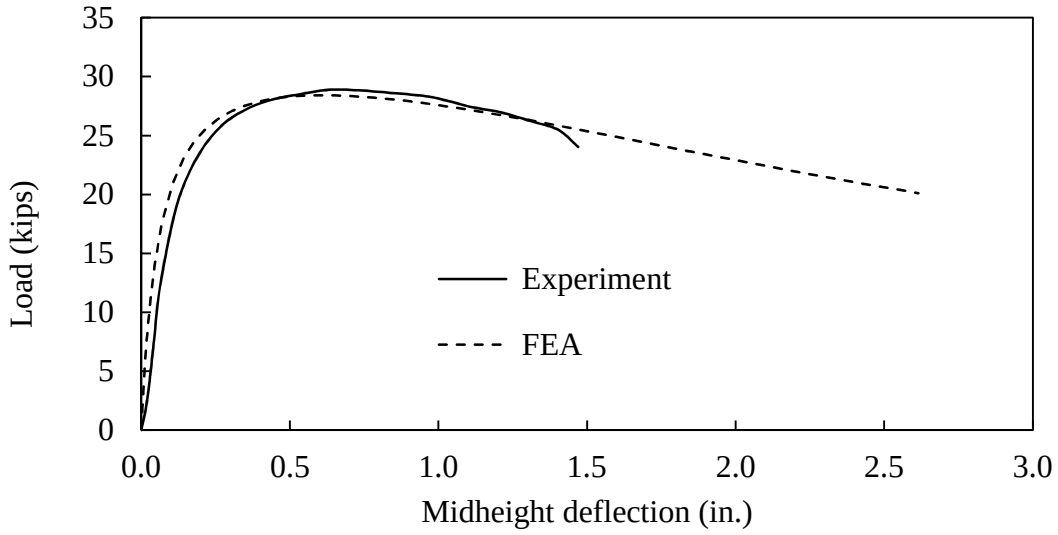

Figure C.26- Load-deflection comparison of experimental and numerical tests (L3-60a)

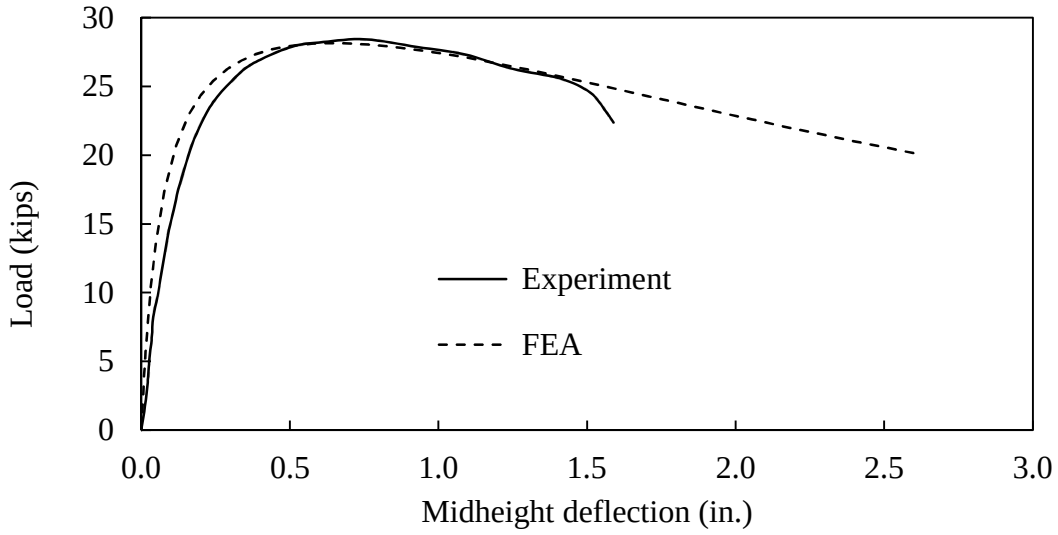

Figure C.27- Load-deflection comparison of experimental and numerical tests (L3-60b)

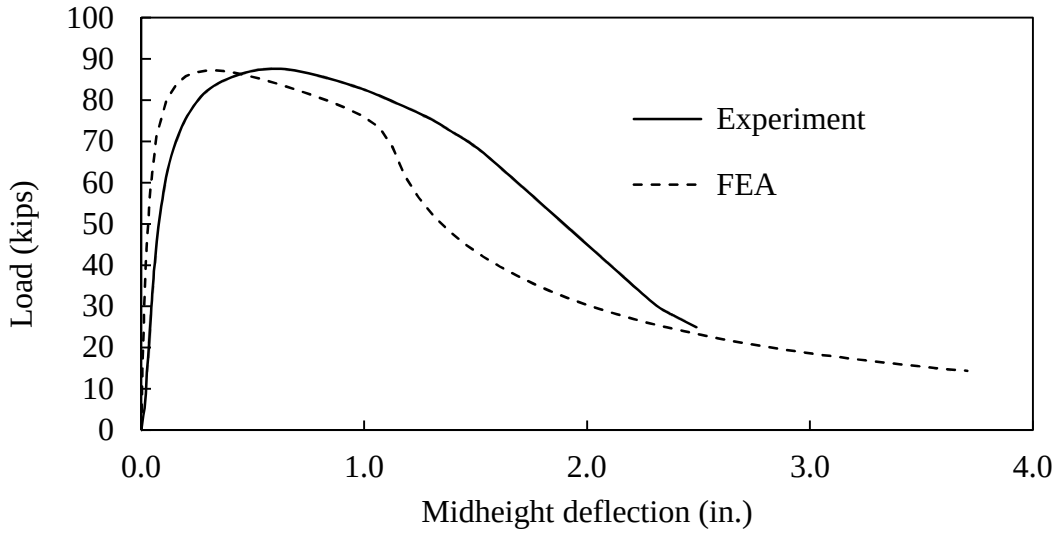

Figure C.28- Load-deflection comparison of experimental and numerical tests (L4-60a)

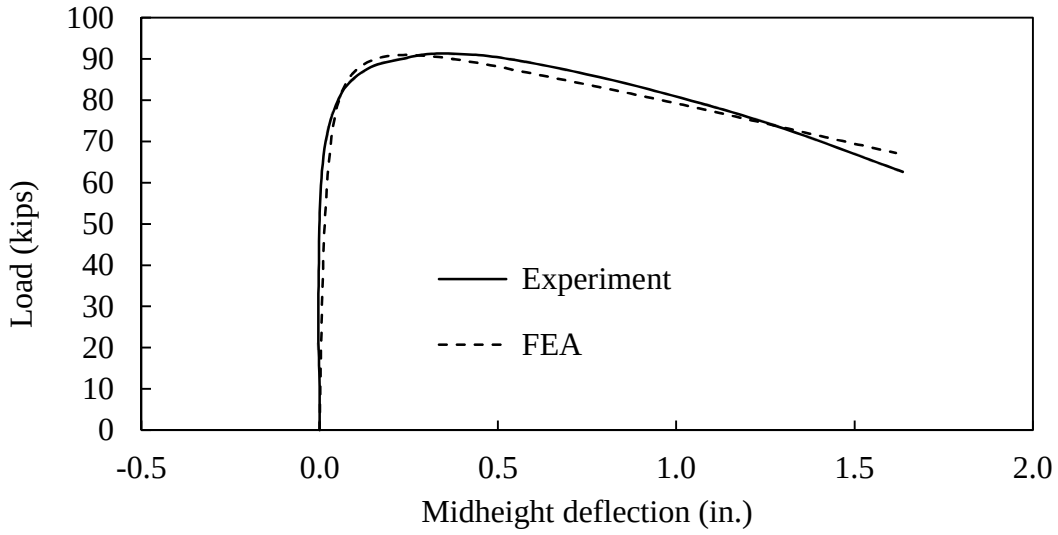

Figure C.29- Load-deflection comparison of experimental and numerical tests (L4-60b)

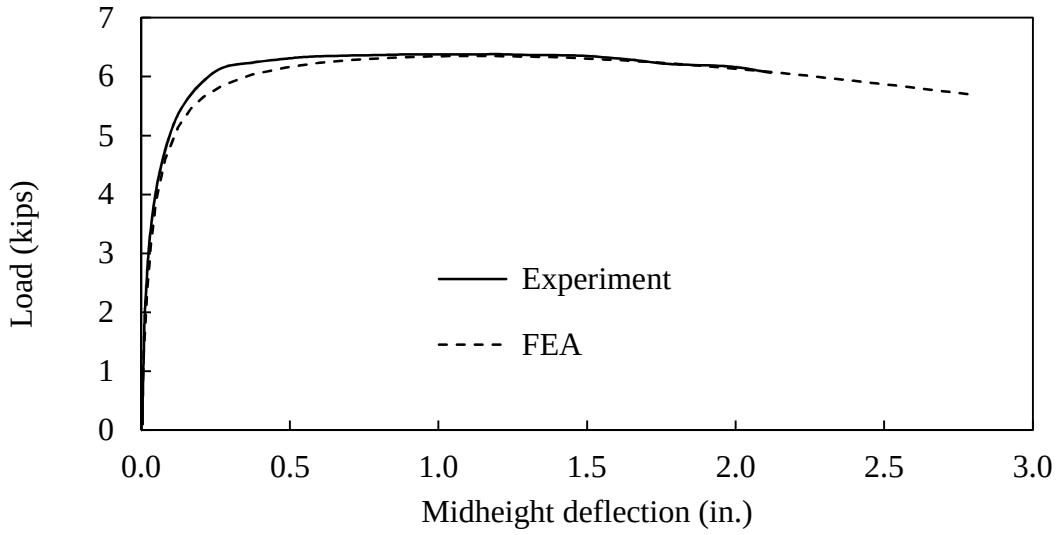

Figure C.30- Load-deflection comparison of experimental and numerical tests (L2-72)

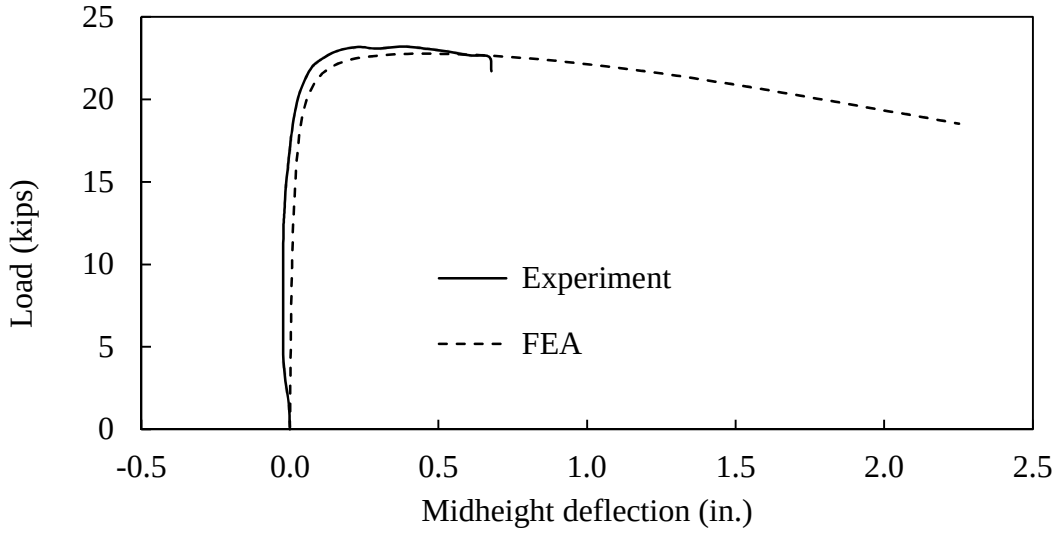

Figure C.31- Load-deflection comparison of experimental and numerical tests (L3-72)

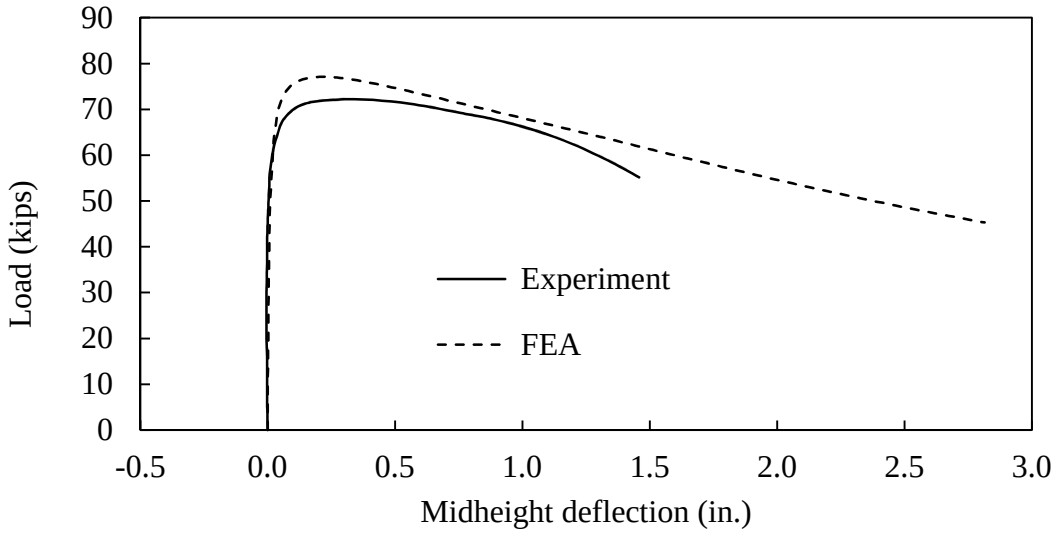

Figure C.32- Load-deflection comparison of experimental and numerical tests (L4-72)

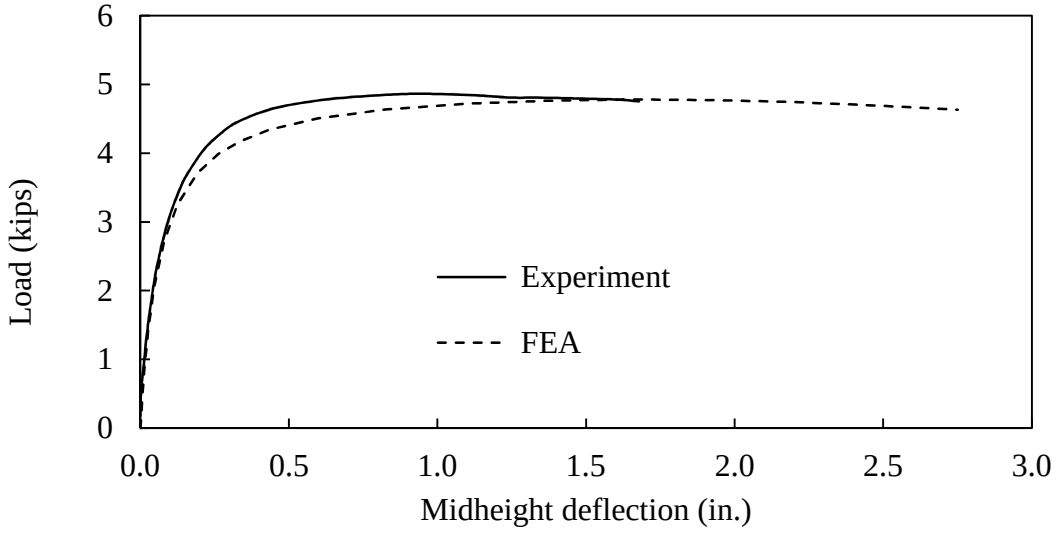

Figure C.33- Load-deflection comparison of experimental and numerical tests (L2-84)

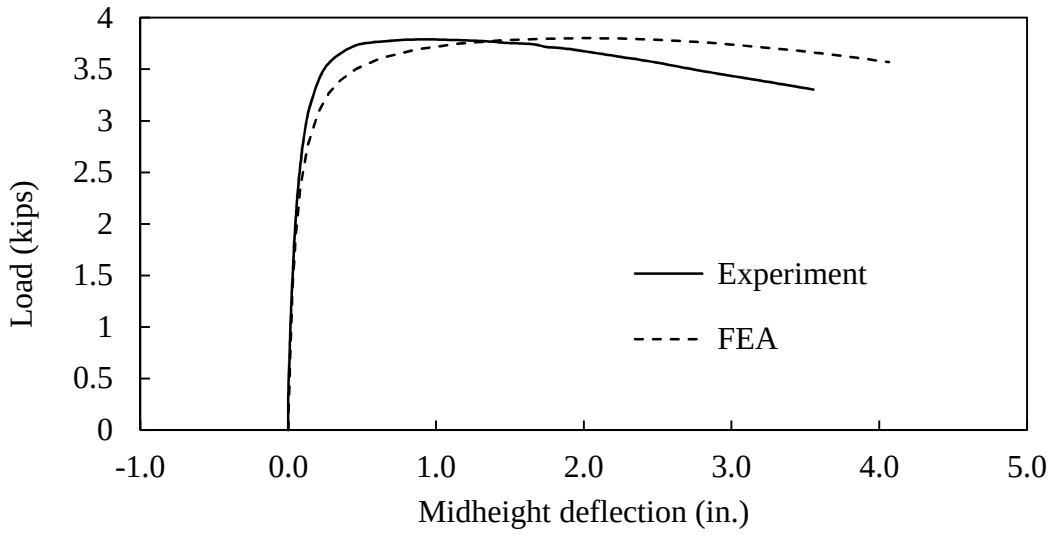

Figure C.34- Load-deflection comparison of experimental and numerical tests (L2-96)

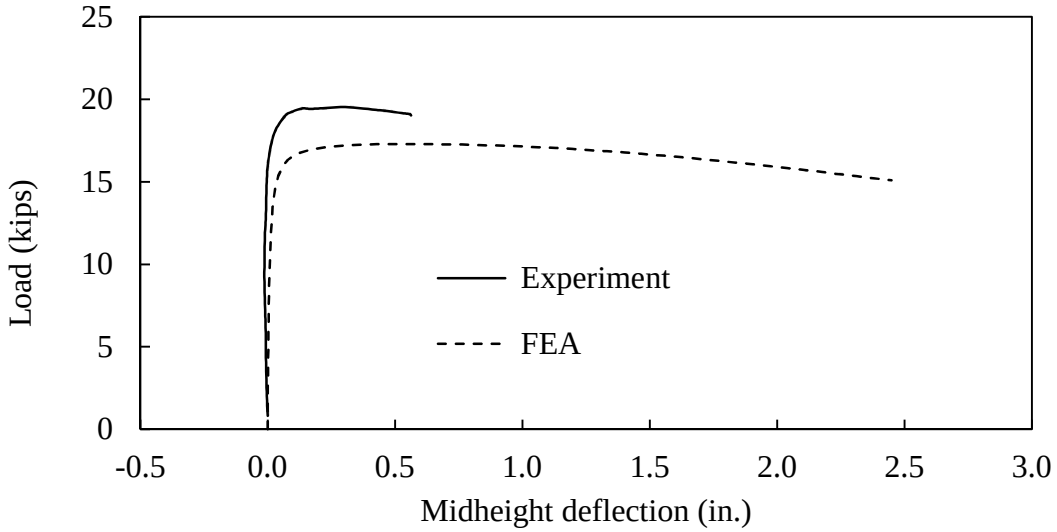

Figure C.34- Load-deflection comparison of experimental and numerical tests (L3-84)

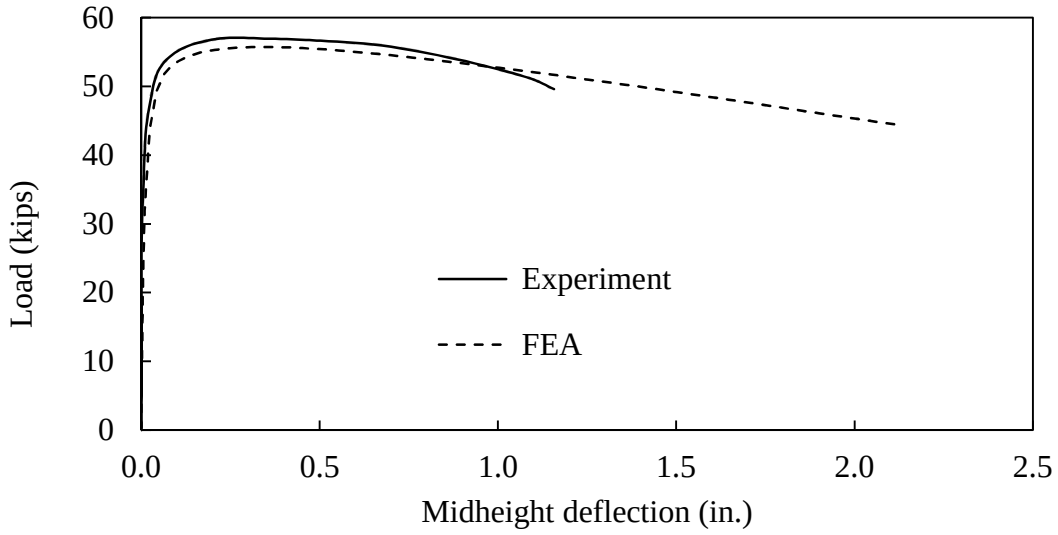

Figure C.35- Load-deflection comparison of experimental and numerical tests (L4-84)

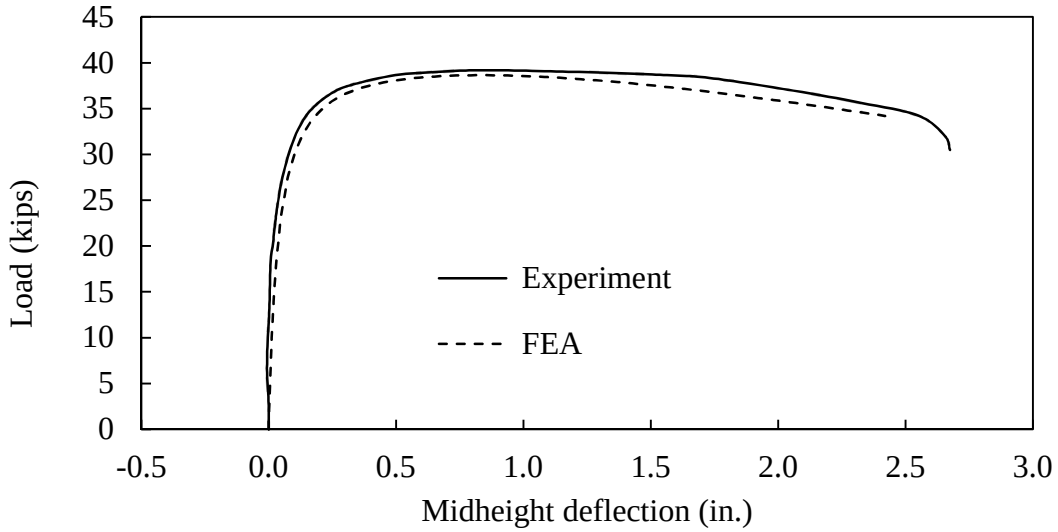

Figure C.37- Load-deflection comparison of experimental and numerical tests (L4-96)

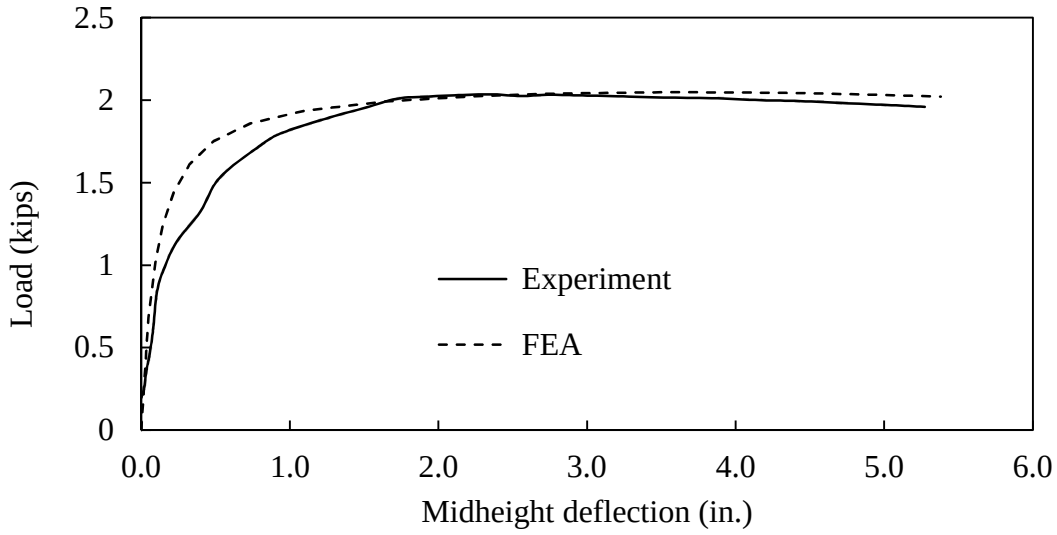

Figure C.38- Load-deflection comparison of experimental and numerical tests (L2-132)

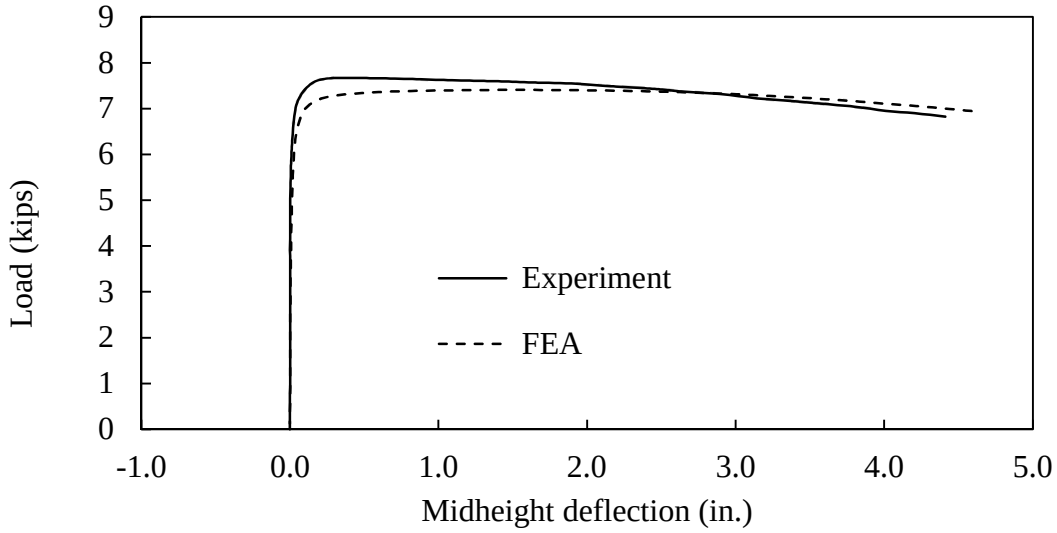

Figure C.39- Load-deflection comparison of experimental and numerical tests (L3-132)

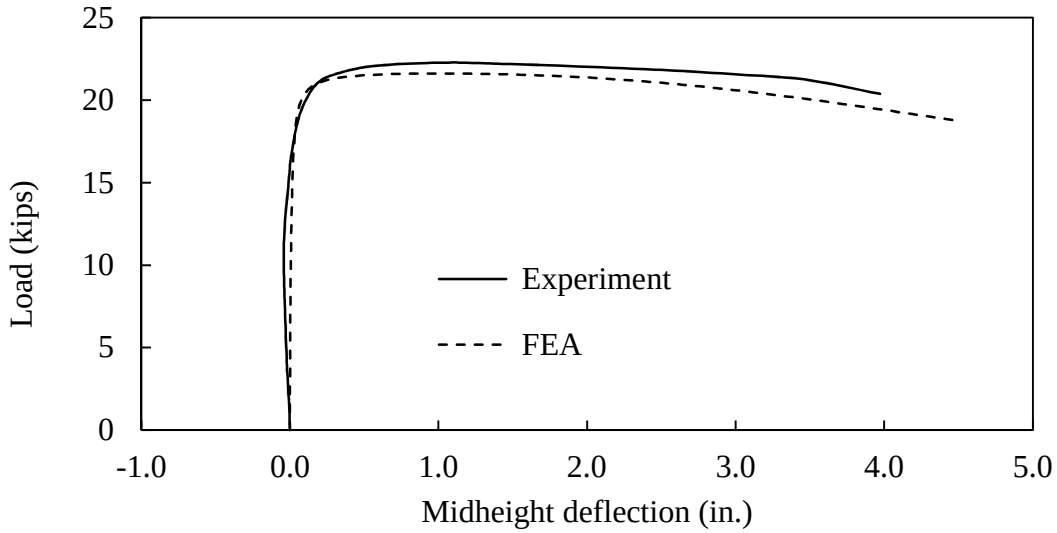

Figure C.40- Load-deflection comparison of experimental and numerical tests (L4-132)

Parametric Studies

Table C.10- Summary of Results from Parametric Studies

	$\frac{L}{r_x}$	σ_{FEM}* (ksi)	Major-Axis Sensitivity		Anisotropic Sensitivity		Computed Strength	
			$\sigma_{y,fix}$ (ksi)	$\frac{\sigma_{y,fix}}{\sigma_{FEM}}$	σ_{aniso} (ksi)	$\frac{\sigma_{aniso}}{\sigma_{FEM\_}}$	$\sigma_{L/1000}$ (ksi)	$\frac{\sigma_{FEM}}{\sigma_{L/1000\_}}$
L2 x 2 x $^1/_4$	31	71.17	71.18	1.00	71.23	1.00	69.96	1.02
(b/t = 7.5)	41	61.26	61.26	1.00	61.29	1.00	60.02	1.02
	51	52.57	52.57	1.00	52.57	1.00	51.25	1.03
	61	45.00	45.01	1.00	45.01	1.00	43.63	1.03
	72	38.20	38.20	1.00	38.21	1.00	36.86	1.04
	82	32.11	32.11	1.00	32.11	1.00	30.93	1.04
	92	26.90	26.90	1.00	26.90	1.00	25.94	1.04
	102	22.61	22.61	1.00	22.61	1.00	21.84	1.04
	112	19.13	19.13	1.00	19.13	1.00	18.53	1.03
	123	16.34	16.34	1.00	16.34	1.00	15.86	1.03
	133	14.08	14.08	1.00	14.08	1.00	13.70	1.03
	143	12.25	12.25	1.00	12.25	1.00	11.94	1.03
	153	10.74	10.74	1.00	10.74	1.00	10.49	1.02
	164	9.49	9.49	1.00	9.49	1.00	9.28	1.02
	174	8.44	8.44	1.00	8.44	1.00	8.27	1.02
	184	7.56	7.56	1.00	7.56	1.00	7.41	1.02
	194	6.80	6.80	1.00	6.80	1.00	6.67	1.02
	205	6.16	6.16	1.00	6.16	1.00	6.05	1.02
L2$^5/_8$x2$^5/_8$x$^1/_4$	30	69.77	70.17	1.01	69.70	1.00	68.87	1.01
(b/t = 10)	41	61.13	61.15	1.00	61.16	1.00	59.98	1.02
	51	52.64	52.64	1.00	52.65	1.00	51.39	1.02
	61	45.19	45.19	1.00	45.20	1.00	43.88	1.03
	71	38.48	38.48	1.00	38.48	1.00	37.18	1.03
	81	32.46	32.46	1.00	32.46	1.00	31.31	1.04
	91	27.28	27.28	1.00	27.28	1.00	26.32	1.04
	102	22.98	22.98	1.00	22.98	1.00	22.21	1.03
	112	19.49	19.49	1.00	19.49	1.00	18.88	1.03
	122	16.66	16.66	1.00	16.66	1.00	16.18	1.03
	132	14.38	14.38	1.00	14.38	1.00	13.99	1.03
	142	12.51	12.51	1.00	12.51	1.00	12.20	1.03
	152	10.98	10.98	1.00	10.98	1.00	10.72	1.02
	163	9.70	9.70	1.00	9.70	1.00	9.49	1.02
	173	8.64	8.64	1.00	8.64	1.00	8.45	1.02
	183	7.73	7.73	1.00	7.73	1.00	7.58	1.02
	193	6.96	6.96	1.00	6.96	1.00	6.83	1.02
	203	6.30	6.30	1.00	6.30	1.00	6.19	1.02

*Major Axis Pinned, Isotropic Yielding, Out-of-Straightness=L/1500

L3$^{1}/_{4}$x3$^{1}/_{4}$x$^{1}/_{4}$	30	58.76	59.18	1.01	58.50	1.00	58.37	1.01
(*b/t* = 12.5)	40	54.89	55.41	1.01	54.80	1.00	54.19	1.01
	51	50.06	50.21	1.00	50.05	1.00	48.95	1.02
	61	43.48	43.48	1.00	43.48	1.00	42.24	1.03
	71	37.10	37.10	1.00	37.10	1.00	35.86	1.03
	81	31.35	31.35	1.00	31.35	1.00	30.24	1.04
	91	26.39	26.39	1.00	26.39	1.00	25.47	1.04
	101	22.26	22.26	1.00	22.26	1.00	21.52	1.03
	111	18.89	18.89	1.00	18.89	1.00	18.30	1.03
	121	16.16	16.16	1.00	16.16	1.00	15.70	1.03
	131	13.95	13.95	1.00	13.95	1.00	13.58	1.03
	142	12.15	12.15	1.00	12.15	1.00	11.84	1.03
	152	10.66	10.66	1.00	10.66	1.00	10.41	1.02
	162	9.43	9.43	1.00	9.43	1.00	9.22	1.02
	172	8.39	8.39	1.00	8.39	1.00	8.21	1.02
	182	7.52	7.52	1.00	7.52	1.00	7.36	1.02
	192	6.77	6.77	1.00	6.77	1.00	6.64	1.02
	202	6.13	6.13	1.00	6.13	1.00	6.01	1.02
L3$^{7}/_{8}$x3$^{7}/_{8}$x$^{1}/_{4}$	30	46.54	46.65	1.00	46.38	1.00	46.31	1.00
(*b/t* = 15)	40	43.27	43.48	1.00	43.20	1.00	42.93	1.01
	50	41.08	41.38	1.01	41.05	1.00	40.59	1.01
	60	39.07	39.38	1.01	39.05	1.00	38.35	1.02
	70	36.54	36.66	1.00	36.53	1.00	35.50	1.03
	81	32.60	32.56	1.00	32.60	1.00	31.42	1.04
	91	27.70	27.70	1.00	27.71	1.00	26.73	1.04
	101	23.40	23.40	1.00	23.40	1.00	22.62	1.03
	111	19.88	19.88	1.00	19.88	1.00	19.26	1.03
	121	17.02	17.02	1.00	17.02	1.00	16.53	1.03
	131	14.70	14.70	1.00	14.70	1.00	14.30	1.03
	141	12.81	12.81	1.00	12.81	1.00	12.48	1.03
	151	11.24	11.24	1.00	11.24	1.00	10.97	1.02
	161	9.94	9.94	1.00	9.94	1.00	9.72	1.02
	171	8.85	8.85	1.00	8.85	1.00	8.66	1.02
	181	7.93	7.93	1.00	7.93	1.00	7.77	1.02
	191	7.14	7.14	1.00	7.14	1.00	7.00	1.02
	201	6.46	6.46	1.00	6.46	1.00	6.34	1.02

L4$^{1}/_{2}$x4$^{1}/_{2}$x$^{1}/_{4}$	30	36.69	36.72	1.00	36.62	1.00	36.53	1.00
(*b/t* = 17.5)	40	33.60	33.68	1.00	33.58	1.00	33.37	1.01
	50	31.83	31.95	1.00	31.82	1.00	31.52	1.01
	60	30.53	30.69	1.01	30.52	1.00	30.11	1.01
	70	29.31	29.48	1.01	29.31	1.00	28.73	1.02
	80	27.88	27.98	1.00	27.88	1.00	27.09	1.03
	90	25.86	25.81	1.00	25.86	1.00	24.88	1.04
	100	22.99	22.93	1.00	22.98	1.00	22.06	1.04
	110	19.87	19.85	1.00	19.87	1.00	19.14	1.04
	120	17.09	17.08	1.00	17.09	1.00	16.55	1.03
	130	14.77	14.77	1.00	14.77	1.00	14.36	1.03
	141	12.86	12.86	1.00	12.86	1.00	12.54	1.03
	151	11.30	11.30	1.00	11.30	1.00	11.03	1.02
	161	9.99	9.99	1.00	9.99	1.00	9.76	1.02
	171	8.90	8.90	1.00	8.90	1.00	8.71	1.02
	181	7.97	7.97	1.00	7.97	1.00	7.81	1.02
	191	7.18	7.18	1.00	7.18	1.00	7.04	1.02
	201	6.50	6.50	1.00	6.50	1.00	6.38	1.02
L5$^{1}/_{8}$x5$^{1}/_{8}$x$^{1}/_{4}$	30	29.01	29.01	1.00	28.98	1.00	28.89	1.00
(*b/t* = 20)	40	26.33	26.35	1.00	26.32	1.00	26.16	1.01
	50	24.89	24.93	1.00	24.88	1.00	24.67	1.01
	60	23.93	23.99	1.00	23.92	1.00	23.65	1.01
	70	23.15	23.23	1.00	23.14	1.00	22.78	1.02
	80	22.38	22.47	1.00	22.38	1.00	21.89	1.02
	90	21.49	21.54	1.00	21.49	1.00	20.84	1.03
	100	20.27	20.24	1.00	20.27	1.00	19.47	1.04
	110	18.57	18.51	1.00	18.57	1.00	17.74	1.05
	120	16.55	16.51	1.00	16.55	1.00	15.84	1.04
	130	14.58	14.56	1.00	14.58	1.00	14.02	1.04
	140	12.82	12.81	1.00	12.82	1.00	12.37	1.04
	150	11.31	11.30	1.00	11.31	1.00	10.97	1.03
	160	10.03	10.69	1.07	10.03	1.00	9.76	1.03
	170	8.94	8.94	1.00	8.95	1.00	8.75	1.02
	180	8.02	8.01	1.00	8.02	1.00	7.85	1.02
	190	7.22	7.22	1.00	7.22	1.00	7.07	1.02

REFERENCES

ABAQUS (2011). *ABAQUS/Standard user's manual, vol. I-III.* , Bibbit, Karlsson, and Sorensen, Pawtucket, RI.

Adluri, S. M. R., and Madugula, M. K. S. (1996a). "Development of Column Curve for Steel Angles." *Journal of Structural Engineering*, 122(3), 318-325.

Adluri, S. M. R., and Madugula, M. K. S. (1996b). "Torsional-flexural buckling strength of steel angles." *Canadian Journal of Civil Engineering*, 23, 260-271.

Adluri, S. M. R., and Murty, K. S. (1996). "Flexural buckling of steel angles: experimental investigation." *Journal of Structural Engineering*, 122(3).

AISC (2005). *Steel construction manual*, American Institute of Steel Construction.

AISC (2012). "AISC Design Guide: Structural Stainless Steel (Draft, v.6)."

Al-Sayed, S. H., and Bjorhovde, R. (1989a). "Experimental study of single angle columns." *Journal of Constructional Steel Research*, 12, 83-102.

Al-Sayed, S. H., and Bjorhovde, R. (1989b). "Inelastic behavior of single angle columns." *Journal of Constructional Steel Research*, 12, 103-118.

AS/NZS 4673 (2001). *Cold formed stainless steel structures*.

ASTM A6-12 (2012). "Standard Specification for General Requirements for Rolled Structural Steel Bars, Plates, Shapes, and Sheet Piling." ASTM International.

ASTM A240-11 (2011). "Standard Specification for Chromium and Chromium-Nickel Stainless Steel Plate, Sheet, and Strip for Pressure Vessels and for General Applications."

ASTM E111-04 (2004). "Standard test for Young's modulus, tangent modulus, and chord modulus."West Conshohocken, PA.

ATI Allegheny Ludlum (2010). "ATI 2003 Technical Data Sheet." A. Properties, ed.

Baddoo, N. R. (2003). "A Comparison of Structural Stainless Steel Design Standards." *Proceedings of the Stainless Steel Structures International Experts' Seminar*Ascot, UK, 131-150.

Baker, J. F., Horne, M. R., and Roderick, J. W. (1949). "The Behaviour of Continuous Stanchions." *Proceedings of the Royal Society of London. Series A, Mathematical and Physical Sciences*, 198(1055), 493-509.

Bažant, Z. P., and Cedolin, L. (1991). *Stability of Structures: Elastic, Inelastic, Fracture, and Damage Theories*, Oxford University Press, New York.

Becque, J. (2010). "Inelastic Plate Buckling." *Journal of Engineering Mechanics*, 136(9), 1123-1130.

Becque, J., and Rasmussen, K. J. R. (2009a). "Experimental investigation of the interaction of local and overall buckling in stainless steel lipped channel columns." *Journal of Constructional Steel Research*, 65, 1677-1684.

Becque, J., and Rasmussen, K. J. R. (2009b). "Experimental Investigation of the Interaction of Local and Overall Buckling of Stainless Steel I-columns." *Journal of Structural Engineering*, 135(11), 1340-1348.

Becque, J., and Rasmussen, K. J. R. (2009c). "A numerical investigation of local-overall interaction of stainless steel lipped channel columns." *Journal of Constructional Steel Research*, 65, 1685-1693.

Becque, J., and Rasmussen, K. J. R. (2009d). "Numerical Investigation of the Interaction of Local and Overall Buckling of Stainless Steel I-Columns." *Journal of Structural Engineering*, 135(11), 1349-1356.

Bentz, D. P., and Prasad, K. R. (2007). "Thermal Performance of Fire Resistive Materials I. Characterization with Respect to Thermal Performance Models." Building and Fire Research Laboratory, National Institute of Standards and Technology, Gaithersburg, MD.

Bezkorovainy, P., Burns, T., and Rasmussen, K. J. R. (2003). "Strength curves for metal plates in compression." *Journal of Structural Engineering*, 129(11).

Bjorhovde, R. (1972). "A Probabilistic Approach to Maximum Column Strength." *Special Conference on the Safety and Reliability of Metal Structures*Pittsburgh, PA.

Bleich, F. (1952). *Buckling Strength of Metal Structures*, McGraw-Hill Book Company, New York.

Bredenkamp, P. J., Human, J. J., and van den Berg, G. J. (1994). "The strength of hot-rolled stainless steel columns." *SSRC Annual Technical Session Proceedings*Bethlehem, PA.

Bredenkamp, P. J., and van den Berg, G. J. (1995). "The strength of stainless steel built-up I-section columns." *Journal of Constructional Steel Research*, 34, 131-144.

Cho, B.-S. (1998). "The In-Plane Shear Properties of Pultruded Materials." Doctor of Philosophy, Georgia Institute of Technology, Atlanta, GA.

Chwalla, E. (1934). "Über die experimentelle Untersuchung des Tragverhaltens gedrückter Stäbe aus Baustahl." *Der Stahlbau*, 7(17).

Chwalla, E. (1935). "Der Einfluss der Querschnittsform auf das Tragvermögen aussermittig gedrückter Baustahlstäbe." *Der Stahlbau*, 8(193).

Coetsee, J. S., Van den Berg, G. J., and Van der Merwe, P. "The behavior of stainless steel lipped channel axially loaded compression members." *Proc., SSRC 1990 Annual Technical Session*.

Crisfield, M. A. (1981). "A fast incremental/iterative solution procedure that handles "snap-through"." *Computers & Structures*, 13(1–3), 55-62.

Dawes, C. (1992). *Laser Welding*, Woodhead Publishing Ltd., London.

Ellobody, E. (2007). "Buckling analysis of high strength stainless steel stiffened and unstiffened slender hollow section columns." *Journal of Constructional Steel Research*, 63, 145-155.

Ellobody, E., and Young, B. (2005). "Structural performance of cold-formed high strength stainless steel columns." *Journal of Constructional Steel Research*, 61, 1631-1649.

Eurocode 3 (2006). "Eurocode 3 - Design of steel structures." *Part 1-4: General rules - Supplementary rules for stainless steels*, European Committee for Standardization,, Brussels Belgium.

Fang, P. J., and Winter, G. (1965). "Torsional-Flexural Buckling of Thin-Walled Open Sections." Cornell University, Ithaca, NY.

Galambos, T. V. (1991). "Design of Axially Loaded Compressed Angles." *Annual Technical Session Proceedings*, SSRC, ed.Chicago, IL.

Gardner, L., and Nethercot, D. A. (2004a). "Experiments on stainless steel hollow sections--Part 1: Material and cross-sectional behaviour." *Journal of Constructional Steel Research*, 60(9), 1291-1318.

Gardner, L., and Nethercot, D. A. (2004b). "Experiments on stainless steel hollow sections--Part 2: Member behaviour of columns and beams." *Journal of Constructional Steel Research*, 60(9), 1319-1332.

Gardner, L., and Nethercot, D. A. (2004c). "Stainless steel structural design: a new approach." *The Structural Engineer*, 21-28.

Gerard, G. (1946). "Secant Modulus Method for Determining Plate Instability above the Proportional Limit." *Journal of Aerospace Sciences*, 13(1), 38-44.

Haaijer, G. (1957). "Paper No. 2968: Plate Buckling in the Strain-Hardening Range." *Transactions of the American Society of Civil Engineers*.

Hammer, E. W., and Petersen, R. E. (1955). "Column Curves for Type 301 Stainless Steel." *Aeronautical Engineering Review*, 14(12), 18.

Handelman, G., and Prager, W. (1948). "Plastic buckling of a rectangular plate under edge thrusts." *ratio*, 100, 5-4v.

Hill, H. N. (1944). "Determination of stress-strain relations from offset yield strength values." *Technical Notes*, NACA, Washington.

Holston, A. (1970). "Buckling of Orthotropic Plates with One Free Edge." *AIAA Journal*, 8(7), 1352-1354.

Horne, M. R. (1956). "The elastic-plastic theory of compression members." *Journal of the Mechanics and Physics of Solids*, 4(2), 104-120.

Huang, Y., and Young, B. (2012). "Material properties of cold-formed lean duplex stainless steel sections." *Thin-Walled Structures*, 54(0), 72-81.

Huber, A. W., and Beedle, L. S. (1954). "Residual stress and the compressive strength of steel." Lehigh University, Bethlehem, PA.

Ilyushin, A. (1947), "The Elasto-Plastic Stability of Plates," NACA (TN 1188), Washington.

Jenkin, C. F. (1920), "Report on materials of construction used in aircraft and aircraft engines," A. R. Committee, London.

Ježek, K. (1934). "Die Tragfähigkeit des exzentrisch beanspruchten und des querbelasteten Druckstabes aus enim ideal plastischen Material." *Sitzungberichte der Akademie der Wissenschaften in Wien*, Akademie der Wissenschaften, Wien.

Johnson, A. L., and Winter, G. (1966). "Behavior of stainless steel columns and beams." *Journal of the Structural Division*, 92(5), 97-118.

Kennedy, J., and Murty, K. S. M. (1972). "Buckling of steel angle and tee struts." *Journal of the Structural Division*, 98, 2507-2522.

Kim, S.-H. (2010). "Stress-strain relationship of grade S32003 duplex stainless steel in tension." Georgia Institute of Technology, Atlanta.

Kitipornchai, S., and Lee, H. W. (1986a). "Inelastic buckling of single-angle, tee and double-angle struts." *Journal of Constructional Steel Research*, 6, 3-20.

Kitipornchai, S., and Lee, H. W. (1986b). "Techinical note: inelastic experiments on angle and tee struts." *Journal of Constructional Steel Research*, 6, 219-316.

Klopper, J. J., Laubscher, R. F., Steuwer, A., and James, M. N. (2011). "An investigation into the effect of weld technique on the residual stress distribution of 3CR12 (DIN 1.4003) built-up structural sections." *Proceedings of the Institution of Mechanical Engineers, Part L: Journal of Materials Design and Applications*, 225(3), 123-132.

Kollbrunner, C. F. (1935). "Das Ausbeulen des auf Druck beanspruchten freistehenden Winkels." ETH, Institut fuer Baustatik, Zurich.

Lagerquist, O., and Olsson, A. "Residual stresses in welded I-girder made of stainless steel and structural steel." *Proc., 9th Nordic Steel Construction Conf.*, 737-744.

Leary, J. R., and Holt, M. (1946), "Column Strength of Aluminum Alloy 14S-T Extruded Shapes and Rod," NACA (TN 1027), Washington.

Lecce, M., and Rasmussen, K. J. R. (2006). "Distortional Buckling of Cold-Formed Stainless Steel Sections: Experimental Investigation." *Journal of Structural Engineering*, 132(4), 497-504.

Liu, Y., and Young, B. (2003). "Buckling of stainless steel square hollow section compression members." *Journal of Constructional Steel Research*, 59(2), 165-177.

Lundquist, E. (1930), "The compressive strength of duralumin columns of equal angle section," NACA (TN 413), Washington.

Madugula, K. S. M., and Ray, S. K. (1984). "Ultimate strength of eccentrically loaded cold-formed angles." *Canadian Journal of Civil Engineering*, 11.

Madugula, M. K. S., Prabhu, T. S., and Temple, M. C. (1983). "Ultimate strength of concentrically loaded cold-formed angles." *Canadian Journal of Civil Engineering*, 10, 60-68.

Marshall, W. T., Nelson, H. M., and Smith, I. A. "Experiments on single-angle aluminum alloy struts." *Proc., Symposium on Aluminum in Structural Engineering*, 30-45.

Popovic, D., Hancock, G. J., and Rasmussen, K. J. R. (1999). "Axial Compression Tests of Cold-Formed Angles." *Journal of Structural Engineering*, 125(5), 515-523.

Pride, R. A., and Heimerl, G. J. (1949), "Plastic Buckling of Simply Supported Compressed Plates," NACA (TN 1817), Washington.

Ramberg, W., and Osgood, W. R. (1943). "Description of stress-strain curves by three parameters."

Rao, N. R. N., Estuar, F. R., and Tall, L. (1963). "Residual Stresses in Welded Shapes." *Welded Built-Up Columns*, Lehigh University, Bethlehem, PA.

Rasmussen, K. J. R. (2003). "Full range stresss-strain curves for stainless steel alloys." *Journal of Constructional Steel Research*, 54, 109-133.

Rasmussen, K. J. R., Burns, T., Bezkorovainy, P., and Bambach, M. R. (2003). "Numerical modelling of stainless steel plates in compression." *Journal of Constructional Steel Research*, 59, 1345-1362.

Rasmussen, K. J. R., and Hancock, G. J. (1990). "Stainless Steel Tubular Columns: Tests and Design." *Tenth International Conference on Cold-formed Steel Structures*, W.-W. Yu, and R. A. LaBoube, eds.St. Louis, MO.

Rasmussen, K. J. R., and Rondal, J. (1997a). "Explicit Approach to the Design of Stainless Steel Columns." *Journal of Structural Engineering*, 123(7), 857-863.

Rasmussen, K. J. R., and Rondal, J. (1997b). "Strength Curves for Metal Columns." *Journal of Structural Engineering*, 123(6), 721-729.

Riks, E. (1972). "The Application of Newton's Method to the Problem of Elastic Stability." *Journal of Applied Mechanics*, 39(4), 1060-1065.

Rossi, B., Jaspart, J.-P., and Rasmussen, K. J. R. (2010). "Combined Distortional and Overall Flexural-Torsional Buckling of Cold-Formed Stainless Steel Sections: Experimental Investigations." *Journal of Structural Engineering*, 136(4), 354-360.

Schafer, B. W. (2008). "Review: The Direct Strength Method of cold-formed steel member design." *Journal of Constructional Steel Research*, 64, 766-778.

SCI, and Euro-Inox (2006). *Design manual for structural stainless steel*, Euro Inox and The Steel Construction Institute.

SEI/ASCE 8-02 (2002). *Specification for the design of cold-formed stainless steel structural members.*, ASCE, New York.

Shanley, F. R. (1947). "Inelastic Column Theory." *Journal of Aeronautical Science*, 14(5).

Singer, J. (1989). "On the applicability of the Southwell plot to plastic buckling." *Experimental Mechanics*, 29(2), 205-208.

Southwell, R. V. (1932). "On the analysis of experimental observations in problems of elastic stability." *Proc. Roy. Soc.*London, 601-616.

Stang, A. H., and Strickenberg, L. R. (1922). "Results of some compression tests of structural steel angles." *Technical Papers of the Bureau of Standards*, 16, 651-667.

Stowell, E. Z. (1948), "A unified theory of plastic buckling of columns and plates," NACA (TN 898), Washington.

Talja, A., and Salmi, P. (1995). *Desing of stainless steel RHS beams, column, and beam-columns*, VTT Building Technology.

Tebedge, N., Alpsten, G., and Tall, L. (1972). "Residual Stress Measurement by the Sectioning Method." *SESA Spring Meeting*, Society for Experimental Stress Analysis, Cleveland, OH.

Theofanous, M., and Gardner, L. (2009). "Testing and numerical modelling of lean duplex stainless steel hollow section columns." *Engineering Structures*, 31, 3047-3058.

Thomas, E. W. (1941). "Torsional Instability of Thin Angle Section Struts." *The Structural Engineer*, 19(5), 73-82.

Thurlimann, B., and Haaijer, G. (1953). "Buckling of Steel Angles in the Plastic Range." *Welded Continuous Frames and Their Components*, Lehigh University, Bethlehem, PA.

Timoshenko, S. P., and Gere, J. M. (1961). *Theory of Elastic Stability*, McGraw-Hill, New York.

van den Berg, G. J. (2000). "The effect of non-linear stress-strain behaviour of stainless steel on member capacity." *Journal of Constructional Steel Research*, 54(1), 135-160.

van den Berg, G. J., and van der Merwe, P. (1988). "The torsional flexural buckling strength of cold-formed stainless steel columns." *Ninth International Specialty Conference on Cold-Formed Steel Structures*St. Louis.

van den Berg, G. J., van der Merwe, P., and Bosch, H. H. "The strength of type 3Cr12 stainless steel point symmetric angles as compression members." *Proc., International Conference on Structural Stability and Design*, A.A. Balkema.

von Karman, T. (1910). "Untersuchengen über Knickfestigkeit." *Mitteilungen über Forschungsarbeiten auf dem Gebiete des Ingenieurwesens*Berlin.

von Karman, T., Sechler, E. E., and Donnell, L. H. (1932). "Strength of thin plates in compression." *Trans. ASME*.

Wakabayashi, M., and Nonaka, T. (1965). "On the buckling strength of angles in transmission towers." *Bulletin: Distaster Prevention Research Institute*, Kyoto University, 1-18.

Wang, C. T. (1948). "Inelastic column theories and an analysis of experimental observations." *Journal of the Aeronautical Sciences*, 15, 283-292.

Wempner, G. A. (1971). "Discrete approximations related to nonlinear theories of solids." *International Journal of Solids and Structures*, 7(11), 1581-1599.

Winter, G. (1947). "Strength of Thin Steel Compression Flanges." *Transactions of the American Society of Civil Engineers*, 112, 527.

Young, B. (2005). "Experimental investigation of cold-formed steel lipped angle concentrically loaded compression members." *Journal of Structural Engineering*, 131(9).

Young, B., and Hartono, W. (2002). "Compression Tests of Stainless Steel Tubular Members." *Journal of Structural Engineering*, 128(6), 754-761.

Young, B., and Liu, Y. (2003). "Experimental Investigation of Cold-Formed Stainless Steel Columns." *Journal of Structural Engineering*, 129(2), 169-176.

Young, B., and Lui, W.-M. (2006). "Tests of cold-formed high strength stainless steel compression members." *Thin-Walled Structures*, 44(2), 224-234.

Ziemian, R. D. (2006). "Guide to stability design criteria for metal structures." John Wiley & Sons, Inc., Hoboken, NJ.

Zureick, A., and Steffen, R. (2000). "Behavior and design of concentrically loaded pultruded angle struts." *Journal of Structural Engineering*, 126(3).

VITA

NICHOLAS A. REYNOLDS

Nicholas Reynolds was born on October 20, 1986 in South Lake Tahoe, CA and grew up in both Carson City, NV and Las Vegas, NV. He graduated from Palo Verde High School in Las Vegas, NV in 2005. Nicholas attended Vanderbilt University in Nashville, TN from 2005-2009, graduating with a B.E. in Civil Engineering. While at Vanderbilt University, Nicholas met his future wife Eleanor, whom he married in 2010. Following his undergraduate studies, Nicholas pursued graduate studies and research at the Georgia Institute of Technology, receiving a M.S. in Civil Engineering in 2011 and a Ph.D. in Civil Engineering in 2013, with an emphasis in Structural Engineering and minor in Mechanics. Nicholas is currently employed as a Research Engineer at the Naval Surface Warfare Center in West Bethesda, MD.